

# Neutron Scattering Investigations of Frustrated Magnets

Tom Fennell

DFRL

Supervisor: Prof. S T Bramwell

*A thesis submitted for the  
degree of Doctor of Philosophy in Chemistry*

ProQuest Number: U642717

All rights reserved

INFORMATION TO ALL USERS

The quality of this reproduction is dependent upon the quality of the copy submitted.

In the unlikely event that the author did not send a complete manuscript and there are missing pages, these will be noted. Also, if material had to be removed, a note will indicate the deletion.



ProQuest U642717

Published by ProQuest LLC(2015). Copyright of the Dissertation is held by the Author.

All rights reserved.

This work is protected against unauthorized copying under Title 17, United States Code.  
Microform Edition © ProQuest LLC.

ProQuest LLC  
789 East Eisenhower Parkway  
P.O. Box 1346  
Ann Arbor, MI 48106-1346

*And this, also, the realities of nature resume their pride of place. It is not with metal that the pilot is in contact, contrary to the vulgar illusions it is thanks to the metal, and by virtue of it, that the pilot rediscovers nature. As I have already said, the machine does not isolate men from the great problems of nature but plunges him more deeply into them.*

Antoine de Saint-Exupéry,

Wind, Sand and Stars

# Abstract

This thesis describes the experimental investigation of frustrated magnetic systems based on the pyrochlore lattice of corner-sharing tetrahedra.  $\text{Ho}_2\text{Ti}_2\text{O}_7$  and  $\text{Dy}_2\text{Ti}_2\text{O}_7$  are examples of spin ices, in which the manifold of disordered magnetic groundstates maps onto that of the proton positions in ice. Using single crystal neutron scattering to measure Bragg and diffuse scattering, the effect of applying magnetic fields along different directions in the crystal was investigated. Different schemes of degeneracy removal were observed for different directions. Long and short range order, and the coexistence of both could be observed by this technique.

The field and temperature dependence of magnetic ordering was studied in  $\text{Ho}_2\text{Ti}_2\text{O}_7$  and  $\text{Dy}_2\text{Ti}_2\text{O}_7$ .  $\text{Ho}_2\text{Ti}_2\text{O}_7$  has been more extensively investigated. The field was applied on  $[00l]$ ,  $[h\bar{h}0]$ ,  $[h\bar{h}\bar{h}]$  and  $[hh2h]$ .  $\text{Dy}_2\text{Ti}_2\text{O}_7$  was studied with the field applied on  $[00l]$  and  $[h\bar{h}0]$  but more detailed information about the evolution of the scattering pattern across a large area of reciprocal space was obtained.

With the field applied on  $[00l]$  both materials showed complete degeneracy removal. A long range ordered structure was formed. Any magnetic diffuse scattering vanished and was entirely replaced by strong magnetic Bragg scattering. At  $T \approx 0.05$  K both materials show unusual magnetization curves, with a prominent step and hysteresis. This was attributed to the extremely slow dynamics of spin ice materials at this temperature.

Both materials were studied in greatest detail with the field applied on  $[h\bar{h}0]$ . The coexistence of long and short range order was observed when the field was raised at  $T = 0.05$  K. The application of a field in this direction separated the spin system into two populations. One could be ordered by the field, and one remained disordered. However, via spin-spin interactions, the field restricted the degeneracy of the disordered spin population. The neutron scattering pattern of  $\text{Dy}_2\text{Ti}_2\text{O}_7$  shows that the spin system was separated into two populations of spin chains, one set ordered and the other only partly so. Cycling the field induced dynamics in these chains, again via spin-spin interactions, as the field acted on the ordered spin chains. These field regulated dynamics were particularly noted in  $\text{Ho}_2\text{Ti}_2\text{O}_7$  where a full field cycle was executed. Raising the temperature in an applied field also activated the dynamics of the partially ordered spin chains. The continued



evolution of the spin system toward a more ordered state, when dynamics can be induced, suggested that a spin ice does indeed have an energetic groundstate.

The remaining two directions probed in  $\text{Ho}_2\text{Ti}_2\text{O}_7$  both have two populations of spins with different Zeeman energies. The competition of the field and the spin-spin interactions was used to investigate the onset of the ice rules regime (field on  $[hh2h]$ , and the breaking of the ice rules by a strong field (field on  $[h\bar{h}\bar{h}]$ ). It was shown that the behavior of  $\text{Ho}_2\text{Ti}_2\text{O}_7$  with field on  $[h\bar{h}\bar{h}]$  was consistent with the “kagomé ice” hypothesis.

# Acknowledgements

*It was the best of times and the worst of times... [1].*

Many people associated with this thesis go two by two, not least the cities in which the work was done. Here are the most important pairings to whom I owe very many thanks, some of the symmetries are surprising:

My supervisors: Steven T Bramwell and Mark Green, for vigilant supervision, enthusiastic contribution and a fair measure of freedom to follow my interests;

My collaborators, neutron scattering mentors and steadying hands on the controls (“what do you mean we can’t go to the heart of the sun?”): Oleg Petrenko and Björn Fåk (PRISMA), Jason Gardner and Bachir Ouladdiaf (D10). I cannot imagine how this work could have been done without their tireless participation, patience and expertise, their uncompromisingly high quality work was invaluable on these experiments;

Cryogenics teams at both sources have shown fantastic commitment and tolerated constant demands: Richard Down and Dave Bates (ISIS) and Jean Louis Raggazzoni (ILL);

Theorists Matt Enjalran and Michel Gingras (Waterloo) for generously producing and sharing the Monte Carlo data;

Crystal growers: The high quality of samples stands as testament to the skills of Geetha Balakrishnan and the group of Barbara Wanklyn;

Clare for pushing me off the roof at the first opportune moment, Andrew Harrison for catching me, his hospitality has considerably reduced the trials and tribulations of writing up;

The peerless Dickon Champion, for endless discussion, some about physics, all of it constructive;

Shadowy figures in the background: Martyn Bull (ISIS) and Garry McIntyre (ILL) for ready help at awkward moments;

Phone a friend perspectives: Jon Goff and Peter Holdsworth;

Perl masters Martin Foster and Naseem Ramsahye for vital labor saving scripts;

Andrew Wildes and Alan Tennant for MatLab hints and tricks;

Symmetry baboozlement: Andrew Wills and Jane Brown;

Cohabitants: Rich and Katie (Mayfair), Sarah and Erika (Marchmont) for being there, man; offices F7 (RI) and 79 (Edinburgh) for tolerance of snoring, music selections and jabbering on the phone;

Friends and family: Graham and Ruth (London), Mary and William (Le Breuil) for support and understanding throughout, Dinah, Donna, Jorge, Simon (special thanks for last minute program production), the KB lunch posse and the EUMC, especially Toby, for arrows, winching and scrubbing.

# Contents

<b>1</b>	<b>Introduction</b>	<b>1</b>
1.1	The Third Law of Thermodynamics . . . . .	1
1.2	The Residual Entropy of Ice . . . . .	2
1.3	Magnetism . . . . .	3
1.3.1	Paramagnetism . . . . .	3
1.3.2	Magnetic Interactions . . . . .	5
1.3.3	Magnetic Order . . . . .	7
1.3.4	Spin Hamiltonians . . . . .	9
1.3.5	Spin Glass Order . . . . .	13
1.4	Frustrated Magnetism . . . . .	13
1.5	The Anderson Mapping . . . . .	18
1.6	The Spin Ice Mapping . . . . .	18
1.6.1	From Ice to Spin Ice . . . . .	20
1.7	Constraint . . . . .	21
1.8	Mechanisms of Degeneracy Removal . . . . .	24
1.8.1	Order by Disorder . . . . .	24
1.8.2	Dipolar Interactions . . . . .	25
1.9	Overview of Frustration . . . . .	26
1.10	Hysteresis and Magnetization Plateaux . . . . .	26
1.10.1	Hysteresis . . . . .	27
1.10.2	Plateaux . . . . .	31
1.11	Summary . . . . .	34

<b>2</b>	<b>Spin Ice</b>	<b>35</b>
2.1	Spin Ice Materials . . . . .	35
2.2	The Importance of Anisotropy . . . . .	37
2.3	Dipolar Spin Ice . . . . .	39
2.4	Dynamics in Spin Ices . . . . .	46
2.5	Spin Ices in Applied Magnetic Fields . . . . .	53
2.6	Kagomé Ice . . . . .	65
2.7	Summary of Spin Ice Properties . . . . .	65
2.8	Other Rare Earth Pyrochlores . . . . .	67
<b>3</b>	<b>Neutron Scattering</b>	<b>69</b>
3.1	Reciprocal Lattice and Diffraction . . . . .	69
3.2	Nuclear Scattering . . . . .	72
3.3	Magnetic Neutron Scattering . . . . .	74
3.4	Extinction . . . . .	76
3.5	Diffuse Scattering . . . . .	81
3.5.1	Diffuse Scattering Analysis . . . . .	81
3.5.2	Diffuse Scattering Calculation for Single Crystals . . . . .	82
3.6	Summary . . . . .	83
<b>4</b>	<b>Analysis of the Structure Factor</b>	<b>85</b>
4.1	The Nuclear Structure Factor . . . . .	86
4.2	The Magnetic Structure Factor with Field Applied on $[00l]$ . . . . .	88
4.3	The Magnetic Structure Factor with Field Applied on $[h\bar{h}0]$ . . . . .	90
4.3.1	The Niitaka Models . . . . .	94
4.4	The Melko Model . . . . .	97
4.5	The Magnetic Structure Factor with Field Applied on $[hhh]$ . . . . .	97
4.6	The Magnetic Structure Factor with Field Applied on $[hh2h]$ . . . . .	100
4.7	Summary . . . . .	103
<b>5</b>	<b>The Field Induced Phases of Holmium Titanate</b>	<b>106</b>
5.1	Experimental details . . . . .	106
5.1.1	POLARIS . . . . .	106

---

5.1.2	D10 . . . . .	107
5.2	Crystal Structure and Extinction Correction . . . . .	109
5.3	Field Applied on $[00l]$ . . . . .	114
5.3.1	Summary of the $[00l]$ Experiment . . . . .	123
5.4	Field Applied on $[h\bar{h}0]$ . . . . .	128
5.4.1	Hysteresis Loop at Base Temperature . . . . .	130
5.4.2	Temperature Scan in Applied Field . . . . .	138
5.4.3	Field Removal After the Temperature Scan . . . . .	140
5.4.4	Summary of the $[h\bar{h}0]$ Experiment . . . . .	143
5.5	Field Applied on $[h\bar{h}\bar{h}]$ . . . . .	145
5.5.1	Hysteresis Loop at 1.8 K . . . . .	148
5.5.2	Hysteresis Loop at 0.05 K . . . . .	152
5.5.3	Summary of $[h\bar{h}\bar{h}]$ Experiment . . . . .	155
5.6	Field Applied on $[hh2h]$ . . . . .	155
5.6.1	Field Scan at 1.9 K . . . . .	164
5.6.2	Field Scan at 2.7 K . . . . .	165
5.6.3	Field Scan at 3.6 K . . . . .	165
5.6.4	Field Scan at 5 K . . . . .	165
5.6.5	Field Scan at 10 K . . . . .	166
5.6.6	Temperature Scan at 2 T . . . . .	166
5.6.7	Summary of $[hh2h]$ Experiment . . . . .	166
<b>6</b>	<b>The Field Induced Phases of Dysprosium Titanate</b>	<b>175</b>
6.1	Experimental Details . . . . .	175
6.1.1	Peak Integration on PRISMA . . . . .	181
6.1.2	Resolution Convolution on PRISMA . . . . .	182
6.2	Zero Field Scattering . . . . .	188
6.3	Field Applied on $[00l]$ . . . . .	199
6.4	Field Applied on $[h\bar{h}0]$ . . . . .	201
6.4.1	Results of the Second Experiment . . . . .	203
6.4.2	Results of the Third Experiment . . . . .	209
6.4.3	Computational Investigations of Model Systems . . . . .	218

6.4.4	Summary of the Third Experiment and Comparison with the Second . . . . .	219
<b>7</b>	<b>Discussion and Conclusions</b>	<b>229</b>
7.1	Dysprosium Titanate and the Dipolar Spin Ice Model . . . . .	229
7.2	Dynamical Regimes in Spin Ices . . . . .	230
7.3	Magnetization Plateaux . . . . .	231
7.4	Field Regulated Dynamics . . . . .	233
7.5	Temperature Activated Dynamics . . . . .	235
7.6	The $Q = X$ State and the True Groundstate . . . . .	235
7.7	Contact with Other Experimental Work . . . . .	237
7.8	Future Work: Theoretical . . . . .	238
7.9	Future Work: Experimental . . . . .	239
7.10	Conclusions . . . . .	240
<b>A</b>	<b>Resolution Calculations for D10</b>	<b>241</b>
A.1	Inversion of the UB Matrix . . . . .	241
A.2	Resolution on D10 . . . . .	246

# List of Figures

1.1	Collinear and non-collinear magnetic structures. . . . .	8
1.2	The effect of an axial crystal field on the degeneracies and Zeeman splittings of an $S = \frac{3}{2}$ ion. . . . .	11
1.3	Spins coupled antiferromagnetically on a triangular plaquette. . . .	14
1.4	Two and three-dimensional lattices built from triangular units. . . .	15
1.5	Triangular Ising Antiferromagnet spin structures. . . . .	17
1.6	Underconstraint in the stacking of Ising spins with ferromagnetic coupling on the pyrochlore lattice. . . . .	19
1.7	The spin ice mapping. . . . .	21
1.8	The spin ice and Anderson mappings. . . . .	22
1.9	Degrees of freedom on 2,3 and 4 spin units. . . . .	23
1.10	Hysteresis loops and Barkhausen noise. . . . .	28
1.11	Magnetization steps in $\text{Mn}_{12}\text{Ac}$ . . . . .	32
1.12	$\text{SrCu}_2(\text{BO}_3)_2$ in the magnetization plateau phase. . . . .	33
2.1	Heat capacity and integrated entropy of $\text{Dy}_2\text{Ti}_2\text{O}_7$ . . . . .	38
2.2	Dipolar spin ice phase diagram. . . . .	41
2.3	$\text{Ho}_2\text{Ti}_2\text{O}_7$ heat capacity fitted with the dipolar spin ice model. . . .	42
2.4	Diffuse scattering in $\text{Ho}_2\text{Ti}_2\text{O}_7$ . . . . .	43
2.5	Mean Field Theory ordering wavevectors for different interaction cutoff distances. . . . .	45
2.6	Heat capacity of a dipolar spin ice model with loop moves. . . . .	47
2.7	Ac susceptibility of $\text{Ho}_2\text{Ti}_2\text{O}_7$ and $\text{Dy}_2\text{Ti}_2\text{O}_7$ . . . . .	49
2.8	Distribution of relaxation times in $\text{Dy}_2\text{Ti}_2\text{O}_7$ . . . . .	51



2.9	Illustration of the effect of relative rates of high and low relaxation processes in a spin ice. . . . .	54
2.10	Single tetrahedron groundstates in different field directions. . . . .	57
2.11	Ordered spin ice structures. . . . .	58
2.12	Magnetization measurements in $\text{Ho}_2\text{Ti}_2\text{O}_7$ . . . . .	59
2.13	Freezing in of long range order in $\text{Ho}_2\text{Ti}_2\text{O}_7$ . . . . .	61
2.14	Temperature modification of $Q = 0$ to $Q = X$ structure in $\text{Ho}_2\text{Ti}_2\text{O}_7$ .	62
2.15	Phase diagram for near neighbor spin ice with field applied on $[00l]$ . .	64
4.1	The pyrochlore unit cell. . . . .	86
4.2	The first Brillouin zone of the f.c.c. lattice. . . . .	87
4.3	$Q=0$ structure and $hk0$ plane reciprocal space. . . . .	91
4.4	The $Q = 0$ $45^\circ$ structure. . . . .	93
4.5	The $Q = X$ structure again. . . . .	95
4.6	Triangular lattice of chains formed by the application of a field. . .	96
4.7	The loop-move groundstate structure again. . . . .	98
4.8	Spin structures for application of field on $[hhh]$ . . . . .	100
4.9	Spin structures for application of field on $[hh2h]$ . . . . .	102
4.10	Peak behaviors with field on $[hh2h]$ . . . . .	103
5.1	Rietveld refinement of powder diffraction data for $\text{Ho}_2\text{Ti}_2\text{O}_7$ collected on the backscattering detector bank of POLARIS . . . . .	112
5.2	Comparison of the quality of $\text{Ho}_2\text{Ti}_2\text{O}_7$ crystals. . . . .	114
5.3	Path through $H/T$ -space with the field applied on $[00l]$ . . . . .	116
5.4	Magnetization with field applied on $[00l]$ . . . . .	118
5.5	Field dependence of the mismatch between calculated and observed intensities for $T=0.7$ K. . . . .	119
5.6	Field dependence of the 400 and 200 peaks at 0.05 K. . . . .	120
5.7	Ewald constructions for double scattering. . . . .	121
5.8	$Q = X$ and $Q = 0$ features in $[00l]$ hysteresis loop. . . . .	124
5.9	$Q = X$ and $Q = 0$ features as remnant $Q = 0$ magnetization is destroyed by rising temperature. . . . .	125
5.10	D10 backgrounds. . . . .	129

5.11	Path through $H/T$ -space with the field applied on $[h\bar{h}0]$ . . . . .	130
5.12	Diffuse features during a hysteresis loop at base temperature measured on D10. . . . .	132
5.13	Bragg peaks in rising field. . . . .	134
5.14	Entire hysteresis loop at 0.05 K with field applied on $[hh0]$ . . . . .	134
5.15	Central region of the hysteresis loop measured at 0.05 K. The peak shown is 002. . . . .	135
5.16	Comparison of evolution of $Q = 0$ (002) and $Q = X$ (001) features. . . . .	138
5.17	Sharpening of the 001 feature as a function of temperature. . . . .	139
5.18	Diffuse features during a temperature scan in applied field measured on D10. . . . .	141
5.19	Bragg peaks and diffuse features during field removal after the temperature scan in applied field, measured on D10. . . . .	142
5.20	The field dependence of Bragg peaks with field on $[h\bar{h}\bar{h}]$ at 1.8 K. . . . .	146
5.21	Magnetization and $R$ -factors with field applied on $[h\bar{h}\bar{h}]$ at 1.8 K. . . . .	150
5.22	Field dependence of the background at the 110 position with field applied on $[h\bar{h}\bar{h}]$ . . . . .	152
5.23	The field dependence of Bragg peaks with field on $[h\bar{h}\bar{h}]$ at 0.05 K. . . . .	153
5.24	Magnetization and $R$ -factors with field applied on $[h\bar{h}\bar{h}]$ at 0.05 K. . . . .	154
5.25	Comparison of peak intensities with field applied on $[hh2h]$ . . . . .	157
5.26	Magnetization and $R$ -factors with field applied on $[hh2h]$ at 1.9 K. . . . .	158
5.27	Magnetization and $R$ -factors with field applied on $[hh2h]$ at 2.7 K. . . . .	159
5.28	Magnetization and $R$ -factors with field applied on $[hh2h]$ at 3.6 K. . . . .	160
5.29	Magnetization and $R$ -factors with field applied on $[hh2h]$ at 5.0 K. . . . .	161
5.30	Magnetization and $R$ -factors with field applied on $[hh2h]$ at 10.0 K. . . . .	162
5.31	Magnetization and $R$ -factors with 2 T field applied on $[hh2h]$ while scanning temperature from 10 - 1.9 K. . . . .	163
5.32	Significance testing of $R$ -factors for field scans at 1.9 and 3.6 K with field on $[hh2h]$ . . . . .	167
5.33	Significance testing of $R$ -factors for field scan at 5 K and temperature scan at 2 T, with field on $[hh2h]$ . . . . .	168
6.1	Paths through $H/T$ space during PRISMA experiments. . . . .	179

6.2	Comparison of integration process for 002 peaks measured at 0.25 and 0.3 T. . . . .	183
6.3	Fits involved in the resolution convolution. . . . .	187
6.4	0, 0, 2 Bragg peak (magnetic) fitted using equation 6.2. . . . .	189
6.5	Exponential decay used to interpolate the fitted values of $\sigma_0$ . . . . .	189
6.6	Exponential decay used to interpolate the fitted values of $\tau$ . . . . .	189
6.7	Scattering intensity in the $hhl$ plane recorded on PRISMA at 20 K. . . . .	190
6.8	Scattering intensity in the $hhl$ plane recorded on PRISMA at 1.3 K. . . . .	190
6.9	Scattering intensity in the $hhl$ plane recorded on PRISMA at 0.3 K with $\phi = -48^\circ$ . . . . .	191
6.10	Scattering intensity in the $hhl$ plane recorded on PRISMA at 0.3 K with $\phi = -32^\circ$ . . . . .	191
6.11	Scattering intensity in the $hhl$ plane recorded on PRISMA at 0.05 K. . . . .	192
6.12	Experimental and theoretical scattering intensity in the $hk0$ plane. . . . .	193
6.13	Slices along $0k0$ at $h00 = 3$ . . . . .	194
6.14	Scattering intensity in the $hhl$ plane recorded on PRISMA at 0.3 K. . . . .	195
6.15	Scattering intensity for the $hhl$ plane calculated by Monte Carlo simulation of the dipolar spin ice model. . . . .	195
6.16	Comparison of experimental and Monte Carlo data for the $hhl$ plane. . . . .	196
6.17	Comparison of zone boundary features with the magnetic form factor of $\text{Dy}^{3+}$ . . . . .	197
6.18	Scattering intensity in the $hk0$ plane recorded on PRISMA at 0.05 K and 1 T. . . . .	200
6.19	Field dependence of Bragg peaks with the field applied on $[00l]$ . . . . .	202
6.20	002 and 003 in zero field, 0.3, 0.5 and 1.0 T applied on $[h\bar{h}0]$ . . . . .	204
6.21	Scattering intensity in the $hhl$ plane recorded on PRISMA at 0.05 K and 1.5 T. . . . .	205
6.22	Fits used in the extraction of intrachain correlation lengths from the 003 feature. . . . .	206
6.23	Intensities and correlation lengths during the hysteresis loop measured in the second experiment on PRISMA. . . . .	208

6.24	Correlation lengths during the temperature scans measured in the second experiment on PRISMA. . . . .	210
6.25	Intensities and correlation lengths during the hysteresis loop measured at base temperature in the third experiment on PRISMA. . .	211
6.26	Intensities and correlation lengths as the temperature was raised in an applied field in the third experiment on PRISMA. . . . .	212
6.27	Intensities during the hysteresis loop measured at 1.9 K in the third experiment on PRISMA. . . . .	213
6.28	Intensities and correlation lengths as the field was removed after field cooling in the third experiment on PRISMA. . . . .	215
6.29	Intensities and correlation lengths during the first hysteresis loop measured at 0.3 K in the third experiment on PRISMA. . . . .	216
6.30	Intensities and correlation lengths during the second hysteresis loop measured at 0.3 K in the third experiment on PRISMA. . . . .	217
6.31	Calculated diffuse scattering patterns for application of field on $[hh0]$ in $\text{Dy}_2\text{Ti}_2\text{O}_7$ . . . . .	220
6.32	Calculated diffuse scattering patterns for application of field on $[hh0]$ in $\text{Dy}_2\text{Ti}_2\text{O}_7(2)$ . . . . .	221
6.33	Time dependence of applied magnetic field. . . . .	223
6.34	Time and field dependence of the 002 peak. . . . .	224
6.35	Comparison of hysteresis loops. . . . .	225
6.36	Field dependence of the 002 peak during a hysteresis loop at 0.05 K and after cooling to the same temperature in 0.4 T. . . . .	226
6.37	Field and temperature dependence of the amplitude of the 003 feature.	228
7.1	Comparison of hysteresis loops with field applied on $[00l]$ for $\text{Dy}_2\text{Ti}_2\text{O}_7$ and $\text{Ho}_2\text{Ti}_2\text{O}_7$ . . . . .	232
A.1	Data slices on D10 . . . . .	246
A.2	Omega scans on D10 in reciprocal space. . . . .	247
A.3	D10 resolution. . . . .	248

# List of Tables

4.1	Spin directions in different spin structure models. . . . .	105
5.1	Crystal structure parameters for $\text{Ho}_2\text{Ti}_2\text{O}_7$ from Rietveld refinements of POLARIS data. . . . .	111
5.2	Refinement parameters for the crystal structure and extinction correction measured on D10 . . . . .	115
5.3	Spin structure models. . . . .	174
6.1	Isotopic abundances and scattering lengths of natural Dysprosium and the enriched sample used in these experiments. . . . .	177

# Chapter 1

## Introduction

### 1.1 The Third Law of Thermodynamics

The third law of thermodynamics, as formulated by Planck, states that “the entropy of a pure solid or liquid in internal thermodynamic equilibrium should be zero at absolute zero” [2]. Since entropy is

$$S = k_B \log W, \tag{1.1}$$

where  $W$  is the number of configurations available to the system, this leads to the condition that the ground state of the system is non-degenerate, and therefore long range ordered. Is it possible to have a system that has a degenerate groundstate? Can it achieve order, and if so, how? What will happen if a unique groundstate cannot be selected<sup>a</sup>?

---

<sup>a</sup>The words unique, and degenerate are employed with rather specific meanings in this work. All magnets are degenerate to some degree, for example an Ising ferromagnet has two degenerate groundstates related by time reversal symmetry. However, the number of groundstates is finite, and remains so, even in the thermodynamic limit. For the Ising ferromagnet there are only ever two groundstates, regardless of the size of the system. Such a system is not frustrated and here these groundstates are described as unique. When the degeneracy increases with the system size, it will eventually become macroscopic. Such a system is frustrated and when discussing degenerate groundstates, we are strictly referring to macroscopic degeneracy in the thermodynamic limit [3].

## 1.2 The Residual Entropy of Ice

The crystal structure of ice was investigated in the early twentieth century and found to pose an enigmatic problem. Although the oxygen atoms were located relatively easily by X-ray diffraction, the hydrogen atoms (i.e. protons) were not. This was not simply a problem of contrast in X-ray diffraction - in fact, the protons are disordered. To attempt to locate the protons, Bernal and Fowler formulated a set of “ice rules” to describe the positions of protons in the structure of ice. They stated that the water molecules remained intact and therefore each oxygen atom had two protons attached by short covalent bonds and two associated by longer hydrogen bonds. Their ice rules essentially said that each oxygen atom must have four associated hydrogen atoms, two close and two distant.

It had been determined experimentally that ice had residual entropy [4]. This was discovered by measuring and integrating the heat capacity from ultra-low temperature up to the gas phase, where the entropy can be computed. The result was a missing contribution to the entropy. At the lowest temperatures ice still has a residual entropy and so is more disordered than would be expected. The reason for this was shown to be the disorder of the protons throughout the ordered oxygen structure. Pauling realized that the ice rules could be satisfied in six different ways for any oxygen atom and that this lead to the residual entropy. An approximate derivation of the magnitude of the configurational entropy is as follows [5]. Consider a sample of ice consisting of  $N$   $\text{H}_2\text{O}$  molecules, each H atom may be in 2 positions, hence there are  $2^{2N}$  possible arrangements. At a single oxygen atom there are  $2^4 = 16$  ways of arranging the 4 H atoms around the oxygen atom. Of these, only six obey the ice rules. The total number of permitted arrangements is therefore

$$W = 2^{2N} \times \left(\frac{6}{16}\right)^N = \left(\frac{3}{2}\right)^N, \quad (1.2)$$

and therefore

$$S = Nk \ln \frac{3}{2}. \quad (1.3)$$

Ice is one of the canonical examples of frustration. It is now known that there is an ordered groundstate, ice-XI, which is favored below 70 K [6]. However, at the

temperature at which the oxygen network forms, the longer ranged interactions which must stabilize this state are of negligible importance and so only the ice rule determines the proton positions, and this is degenerate, or under-constrained. As the ice is cooled further, the molecular reorientation dynamics become so slow that it is not possible to obtain this phase in pure samples (it was observed by doping with  $\text{OH}^-$  ions which leave vacancies in the hydrogen bonded network, allowing reorientation). As with the frustrated magnets discussed below, the degeneracy can only be resolved when a minor perturbation to the energetics becomes important. Even if a degeneracy lifting perturbation is available, when a sufficiently low temperature is reached the dynamics of the system are so slow that the ordered state may never be selected.

## 1.3 Magnetism

Magnetism is an enormous field of study with aspects ranging from the theoretical investigation of critical phenomena and phase transitions to experimental geophysics. This thesis is concerned with an aspect of the field often called model magnetism. The term model magnetism derives from the use of magnetic systems as a starting point for the solution of statistical thermodynamical problems.

### 1.3.1 Paramagnetism

Thermodynamic analogies with fluids begin with the ideal paramagnet. The paramagnetic phase is a collection of randomly oriented, non-interacting magnetic moments. This is analogous to an ideal gas. Thermodynamic relations can be derived by substituting the variables magnetization for the negative of the density and applied field for pressure [7]. The foremost failure of the ideal gas is the neglect of interactions between the gas molecules. The presence of magnetic interactions means that real paramagnets also deviate from ideality. The interactions cause a phase transition, usually into an ordered phase such as a ferromagnet. The ideal paramagnet is worth further attention. Experimentally interesting quantities are the susceptibility and the magnetization. These can be calculated by application of quantum and statistical mechanics [8].



The magnetic moment of an atom or ion in free space is

$$\mu = \gamma \hbar \mathbf{J} = -g\mu_B \mathbf{J}, \quad (1.4)$$

where the total angular momentum  $\hbar \mathbf{J}$  is the sum of orbital and spin angular momentum. The constant  $\gamma$  is the gyromagnetic ratio and  $g$  is the spectroscopic splitting factor ( $g\mu_B = -\gamma \hbar$ ). For an electron  $g = 2.0023$ , and is usually taken as 2.00. For a free atom the  $g$  factor is given by

$$g = 1 + \frac{J(J+1) + S(S+1) - L(L+1)}{2J(J+1)}. \quad (1.5)$$

In absence of a field the energy levels of the ion are degenerate. The application of a field will split the levels, depending upon the projection of the moment in the field direction. The simplest system is an ensemble of spin  $\frac{1}{2}$  ions. The energy levels of the ions in the field are

$$U = -\mu \cdot \mathbf{B} = m_J g \mu_B B, \quad (1.6)$$

$m_J$  is the azimuthal quantum number and has values  $J, J-1, \dots, -J$ . In this case  $m_J = \pm \frac{1}{2}$  and  $g = 2$ . This results in a familiar two level splitting with separation  $2\mu_B B$ .

The two levels correspond to parallel and antiparallel projections of the moment on the field direction. The antiparallel alignment of the spin with the field is energetically unfavorable. This creates a population difference. The populations of the levels depend on the available thermal energy and the strength of the applied field. By application of the Boltzman distribution the populations are

$$\frac{N_1}{N} = \frac{\exp(\frac{\mu_B B}{k_B T})}{\exp(\frac{\mu_B B}{k_B T}) + \exp(\frac{-\mu_B B}{k_B T})}; \quad (1.7)$$

$$\frac{N_2}{N} = \frac{\exp(\frac{-\mu_B B}{k_B T})}{\exp(\frac{\mu_B B}{k_B T}) + \exp(\frac{-\mu_B B}{k_B T})}; \quad (1.8)$$

where  $N_1$  and  $N_2$  are the populations of the lower and upper levels, and  $N = N_1 + N_2$  is the total number of atoms.

Since there is a population difference there will also be a net moment. With  $N$  atoms per unit volume (and  $x = \frac{\mu_B B}{k_B T}$ ) the net magnetization is

$$M = (N_1 - N_2)\mu = N\mu \cdot \frac{\exp x - \exp -x}{\exp x + \exp -x} = N\mu \tanh x. \quad (1.9)$$

This is a special case for  $J = \frac{1}{2}$ . In a magnetic field an atom with angular momentum quantum number  $J$  has  $2J+1$  equally spaced levels. The magnetization is given by

$$M = NgJ\mu_B B_J(x), \quad \left( x = \frac{gJ\mu_B B}{k_B T} \right), \quad (1.10)$$

where  $B_J$  is the Brillouin function and is defined by

$$B_J(x) = \frac{2J+1}{2J} \coth\left(\frac{(2J+1)x}{2J}\right) - \frac{1}{2J} \coth\left(\frac{x}{2J}\right). \quad (1.11)$$

For  $x \ll 1$

$$\coth x = \frac{1}{x} + \frac{x}{3} - \frac{x^3}{45} + \dots, \quad (1.12)$$

and the susceptibility is

$$\frac{M}{B} \cong \frac{NJ(J+1)g^2\mu_B^2}{3k_B T} = \frac{C}{T}. \quad (1.13)$$

The constant  $C$  is the Curie constant. It describes the common observation that the inverse of the susceptibility of a paramagnet is proportional to temperature.

Equation 1.13 is the limiting form of the Curie Law, which applies when  $\frac{gJ\mu_B B}{k_B T} \ll 1$ . This is the high temperature limit when thermal fluctuations overcome all spin-spin interactions. Experimentally it is observed that as the temperature is decreased, and the magnetic interactions become important, the susceptibility ( $\chi$ ) approximately has the form [9]

$$\chi = \frac{C}{T - \theta_{CW}}, \quad (1.14)$$

where  $\theta_{CW}$  is the Curie-Weiss constant. The correction term  $\theta_{CW}$  has units of temperature and may be positive or negative. The sign of the Curie-Weiss constant reflects the nature of the ordered phase. The system is described as ferromagnetic if  $\theta_{CW}$  is positive and antiferromagnetic if  $\theta_{CW}$  is negative. In the archetypal ferromagnet all the moments are aligned in the same direction. Conversely the antiferromagnet has all nearest neighbor spins opposed.

### 1.3.2 Magnetic Interactions

There are different pathways by which magnetic moments may interact. These are direct exchange, the RKKY interaction, superexchange, and the dipolar interaction [10].

### Direct Exchange

This is an electronic effect. Orbital overlap between two atoms means that their electrons become correlated. Coulombic repulsion is minimized and the Pauli exclusion principle satisfied by keeping the electrons well separated and anti-parallel. This is not an important mechanism in real materials as the overlap of the magnetic  $d$  or  $f$  electron wavefunctions is extremely small.

### RKKY

This is an indirect-exchange mechanism which occurs only in metallic systems as it is mediated by conduction electrons. The presence of a localized magnetic moment in a sea of conduction electrons causes an oscillation in the susceptibility of the conduction electrons, and this can couple two spins. The RKKY interaction is stronger and longer ranged than the direct exchange interaction and is important in magnetic alloys.

### Superexchange

Superexchange is usually the most important type of magnetic interaction in insulators and semiconductors. Like the direct exchange mechanism it is mediated by orbital overlap. However, this occurs via an intermediate ligand or anion. Usually superexchange interactions are antiferromagnetic, but ferromagnetic exchange may occur depending on the orbitals and angles involved. Superexchange pathways are short, usually confined to nearest neighbors, though may extend to second or third nearest neighbors.

### Dipolar Interactions

The dipolar interaction is present in all magnets but is weak when the moments are small, it becomes most important in rare earth magnets where moments are large. It occurs through space and is anisotropic and long ranged, due to the  $1/r^3$  dependence. It has the form:

$$\mathbb{H}_{ij}^{\text{dip}} = \frac{1}{r_{ij}^3} [\mu_i \cdot \mu_j - 3(\mu_i \cdot \hat{r}_{ij})(\mu_j \cdot \hat{r}_{ij})]. \quad (1.15)$$

### 1.3.3 Magnetic Order

Diffraction of neutrons below the ordering temperature is the pre-eminent technique for investigating magnetic order at the microscopic level. Consequently much of the discussion of magnetic structures is couched in terms originating in the language of scattering theory and diffraction from lattices. The magnetic structure is a periodic property of the crystal. Evidently it need not have the same period as the atomic structure of the crystal. Let us consider the magnetic ordering to be a distribution of moments  $\mathbf{m}_{lj}$  associated with the Bravais sublattice  $j$  of the nuclear unit cell. Evidently it can be Fourier expanded as

$$\mathbf{m}_{lj} = \sum_{\mathbf{k}} \mathbf{m}_{\mathbf{k}j} \exp(-i\mathbf{k} \cdot \mathbf{R}_l) \quad (1.16)$$

where  $\mathbf{R}_l$  is the position of the  $l$ th unit cell [11]. The wavevector  $\mathbf{k}$  is of central importance in the determination and description of the magnetic structure. It is a propagation vector describing the relation between the nuclear basis and the magnetic superlattice [12]. The wavevector  $\mathbf{k}$  is one member of a set of equivalent wavevectors  $\mathbf{k}_p$  called the star of  $\mathbf{k}$ . The other wavevectors in the star are obtained by applying the symmetry operations of the paramagnetic group (the space group) to  $\mathbf{k}$ . A magnetic structure may be characterized by more than one wavevector giving single- $\mathbf{k}$  or multi- $\mathbf{k}$  structures. The magnetic structure belongs to magnetic symmetry group. These contain the information of the crystallographic space group, and also additional symmetry operations to take account of the magnetic moment at each site [13, 14]. Many ordered structures are possible since there are 1421 magnetic symmetry groups. The structure may be collinear, non-collinear, or helical. Examples are depicted in 1.1. The essential feature of all magnetic structures is that the order is invariant under arbitrary lattice translations (with consideration of the propagation vector), and that the magnetic energy is minimized.

The difference between the ordered phase and the paramagnet is a statistical one [15]. From the random distribution of spins in the paramagnet a phase is formed in which, on average, the spins are correlated. The ordering transition in a magnetic material is a thermodynamic phase transition. There will be an associated divergence in a thermodynamic quantity at  $T_c$  [16]. The change in

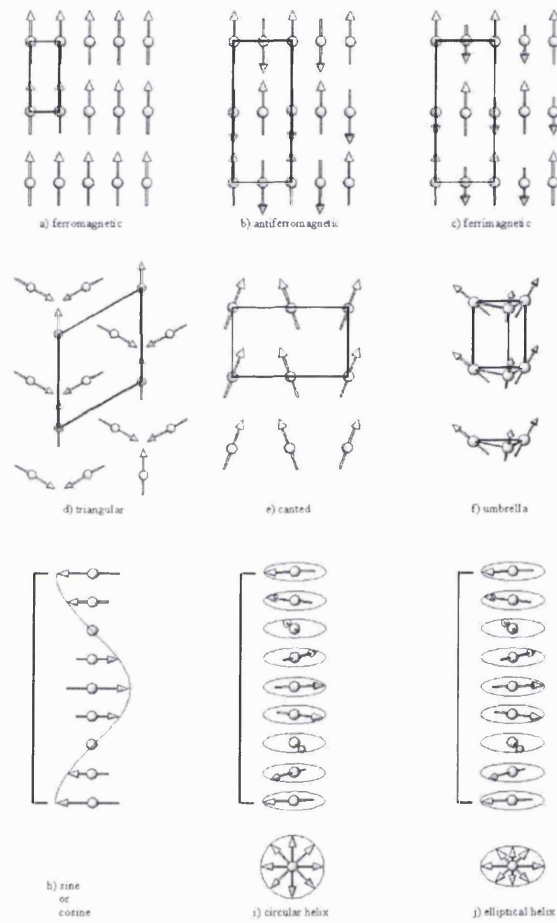


**Figure 1.1:** Collinear and non-collinear magnetic structures [12].

properties of the system as the phase boundary is crossed can be described by an order parameter  $\phi$ . The order parameter is defined differently for different systems, it is a quantity whose thermal average vanishes above the transition temperature.  $\phi$  may fluctuate in space and time, in general the thermal average over a long period of equilibrium is of interest [17]. For a ferromagnet it would be the instantaneous mean magnetization, for an antiferromagnet two (for collinear order) sublattice magnetizations can be used as separate order parameters.

Another useful parameter that will change as a magnet enters an ordered phase is a correlation function. In general  $\langle \mathbf{S}_i \cdot \mathbf{S}_j \rangle$  is a correlation function, where  $\langle \dots \rangle$  is a thermal average. The correlation function shows how closely correlated different parts of an interacting system are. If the spins are non-interacting the correlation function is simply a product of individual spin contributions, i.e.  $\langle \mathbf{S}_i \mathbf{S}_j \rangle = \langle \mathbf{S}_i \rangle \langle \mathbf{S}_j \rangle$ , with  $i \neq j$ . A two-point connected correlation function describes the correlation between two spins  $i$  and  $j$ , for example, in the system. It is formulated to take account of the correlation due to interactions only [17]. This is achieved by subtracting the contribution due only to temporal correlation of individual spins with themselves, as

$$G_c^{(2)}(i, j) = \langle \mathbf{S}_i \mathbf{S}_j \rangle - \langle \mathbf{S}_i \rangle \langle \mathbf{S}_j \rangle. \quad (1.17)$$

As the temperature is decreased correlation due to interactions between spins increases as thermal fluctuations become less effective at randomizing the spins. Short-range correlation occurs as  $T_c$  is approached, and on reaching  $T_c$  the correlation length diverges and the phase transition occurs. Once  $T < T_c$  the system has long range order and the order parameter is finite. Even below  $T_c$  the moments continue to fluctuate. The ordered structure is the time average of the moment distribution. These fluctuations continue to decrease as the sample is cooled further and so the order parameter continues to rise.

### 1.3.4 Spin Hamiltonians

In order to understand why the system selects a particular ordered state the different factors influencing the spins must be considered. The ordering transition is a co-operative effect and the divergence in the thermodynamic quantities at  $T_c$  is due to the divergence of the correlation length and the fluctuation of the order

parameter on all length scales. Co-operative phenomena depend on the way in which order is propagated through the system from one spin to the next [7].

To describe the magnetism of a compound a spin Hamiltonian is used to determine energies of microstates of the system. Application of statistical thermodynamics then allows the calculation of properties such as the specific heat or susceptibility, as in the ideal paramagnet discussed above. In general the energy of a state is determined by the moments (size and type) and exchange interactions with neighbors and further neighbors. Terms can be added to allow, for example, coupling to an easy axis in the crystal structure, coupling to an applied field and for dipolar exchange.

The first important question in the construction of a spin Hamiltonian is the nature of the moment. As mentioned previously, problems may be formulated for classical or quantum cases. Evidently an atomic magnetic moment is an object which will be best described by quantum mechanics, but classical problems are more readily soluble. A quantum mechanical moment has both spin and orbital angular momentum contributions. However, this can be expressed as an effective spin with a suitably adjusted  $g$  value. In problems with quantum moments the effect of this parameterization is to allow the use of spin operators only in the Hamiltonian. For example if the ion in question has only two accessible energy levels, or is constrained to two distinct directions, it can be described by an effective or fictitious spin  $\frac{1}{2}$  [15, 18]. However, it is very difficult to make fully quantum mechanical models tractable on an extended lattice. They can be simplified by replacing the quantum spins with classical vector spins. Terms involving the spin operators can be replaced by classical expressions for the energy.

The ion is strongly influenced by its environment [9]. The crystal field is very important in determining the energy level splittings of an ion. In a free ion the energy levels of the ion are degenerate. Application of a magnetic field leads to the Zeeman splitting of the levels, as in equation 1.4. However, if the free ion were considered in a crystal field then the degeneracy of the levels would be partially raised. For example if  $m_s = \frac{3}{2}$  then an axial crystal field will resolve the  $m_s = \pm\frac{1}{2}, \pm\frac{3}{2}$  degeneracy. The  $\pm\frac{3}{2}$  levels are split from the  $\pm\frac{1}{2}$  levels. Application of a field will then cause a Zeeman splitting into two separate doublets, as shown

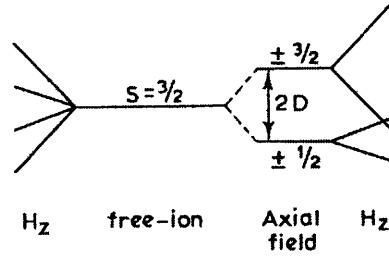


**Figure 1.2:** The effect of an axial crystal field on the degeneracies and Zeeman splittings of an  $S = \frac{3}{2}$  ion [9].

in figure 1.2 [9]. The crystal field is a zero field splitting as it is intrinsic to the material and arises without application of a field. The symmetry of the crystal field may mean that the zero field splitting will differ depending on direction. For example a tetragonal crystal field will lead to two zero field splitting parameters, one parallel and one perpendicular to the principal axis of the molecule.

The crystal field is essential in the effective spin approximations mentioned above. It is the zero field splitting that leads to situations in which only the lowest levels are available. It is the anisotropy of the crystal field that leads to an easy axis to which the moment is constrained. Both of these effects are essential in the discussion of  $\text{Ln}_2\text{Ti}_2\text{O}_7$  below [19].

Having described the energy levels and anisotropy which determine the behavior of an isolated spin, it is necessary to consider interactions with other spins. The first approximation available is the Mean Field Theory (MFT). The basic assumption of MFT is that the spins interact by an effective molecular or mean field. The strength of the mean field is proportional to the magnetization. In a mean field theoretical derivation of the Curie law (1.13) the applied field term is augmented by a molecular field  $H_m$  to give an effective field. It is assumed that the molecular field is proportional to magnetization so that  $H_m = \lambda M(T, H)$  and so the effective field is

$$H_{eff} = H + \lambda M(T, H), \quad (1.18)$$

where  $\lambda$  is the molecular field parameter. Ultimately this leads to a derivation



of the Curie-Weiss Law (equation 1.14) in which it is found that the correction term  $\theta_{CW} = \lambda C = T_c$ . This is the crudest form of MFT in which the form of the molecular field is completely ignored [7].

To take a further step requires some microscopic model for the exchange interactions between spins. The simplest interaction Hamiltonians allowing only for exchange interactions with the nearest neighboring spins can be generalized as

$$\mathbb{H} = -2J \sum_{i>j} [aS_i^z S_j^z + b(S_i^x S_j^x + S_i^y S_j^y)] \quad (1.19)$$

where summation is over nearest neighbors only and  $J$  is the exchange constant [20]. If  $a = b = 1$  the interactions are wholly isotropic, this is known as the Heisenberg model. If  $a = 1$  and  $b = 0$  the Ising model is obtained. In this case the spins are one dimensional vectors and are constrained to lie on an axis. They can point only “up” or “down”. Exchange is considered only between the  $z$ -components of the spins. The third common case is the  $XY$  model in which  $a = 0$  and  $b = 1$ .  $XY$  spins only interact within the  $XY$  plane.

Realization of these spin models depends largely on the crystal field. As mentioned previously a strongly anisotropic crystal field will constrain the spins to their easy axes and this is a common way to achieve an experimental system with Ising character. The same effect will also lead to a planar Heisenberg magnet if the spin is constrained to the plane perpendicular to the axis of the crystal field. This is not exactly the same as the  $XY$  model where the interactions but not the spins are constrained to the easy plane. It is much harder to realize a truly isotropic Heisenberg model. Real crystals have several sources of anisotropy, chief of which is the crystal field. Cubic crystal fields are rare because a Jahn-Teller distortion is usually favored. The best way to avoid this is to use a “spin-only” ion such as  $Gd^{3+}$  [20].

These three models have been extensively investigated. The Ising model is only classical due to its violation of the uncertainty principle if applied to a quantum spin. Quantum and classical versions exist for the other models. The effects of lattice and spin dimensionality are the central themes of investigation [20]. As generalizations it can be stated that the three dimensional models are all expected to order at finite temperatures and to show quasi-classical behavior. As the lattice

dimensionality is decreased and the spin dimensionality is increased the transition to order occurs at lower and lower temperature. For all one-dimensional models no long range order occurs at any temperature greater than zero [20]. Ultimately, and in contrast to the theoretical models discussed below, order is achieved, even if only at zero temperature.

### 1.3.5 Spin Glass Order

The preceding discussion has concerned magnets in which there is no appreciable structural disorder. There is another type of magnet in which the spin sites are disordered. The canonical example of this type of magnet is dilute alloy containing magnetic ions such as  $\text{Au}_{1-x}\text{Mn}_x$ . The characteristic feature of the spin glass is a freezing transition in which the system changes from a paramagnet to a history dependent frozen state. The reason for this is the random distribution of the magnetic ions. Locally clusters of spins can minimize their energies but between clusters are spins which cannot simultaneously minimize their interaction energies with all their neighbors. The frozen state has lead to the name spin glass for these materials [10]. The essential features of the spin glass are the structural disorder and the bond disorder. Bond disorder is due to different nearest neighbor distances at different sites and also exchange interactions with distance dependent sign.

## 1.4 Frustrated Magnetism

Magnetism is often a testing ground for statistical mechanical theories, and the concepts of frustration are no exception. The majority of work on frustration addresses the behavior of magnets.

One of the definitions of a geometrically frustrated magnet is a magnet with a non-unique groundstate. The other common definition is a system in which the energy of the interactions of all the spins cannot be simultaneously minimized. For example if three spins are arranged at the corners of a triangle, and coupled antiferromagnetically, it can be seen that if the orientation of one spin on a triangle is chosen, then each of the other two cannot simultaneously satisfy their lowest energy alignment with both neighbors (see figure 1.3).

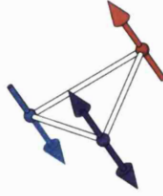


**Figure 1.3:** Spins coupled antiferromagnetically on a triangular plaquette. With the blue and red spin aligned antiparallel, it is impossible for the purple spin to minimize its exchange energy with both. Either alignment of the purple spin is equally favorable, and both have unfavorable interactions between two of the spins.

It is important to add that these conditions must arise due to the geometry of the lattice alone, hence geometrical frustration. Site disorder leading to frustration and ground states lacking in long range order occurs in the spin glasses. In geometrical frustration the structures are treated by theorists as being perfectly structurally ordered. Often this is a good approximation to the experimental situation. An experimental definition is that the system remains in some sort of paramagnetic state well below  $T = \theta_{CW}$ .

All frustrated lattices have one essential feature in common, namely that they are based on triangular units (these units are also referred to as plaquettes, or simplices, connected to form a simplex lattice) [21, 22]. In two dimensions the triangular and kagomé are triangle based lattices. If the triangles are connected in three-dimensions it can be seen that the three-dimensional sub-unit obtained is a tetrahedron. Addition of tetrahedra leads to a f.c.c. lattice for edge sharing and the pyrochlore lattice for corner sharing tetrahedra. These frustrated lattices are illustrated in figure 1.4.

The first geometrically frustrated lattice to receive theoretical attention was the triangular Ising net (with the Ising axis perpendicular to the plane of the lattice) which was investigated by Wannier [23]. The results obtained are generally true in a qualitative sense for other frustrated lattices. The ferromagnet is not frustrated as all the spin interactions can be easily satisfied. However, for antiferromagnets

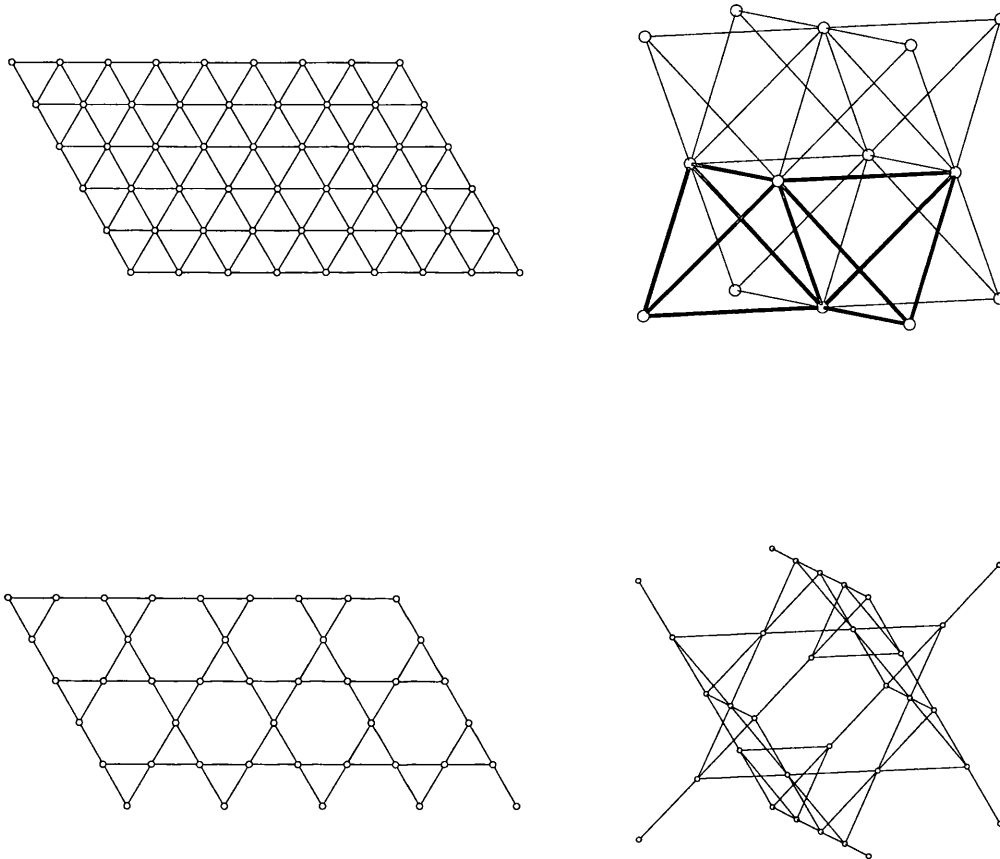


**Figure 1.4:** Four lattices built from triangular units. In two dimensions edge sharing triangles give a simple triangular lattice (top left). The three-dimensional analog is a face centered cubic lattice which contains edge sharing tetrahedra (top right, two tetrahedra have been highlighted). Corner linked triangles in two dimensions form a kagomé lattice, with distinctive star motif (bottom left). In three dimensions, corner sharing tetrahedra form a pyrochlore lattice, which contains kagomé planes linked by interstitial tetrahedra (bottom right).

the final arrangement contains at least one third “wrong” interactions.

Examples for a triangular lattice are shown in figure 1.5. The first has a periodic arrangement of spins, even if the interactions are not all favorable, and as such could represent a unique groundstate. Wannier showed that the fundamental difference between frustrated and unfrustrated lattices is not the absence of an ordered groundstate, but the presence of many disordered groundstates.

In figure 1.5 the ordered spin structure can be viewed as being constructed from chains of alternating spins. In this case they are stacked perfectly. Wannier describes a structure of the same energy produced by independent stacking of the chains with a large number of “stacking errors.” The periodic structure has been destroyed but the energy remains the same. More complicated considerations are required to produce a finite entropy arrangement. One way in which this was achieved was to divide the triangular lattice into three sublattices. Spins were fixed “up” on one and “down” on another. This means that around any spin of the third sublattice there are equal numbers of favorable and unfavorable interactions, regardless of its orientation. Consequently any of these spins can be flipped without any energy cost. Furthermore, if three of these free spins should have the same sign then the central spin can also be flipped, contributing further to the weight of the groundstate. From these considerations alone the zero-point entropy is

$$S(0) > \frac{5}{12} R \ln 2 = 0.288811 R. \quad (1.20)$$

Long range order offers no energy advantage for these systems. In the final part of figure 1.5 two domains of long range order adjoin each other across a boundary region. The barrier region can be constructed such that its energy is the same as that of the ordered regions. Because of this there is an extensive number of disordered groundstates. Consequently the ordered structure is unlikely to be realized because it has a very low statistical weight. The collection of groundstates, some ordered, but the vast majority disordered, which is possessed by a frustrated magnet has since been named a “manifold.”

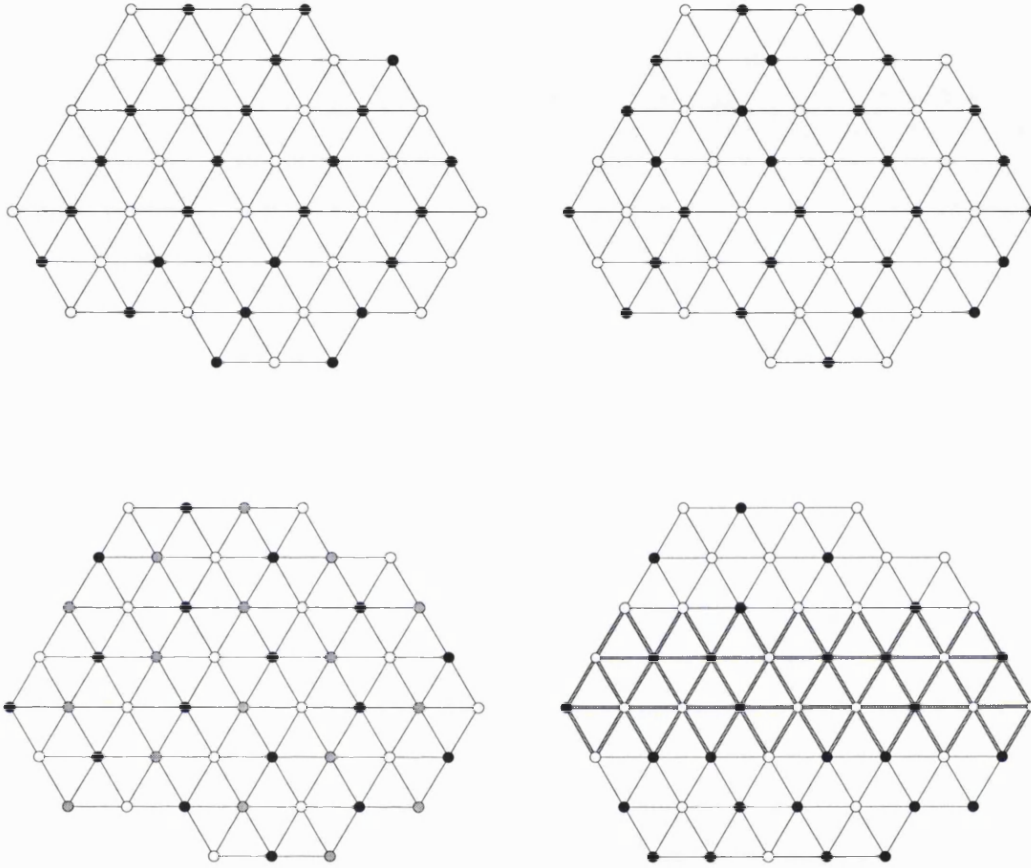


**Figure 1.5:** Spin structures of the triangular lattice antiferromagnet as envisaged by Wannier (up and down spins are represented as black or white atoms respectively) [23]. All the structures have the same internal energy, but different entropies. A manifold of degenerate groundstates is possible, it contains fully ordered states (such as the one at top left). This ordered structure can be disrupted by stacking errors with no energy cost (as at top right). At bottom left a structure with finite entropy has been produced, the grey spins experience equal numbers of favorable and unfavorable interactions and so can be flipped with no energy cost. At bottom right the structure consists of two regions of long range order, separated by a boundary, this can be constructed so that all regions have the same energy. Wannier used this to illustrate the point that long range order offers no energetic advantage to these systems.

## 1.5 The Anderson Mapping

Anderson discussed both charge and antiferromagnetic order in spinels [24]. During this work, the first analogy between a magnet and the ice problem was noted. The spinels contain a pyrochlore lattice (which is cubic). Anderson was considering either the charge ordering of two cations, or an antiferromagnet and so populated the lattice with two species  $+$  and  $-$ , which must be paired whenever possible. The number of pairs is maximized by putting two of each on each tetrahedron.

The relation to Pauling's ice problem is as follows. The pyrochlore lattice contains two types of tetrahedron (say A and B, or more descriptively, up and down, see figure 1.4 or 1.6) each sharing spins only with tetrahedra of the other type. The oxygen atom of the ice structure is at the center of the tetrahedra. If the  $+$ s on one set (i.e. up or down tetrahedra) of tetrahedra represent "proton near oxygen atom" and vice versa for the other set, then the problems become the same. The structure of common water ice is not really cubic. The tetrahedra of the pyrochlore lattice are arranged on a diamond lattice, only if they were arranged on a lattice with hexagonal symmetry would it be identical with ice. The actual lattice was referred by to Anderson as a "cubic ice" (ice has many phases, and it is possible to produce a cubic ice).

This mapping describes an antiferromagnet with uniaxial Ising symmetry. Such a system cannot exist because the axis which is chosen will be arbitrary and does not reflect the cubic symmetry of the lattice. This is the major problem with the mapping from an experimental point of view. However, it does represent the first relation of the two problems. The relation of the uniaxial antiferromagnet and the ice problem is depicted in figure 1.8.

## 1.6 The Spin Ice Mapping

The statement that frustration is a property only of antiferromagnets has been found to be untrue for Ising spins on the pyrochlore lattice [25]. Since the pyrochlore lattice is cubic, appropriate Ising easy axes are the  $\langle 111 \rangle$  directions. This corresponds to the spins pointing either into or out of a tetrahedron (see figure 1.6). The groundstate of a single *antiferromagnetic* tetrahedron has all four

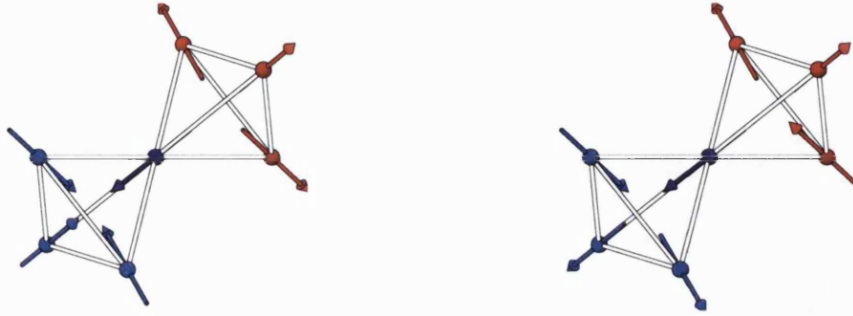


**Figure 1.6:** Stacking of antiferromagnetic (left) and ferromagnetic (right) tetrahedra. In the antiferromagnetic case specifying the state of the blue tetrahedron as “all in” is enough to propagate order through the purple atom to the red tetrahedron which is constrained to be “all out”. In the ferromagnetic case specifying the state of the blue tetrahedron does not constrain the red one. One “two-in-two-out” groundstate is shown but with the purple spin in this position three others are possible (for the red tetrahedron alone). This underconstraint leads to a manifold of spin ice states.

spins pointing either into or out of the tetrahedron. Spins pointing into tetrahedra of type A point out of tetrahedra of type B. Both A and B tetrahedra have unique spin arrangements and the stacking of the A and B tetrahedra leads to a long range ordered groundstate. This is the non-collinear structure of  $\text{FeF}_3$  [26]. The propagation of order by stacking antiferromagnetic tetrahedra is illustrated in figure 1.6.

When the coupling is *ferromagnetic* the groundstate of the tetrahedron has two spins pointing into the center and two spins pointing out [25]. On a single tetrahedron this can be achieved in six different ways. If another tetrahedron is added to the first, the arrangement of spins on the first tetrahedron does not completely constrain the arrangement of spins on the second. The stacking of the tetrahedra therefore leads to a manifold of degenerate states. An illustration of how imposing the ferromagnetic groundstate on one tetrahedron does not fully constrain the selection of the groundstate of the adjacent tetrahedron is shown in figure 1.6.

Two elegant arguments allow the determination of the groundstate degeneracy and associated configurational entropy. The first is the calculation of the con-



figurational entropy of ice (given above); the second is the mapping of the spin problem onto the ice problem.

### 1.6.1 From Ice to Spin Ice

Consider a cubic ice structure in which the oxygen atoms lie on a diamond lattice and the protons lie on the oxygen-oxygen line. If tetrahedra are constructed by joining the oxygen-oxygen midpoints a pyrochlore lattice is obtained. There is no atom at the vertex of the tetrahedron which has been constructed in the ice structure, as the hydrogen atoms are not symmetrically disposed about the oxygen atom. All the protons are displaced from the tetrahedral vertices, but can be located by adding a displacement vector. Since the oxygen atom is at the center of the tetrahedron two of these vectors will point into the tetrahedron to locate the covalently bonded protons. The other two vectors will point out from their vertices to the distant H-bonded protons. The arrangement of spins forming the groundstate of the Ising pyrochlore ferromagnet is obtained, and it is expected that the magnet will enter a disordered phase with the same configurational entropy as ice when it is cooled below  $\theta_{CW}$ . The model is referred to as the spin ice model [25]. The mapping is depicted in figure 1.7.

An interesting departure of spin ice physics from ordinary ice is the ease with which a degeneracy removing perturbation such as an applied magnetic field can be applied. In cubic crystals there are three special directions along which a field is conventionally applied in such a study. These are  $[h00]$ ,  $[hh0]$ , and  $[hhh]$ . The different relationships of the three applied field directions to the tetrahedral units of the pyrochlore lattice suggest that there will be different degeneracy removal schemes associated with each (different ordered groundstates on a single tetrahedron are depicted in figure 2.10 and for a full unit cell in figure 2.11).

The aim of the experiments presented in this thesis was to further investigate the  $H, T$  phase space and history dependence of spin ice. Using neutron scattering, the evolution of the spin ice correlations could be investigated microscopically. Also, it was hoped to use the magnetic field to encourage relaxation at low temperature, and therefore access a predicted groundstate. Finally, the boundaries of the ice rule regime were to be probed, either using high fields which drive the

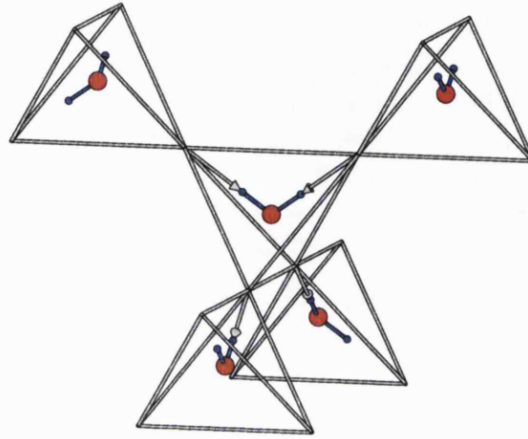


**Figure 1.7:** The spin ice mapping, the tetrahedron joins oxygen-oxygen mid points, the displacement vectors relate the H atom positions to the groundstates of an Ising ferromagnet on a tetrahedral unit.

magnet into broken ice rule states, or by using a field and temperature range that would show the onset of ice rule correlations.

## 1.7 Constraint

The two views of frustration described above (i.e. inability to minimize energy or macroscopic degeneracy) can be connected directly by the concept of constraint. Maxwell introduced constraints in the context of the structural mechanics of bridges [27]. The concept of constraint revolves around the conditions, or constraints, which must be fulfilled to specify the groundstate, and the number of degrees of freedom of the system [28].

For the Heisenberg pyrochlore antiferromagnet it can be shown that the ground state is extensively degenerate by a counting argument which runs as follows [29]. Consider a lattice made up of corner sharing units (i.e triangles or tetrahedra) with  $q$  sites on each, and  $n$ -component classical vector spins  $\mathbf{S}_i$  of unit length. For

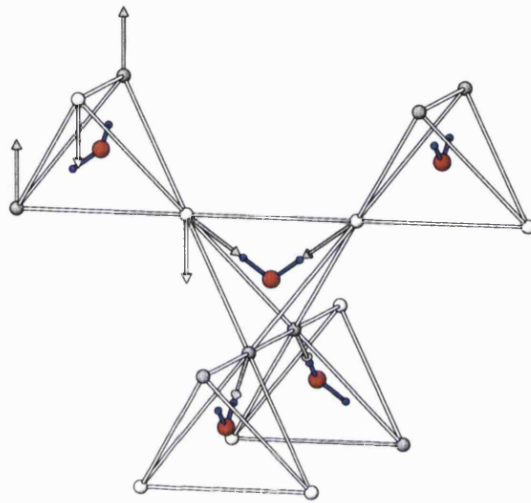


**Figure 1.8:** The spin ice mapping again, illustrating its relation to the Anderson mapping. The top left tetrahedron shows the non-physical uniaxial antiferromagnet, with up and down spins in grey and white. There are two pairs of up and down spins, but also frustrated interactions. This tetrahedron is an “up” tetrahedron so grey represents “proton-near-oxygen” in the ice structure. The central tetrahedron is a “down” tetrahedron so the colors are reversed, grey now represents “proton-distant-from-oxygen.” The spin ice mapping is shown on the central tetrahedron for comparison, it is considerably more transparent than the Anderson mapping.

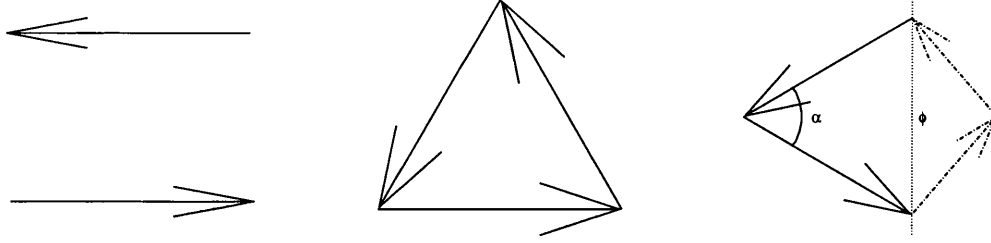


**Figure 1.9:** Continuous spins on 2, 3 and 4 spin units satisfying the condition  $\mathbb{L} = 0$ , the antiferromagnetic groundstate. The dashed pair of spins is rotated out of the plane by an angle  $\phi$ . Four spins have the two continuous degrees of freedom  $\alpha$  and  $\phi$  meaning that the groundstate is degenerate. The constraint that  $\mathbb{L} = 0$  is not sufficient to uniquely specify the groundstate [28].

the pyrochlore  $q = 4$  and  $n = 3$ . The Hamiltonian is

$$\mathbb{H} = J \sum_{\langle i, j \rangle} \mathbf{S}_i \cdot \mathbf{S}_j = \frac{J}{2} \sum_{\alpha} |\mathbb{L}_{\alpha}|^2 - \frac{J}{2} Nq, \quad (1.21)$$

where the sum on  $\langle i, j \rangle$  runs over all neighboring pairs, and the sum on  $\alpha$  runs over the  $N$  units making up the system, and  $\mathbb{L}_{\alpha}$  is the total spin in unit  $\alpha$  [29]. As described by Villain a configuration is a ground state if  $\mathbb{L}_{\alpha} = 0$  for all individual plaquettes simultaneously [30].

The system has  $F = \frac{N(n-1)q}{2}$  degrees of freedom. To ensure  $\mathbb{L}_{\alpha} = 0$  for all  $\alpha$  there must be  $K = Nn$  constraints. The manifold of degenerate groundstates therefore has dimension  $D = F - K$  if the constraints are independent. For the pyrochlore  $F - K = N$  and so the groundstate degeneracy is extensive [29].

In a pyrochlore Heisenberg antiferromagnet, units of  $q$  spins are subject to the constraint that their total spin  $\mathbb{L} = 0$ . For Heisenberg spins if  $q$  is two or three, the condition  $\mathbb{L} = 0$  is sufficient to specify the groundstate. However, for four spins this constraint is insufficient to determine the groundstate uniquely as the groundstates can be constructed with two continuously varying degrees of freedom,  $\alpha$  and  $\phi$  (see figure 1.9). The fact that the groundstate has degrees of freedom is equivalent to saying it is degenerate. A system is underconstrained, and therefore frustrated, if the rule which specifies the coupling of spins is unable to specify a unique groundstate.

The ice rules are also an example of underconstraint. One can view the in-

ability to propagate order through the system by specifying the state of a single tetrahedron as due to a lack of constraint. The two-in-two-out condition is not sufficient to propagate the order to further neighbors, and so the system is underconstrained. Later it will be shown that in some applied field situations, the nearest neighbor nature of the ice rule means that the system is still not sufficiently constrained to achieve complete order.

## 1.8 Mechanisms of Degeneracy Removal

Early and important theoretical insight was provided by Villain in a discussion of insulating spin glasses [30]. One case considered by Villain was an antiferromagnet with no well defined ground state. Such a condition is realized in the Heisenberg pyrochlore antiferromagnet. The groundstate is not well defined because of the degeneracy. Villain reasoned that any state in which all the tetrahedra separately have their energy minimized is a groundstate. In absence of dilution the groundstate of a tetrahedron can be obtained by associating the four spins in two antiparallel pairs. This leads to an infinite number of possible ground states which can be formed from independent, antiferromagnetic closed loops in the lattice. The disordered, degenerate state of the system was named a “cooperative paramagnet.” The term is now commonly used to describe the paramagnetic regime observed experimentally below  $T_F$ . It was expected that in real systems, impurities or weak forces such as dipole interactions or thermal fluctuations would remove the degeneracy [30].

### 1.8.1 Order by Disorder

Villain cited thermal fluctuations as a possible degeneracy removing mechanism. This phenomenon is called “order by disorder” (or OBD) [31, 32]. It is associated with systems in which there is a degenerate ground state manifold and so is very important in frustration. OBD operates at a small but finite temperature  $T = 0^+$ . The ground state manifold contains many groundstates, some are ordered, most are not. The thermal fluctuations allow the system to sample different groundstates. Usually there are a greater number of softer and more easily excitable states

associated with the ordered groundstates and so these are entropically selected. Order by disorder has been shown to cause an ordering transition in both the pyrochlore magnet with local  $XY$  anisotropy and a transition to spin nematic order in the classical Heisenberg kagomé antiferromagnet [31, 32, 33], but does not select an ordered groundstate for the Heisenberg pyrochlore antiferromagnet [29, 34].

### 1.8.2 Dipolar Interactions

Another mechanism postulated by Villain for removing the degeneracy of the groundstate is the dipolar interaction. The dipolar interaction is regarded as a mechanism of degeneracy removal because it is ordinarily weaker than the exchange interactions. Consequently it does not become significant until an energy scale well below the exchange interaction has been reached. Because the interaction is long ranged and anisotropic, it is expected to be particularly effective in removing degeneracy. In a system such as the Heisenberg pyrochlore antiferromagnet, the exchange interaction is isotropic and degenerate. The anisotropy of the dipolar interaction is expected to break this symmetry and so remove the degeneracy.

This has also been investigated for the Heisenberg pyrochlore antiferromagnet [35, 36]. At a mean field level it was found that the inclusion of the dipolar interaction in the nearest neighbor Heisenberg Hamiltonian only partially removed the degeneracy [35]. The complete degeneracy of Fourier modes within the Brillouin zone (“degeneration zone”) observed in the absence of the dipolar interaction [37] was reduced to “degeneration lines” along the star of the  $[hhh]$  direction. It was expected that thermal or quantum fluctuations would remove this degeneracy and lead to order. If further neighbor interactions were considered, it was found that the presence of second and/or third nearest neighbor exchange interaction and the dipolar interaction lead to a unique ordered state [37, 35]. The strength of the dipolar coupling used in the mean field calculations was based on an experimental estimate of the dipole moment of the  $Gd^{3+}$  ion in  $Gd_2Ti_2O_7$ , a potential example of a pyrochlore Heisenberg antiferromagnet. If other values are considered it has been found that if  $J_{dd}/J_{ex} > J_c \cong 5.7$  then an ordered state is formed without recourse to further neighbor interactions [36].

## 1.9 Overview of Frustration

Frustration is synonymous with competing interactions. These are common in many condensed matter systems. Intense frustration can induce novel cooperative effects, this is why it is interesting [38]. Firstly, it is interesting to see how the frustration is resolved. For example it is sometimes argued that a folding protein has an enormous number of configurations available. The timescale for sampling a significant number of them is astronomical, yet proteins fold promptly and precisely into a complex functional form. Somehow the protein system is able to resolve the competing interactions and select the structure. Alternatively there is the view that if the system is frustrated, it will not be able to order in a conventional way, and this will ultimately lead to new cooperative behaviors. For example, if Planck's formulation of the third law holds, then a frustrated spin system must still select a unique groundstate. It is suggested that this may exhibit some unexpected type of order. A common suggestion is that this might be a route to a new type of superconductivity. By frustrating the spin system, a new type of electronic order will be produced.

Generally it is expected that in real frustrated magnets the situation will depend on the dynamics. If the dynamics can be retained, a minor perturbation will eventually become important and when a low enough temperature is reached it will remove the degeneracy. Models which remain disordered at zero temperature have no perturbations included. If the dynamics become slow then the system will freeze into some disordered state which was determined by the degenerate constraints. Degeneracy removing perturbations may be ineffective because the system is unable to evolve. The spin ices mentioned above and discussed further in the next chapter are an example of this.

## 1.10 Hysteresis and Magnetization Plateaux

A frequent observation in these studies are magnetization curves with steps and hysteresis. Some of the reasons for these phenomena are introduced here. In general there are two origins, either non-equilibria, or exotic quantum mechanical mechanisms.

### 1.10.1 Hysteresis

Hysteresis is one of the defining characteristics of ferromagnetism. It is observed that when cycling the field (below  $T_c$ ) different magnetization curves are recorded depending on many features such as the reversal field, the cycle number and rate of field sweeping (see figure 1.10). The majority of measurement and discussion of hysteresis concerns ferromagnets. In these cases the non-equilibrium effects are the most important. Entirely quantum-mechanical hysteresis is a much newer discovery and is a property of single molecule magnets.

#### Hysteresis in Ferromagnets

Hysteresis in ferromagnets is due to the interplay of a free energy landscape which is evolving as the field changes, and the relaxation processes operating in the sample [8, 39]. The free energy landscape of a ferromagnet depends on several terms. Exchange energy and anisotropy combine to favor uniform magnetization along specific crystalline directions. Magnetostatic energy competes to form states with zero average magnetization. Other effects such as structural disorder may also play a role. In zero field the competing interactions form a domain structure. The complicated free energy landscape has many local minima and each is a different domain structure. If the temperature is low and the energy landscape has high barriers the system can be trapped in a particular domain structure, this is a metastable state.

As the field is swept the importance of the different interactions changes and so does the free energy landscape. Domain structures become unstable and must adjust to new and more favorable arrangements. The field sweep crosses a series of thresholds where the domain structure becomes unstable and must change. Each time it does so, there is a small change in the magnetization. Often a hysteresis loop is depicted with smoothly changing magnetization. They actually have a complicated fine structure consisting of tiny stepwise changes in magnetization, separated by flat sections where the domain structure is stable. This is the Barkhausen effect, often referred to as Barkhausen noise due to its appearance as a random series of voltage spikes induced in a measuring coil (see figure 1.10).

The adjusting of the domain structure depends on the relaxation mechanisms



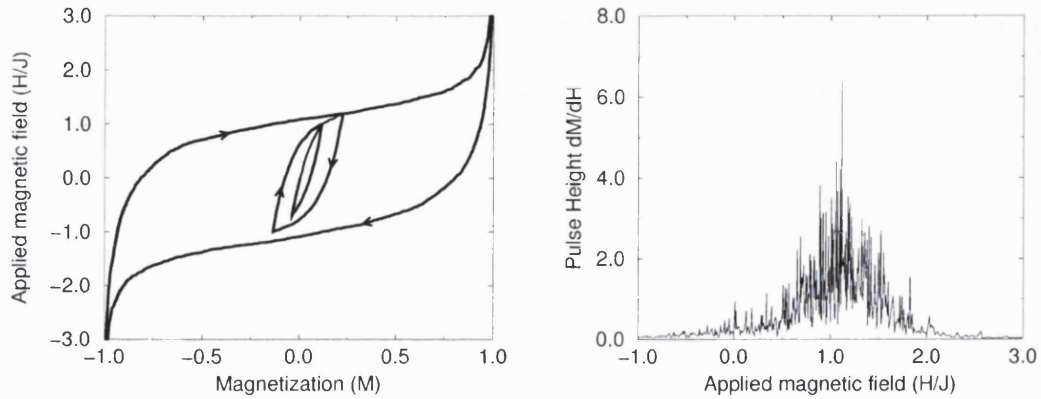


**Figure 1.10:** Hysteresis loops and Barkhausen noise in the random field Ising model [40]. The magnetization of a hysteretic system depends on the cycle number and field sweeping regime (left). It does not grow smoothly as a function of field, but in irregular jumps (these can be seen in the main loop, particularly at larger fields). The jumps are sudden avalanche like spin relaxation events known as Barkhausen noise. They are largest and most frequent when the magnetization is changing most rapidly (right).

operating. The change in structure must take a finite time. In the ideal case in which it is instantaneous, the rate of field sweeping will be unimportant as it does not approach the timescale of domain movement. This approximation is known as rate-independent hysteresis. In reality if the timescale of the Barkhausen jumps is long enough for an appreciable field change during the rearrangement, then the hysteresis becomes rate-dependent. Also, the system only remains in a local minimum indefinitely at zero temperature. At finite temperature thermal fluctuations may relax the system by allowing it to escape an energy minimum, even without a change in field.

Barkhausen noise has been extensively investigated by theorists, in particular Sethna and co-workers [40, 41]. The size of a Barkhausen noise event can vary over six orders of magnitude, and this is why it is so interesting. One possible

explanation would be that individual events represented the flipping of individual grains. This is not possible as the grain size distribution is never so large. Large events must involve many grains coupled together. Because events occur with such a wide variety of scales Barkhausen noise is often interpreted as an avalanche phenomenon. As with avalanches, the system is driven (by sweeping the field, or adding snow with constant gravity effective) and small events may occur, or the system may stick in a marginally stable state until a threshold is reached, and a system spanning large event occurs.

To understand these effects Sethna *et al.* have used a random field Ising model [40, 41]. The idea being to introduce some disorder into a conventional Ising magnet. The spins are coupled to nearest neighbors and there is an external field, an additional random term is added to the field at each site, giving a bias to either of the Ising up or down orientations. The Hamiltonian is

$$\mathbb{H} = - \sum_{ijn.n.} JS_i S_j - \sum_i (H(t) + h_i) s_i, \quad (1.22)$$

where  $H(t)$  is the homogenous external field and  $h_i$  is the random field component at site  $i$ . The random fields are distributed according to

$$P(h) = \exp(-h^2/2R^2)/\sqrt{2\pi}R. \quad (1.23)$$

$R$  represents the disorder, a wide distribution of event sizes only occurs when the disorder and coupling are finely balanced. When  $R \gg J$  only small avalanches occur. If the coupling is very strong ( $R \ll J$ ) then only a single large avalanche will occur. Sethna *et al.* discovered that the properties of their model could be described by simple power laws. They described the exponents as critical exponents [40, 41].

The paradigm of self-organized criticality has become popular for explaining avalanche phenomena [42]. Self-organized criticality is a theory for describing the complex behavior of strongly correlated, non-equilibrium dynamical systems such as rice piles. Such a system can organize itself in a state with complex temporal and spatial correlations (i.e. there is no characteristic event size), yet its statistical properties are described by simple power laws. However, not all power law behavior is indicative of self organized criticality and it is suggested that Barkhausen noise

is an example of a “power law by sweeping of an instability” [43]. Sethna *et al.* attribute the power law behavior to the proximity of a “plain old critical point” [40, 41]<sup>b</sup>.

### Hysteresis in molecular magnets

Recently there has been much interest in magnetic materials composed of clusters of metal atoms [44, 45]. In these materials unusual hysteresis loops can be observed. Rather than containing the fine structure of small jumps typical of Barkhausen noise, these contain a small number of large jumps. The number and location of jumps depends on the temperature.

The most famous example is  $[\text{Mn}_{12}\text{O}_{12}(\text{CH}_3\text{COO})_{16}(\text{H}_2\text{O})_4] \cdot 2\text{CH}_3\text{COOH} \cdot 4\text{H}_2\text{O}$ , or  $\text{Mn}_{12}\text{Ac}$  [44, 45]. Crystals of this compound consist of widely separated clusters of twelve manganese atoms. The cluster has a core of four  $\text{Mn}^{4+}$  atoms surrounded by a crown of eight  $\text{Mn}^{3+}$  ions (see inset of figure 1.11). The spins of the ions are strongly coupled in two opposed ferromagnetic sublattices giving an entity with total spin  $S = 10$ . The coupling is sufficiently strong (this structure persists above 50 K) that in a temperature range of  $T \approx 1 - 3$  K a crystal of  $\text{Mn}_{12}\text{Ac}$  consists of a large array of identical nanomagnetic particles.

The symmetry of the molecule and the crystal imposes a strong uniaxial anisotropy. In zero field the energy barrier between two opposite orientations of  $S$  on the anisotropy axis is 60 K. On the timescale of a typical ZFC experiment, transitions between the two are blocked below about 3 K (this is observed clearly in FC/ZFC experiments). Above the blocking temperature the susceptibility is well described by a superparamagnet with  $S = 10$ . Below the blocking temperature the hysteresis loop measured with the field applied on the easy axis, contains regularly spaced jumps when the field is in the direction of  $\mathbf{M}$ , but not when the field is opposed

---

<sup>b</sup>Using renormalization group calculations they were able to show that at the mean field level there is a fixed point and transition where the system is about to undergo an infinite avalanche. The fixed point was unstable in lower dimensions, but a perturbative calculation was used to find a new one. Also their avalanche size distributions for different disorders close to  $R_c$  could be scaled and collapsed onto each other. They found that their model has a wide critical range and used this to explain rather limited experimental power laws as falling in this critical range but not necessarily being close or distant enough to the fixed point to agree well with the theory.

to  $\mathbf{M}$ , see figure 1.11. The jump fields are temperature independent.

The temperature dependence of the relaxation time follows an Arrhenius law indicating a thermal process. However, the relaxation rate as a function of field has maxima at the jump fields. The explanation for this behavior is that thermal relaxation is being augmented by thermally assisted resonant tunnelling. Each time the field reaches one of the critical values the levels in the potential wells of the two orientations are matched. Resonant tunnelling can then take place between each pair of matched levels. Tunnelling is most significant from the upper levels and this is why the process is thermally assisted. If the temperature is lowered below the blocking temperature the upper levels become depopulated and the transitions are completely blocked. Thermal overbarrier transitions also occur, but at a tunnelling field there is an additional contribution to the relaxation which produces the maximum. The observed hysteresis loop is intermediate between a smooth reversible magnetization curve obtained for infinitely slow field sweeping, and a square one for infinitely fast sweeping when no molecule can change orientation until the field matches the anisotropy barrier.

### 1.10.2 Plateaux

A magnetization plateau is different to either a Barkhausen jump, or the stepped hysteresis loops of the molecular magnets. They are inherently quantum mechanical in origin. Unlike Barkhausen jumps a magnetization plateau occurs in an otherwise smooth magnetization curve, at some rational fraction of the saturation magnetization. It does not have the complicated hysteresis or rate dependence of the steps in the hysteresis loop of a molecular magnet such as  $\text{Mn}_{12}\text{Ac}$ . One example will be described to illustrate the type of processes which occur [46, 47].

$\text{SrCu}_2(\text{BO}_3)_2$  is a realization of the Shastry-Sutherland model. This model is for a two-dimensional material containing alternating orthogonal dimers (in figure 1.12 these can be seen forming chains slanting diagonally across the unit cell). The Hamiltonian is

$$\mathbb{H} = J_1 \sum_{\langle i,j \rangle} \mathbf{S}_i \cdot \mathbf{S}_j + \sum_{\langle i,k \rangle} \mathbf{S}_i \cdot \mathbf{S}_k, \quad (1.24)$$

where  $J_1$  is the exchange within a dimer, and  $J_2$  is the exchange between spin  $i$  in

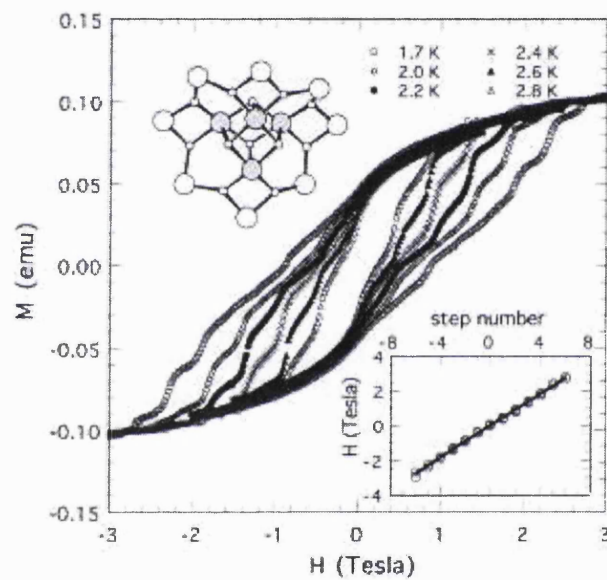


**Figure 1.11:** Hysteresis loops of a  $\text{Mn}_{12}\text{Ac}$  crystal with the field applied parallel to the easy axis. The structure of the  $\text{Mn}_{12}\text{Ac}$  core is shown as an inset. The other inset illustrates the even spacing of the steps by plotting the jump field against the step number [44].

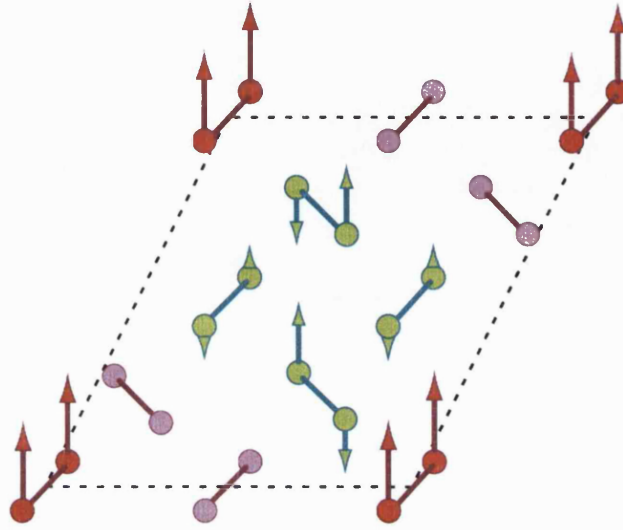


**Figure 1.12:**  $\text{SrCu}_2(\text{BO}_3)_2$  in the magnetization plateau phase. [46]. The alternating orthogonal dimers of the Shastry-Sutherland model can be seen in chains slanting across the unit cell. In the plateau phase at  $1/8$  of saturation magnetization a fraction of the dimers have been excited from singlets to triplets.

a given dimer, and its nearest neighbors in other dimers (each spin has four such neighbors) [48].

$\text{SrCu}_2(\text{BO}_3)_2$  contains a frustrated two dimensional lattice of  $\text{Cu}^{2+}$  dimers, pairs of  $S = 1/2$   $\text{Cu}^{2+}$  ions coupled antiferromagnetically. The groundstate of a  $\text{Cu}^{2+}$  dimer is a singlet, in which the spins are paired and  $S = 0$ . The groundstate of the dimer crystal is a singlet spin liquid. A dimer can be excited into a triplet state in which  $S = 1$  and  $S_z = +1, 0, -1$ . The triplet excitation can move through the lattice by hopping from one dimer to the next. Application of an external magnetic field has no effect on the  $S = 0$  singlets but leads to a splitting of the triplets. The component of the triplet parallel to the field is lowered in energy, and so is the energy required to excite it, eventually reaching zero.

The triplet components with  $S_z = 1$  can be regarded as bosons with a repulsive interaction (which prevents more than one being present on the same dimer). The boson density is controlled by the coupling to the external magnetic field and is proportional to the total magnetization. A system of interacting bosons is produced

whose groundstate depends on the balance between kinetic energy and repulsion. When repulsion is dominant and the boson density per dimer is a rational fraction, the bosons can form a superlattice to minimize the repulsive interactions (see figure 1.12). When this occurs, raising the field to create more bosons will produce a “separated interstitial-vacancy pair” in the boson superlattice. There will be a finite energy cost and jump in the chemical potential associated with this process, which is manifested as a plateau in the magnetization at the fractional boson density. A direct measurement of the superlattice formed in  $\text{SrCu}_2(\text{BO}_3)_2$  has recently been achieved using NMR in fields of 27 T [47]. The transition into the superlattice state appears to be first order, so that it can be described as the crystallization of a dilute bosonic fluid.

## 1.11 Summary

This introduction has hopefully provided some insight into problems from the entire history of the study of magnetism. From hysteresis in ferromagnets, originally studied by Weiss, to modern quantum magnetism, all are of importance in the studies reported later.

# Chapter 2

## Spin Ice

### 2.1 Spin Ice Materials

The  $b$ -sites of the spinel structure  $AB_2O_4$  (e.g.  $ZnCr_2O_4$ ), the transition metal sites of the ternary fluorides  $AMM'F_6$  (e.g.  $CsNiMnF_6$ ) and the two metal positions in a series of oxides  $M_2M'_2O_7$  (e.g.  $Y_2Mn_2O_7$ ) all form pyrochlore lattices. The series of rare earth titanates  $Ln_2Ti_2O_7$  were studied as  $Ti^{4+}$  is non-magnetic allowing the effects of a single pyrochlore lattice to be isolated. This situation is also realized in the related compounds such as  $Ho_2GaSbO_7$ . The experimental origins of the spin ice model are in the investigation of the rare earth titanate pyrochlores of general composition  $Ln_2Ti_2O_7$ , in particular  $Ho_2Ti_2O_7$ .

Heat capacity measurements were originally made by Blöte *et al.* on various rare earth oxides of the type  $R_2M_2O_7$  [49]. Their study included  $Dy_2Ti_2O_7$  and  $Ho_2GaSbO_7$ . The heat capacity of  $Ho_2GaSbO_7$  was observed to be very flat between 0.3 and 1.5 K. By comparison with other Ho compounds they attributed the low temperature part of the heat capacity to the nuclear spins. The hyperfine splitting was described using a Schottky anomaly for a system of eight energy levels with a total splitting of  $7 \times 0.3$  K. No clear explanation of the rest of the heat capacity was made but they noted that it could be fitted by a variety of two level systems such as a crystal field doublet, or a pair of singlets. Their measurements of  $Dy_2Ti_2O_7$  showed no sharp feature. They could only extrapolate the entropy to about  $3/4R \ln 2$  and suggested that the missing contribution would be



found in more precise measurements at higher temperatures. Amongst other things that they also noted were that  $\text{Dy}_2\text{Ti}_2\text{O}_7$  has strongly anisotropic properties with  $g_\perp \approx 0$  and  $g_\parallel = 17$  giving a  $J_z = \pm 15/2$  groundstate, and despite the absence of a peak in the heat capacity, one is observed in the susceptibility at  $T \approx 0.9$  K.

The crystal structure of the  $\text{Ln}_2\text{Ti}_2\text{O}_7$  materials was originally suggested to be of the pyrochlore type by Roth [50]. This was confirmed by Knop [51] in a detailed study of  $\text{Er}_2\text{Ti}_2\text{O}_7$ . The space group is  $\text{Fd}\bar{3}\text{m}$  and the metals are divided between  $16c$  ( $\text{Er}^{3+}$ ) and  $16d$  ( $\text{Ti}^{4+}$ ). Oxygen occupies two positions,  $48f$  and  $8a$ . The  $8a$  oxygen atoms are at the center of the rare earth tetrahedra. The only adjustable parameter is the  $x$  coordinate of the  $48f$  position. This controls the oxygen coordination around the rare earth ions. The coordination polyhedron may vary between a regular cube and a situation with a equatorial puckered hexagon of oxygen atoms surrounding the rare earth ion and two axial oxygen atoms (which are  $8a$  positions). The axial oxygen atoms are considerably closer and this creates a highly anisotropic crystal field with  $D_{3d}$  symmetry.

The  $\text{Ho}^{3+}$  ion has a  $^5I_8$  groundstate which is split by this crystal field such that the lowest lying level is a doublet composed almost entirely of the  $|J, J_z\rangle = |8, \pm 8\rangle$  components [25, 52, 53]. This level is well separated from the next excited state (at 20.4 meV [52]). Consequently there is a strong easy axis anisotropy estimated at  $T \approx 300$  K [52, 53]. This is manifested in the bulk high field magnetization [18], where the moment measured for  $\text{Ho}^{3+}$  is a little over half the theoretical free ion value of  $\mu = 10.61\mu_B$ . The strong anisotropy constrains the spins to the  $\langle 111 \rangle$  axes of the crystal structure.

Also it was observed that in  $\text{Ho}_2\text{Ti}_2\text{O}_7$   $\theta_{CW} \approx +1.9 \pm 0.1$  K. The strong anisotropy and ferromagnetic coupling made  $\text{Ho}_2\text{Ti}_2\text{O}_7$  a strong candidate for the realization of a spin ice. This was further investigated by neutron scattering and  $\mu\text{SR}$  measurements [25, 54]. Both showed that no transition to a magnetically ordered state occurs down to temperatures of 0.05 K. Neutron scattering shows a considerable build up of diffuse scattering indicating short range correlations. The diffuse scattering pattern was found to be consistent with Monte Carlo simulations of a model with nearest-neighbor ferromagnetic exchange only, which is known as “nearest neighbor spin ice” (see figure 2.4).

On the basis of similar susceptibility properties,  $\text{Dy}_2\text{Ti}_2\text{O}_7$  and  $\text{Yb}_2\text{Ti}_2\text{O}_7$  were also suggested to be spin ice materials [55]. The free ion groundstate of  $\text{Dy}^{3+}$  is  ${}^6H_{\frac{15}{2}}$  and in the crystal field this is split such that the lowest level is a  $|\frac{15}{2}, \pm\frac{15}{2}\rangle$  doublet. As in  $\text{Ho}_2\text{Ti}_2\text{O}_7$  the next level is well above this and so at low temperatures  $\text{Dy}_2\text{Ti}_2\text{O}_7$  effectively has two state spins constrained to the  $\langle hhh \rangle$  axes.

A convincing demonstration of the spin ice groundstate in  $\text{Dy}_2\text{Ti}_2\text{O}_7$  was provided by Ramirez [56]. The residual entropy of water ice was obtained by measuring the heat capacity from liquid helium temperatures to the gas phase, integrating and then subtracting from the gas phase entropy calculated on the basis of spectroscopic measurements. In direct analogy to this measurement, the heat capacity of  $\text{Dy}_2\text{Ti}_2\text{O}_7$  from 0.2 – 12 K was measured and integrated. The heat capacity itself shows no sharp features suggestive of ordering processes. There is a rather broad peak, falling close to zero on the low temperature side, suggesting that the spins do indeed freeze (see figure 2.1). At 12 K the entropy of the material is expected to be that of a collection of two state spins (the value is  $R \ln 2 \approx 5.76 \text{ J mol}^{-1} \text{ K}^{-1}$ ) but the measured entropy is considerably lower than this (see figure 2.1). The difference ( $1.86 \text{ J mol}^{-1} \text{ K}^{-1}$ ) is close to the residual entropy calculated by Pauling for ice, suggesting that  $\text{Dy}_2\text{Ti}_2\text{O}_7$  does indeed freeze into an ice rule obeying disordered state. In light of the spin ice interpretation the unexplained features of Blöte's measurements are clarified. The heat capacity of  $\text{Ho}_2\text{Ti}_2\text{O}_7$  is complicated by the large nuclear spin ( $I = \frac{7}{2}$ ) of Ho. This can be accounted for with an appropriate Schottky anomaly as in the work of Blöte *et al.* [49]. If this contribution is removed the remaining electronic contribution is well described by the dipolar spin ice model discussed below [57] (see figure 2.3).

## 2.2 The Importance of Anisotropy

The preceding discussion often touches on the strong anisotropy of the crystal fields in the  $\text{Ln}_2\text{Ti}_2\text{O}_7$ . Evidently it is an important simplifying factor in the clear relations in the spin ice mapping that the spins are constrained to the  $\langle hhh \rangle$  axes of the tetrahedron. In a real material it might be expected that infinite anisotropy would not occur. A system with continuous spins and finite anisotropy was studied

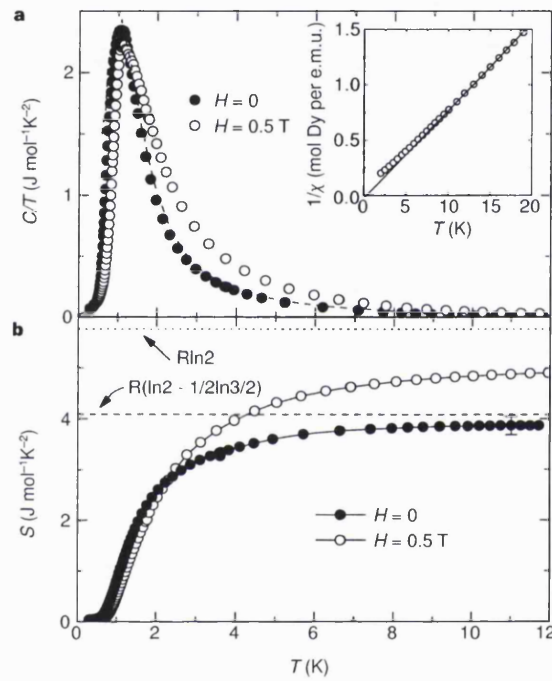


**Figure 2.1:** Heat capacity of  $\text{Dy}_2\text{Ti}_2\text{O}_7$  (top), and integrated entropy (bottom) showing the expected value for Ising spins (dotted horizontal line), and the expected value for the a spin ice with residual entropy (dashed horizontal line) [56].

by Champion *et al.* using Monte Carlo simulations [58]. Using the Hamiltonian

$$\mathbb{H} = -J \sum_{\langle i,j \rangle} \mathbf{S}_i \cdot \mathbf{S}_j - D \sum (\mathbf{S}_i \cdot \mathbf{d}_i)^2 - \sum_i \mathbf{H} \cdot \mathbf{S}_i, \quad (2.1)$$

where the  $\mathbf{S}_i$  are classical spin vectors and  $\mathbf{H}$  the applied magnetic field. The cubic crystal fields of magnitude  $D$  are along the four  $\mathbf{d}_i = \langle hhh \rangle$  directions. The Hamiltonian describes the transition from nearest neighbor spin ice ( $D/J \rightarrow \infty$ ) to ordinary (collinear) ferromagnetic behavior ( $D/J \rightarrow 0$ ).

For all finite  $D/J$  they found a transition to an ordered state. Only in the  $D/J \rightarrow \infty$  limit is the nearest neighbor spin ice behavior recovered. The continuous spins allow relaxation off the  $\langle hhh \rangle$  directions. This allows the system to regain some of the frustrated bond energy, at the expense of some crystal field energy. The greatest gain in energy occurs when the system relaxes into an ordered state. Consequently the perturbation introduced into the nearest neighbor spin ice model by finite anisotropy always leads to ordering. The ordered states obtained all involve a collective symmetry breaking and have a structure in which each “up” tetrahedron has the same arrangement of two-spins-in-two-spins-out. This is similar to the  $Q = 0$  state discussed below. It is illustrated in figure 2.11.

## 2.3 Dipolar Spin Ice

The nearest neighbor spin ice model reproduces qualitatively the neutron scattering pattern recorded for  $\text{Ho}_2\text{Ti}_2\text{O}_7$  but does not account for detailed features. A more detailed model, subsequently known as dipolar spin ice, was proposed by Den Hertog and Gingras [59].

The rare earth cations have very large magnetic moments and so dipolar interactions are expected to be very important. Also it was suggested that any nearest neighbor superexchange in  $\text{Ho}_2\text{Ti}_2\text{O}_7$  would in fact be antiferromagnetic [60]. In light of these two conditions the disorder is surprising. The dipolar interaction is long ranged and expected to be non-degenerate, and the antiferromagnetic exchange alone should be enough to cause ordering.

The first attempts to take into account the dipolar interaction were made by Siddharthan *et al.* [60]. Monte Carlo simulations were carried out using a calcu-

lated value of  $D$  and a value of  $J$  extracted from the susceptibility. The dipolar interaction was truncated at a distance of five neighbors. This work concluded that  $\text{Ho}_2\text{Ti}_2\text{O}_7$  was not a spin ice at all. It was argued that at a temperature of  $T \approx 0.6$  K  $\text{Ho}_2\text{Ti}_2\text{O}_7$  falls out of thermal equilibrium and that at this point the system is undergoing a transition to a partially ordered state. No account of the nuclear hyperfine levels was made in the interpretation of the heat capacity. In the simulations a sharp feature in the heat capacity and a large fall in the energy of the system were observed at this temperature. In direct contradiction to already existing data, these were taken as evidence of the transition to partial order.

Neutron scattering and  $\mu\text{SR}$  experiments at temperatures down to 0.035 K had already confirmed the absence of any order in  $\text{Ho}_2\text{Ti}_2\text{O}_7$  (in zero field) [25, 54, 61]. In  $\mu\text{SR}$  experiments it was found that there was no significant difference between spectra obtained at 4 K and 0.046 K. This shows that there is no phase transition and also that the spin dynamics do not change in this temperature range (at least on this timescale). The absence of the phase transition was also confirmed by neutron scattering. No significant change in the intensity of Bragg peaks occurred, indicating that they were all nuclear peaks. No new Bragg peaks were observed either. Strong diffuse scattering was observed due to ferromagnetic short-range order [25, 54].

Subsequently, the dipolar interaction was extended to an effectively infinite range by den Hertog and Gingras using Ewald summation techniques [59]. They showed that truncating the dipolar interaction introduced spurious features. When the dipolar interaction was truncated at a distance of five neighbors a sharp feature was observed. If the dipolar interaction was extended to ten neighbors the feature was softened and rounded. Truncation at the nearest neighbor produces a model with the same properties as the nearest neighbor spin ice/  $\langle hhh \rangle$  ferromagnetic model.

Using the Hamiltonian

$$\mathbb{H} = -J \sum_{\langle i,j \rangle} \mathbf{S}_i^{\mathbf{z}_i} \cdot \mathbf{S}_j^{\mathbf{z}_j} + Dr_{nn}^3 \sum_{\langle i,j \rangle} \frac{\mathbf{S}_i^{\mathbf{z}_i} \cdot \mathbf{S}_j^{\mathbf{z}_j}}{|\mathbf{r}_{ij}|^3} - \frac{3(\mathbf{S}_i^{\mathbf{z}_i} \cdot \mathbf{r}_{ij})(\mathbf{S}_j^{\mathbf{z}_j} \cdot \mathbf{r}_{ij})}{|\mathbf{r}_{ij}|^5} \quad (2.2)$$

in which  $\mathbf{S}_i^{\mathbf{z}_i}$  labels the Ising moment of magnitude  $|S| = 1$  at site  $i$  with local Ising axis  $\mathbf{z}_i$ , a phase diagram for  $J$  and  $D$  was made (see figure 2.2).

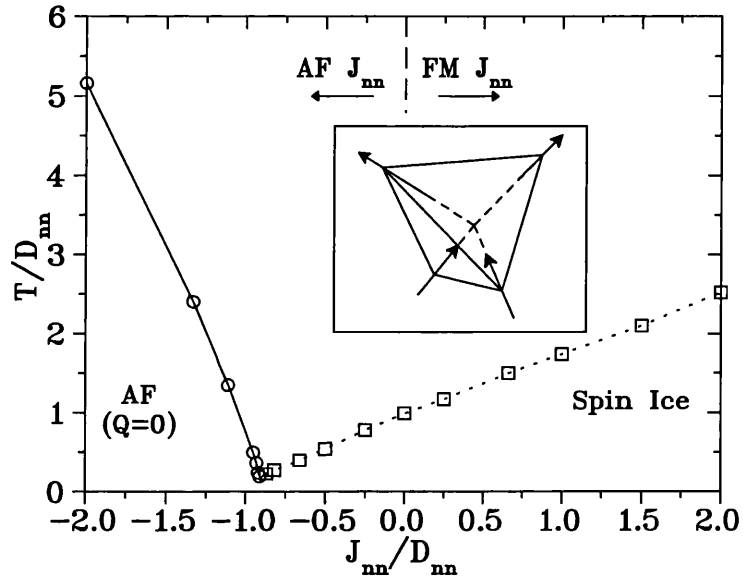


**Figure 2.2:** Phase diagram for competing dipolar and antiferromagnetic exchange interactions showing transition into either ordered antiferromagnetic or ice rule groundstates as a function of relative interaction strengths and temperature. As the antiferromagnetic exchange interaction is made stronger it competes with the dipolar interactions. Eventually the dipolar interactions are overwhelmed and the system is driven into antiferromagnetic order [59].

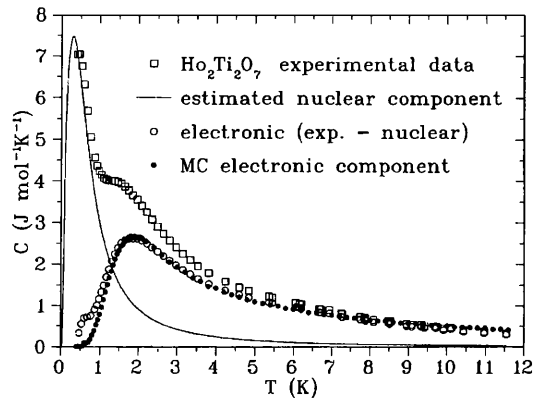


**Figure 2.3:**  $\text{Ho}_2\text{Ti}_2\text{O}_7$  heat capacity fitted with the dipolar spin ice model [57]. The nuclear component has been subtracted as described by Blöte [49].

They found that if  $J$  was made sufficiently large and negative it could overwhelm the dipole interactions and drive the system into antiferromagnetic order. This behavior persisted up to  $\frac{J_{nn}}{D_{nn}} \approx -0.91$ . For sufficiently small, but still antiferromagnetic,  $J_{nn}$  the system was a spin ice. For all  $J_{nn} > 0$  the system was also a spin ice. They characterized a spin ice by integrating the specific heat. It agreed exactly with the Pauling estimate. The exchange parameters used by Siddharthan *et al.* were also found to lie within the spin ice regime. Using the specific heat peak height and temperature location for the various values of  $D$  and  $J$  used in the simulations, values of  $J_{nn}$  were obtained for both  $\text{Ho}_2\text{Ti}_2\text{O}_7$  and  $\text{Dy}_2\text{Ti}_2\text{O}_7$  in good agreement with experimental estimates.

Using these parameters it was demonstrated that the specific heat of  $\text{Dy}_2\text{Ti}_2\text{O}_7$  could be reproduced accurately. The dipolar spin ice hamiltonian and the nuclear Schottky anomaly of Blöte were combined to fit the heat capacity of  $\text{Ho}_2\text{Ti}_2\text{O}_7$  (see figure 2.3). In addition neutron scattering patterns for dipolar spin ice states were calculated (see figure 2.4). It was found that the dipolar spin ice model captured the details of the scattering pattern much more effectively than the nearest neighbor spin ice [57].

Although the dipolar spin ice model was clearly very successful in accounting for the static properties of  $\text{Ho}_2\text{Ti}_2\text{O}_7$  there remains an important question about it. The dipolar interaction is anisotropic and long ranged. It is therefore expected

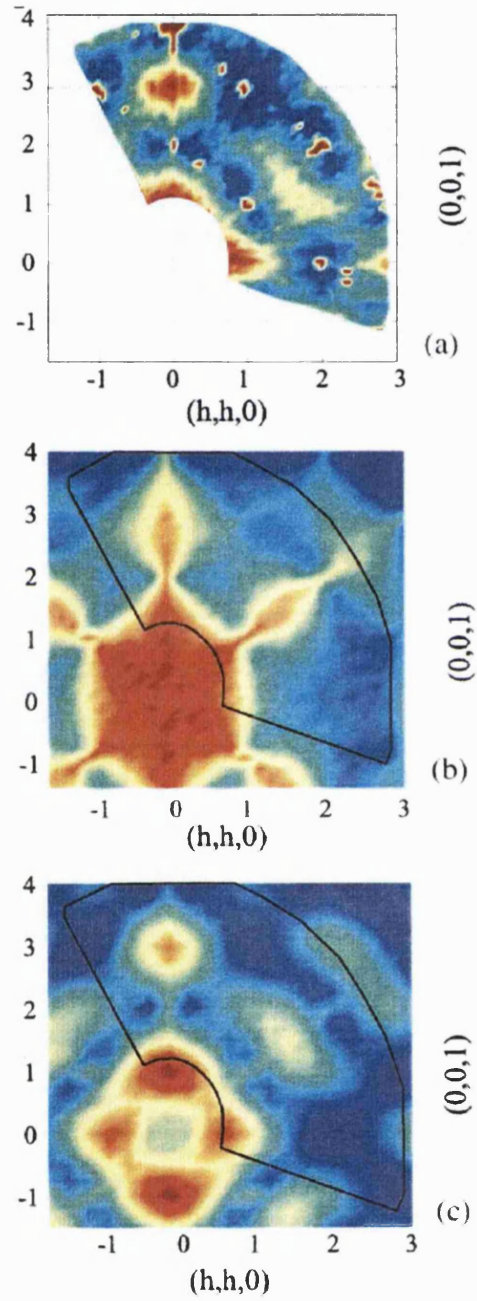


**Figure 2.4:** Diffuse scattering in  $\text{Ho}_2\text{Ti}_2\text{O}_7$  measured on PRISMA (top), calculated using the near neighbor spin ice model (middle), and the dipolar spin ice model (bottom) [57].



to select an ordered groundstate. Why does this not happen in a spin ice? This has also been addressed by Gingras and den Hertog [62], though it has been subsequently stated by Bramwell and Gingras that this point still requires further clarification [38].

The existence of a groundstate manifold is due to “underconstraints” in the energetics, i.e. the constraints which determine the energy of the groundstate are insufficient for order. For example, in near neighbor spin ice the only constraint is the “two-in-two-out” ice rule, which is degenerate. It is expected that the complexity of the dipolar interaction beyond nearest neighbors should introduce sufficient constraints to ensure order at a temperature  $T_c(J, D) \approx O(D_{nn}/k_B) \approx 2$  K. The argument proposed by Gingras and den Hertog is that the degeneracy removing energetics are also frustrated.

In order to investigate this effect they used a mean field theory with dipolar interactions extending to a cut-off [62]. Following Reimers *et al.* [37] they calculated the eigenvalues of the spin-spin interaction matrix and searched for the wavevector with the absolute maximum eigenvalue, which represents a soft mode. They found that for nearest neighbor dipolar interactions (with or without antiferromagnetic interactions suitable for the spin ice regime) the spectrum of eigenvalues was completely flat. It was noted that since the nearest neighbor spin ice model maps to an antiferromagnetic Heisenberg model [24, 25, 63], it was expected that the spectrum should be the same as that obtained for the antiferromagnet by Reimers *et al.* [37]. With extending cutoff distances of order 5-10 neighbors, they observed a cutoff dependent ordering wavevector expected to produce incommensurate Néel order, in contrast to the partial order suggested by Siddharthan [60] (maximal eigenvalue spectra are shown in figure 2.5 for various cutoff distances [62]).

When the cut-off becomes larger the spectrum of eigenvalues begins to flatten. As the cutoff distance becomes infinite the spectrum is so flat that the system is quasi-degenerate again. There is a weak maximum which does imply that there is a unique groundstate, different to the state obtained by Champion *et al.* [58] but that the ordering temperature is of order  $T_c/D \approx 0.1$  K. The transition into this state is discussed further below. Interestingly here the dipolar forces, usually expected to be degeneracy removing, actually restore the spin ice behavior.

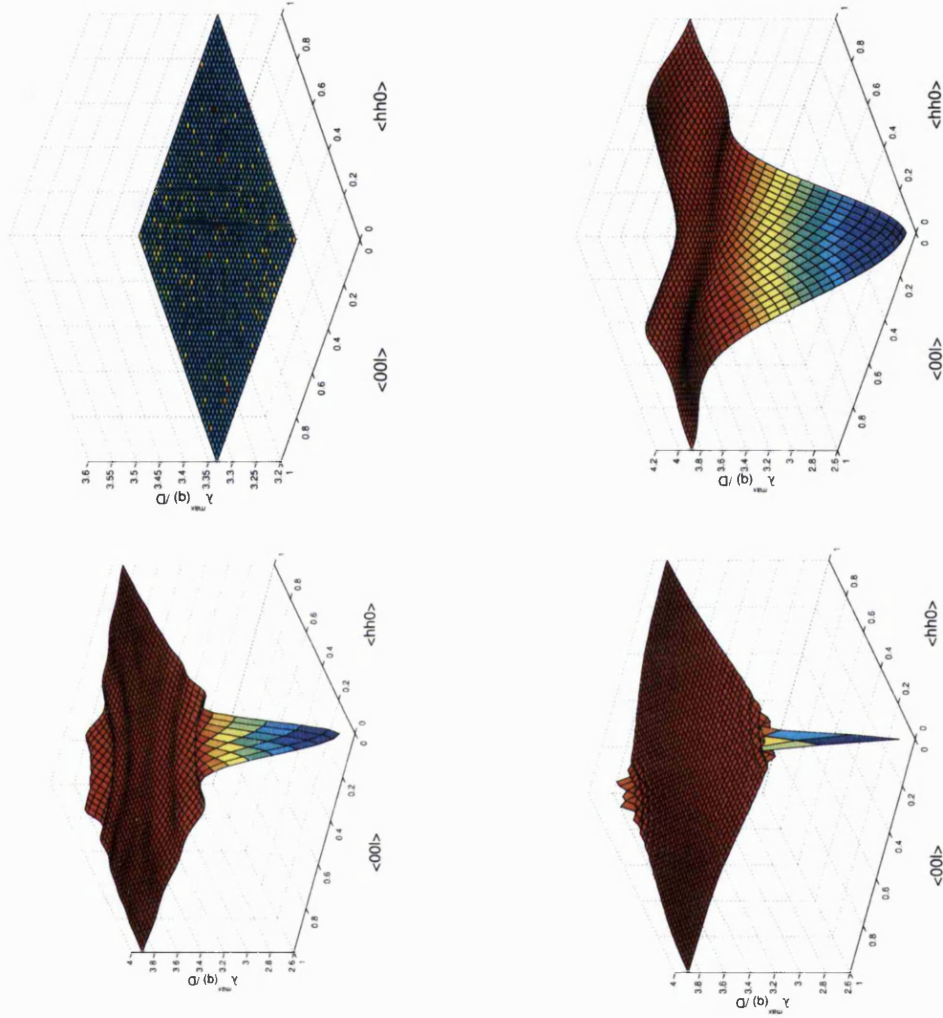


**Figure 2.5:** Change in ordering wavevector calculated by Mean Field Theory as a function of dipolar interaction cutoff distance. When the cut off is at the first neighbor (top left) the spectrum is identical to the Heisenberg antiferromagnet and there is no order. As the cutoff is extended to 10 (top right), 100 (bottom left) and 1000 (bottom right) nearest neighbors the ordering wavevector changes and the spectrum becomes increasingly flat until it is quasi-degenerate when the cutoff is infinite [62]. The downward spike at  $\mathbf{k} = 0$  is due to the conditional convergence of the dipolar lattice sum at this  $\mathbf{k}$  value.

## 2.4 Dynamics in Spin Ices

The Mean Field Analysis described above suggests that there is an ordered ground-state [62]. Monte Carlo simulations with single spin flip dynamics suggest that a spin ice will freeze into a disordered state determined by the ice rules [59, 57]. Experiments have failed to detect any ordering process [25, 57]. In their original investigation of the dipolar interaction den Hertog and Gingras hypothesized that the groundstate manifold may be a rugged energy surface and so although it contains ordered states, the system is unable to select them as it becomes frozen into a disordered state [59].

The history dependence of the sample when subject to applied fields and temperature changes suggests that this is true. For example, if magnetic order is induced by an applied field which is subsequently removed the intensity of the magnetic peaks decreases but does not disappear [25]. This would occur if the magnetic order was frozen in and large energy barriers prevent the sample from relaxing again.

The lowest energy excitation of a spin system of this type is a concerted flipping of a loop of spins which contains the same number of “in” and “out” spins. In a standard Monte Carlo simulation these types of move cannot occur as only single spin flips are possible. In a simulation with single spin flips the manifold of spin ice states necessarily becomes rugged, because to move between the states requires at least one move into a non-ice rules state which has an associated high energy cost. This ensures that the dynamics are extremely slow and it is impossible for the system to fully explore the manifold within any reasonable timescale. In order to preserve the dynamics of the system to lower temperatures, loop moves were introduced by Melko *et al.* [64].

Using single spin flips the dynamics are indeed frozen out once the short range spin ice correlations have built up. Using a combination of the single spin flips and loop moves this feature is reproduced, but the loop moves persist to much lower temperature. Below the formation of the disordered ice rules state the system undergoes an extremely sharp first order phase transition to an antiferromagnetic long range ordered state which also obeys the ice rules (see figure 2.6 and 4.7 for the structure). This agrees well with the mean field analysis, as the ordering

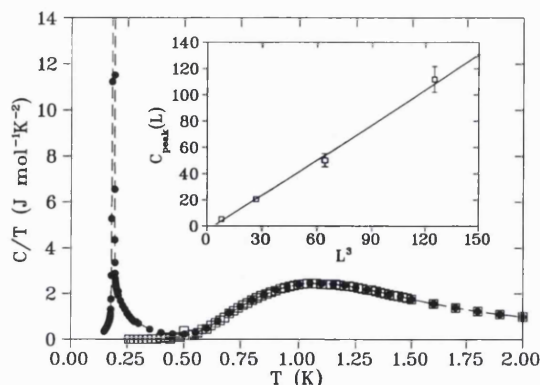


**Figure 2.6:** Heat capacity of a dipolar spin ice model with loop moves, the “normal” part of the heat capacity described previously is the broad feature. The inclusion of loop moves allows the sharp transition. Inset: a finite size scaling analysis consistent with the transition being first order [64].

wavevector is the same. Theoretically it is now expected that there is a single ordered state, in agreement with the mean field analysis and normal expectations for the dipolar interaction. However, as with water ice, experimental observation of this state will depend critically on the real dynamics of these systems. The dynamics of  $\text{Ho}_2\text{Ti}_2\text{O}_7$  and  $\text{Dy}_2\text{Ti}_2\text{O}_7$  have been investigated by AC susceptibility [65, 66, 67, 68], neutron spin echo spectroscopy [69] and inelastic neutron scattering [70].

The study of Fukazawa *et al.* [65] used AC susceptibility to search for the postulated ordering transition of Gingras *et al.* in  $\text{Dy}_2\text{Ti}_2\text{O}_7$  [64]. The study was careful but limited. They concluded that below 0.5 K no spin dynamics on the experimental timescale were detected and that therefore the system was frozen and could not move through the manifold into the ordered state [65]. All the studies show that the dynamics of spin ices become extremely slow at low temperature, and this is one likely reason that the loop moves groundstate has not yet been observed in a real system. However, the other studies show that the dynamics are more complicated than a simple, single freezing transition.

The investigations of the frequency dependence of the AC susceptibility of both  $\text{Ho}_2\text{Ti}_2\text{O}_7$  and  $\text{Dy}_2\text{Ti}_2\text{O}_7$  by Matsuhira *et al.* [66, 67] represent the most detailed study of spin relaxation in spin ices. They found  $\text{Ho}_2\text{Ti}_2\text{O}_7$  to be somewhat simpler.

Below  $T \approx 0.6$  K  $\chi'$  and  $\chi''$  are zero, indicating no further relaxation. Above this there is a peak in both  $\chi'$  and  $\chi''$  with maximum at  $T \approx 1$  K (see figure 2.7). This is suggested to be the freezing process in which the spin ice correlations become locked in. The exact peak temperature is frequency dependent and follows an Arrhenius law with an activation energy of 27.5 K and a characteristic relaxation time of order  $10^{-10}$  seconds.

Matsuhira *et al.* also investigated  $\text{Dy}_2\text{Ti}_2\text{O}_7$  [67] (see figure 2.7). Their treatment of this material is more complicated due to the observation of two distinct relaxation processes. A similar study has also been made by Snyder *et al.* [68] and the interpretation differs significantly.

At temperatures of  $T \approx 1$  K Matsuhira *et al.* observed a feature which appears to be essentially analogous to that in  $\text{Ho}_2\text{Ti}_2\text{O}_7$ . In data recorded at 500 Hz there is a feature at  $T \approx 15$  K which becomes a peak at 19 K at 10 KHz. However, it is completely absent from low frequency and dc data. As for  $\text{Ho}_2\text{Ti}_2\text{O}_7$ , the 1 K feature can be fitted to the Arrhenius law with an activation energy of 10 K and a relaxation time which rapidly increases with falling temperature. The higher temperature feature can also be fitted to an Arrhenius law with an activation energy of 220 K and a relaxation time of  $5 \times 10^{-11}$  seconds. If this law persists to lower temperature then the characteristic time scale will be beyond the typical window of the dc measurement below  $T \approx 8$  K. It appears that there is a crossover of the dominant relaxation mechanism from the high-frequency region to the low-frequency region at around 10 K.

Because the upper feature is absent in the dc data the frequency dependence was further investigated as an unusual relaxation process was anticipated. A plot of  $\chi''$  vs.  $\chi'$  revealed that the relaxation was not described by the Cole-Cole formula. Instead the data were analyzed using the Davidson-Cole formula<sup>a</sup>. They

---

<sup>a</sup>The Cole-Cole plot was developed in the study of dielectrics such as rosin oil, ice and slate [71]. It was found that a convenient way to work with the data was to plot the two components ( $\epsilon'$  and  $\epsilon''$ ) of the complex dielectric constant ( $\epsilon^*$ ) against each other, for each measured frequency (i.e. as an Argand diagram). For a material relaxing by a simple Debye process, the plot is a semicircle. It is centered on the real ( $\epsilon'$ ) axis and intercepts this axis at  $\epsilon_0$  (the static value), and  $\epsilon_\infty$  (the high frequency value). The semicircle is the locus of the dielectric constant as  $\omega$  varies from zero to  $\infty$ . Equivalent theories for paramagnets predict the same frequency dependence [72, 73]. Cole

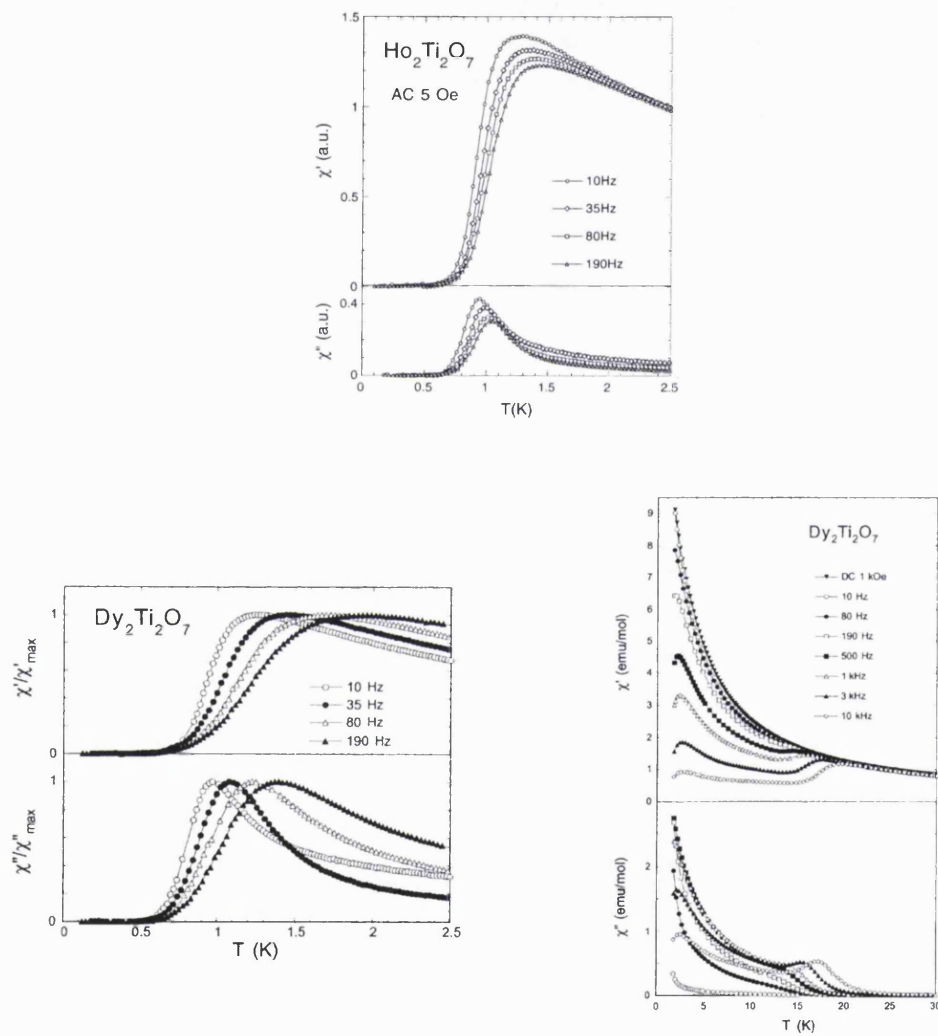


**Figure 2.7:** Ac susceptibility of  $\text{Ho}_2\text{Ti}_2\text{O}_7$  (top) and  $\text{Dy}_2\text{Ti}_2\text{O}_7$  (bottom left and right) [66, 67].  $\text{Ho}_2\text{Ti}_2\text{O}_7$  shows only one relaxation process in these measurements, whereas  $\text{Dy}_2\text{Ti}_2\text{O}_7$  shows two.

accounted for the two features with a distribution of relaxation times which has a cut off and a tail to short times (see figure 2.8). The cutoff time,  $\tau_c$ , shifts to ever longer times with falling temperature. This extends the tail across a wider range of timescales. This means fast processes are important at high temperature only, as the tail decreases in magnitude as the temperature falls. The high temperature feature is therefore caused by a shift of  $\tau_c$  through the time window of the high frequency measurement at these temperatures. As the temperature falls through the crossover region the  $\chi' - \chi''$  plot becomes closer to a semi-circle again, suggesting that there is now a single relaxation with a narrow time distribution. They concluded that the low temperature feature was the establishment of the spin ice regime and that the origin of the crossover and the high temperature process was unknown.

Snyder *et al.* [68] collected data under the same conditions and it included the same features. Contrastingly, they concluded that the higher temperature feature was the spin ice freezing transition. However, they offer no interpretation of the low temperature peak clearly present in their data and imply that the high temperature peak of  $\text{Dy}_2\text{Ti}_2\text{O}_7$  is analogous to the only peak of Matsuhira's  $\text{Ho}_2\text{Ti}_2\text{O}_7$  data. They found that  $E_a = 210$  K for their relaxation process. They concluded that the process responsible was single spin flips. At high temperatures the spins can flip uncorrelated with their neighbors. At low temperatures these flips are precluded due to spin-spin correlations, hence the system freezes. They demonstrated the importance of spin-spin interactions by showing that the feature is strongly suppressed by diamagnetic dilution. However, they do not explain why their freezing transition occurs at an energy scale much higher than that of the

---

and Cole found that many materials did not show a semi-circle, but rather a circular arc, with the center depressed from the  $\epsilon'$  axis. The Cole-Cole formula, which can be used to fit these arcs, is  $\epsilon^* - \epsilon_\infty = (\epsilon_0 - \epsilon_\infty)/[1 + (i\omega\tau_0)^{1-\alpha}]$  where  $\epsilon^*$  is the complex dielectric constant,  $\omega$  is the angular frequency, and  $\tau_0$  is a generalized relaxation time. The parameter  $\alpha$  varies between 0 and 1. If  $\alpha = 0$  the result is the same as the original one of Debye. In studies of glycerine Davidson and Cole found a new response [74, 75]. At high frequencies the locus is similar to the arc function of Cole and Cole, but at low frequencies it approaches the semi-circle of simpler theories. The Debye form describes relaxation by a simple process. When the Davidson-Cole form is required, a distribution of simple relaxation processes is envisaged. The distribution is continuous, up to a cutoff, which is  $\tau_0$ .

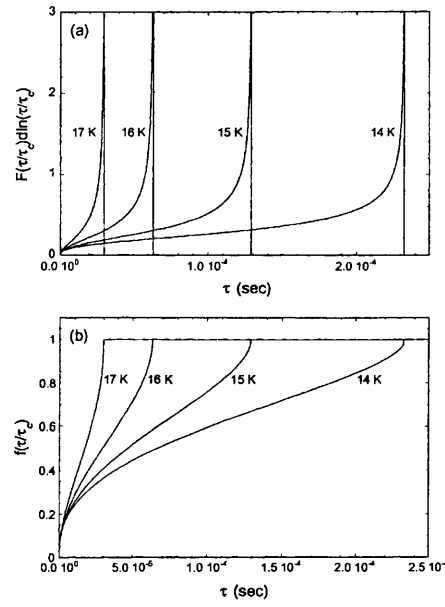


**Figure 2.8:** Distribution of relaxation times in  $\text{Dy}_2\text{Ti}_2\text{O}_7$  (top), and the fraction of processes with relaxation time less than  $\tau$  (bottom) [67]. The cut-off form of the distribution function can be clearly seen (top). Also as the temperature falls and the cut-off moves to longer times the importance of fast processes can be seen to decrease. As the tail of the distribution extends across wider ranges of timescale the fraction of fast process falls.



spin interactions. The experimental facts are not readily reconciled. The central question raised by comparing the work of Matsuhira *et al.* [66, 67], and Snyder *et al.* [68], is why there is no high temperature peak in  $\text{Ho}_2\text{Ti}_2\text{O}_7$ ? If both compounds are spin ices, it is expected that their freezing will be the same, with only slightly different energy scales.

Quite extensive studies of  $\text{Ho}_2\text{Ti}_2\text{O}_7$  have been made using inelastic or quasi-elastic neutron scattering [70]. No spin dynamics were observed. This is because the dynamics of spin ices are so slow that the characteristic timescale of inelastic neutron scattering experiments is much too short to be useful.

Neutron spin echo spectroscopy (NSE) is a novel neutron scattering technique which can operate at a much longer timescale than conventional neutron experiments. NSE measures  $S(\mathbf{Q}, t)$  which contains far more information about spatio-temporal spin relaxations than ac-susceptibility which measures  $\chi'(0, \omega)$  and  $\chi''(0, \omega)$ . The NSE measurement can be related to a susceptibility measurement by a Fourier transform and Kramers-Kronig inversion of  $S(\mathbf{Q}, t)$  [69].

$\text{Ho}_2\text{Ti}_2\text{O}_7$  has been quite extensively investigated using NSE [69]. The NSE results were compared and correlated with more susceptibility measurements. An explanation was advanced for the difference between  $\text{Ho}_2\text{Ti}_2\text{O}_7$  and  $\text{Dy}_2\text{Ti}_2\text{O}_7$  observed by Matsuhira *et al.* [66, 67, 69]. The relaxation function of  $\text{Ho}_2\text{Ti}_2\text{O}_7$  was measured as a function of temperature between 0.05 and 200 K. These relaxation functions were fitted to a simple exponential function:

$$F(Q, t) = (1 - B) \exp(-\Gamma(T)t). \quad (2.3)$$

The frequencies  $\Gamma(T)$  can be fitted to an Arrhenius expression giving an attempt frequency of  $1.1 \pm 0.2 \times 10^{11}$  Hz and an activation energy of  $293 \pm 12$  K. An important fact that was established by the use of a neutron scattering technique was the  $Q$ -independence of the relaxation function. This process was named the “high” process. It appears to be due to a single ion flipping mechanism, hence it is  $Q$ -independent and has an activation energy close to the lowest crystal field levels.

The NSE signal was extrapolated into the ac-susceptibility time window. This implied that the missing 15 K peak should be present. Additional susceptibility measurements were made in applied fields and the peak appeared [69]. By careful

normalisation it could be observed even in very small fields. The frequency shift of the peak implied the expected activation barrier of  $\sim 250$  K.

A 1 K peak was also observed by susceptibility and this could be fitted to a relaxation process with attempt frequency of order  $10^{10}$  Hz and  $E_a \approx 20$  K. The reverse extrapolation into the NSE time window implies that this process should be visible above 4 K. The fact that it is not means it does not exist on the shorter timescales of the NSE experiment. This was referred to as the “low” process.

At short timescales (i.e. in the NSE experiment) relaxation is by the high process. At longer timescales the low process acts as a “cut-off” and drives  $S(Q, t)$  to zero. Both processes relax the same set of thermal fluctuations. This is clear because the high process also drives  $S(Q, t)$  to zero, not a finite number. If this were not the case correlations would remain that were static in the NSE experiment. Therefore, whichever process is fastest at a given temperature relaxes all the thermal fluctuations in the spin system.

The low process is responsible for the 1 K peak. In order to observe the 15K peak the low process must be sufficiently slow for the high process to provide significant relaxation in the ac-susceptibility time window. Apparently the applied field suppresses the low process, revealing the peak. The rate of the low process in  $\text{Dy}_2\text{Ti}_2\text{O}_7$  must be slower so that the 15 K peak is observed. In  $\text{Ho}_2\text{Ti}_2\text{O}_7$ , diamagnetic doping greatly increases the rate of the low process and the same effect in  $\text{Dy}_2\text{Ti}_2\text{O}_7$  will lead to the disappearance of the peak as the high process is cut off by the accelerated low process. It appears that the underlying processes of the two spin ices are the same but that the observed dynamics are controlled by the relative rates of the two processes. Therefore the small difference in energy scale leads to a large difference in experimental observation (this is illustrated schematically in figure 2.9).

## 2.5 Spin Ices in Applied Magnetic Fields

An interesting departure of spin ice physics from ordinary ice is the ease with which a degeneracy removing perturbation can be applied. The most useful is an applied magnetic field. In cubic crystals there are three special directions along

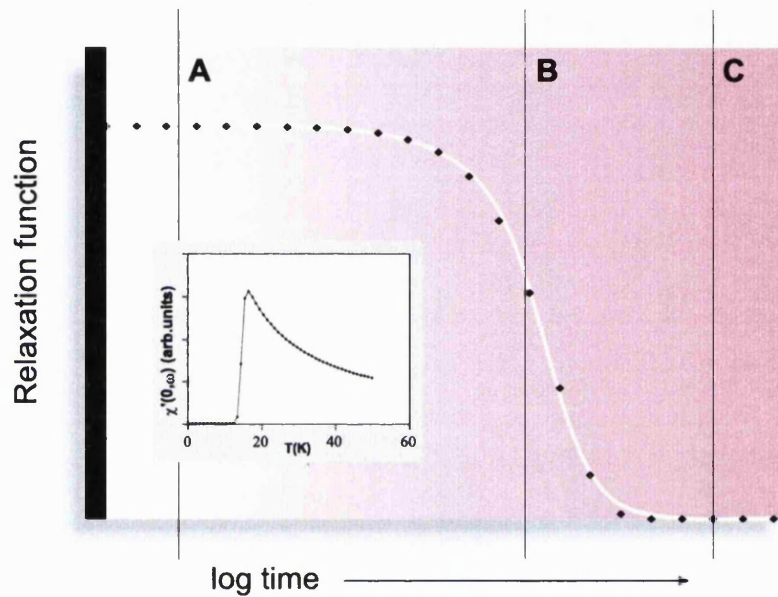


**Figure 2.9:** Inset: the extrapolated ac susceptibility  $\chi'(0, 103 \text{ Hz})$  corresponding to the “high” process measured by the NSE technique, showing a peak at 15 K. Main figure: the schematic relaxation function in the ac-susceptibility time window, showing how the 15 K peak is revealed in the spin ice materials. Vertical lines A, B, C denote the “cut-off” of  $S(Q, t)$  due to the “low” process. When the low process is (relatively) fast, as at A, the peak is not present, as all relaxation is due to the low process. In the intermediate situation (B) the peak is just observed, as in  $\text{Dy}_2\text{Ti}_2\text{O}_7$ . When the high process dominates the relaxation (C) the peak is clearly observed. An applied field reveals the peak by shifting the cut-off to longer times (case C), while diamagnetic dilution eliminates it by shifting the cut-off to shorter times (case A) [69].

which a field is conventionally applied in such a study. The first is  $[h00]$ , a cell edge, or perpendicular to one edge of a tetrahedron. The second is  $[hh0]$ , a unit cell face diagonal and parallel to a tetrahedron edge. The last is  $[hhh]$ , a unit cell body diagonal and parallel to one of the Ising axes of a tetrahedron. The different relationships of the three applied field directions to the tetrahedral units of the pyrochlore lattice suggest that there will be different degeneracy removal schemes associated with each (different ordered groundstates on a single tetrahedron are depicted in figure 2.10 and for a full unit cell in figure 2.11).

Applying a field on  $[h00]$  is expected to fully remove the degeneracy. This is because every spin has a component in the direction of the field. Each tetrahedron will be driven into a spin ice state with a net moment in the field direction. This is an unusual type of ferromagnet in which non-collinear order is observed. The periodicity of the magnetic structure is the same as the crystal lattice and the symmetry is not lowered so magnetic Bragg peaks are expected only at the nuclear positions. The propagation vector is therefore  $\mathbf{k} = 0$  but historically this has been called the  $Q = 0$  structure.

Similarly if the field is applied on  $[hhh]$  it is expected that the degeneracy will be fully removed. In this case all the spins have a component in the field direction, but the groundstate in a strong field is not an ice rules state. Because the field is directed along an easy axis, one of the spins will be pinned pointing into or out of the tetrahedron. The other three spins will also point in the same sense leading to an umbrella type structure and a “three-in-one-out” or “one-in-three-out” type arrangement.

The  $[hh0]$  direction is the most complicated. Two spins on a tetrahedron have a component in this direction. The field pins one spin in and one out. The other two spins are exactly perpendicular to this direction and so are not pinned by the field, but the ice rule means that they also form an in/out pair. The two groups of spins form chains, either parallel or perpendicular to the field. Each chain has a magnetic moment in the sense of the chain. Because the ice rules are only constraining nearest neighbors, they do not couple adjacent chains (i.e. perpendicular chains to other perpendicular chains). This means that the field is unable to fully remove the degeneracy. Adjacent chains may be parallel or antiparallel. All the chains in

the field direction are expected to be parallel. If all the perpendicular chains are also parallel then the structure is again  $Q = 0$  but the moment of the structure is at  $45^\circ$  to the applied field. If successive perpendicular chains are reversed then a different structure is obtained. This has a net moment in the direction of the applied field. Although the unit cell is the same size, the symmetry is reduced as parts of the tetrahedral basis become inequivalent on related tetrahedra. Due to the appearance of magnetic Bragg peaks at positions such as 110 this structure is historically known as  $Q = X$ .

There are six principal reports of the experimental behavior of spin ices in applied fields. One involves neutron scattering at low temperature [25, 54], the second uses heat capacity measurements [56], the others are magnetization measurements on single crystals [65, 76, 77, 78, 79]. Theoretical investigations have also been made [55, 58, 65, 80].

The magnetization studies have used  $\text{Ho}_2\text{Ti}_2\text{O}_7$  [76, 77] and  $\text{Dy}_2\text{Ti}_2\text{O}_7$  [65, 78, 79]. In all the studies single crystals were oriented with a special direction on the applied field and the magnetization was measured using a magnetometer. All observed the same general features which are expected from simple calculations. These are rapid saturation of the magnetization for the field applied on  $[00l]$  or  $[hh0]$  and a plateau in the magnetization when the field is applied on  $[hhh]$  (one set of measurements is shown in figure 2.12). Because of the strongly anisotropic properties of these systems the magnetization is expected to saturate at three different and distinctive values for the three applied field directions (as in figure 2.12). The key difference between the studies is whether this is observed [65, 77] or not [76]. No explanation is yet available for the observation of identical saturation magnetization in all three directions made by Cornelius and Gardner [76]. The remaining study focuses entirely on the formation of a “kagomé ice” state and is described in section 2.6 [78, 79].

The neutron scattering study of Harris *et al.* is of particular relevance as in technique and approach it is the study most closely resembling this work [25]. In this work a large single crystal of  $\text{Ho}_2\text{Ti}_2\text{O}_7$  was aligned with the  $[h\bar{h}0]$  direction vertical, giving the  $hhl$  scattering plane later discussed in this work. On cooling in zero field no change was observed on any Bragg peaks, no transition to a

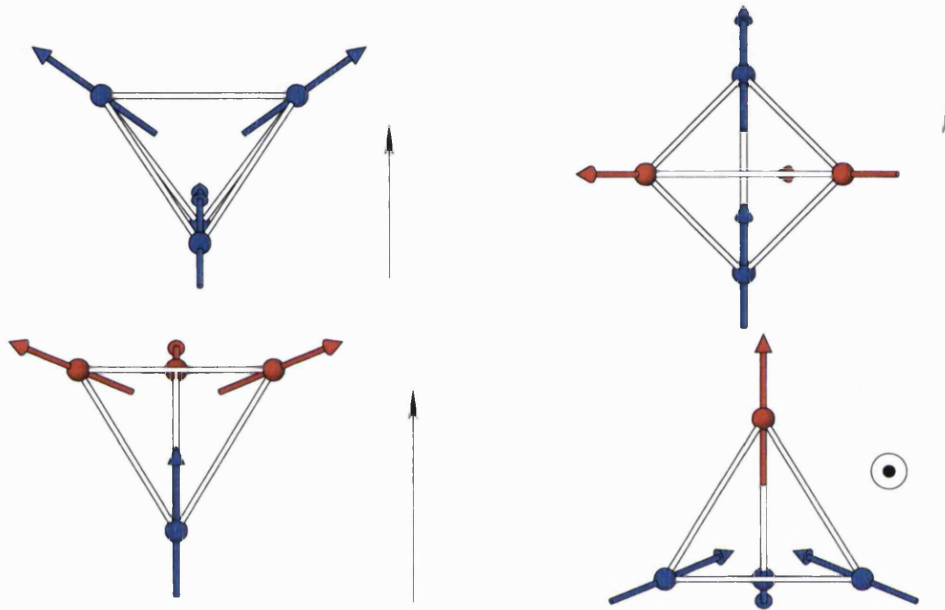


**Figure 2.10:** Different ground states on single tetrahedra, the applied field direction is shown by the arrow, or its projection. Top left is the single tetrahedron with field applied on  $[00l]$ , all the spins are pinned by the field. Top right is with the field on a  $[hh0]$  type direction, which is the edge of a tetrahedron, only two spins are pinned by the field (blue), two remain free (red). Bottom left is with the field applied on  $[hhh]$ , a threefold axis of the tetrahedron (vertical in this picture). One spin is exactly parallel to the field (blue) and three are less strongly pinned (red). In this groundstate the ice rule has been broken as there is one spin in and three out. Bottom right has the field on a  $[hh2h]$  type direction which bisects a triangular face of the tetrahedron (here the basal face), pinning three spins (blue) and leaving one free (red), the ice rules dictate the orientation of this spin.

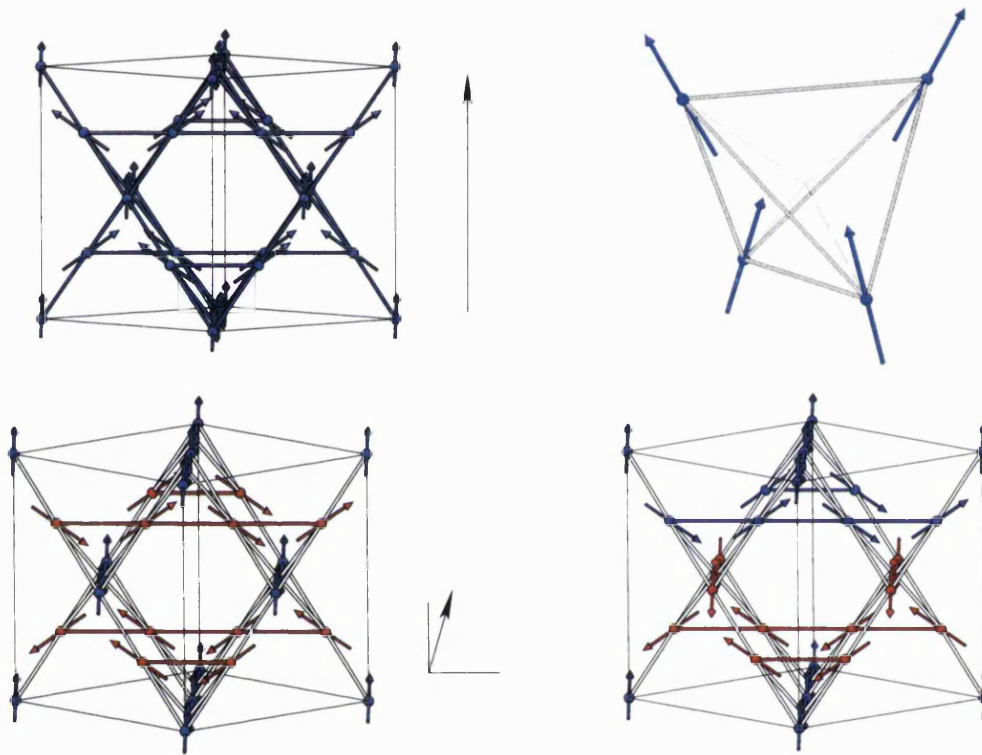


**Figure 2.11:** Different ordered structures consistent with the ice rules. Applied fields are indicated by the arrows. Top left is the  $Q = 0$  structure expected when the field is applied on  $[00l]$  (parallel to the cell edge in the plane of the page). Top right is the canted groundstate obtained by Champion *et al.* [58], which is identical to  $Q = 0$  except that the spins are not confined to the easy axes. Bottom left is a  $Q = X$  structure obtained when the field is applied on  $[hh0]$  (parallel to the face diagonal into the plane of the paper). The spins are separated into parallel (blue) and transverse (red) chains. Bottom right is the ordered structure found by Melko *et al.* [64]. It compares closely to  $Q = X$  except that antiparallel chains are obtained in both senses making it a true antiferromagnet.

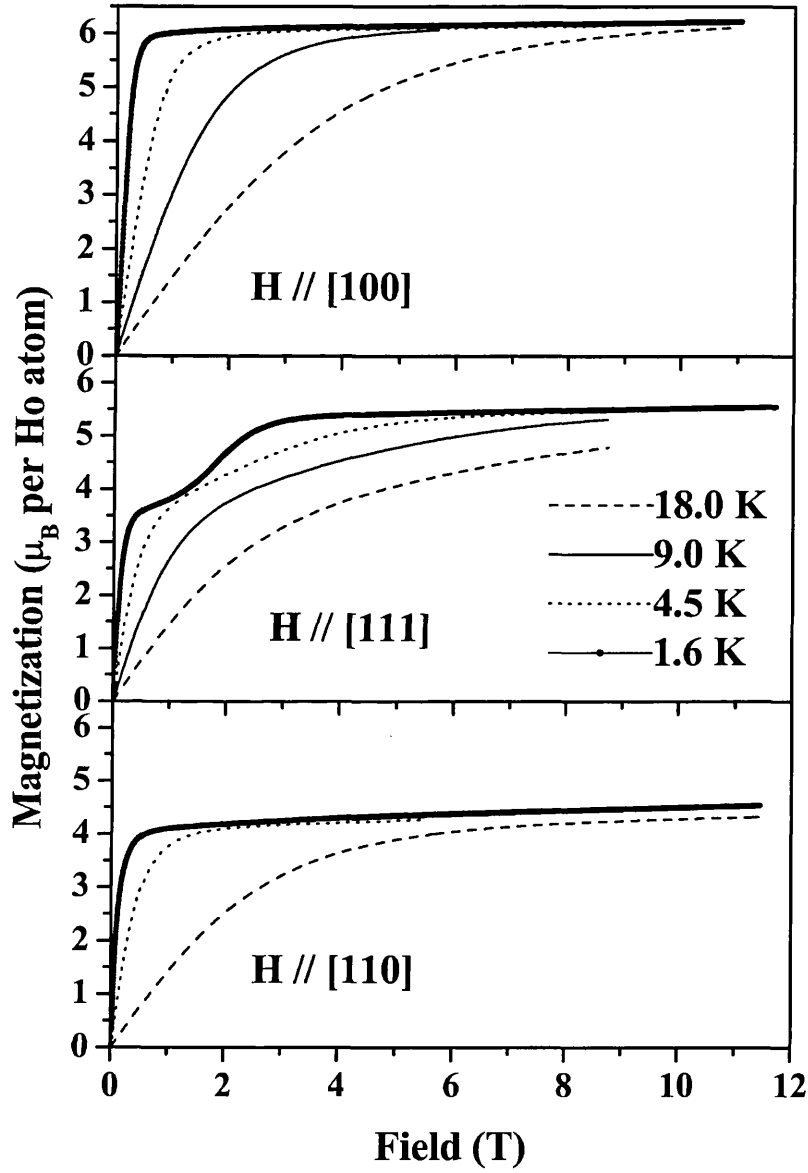


**Figure 2.12:** High temperature magnetization measurements in  $\text{Ho}_2\text{Ti}_2\text{O}_7$  [77]. Different magnetization properties with different applied field directions reflect the highly anisotropic properties of  $\text{Ho}_2\text{Ti}_2\text{O}_7$ .



magnetically ordered state occurred. At 0.35 and 1.8 K strong diffuse scattering was observed. At 0.35 K the sharpness of the diffuse scattering suggested that correlations extended up to four neighbors.

The behavior in applied fields was described as both dramatic and unusual. It was found that a field as small as 0.1 T was sufficient to cause the appearance of strong magnetic Bragg peaks, at any temperature in the range 0.35-50 K. These Bragg peaks appeared at positions such as 002, or 111, which are zone centers, and so this was referred to as a  $Q = 0$  structure. Increasing the field lead to the saturation of intensity from this structure. When working at 0.35 K, they found that removing the field did not completely destroy the intensities, a small intensity remained which could be destroyed by heating the sample to 1 K. They concluded that long range order could be frozen into the sample at this temperature (see figure 2.13).

Scattering was also observed at other positions in reciprocal space such as 001. This type of scattering was found to be even more complicated than the Bragg scattering. The width and intensity depended on temperature, field and history. On raising the field at 0.35 K they found that the intensity increased, but much stronger fields were required than for the  $Q = 0$  Bragg peaks. The  $Q = 0$  Bragg peaks would appear in fields of as little as 0.1 T, but a field of 0.5 T was required for the onset of this diffuse scattering. At 0.35 K the scattering remains quite broad for all fields. If the temperature was then raised to 2.0 K, whilst maintaining the field at 2 T, the diffuse scattering became much sharper and the intensity increased greatly, passing through a maximum at  $T \approx 1.4$  K and then disappearing. The  $Q = 0$  peaks remained constant during this scan (see figure 2.14).

This observation was interpreted as a modification of the  $Q = 0$  structure, which becomes stable at 1.4 K. It was named the  $Q = X$  structure. They obtained a value of  $4.6(5) \mu_B$  for the ordered moment in the  $Q = 0$  structure. They were unable to make any estimate for the  $Q = X$  structure as insufficient data were available. They concluded that the  $Q = X$  structure previously described was “consistent” with their observations. Finally they noted that the strong single-ion anisotropy is probably responsible for large energy barriers between groundstates which causes spin freezing.

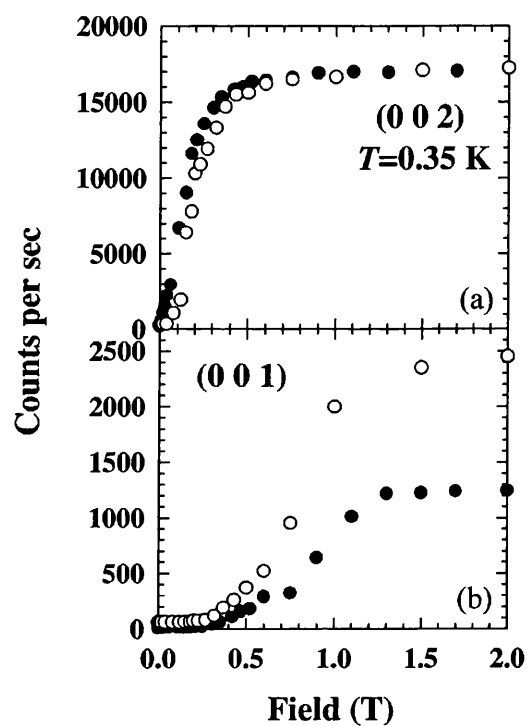


**Figure 2.13:** The full circles show zero field cooled measurements while the open circles are points measured after a field of 0.5 T was applied and removed before the measurements began. The sample is strongly history dependent and long range order can be frozen in [25].

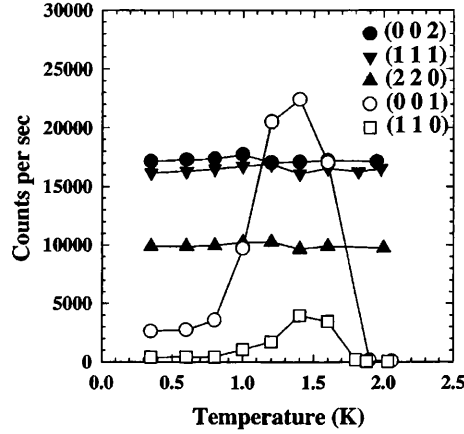


**Figure 2.14:** These measurements were made while heating in an applied field. The open circles are  $Q = X$  peaks and the full circles are  $Q = 0$  peaks. The measurement shows that thermal activation is required for the modification of the  $Q = 0$  to the  $Q = X$  structure [25].

The heat capacity work by Ramirez *et al.*, which was discussed in the context of the residual entropy of a spin ice, also contains some data for applied fields [56]. The particular problem with this data is that it is measured using a powder and so the field is applied along any crystallographic direction imaginable. In addition to determining the residual entropy of  $\text{Dy}_2\text{Ti}_2\text{O}_7$  the heat capacity was measured in the range 0.1 – 10 K in fields of 0-6 T. Three small sharp peaks appear in the heat capacity in finite fields. These peaks are field independent, occurring always at  $T_p = 0.34, 0.47$  and 1.12 K. These peaks are attributed to the ordering of spins not pinned by the field. Their small contribution to the entropy of the sample is then explained by the fact the measurement was made on a powder and so only a small proportion of crystallites are well enough aligned to have unpinned spins.

Theoretical studies of spin ices in applied fields have also been made, these are by Harris *et al.* [55], Champion *et al.* [58], and Siddharthan *et al.* [80]. Harris *et al.* used a classical Ising Hamiltonian

$$\mathbb{H} = -\frac{1}{2}J \sum_{i,j} \mathbf{S}_i^z \cdot \mathbf{S}_j^z - \sum_i \mathbf{H} \cdot \mathbf{S}_i^z \quad (2.4)$$

in Monte Carlo simulations [55]. The first summation is over nearest neighbors

only. No ordering was observed in zero field, as expected for a near neighbor spin ice. Simulations were then carried out with applied fields on the three symmetry directions:  $[00l]$ ,  $[hh0]$ , and  $[hhh]$ . They observed that the magnetization depends on the direction of the applied field, as described above, and that the field and exchange interactions compete in the formation of ice rule/non-ice rule states with the field applied on  $[hhh]$ .

Subsequently they present more details of the simulations for the  $[00l]$  direction. In this case the magnetization has a positive curvature until it reaches full saturated order, at which point there is a discontinuous change into the saturated state. This is characteristic of a field induced phase transition. By simulating as a function of temperature in different applied fields a section of the  $H/T$  phase diagram was covered. In zero field the system shows no ordering transition and the heat capacity consists of a single Shottky anomaly due to isolated spin flips. In small fields a very sharp peak occurs below the Shottky anomaly, this is the phase transition. For higher fields the transition temperature is higher and the sharp peak moves closer to the Shottky anomaly and eventually for  $HS/J > 1.5$  the two merge into a single smooth feature. There is a change in behavior as the field is increased. The sharp peak is indicative of a first order phase transition, which changes into a continuous ordering process.

The moving first order phase transitions give a line in the phase diagram, which is eventually terminated by a critical point. This is analogous to the pressure-temperature phase diagram of a liquid-gas system. The analogy is made by comparing the scalar value of the magnetization with the density of the fluid. There are two phases with a finite magnetization. One has high entropy and enthalpy and is below the coexistence line, the phase above the coexistence line has low entropy and enthalpy, but both have a broken magnetic symmetry (i.e. finite magnetization, or density in the fluid case). A triple point occurs at  $H = T = 0$  (the phase diagram is shown in figure 2.15).

The continuous spin ice model of Champion *et al.* reproduces this phase diagram in the limit of infinite anisotropy (because in that case it is the same model) [58]. As the anisotropy decreases the triple point moves to higher and higher temperatures and the critical lines shorten. Eventually when the anisotropy

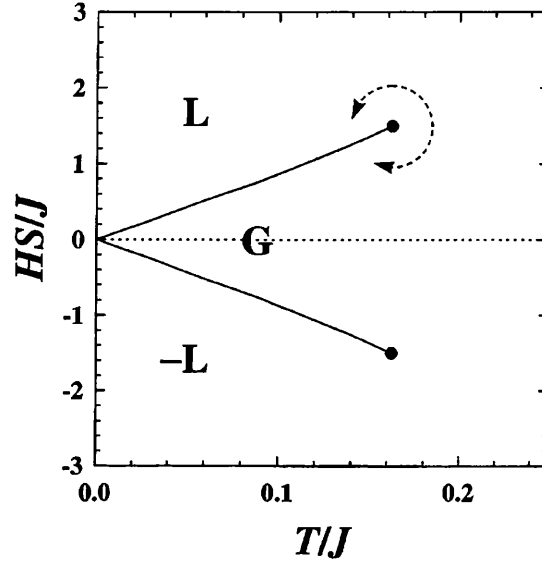


**Figure 2.15:** Phase diagram for near neighbor spin ice with field applied on  $00l$ . The full lines show the line of field induced first order phase transitions, terminating in critical points. L and G represent the liquid and gas phases respectively [55].

becomes small there is a single line of first-order transitions along the zero field axis of the phase diagram, typical for a ferromagnet.

The work of Siddharthan *et al.* [80] is chiefly concerned with the dipolar interaction (discussed above in the section “Dipolar Spin Ice”) but does include a brief description of the effect of an increasing applied field on the simulation. Two field directions are mentioned,  $[hhh]$  and the unusual  $[h\bar{h}\sqrt{2}h]$ . The simulations appear to be at very low effective temperatures as the changes in magnetization are extremely abrupt. For the  $[hhh]$  direction a single major step is observed with two tiny minor ones. The  $[h\bar{h}\sqrt{2}h]$  shows many small steps apparently superimposed on two larger ones. It is suggested that these steps are due to a series of magnetic transitions.

## 2.6 Kagomé Ice

The newest development in the field of spin ice is the concept of Kagomé ice. This concept has been arrived at from two directions. One is the simulations of a Ising Kagomé ferromagnet by Wills *et al.* [81]. The other is the magnetization measurements of Matsuhira on  $\text{Dy}_2\text{Ti}_2\text{O}_7$  with the field applied on  $[hhh]$  [78, 79].

When measuring the magnetization of  $\text{Dy}_2\text{Ti}_2\text{O}_7$  with the field applied on  $[hhh]$  below 1 K Matsuhira *et al.* found the distinctive plateau expected in theory [55, 80] and demonstrated also in other measurements [65, 77, 76]. However, they investigated this plateau phase quite extensively and were able to make very interesting observations which had been overlooked in other investigations. Their significant realization was that in the plateau phase three spins on each tetrahedron remain disordered.

Heat capacity measurements in applied fields were used to test their hypothesis that the plateau phase would have a residual entropy. In zero field the entropy was measured as  $\approx 1.6 \text{ J (mol Dy)}^{-1}$ , in agreement with other estimates, and that for a spin ice. In the field range 0.25 – 0.75 T, where the plateau phase is developed, the magnetic entropy is  $0.8 \pm 0.1 \text{ J (mol Dy)}^{-1}$ . Unfortunately a finite entropy of  $\approx 0.4 \text{ J (mol Dy)}^{-1}$  was measured in strong fields, when in fact zero entropy was expected. This was attributed to inaccuracy in estimating the entropy contributions from higher temperatures. This is particularly exacerbated in the high field data as all the features have been shifted toward higher temperatures.

## 2.7 Summary of Spin Ice Properties

The measured, calculated and predicted properties of spin ices have been extensively introduced. They will be summarized very briefly.

A spin ice is a frustrated pyrochlore magnet. Unlike other frustrated magnets which are invariably antiferromagnets, spin ices are ferromagnets. Strong anisotropy confining the spins to the  $\langle hhh \rangle$  directions is required for this effect. The source of the frustration depends on the model used. If a nearest neighbor model is employed, then the frustration is due to underconstraint in the ice rule which specifies the groundstate. If the dipolar spin ice model is being used then

the frustration comes from some sort of self-screening of the dipolar interaction. So far spin ice behavior is recorded in  $\text{Ho}_2\text{Ti}_2\text{O}_7$ ,  $\text{Dy}_2\text{Ti}_2\text{O}_7$  and  $\text{Ho}_2\text{Sn}_2\text{O}_7$ .

Because the magnet is frustrated no order is observed down to 0.05 K, at least in zero field. The two different models make different predictions about the eventual groundstate of a spin ice. The nearest neighbor model predicts only a short range ordered state. With simple spin flip dynamics the dipolar spin ice model also predicts a short range ordered state, although the exact correlations are somewhat different. However, these dynamics become extremely slow at very low temperatures. If the dynamics are restored using moves involving loops of spins, then an ordered groundstate is found. The transition to the ordered groundstate is at a temperature well below the energy scale of the dipolar interaction. Experimentally no sign of this ordered state has yet been found. As a spin ice is cooled in zero field it settles into a state characterized by short-range correlations and extremely slow or frozen dynamics. At very low temperatures the slow dynamics make the sample history dependent. Applied magnetic fields can be used to investigate removal of the degeneracy. So far complicated field and temperature dependencies have been observed with the field on  $[\bar{h}\bar{h}0]$  at very low temperature, and direction dependent magnetization at high temperature.

The aim of the experiments presented in this thesis was to further investigate the  $H, T$  phase space and history dependence of spin ice. Using ultra-low temperature single crystal neutron scattering the evolution of the spin ice correlations can be investigated microscopically. An applied field was to be used to search for the postulated liquid-gas critical point [55]. Also it was hoped to use the magnetic field to encourage relaxation at low temperature, and therefore access the predicted groundstate [64]. Finally, the boundaries of the ice rule regime were to be probed, either using high fields which drive the magnet into broken ice rule states, or by using a field and temperature range that would show the onset of ice rule correlations.

## 2.8 Other Rare Earth Pyrochlores

Much interest has been shown in  $\text{Ho}_2\text{Ti}_2\text{O}_7$  and  $\text{Dy}_2\text{Ti}_2\text{O}_7$  where the strong anisotropy leads to Ising like moments and spin ice states. Other rare earth titanates have also been investigated. The anisotropy in  $\text{Er}_2\text{Ti}_2\text{O}_7$  is of the opposite sign and so it is an  $XY$  pyrochlore [52, 54]. It is stated that the continuous degrees of freedom in this case prevents frustration [52]. However, this is not actually true.  $\text{Er}_2\text{Ti}_2\text{O}_7$  is a pyrochlore antiferromagnet and is therefore frustrated to some degree [63]. Only the anisotropic antiferromagnet has a unique groundstate [63, 82]. Increasing the degrees of freedom available to the spin does not relieve the frustration in any sense, in fact, it leads to more groundstates. Despite this it is clear that  $\text{Er}_2\text{Ti}_2\text{O}_7$  is able to select a unique groundstate [33, 54]. In theory the  $XY$  pyrochlore undergoes an order-by disorder transition and the ordered state of  $\text{Er}_2\text{Ti}_2\text{O}_7$  that is selected is consistent with this theory [33].

$\text{Gd}_2\text{Ti}_2\text{O}_7$  [35] and  $\text{Tb}_2\text{Ti}_2\text{O}_7$  [19, 83] have also been studied experimentally. For  $\text{Gd}_2\text{Ti}_2\text{O}_7$  bulk measurements indicate an ordering transition at 0.97 K. The spin-only nature of  $\text{Gd}^{3+}$  ( $S = 7/2$ ) means this is expected to be an isotropic ion [20]. Solution of the magnetic structure has shown that  $\text{Gd}_2\text{Ti}_2\text{O}_7$  is considerably more complex than was expected. The magnetic structure is partially ordered, with a separation into ordered spins in kagomé planes with disordered interstitial spins [84]. This does not agree at all with theory [35, 36].

$\text{Tb}_2\text{Ti}_2\text{O}_7$  has been found to be a collective paramagnet at temperatures down to 0.07 K [83]. Understanding  $\text{Tb}_2\text{Ti}_2\text{O}_7$  requires very careful consideration of the crystal field [19]. If the  $\text{Tb}^{3+}$  environment were perfectly cubic then it is expected that the ion will have a non-magnetic groundstate. It is also possible that there is no permanent moment on the  $\text{Tb}^{3+}$  and the moment is induced by a “collective bootstrapping” of the magnetic (exchange and/or dipolar) interactions. In this case it is expected that due to the absence of interactions a very dilute sample of  $(\text{Tb}_x\text{Y}_{1-x})_2\text{Ti}_2\text{O}_7$  will be non-magnetic. Experimental measurements suggest that such an energy level scheme is inappropriate and that there is indeed a permanent moment on the  $\text{Tb}^{3+}$  site. Crystal field calculations are in good agreement with the experimental data and suggest that the moment is strongly anisotropic and Ising like. The excitations are of lower energy than for the other systems of this



---

type and so the Ising description only applies at temperatures below 10 K. Since  $\text{Tb}_2\text{Ti}_2\text{O}_7$  has antiferromagnetic coupling it is not clear why it fails to order in the  $\text{FeF}_3$  structure. The most plausible explanation of the co-operative paramagnetism is that there are competing interactions, as in  $\text{Dy}_2\text{Ti}_2\text{O}_7$ . Further neighbor and dipolar interactions prevent the ordering transition from occurring [19].

# Chapter 3

## Neutron Scattering

The theories of neutron and X-ray scattering by crystals are well described in many books. Each treats the same central concepts in a slightly different way. The books employed during my PhD and ultimately during the concoction of this chapter are by Kittel, Rosssat-Mignod, Squires, Dunitz, Azaroff, Nield and Keen, and Lovesey [8, 11, 85, 86, 87, 88, 89, 90].

The theory of neutron scattering, as introduced by Squires or Lovesey builds from the ground up by considering the scattering of neutrons from ever more complicated cases until the system has become a crystal [85, 89, 90]. The X-ray crystallography books often take a more geometrical approach, being less concerned with the mechanics of the scattering process itself [86, 87]. The fundamental approach of Squires or Lovesey is ultimately more useful in neutron scattering as it allows the incorporation of inelastic and magnetic scattering, and polarization effects. The description given here starts with the geometrical approach. Subsequently some of the details of the scattering of neutrons by nuclei and electrons will be illustrated.

### 3.1 Reciprocal Lattice and Diffraction

Following Dunitz we consider an abstract scattering system [86]. The treatment by Dunitz involves a distribution of electrons, as the discussion was focussed entirely on X-ray scattering. Here the details of the scattering system are completely

ignored, only the geometry is of interest. Consider a volume element  $d\mathbf{r}$  containing  $\rho(\mathbf{r})d\mathbf{r}$  scatters at distance  $\mathbf{r}$  from the origin with incident and scattered waves given by unit vectors  $\hat{\mathbf{k}}_0$  and  $\hat{\mathbf{k}}$ . The wave that we are considering has form  $A_0 \cos 2\pi\nu t$ . It propagates with velocity  $v$  so at some distance  $x$  from the source, at time  $t$ , the phase is

$$2\pi\nu(t - x/v), \quad \text{or} \quad 2\pi(\nu t - x/\lambda). \quad (3.1)$$

At a given time  $t$  an increase in distance  $\Delta x$  corresponds to a decrease in phase of  $2\pi\Delta x/\lambda$ .

The paths of the waves scattered at the origin and at  $\mathbf{r}$  differ. The latter is longer by  $\mathbf{r} \cdot (\hat{\mathbf{k}}_0 - \hat{\mathbf{k}})$  and so the phase of the wave scattered at  $\mathbf{r}$  is  $2\pi\mathbf{r} \cdot (\hat{\mathbf{k}} - \hat{\mathbf{k}}_0)/\lambda$  with respect to the origin. The complex amplitude of the wave scattered at  $\mathbf{r}$  is proportional to

$$\rho(\mathbf{r}) \exp[2\pi i \mathbf{r} \cdot (\hat{\mathbf{k}} - \hat{\mathbf{k}}_0)/\lambda] d\mathbf{r}, \quad (3.2)$$

which we rewrite as

$$\rho(\mathbf{r}) \exp(2\pi i \mathbf{Q} \cdot \mathbf{r}) d\mathbf{r}, \quad (3.3)$$

where  $\mathbf{Q} = (\hat{\mathbf{k}} - \hat{\mathbf{k}}_0)/\lambda$ .

If  $\rho(\mathbf{r})$  describes some continuous distribution of scatterers, the complex amplitude of the superposition of the scattered wavelets is obtained by integration:

$$F(\mathbf{Q}) = \int \rho(\mathbf{r}) \exp(2\pi i \mathbf{r} \cdot \mathbf{Q}) d\mathbf{r}. \quad (3.4)$$

$\mathbf{Q}$  is the scattering vector, it bisects the angle between  $\hat{\mathbf{k}}$  and  $-\hat{\mathbf{k}}_0$  and has dimensions of reciprocal length. This angle is  $2\theta$  so  $|\mathbf{Q}| = 2 \sin \theta / \lambda$ .  $F(\mathbf{Q})$  depends on the distribution of scatterers and on  $\mathbf{Q}$ ; it is the structure factor.

Now the scattering system must be specified as a crystal of sorts. We specify a lattice with a basis of a single point scatterer constructed by

$$\mathbf{r}(n_1, n_2, n_3) = n_1 \mathbf{a}_1 + n_2 \mathbf{a}_2 + n_3 \mathbf{a}_3 \quad (3.5)$$

( $n_i$  are integers and  $\mathbf{a}_i$  are the basis vectors). The unit cell can be defined by  $\mathbf{a}_i$  and its volume  $V = \mathbf{a}_1 \cdot \mathbf{a}_2 \otimes \mathbf{a}_3$ . At this point we introduce the reciprocal lattice construction. We define another set of vectors  $\mathbf{b}_i$  reciprocal to the set  $\mathbf{a}_i$  such that

$$\mathbf{a}_j \cdot \mathbf{b}_j = 1 \quad \text{and} \quad \mathbf{a}_j \cdot \mathbf{b}_k = 0 \quad \text{if } j \neq k, \quad (3.6)$$

giving three vectors

$$\mathbf{b}_1 = \frac{\mathbf{a}_2 \otimes \mathbf{a}_3}{\mathbf{a}_1 \cdot \mathbf{a}_2 \otimes \mathbf{a}_3} = \frac{\mathbf{a}_2 \otimes \mathbf{a}_3}{V}, \quad (3.7)$$

$$\mathbf{b}_2 = \frac{\mathbf{a}_1 \otimes \mathbf{a}_3}{\mathbf{a}_2 \cdot \mathbf{a}_1 \otimes \mathbf{a}_3} = \frac{\mathbf{a}_1 \otimes \mathbf{a}_3}{V}, \quad (3.8)$$

$$\mathbf{b}_3 = \frac{\mathbf{a}_1 \otimes \mathbf{a}_2}{\mathbf{a}_3 \cdot \mathbf{a}_1 \otimes \mathbf{a}_2} = \frac{\mathbf{a}_1 \otimes \mathbf{a}_2}{V}, \quad (3.9)$$

which are the reciprocal lattice basis vectors (with dimensions of reciprocal length).

The scattering vector  $\mathbf{Q}$  has dimensions of reciprocal length so can be expressed as

$$\mathbf{Q}(h_1, h_2, h_3) = h_1 \mathbf{b}_1 + h_2 \mathbf{b}_2 + h_3 \mathbf{b}_3, \quad (3.10)$$

and scalars such as  $\mathbf{Q} \cdot \mathbf{r}$  become

$$\mathbf{Q}(h_1, h_2, h_3) \cdot \mathbf{r}(n_1, n_2, n_3) = h_1 n_1 + h_2 n_2 + h_3 n_3. \quad (3.11)$$

The structure factor of this lattice of point scatters has become

$$F(\mathbf{Q}) = c \sum_{n_i} \exp(2\pi i \mathbf{Q} \cdot \mathbf{r}) \quad (3.12)$$

$$F(\mathbf{Q}) = c \sum_{n_1, n_2, n_3} \exp[2\pi i (h_1 n_1 + h_2 n_2 + h_3 n_3)], \quad (3.13)$$

and the individual contributions of the sum are in phase only if

$$h_1 n_1 + h_2 n_2 + h_3 n_3 = \text{integer}. \quad (3.14)$$

Since  $n_i$  are integers so  $h_i$  must also be.

Constructive interference (diffraction) only occurs when  $\mathbf{Q} = (\hat{\mathbf{k}} - \hat{\mathbf{k}}_0)/\lambda$  is a reciprocal lattice vector. The above equations show that the reciprocal lattice and the direct lattice are related as a Fourier transform pair. The Brillouin zone is defined as a Wigner-Seitz primitive cell in the reciprocal lattice. It is constructed by taking perpendicular bisectors to the reciprocal lattice vectors joining a central point with its nearest neighbors. Because there is a reciprocal lattice point at the center of every Brillouin zone, Bragg peaks can be represented in reciprocal space as occurring at the center of Brillouin zones. The diffraction pattern therefore maps the centers of the Brillouin zones and is an image of the reciprocal lattice.

## 3.2 Nuclear Scattering

The purpose of this section is to briefly introduce the formal derivation of neutron scattering equations with particular respect to those used later in actual calculations. This theory begins with the definition of scattering cross-sections. A beam of monochromatic neutrons is incident on some target scattering system. Various types of measurement may be made on the scattered neutrons, and the result is expressed in terms of the cross-section. The partial differential cross-section (ignoring the spin states of the neutron) is defined as

$$\frac{d^2\sigma}{d\Omega dE'} = \frac{\text{(number of neutrons scattered per second into a small solid angle } d\Omega \text{ in the direction } \theta, \phi \text{ with final energy between } E' \text{ and } E' + dE')}{\Phi d\Omega dE'}, \quad (3.15)$$

where  $\Phi$  is the incident flux of neutrons. If the energy is not analyzed then the measurement corresponds to the differential cross-section

$$\frac{d\sigma}{d\Omega} = \frac{\text{(number of neutrons scattered per second into } d\Omega \text{ in the direction } \theta, \phi)}{\Phi d\Omega}. \quad (3.16)$$

The theory itself is a quantum mechanical scattering theory in which the state of the system and neutron before and after scattering are considered. The differential cross section  $(d\sigma/d\Omega)_{\lambda \rightarrow \lambda'}$  represents the sum of processes in which the state of the scattering system changes from  $\lambda$  to  $\lambda'$ , and the state of the neutron changes from  $\mathbf{k}$  to  $\mathbf{k}'$ . The sum is taken over all the values of  $\mathbf{k}'$  that lie in the small solid angle  $d\Omega$  in the direction  $\theta, \phi$ , the values of  $\mathbf{k}$ ,  $\lambda$ , and  $\lambda'$  remaining constant. From the definition of  $d\sigma/d\Omega$  given in 3.16 this is

$$\left(\frac{d\sigma}{d\Omega}\right)_{\lambda \rightarrow \lambda'} = \frac{1}{\Phi} \frac{1}{d\Omega} \sum_{\mathbf{k}' \text{ in } d\Omega} W_{\mathbf{k}, \lambda \rightarrow \mathbf{k}', \lambda'}, \quad (3.17)$$

where  $W_{\mathbf{k}, \lambda \rightarrow \mathbf{k}', \lambda'}$  is the number of transitions per second from the state  $\mathbf{k}$ ,  $\lambda$  to the state  $\mathbf{k}'$ ,  $\lambda'$ . This can be evaluated using Fermi's golden rule and eventually gives

$$\left(\frac{d\sigma}{d\Omega}\right)_{\lambda \rightarrow \lambda'} = \frac{k'}{k} \left(\frac{m}{2\pi\hbar^2}\right)^2 |\langle \mathbf{k}' \lambda' | V | \mathbf{k} \lambda \rangle|^2, \quad (3.18)$$

where  $V$  is the potential for the neutron-nucleus system and  $m$  is the mass of the neutron.

The use of the golden rule involves equating a sum over a range of states to an expression evaluated at a particular  $\mathbf{k}'$ . However, for fixed  $\mathbf{k}$ ,  $\lambda$ , and  $\lambda'$ , there is a very narrow range of  $|\mathbf{k}'|$  values for which transitions are probable. The center of this range corresponds to conservation of energy in the overall neutron-scatterer system. Because of this, all the scattered neutrons in the  $(d\sigma/d\Omega)_{\lambda \rightarrow \lambda'}$  cross section have the same energy. Consequently the partial differential cross section is

$$\left( \frac{d\sigma}{d\Omega dE'} \right)_{\lambda \rightarrow \lambda'} = \frac{k'}{k} \left( \frac{m}{2\pi\hbar^2} \right)^2 |\langle \mathbf{k}'\lambda' | V | \mathbf{k}\lambda \rangle|^2 \delta(E_\lambda - E_{\lambda'} + E - E'), \quad (3.19)$$

where  $E$  and  $E'$  are the initial and final energies of the neutron, and  $E_\lambda$  and  $E_{\lambda'}$  the scattering system. The utility of this approach is due to the fact that any potential can be used where  $V$  has been written. The basic scheme can be followed for either nuclear or magnetic scattering with interchanged potential functions. The potential function used for nuclear scattering is the Fermi pseudo-potential,

$$V(\mathbf{r}) = \frac{2\pi\hbar^2}{m} b\delta(\mathbf{r}), \quad (3.20)$$

where  $b$  is the scattering length, and the  $\delta(\mathbf{r})$  dependence ensures the interaction is very short ranged.

The derivation continues over many more pages, the important features are described below. Firstly an experiment measures one of the cross sections defined above, not one in which the scattering system undergoes a specific transition from one state to another. Because of this  $(d\sigma/d\Omega dE')_{\lambda \rightarrow \lambda'}$  must be summed over all final states  $\lambda'$ , and then averaged over all initial states. This averaging is carried out using the probabilities of the system being in each state  $\lambda$  as given by the Boltzmann distribution.

Real scattering systems often have a variable scattering length at different sites. This is because of nuclear spins and/or isotopes. The effect is to separate the cross section into two terms, coherent and incoherent. Coherent scattering depends on the correlation between the positions of the same nucleus at different times, and on the correlation of different nuclei at different times. It therefore gives rise to interference effects. Assuming there is no correlation between position and scattering length, the coherent scattering will depend on the average scattering length. The incoherent scattering depends only on the correlation of the positions

of the same nucleus at different times and does not give rise to interference effects. The incoherent scattering is due to the random distribution of deviations of the scattering lengths from the mean value and depends on  $(\bar{b}^2 - (\bar{b})^2)$ . The coherent elastic scattering contribution from a crystalline material is the Bragg scattering

$$\left(\frac{d\sigma}{d\Omega}\right)_{\text{coh el}} = N \frac{(2\pi)^3}{v_0} \sum_{\mathbf{G}} \delta(\mathbf{Q} - \mathbf{G}) |F_N(\mathbf{Q})|^2, \quad (3.21)$$

where  $F_N(\mathbf{Q})$  is the nuclear unit cell structure factor given by

$$F_N(\mathbf{Q}) = \sum_j \bar{b}_j \exp(2\pi i \mathbf{Q} \cdot \mathbf{r}_j) \exp(-W_j), \quad (3.22)$$

where  $\bar{b}_j$  is the average scattering length of atom  $j$ ,  $\mathbf{Q}$  is the scattering vector, and  $\mathbf{r}_j$  the vector of fractional coordinates of atom  $j$  in the unit cell.  $W_j$  is the Debye-Waller factor of atom  $j$ , which reflects the thermal motion of the atom about its equilibrium position.

Equation 3.22 forms the basis of calculating the intensity of a nuclear peak. the sum over  $\mathbf{G}$  can be omitted as only a single peak is being calculated, the  $\delta$ -function simply says the equation only works at the Bragg peak. The prefactor would eventually be absorbed into a scale factor.

### 3.3 Magnetic Neutron Scattering

Despite its neutrality, the neutron has a magnetic moment,  $\mu_n$ . This means that the neutron interacts with unpaired electrons. This is because of the energy of the neutron magnetic moment in the magnetic field arising from these electrons. For a single electron with momentum  $\mathbf{p}$  at a position  $\mathbf{r}$  the field experienced by a neutron is

$$V_M(\mathbf{r}) = -\mu_n \cdot \mathbf{H} = -\mu_n \cdot \left( \text{curl} \frac{\mu_e \otimes \hat{\mathbf{r}}}{r^2} - \frac{2\mu_B \mathbf{p}_i \otimes \hat{\mathbf{r}}}{\hbar r^2} \right). \quad (3.23)$$

where  $\mu_n = -\gamma \mu_N \sigma$ , in which  $\gamma = 1.913$ ,  $\mu_N$  is the nuclear magneton, and  $\sigma$  is the Pauli spin operator for the neutron. The first term of equation 3.23 arises from the spin of the electron, and the second from its orbital motion. Magnetic scattering is more complicated than nuclear because both the dipole-dipole interaction for spin,

and dipole-current interaction for orbital motion are long ranged and non-central. This also means that a form-factor must be introduced for magnetic scattering as, like X-ray scattering, the non-central interaction means that scattering at large  $2\theta$  is weak compared to low angle. The appearance of the spin operator of the neutron in the magnetic potential is the reason that polarized neutron scattering is such a powerful tool for the microscopic investigation of magnetic materials.

With an unpolarized beam the cross section is a sum of the nuclear and magnetic parts. It turns out that the magnetic scattering is due to the total magnetization of a magnetic ion, i.e. both the spin and orbital components. However, it is only the component of the magnetic moment perpendicular to the scattering vector that is actually involved in the scattering process. These considerations mean that the total cross section can be calculated as

$$\frac{d\sigma}{d\Omega}(\mathbf{Q}) = \frac{d\sigma_N}{d\Omega}(\mathbf{Q}) + \frac{d\sigma_M}{d\Omega}(\mathbf{Q}), \quad (3.24)$$

where

$$\frac{d\sigma_M}{d\Omega}(\mathbf{Q}) = N \frac{(2\pi)^3}{v_0} \sum_{\mathbf{G}} \sum_{\mathbf{k}} |\mathbf{F}_{M\perp}(\mathbf{Q})|^2 \delta(\mathbf{Q} - \mathbf{k} - \mathbf{G}). \quad (3.25)$$

with

$$\mathbf{F}_{M\perp}(\mathbf{Q} = \mathbf{G} + \mathbf{k}) = \sum_j \mathbf{S}_{\perp j} \exp 2\pi i \mathbf{Q} \cdot \mathbf{r}_j. \quad (3.26)$$

The perpendicular spin component can be found using the identity

$$\mathbf{S}_{\perp} = \mathbf{S} - (\mathbf{S} \cdot \hat{\mathbf{Q}}) \hat{\mathbf{Q}}. \quad (3.27)$$

The alternative  $\delta$ -function to the nuclear scattering cross section (compare equations 3.21 and 3.25) is due to the fact that the magnetic unit cell need not have the same size or symmetry as the nuclear one. If the two are different then additional magnetic Bragg peaks can occur. However, these are always related to the nuclear Bragg peaks by a propagation vector. When the magnetic structure is commensurate and not symmetry lowering (e.g. a ferromagnet), the propagation vector is  $\mathbf{k} = 000$  and the magnetic Bragg peaks occur only at the nuclear positions. In general each Brillouin zone will contain a single nuclear Bragg peak which will have a number of magnetic Bragg peaks about it, related by each distinct  $\mathbf{k}$ , and its symmetry equivalents.



### 3.4 Extinction

Early X-ray diffraction studies showed that the integrated intensities of strong reflections were often in poorer agreement with theory than those of weak reflections. This is the characteristic feature of extinction.

Previously the central part of the kinematic theory of crystal optics was outlined, i.e. that diffraction occurs only when a rather rigorous geometry is satisfied. The average scattering cross section per unit volume of the crystal can be calculated in this framework and is found to be

$$I = \left| \frac{aFK}{V} \right|^2 \frac{\lambda^3}{\sin 2\theta}. \quad (3.28)$$

where  $a$  is a constant (depending whether X-rays or neutrons are being scattered),  $F$  is the unit cell structure factor,  $K$  the coefficient of polarization (1 for neutron diffraction), and  $V$  the unit cell volume. In this kinematic theory no account of the extinction effect is made. The reason for this is the approximation that the incident beam is unchanged throughout the crystal. Of course this is not true because the incident beam is being attenuated progressively by the Bragg scattering. Not only is the incident beam being attenuated, but it can also be augmented by a rescattering of the Bragg scattered radiation.

Ultimately the dynamical theory must be invoked but this is intractable for anything but the simplest situation. The kinematical theory can be adapted to allow for extinction by introducing a correction coefficient,

$$F_c = yF_{\text{obs}}. \quad (3.29)$$

Although it is possible to use an entirely empirical correction in this equation, increasingly complicated theoretical derivations of the correction exist. These are due to Darwin, Zachariasen and Becker and Coppens [91, 92, 93].

Darwin showed that (for X-rays) when attenuation of the incident beam was included, the incident beam should be completely extinguished after it had penetrated the crystal to a very small depth. This would have made the intensity independent of absorption, which was already known not to be the case. Because of this, Darwin proposed that most crystals are imperfect and introduced the mosaic model of a crystal. This was a simplifying assumption used by Darwin and

some older crystallographic authors argue that it should not be taken too seriously as a depiction of the actual internal structure of a crystal [86, 87]. In discussing extinction it is usual to talk of perfect crystals, (ideally) imperfect crystals (mosaic crystals with suitable mosaic parameters), and real crystals. A mosaic crystal consists of small blocks of perfect material separated by discontinuities and misaligned by some small amount. This concept solves Darwin's problem because the divergence of the incident beam means only a small proportion is totally reflected at the crystal surface, and the remainder can propagate through the crystal until suitably oriented mosaic blocks are encountered.

Two different types of extinction can be defined. Primary extinction is due to the attenuation of the incident beam as it passes through a single block. This is important in perfect crystals. The diffracted beam is less intense than might be expected as the shielded lower layers cannot contribute their expected intensity. An ideally imperfect crystal has such small blocks that primary extinction can be neglected.

Secondary extinction occurs when the incident beam is attenuated by scattering in one block and subsequently reaches another with the same alignment. The second block is being shielded by the first and again the scattered intensity is less than expected. This type of extinction is a property of imperfect/mosaic crystals and its severity depends on the size of the blocks and their angular distribution (mosaic spread). In a real crystal both effects may be operating, depending on the crystal quality.

The calculations of the extinction parameter by Zachariasen and by Becker and Coppens have a similar beginning, and proceed in a similar way, but differ in detail so that their final form is quite different [92, 93]. Their results differ due to errors in Zachariasen's derivation and the more general coordinate system used by Becker and Coppens [93]. The crystal is first assumed to be perfect. It is oriented such that the reflecting plane is vertical and so the diffraction condition is controlled by rotation of a single angle  $\epsilon_1$ . The start point is a pair of coupled differential equations:

$$\frac{\partial I_0}{\partial x_1} = -\sigma(I_0 - I) \quad (3.30)$$

$$\frac{\partial I}{\partial x_2} = -\sigma(I - I_0) \quad (3.31)$$

$$\frac{\partial I_0}{\partial x_1} + \frac{\partial I}{\partial x_2} = 0. \quad (3.32)$$

The coordinate system depends which theory is being discussed, all the equations presented here come from the Becker and Coppens derivation [93] where  $x_1$  is the distance along the incident beam and  $x_2$  along the scattered beam. The quantity  $\sigma$  is the scattering cross section of a volume element of the crystal, it is dependent on  $\epsilon_1$ . It is assumed that  $\sigma(\epsilon_1)$  is constant inside the crystal, and can be calculated from the kinematical theory, i.e.

$$\sigma(\epsilon_1) = J_0^{-1} v^{-1} P_k(\epsilon_1), \quad (3.33)$$

where  $P_k(\epsilon_1)$  is the power recorded in the detector (for a given direction of incident beam) and  $J_0$  is the intensity of the incident beam. Integration over  $\epsilon_1$  therefore gives the kinematical integrated intensity  $\mathbb{P}_k = \int P(\epsilon_1) d\epsilon_1 = J_0 v Q$  ( $v$  is the irradiated crystal volume).

The object of both theories is then to solve the differential equations and produce  $y$ . The boundary conditions for the differential equations can be specified at the surface of the crystal. Where the incident beam first reaches the surface of the crystal it has intensity  $I_0 = J_0$ . There will be a similar point where the scattered beam has zero intensity.

The power of the diffracted beam  $P(\epsilon_1)$  is given by an integral over the volume of the crystal. Becker and Coppens determined how the intensity  $I_0$  at some point  $M(x_1, x_2)$  is related to  $I_0$  at preceding points  $N(u_1, u_2)$  such that radiation travels from  $N$  to  $M$  by a single re-scattering, the result is

$$\begin{aligned} I_0(x_1, x_2) &= J_0 \exp(-\sigma t_1) + \sigma^2 \{ \exp[-\sigma(x_1 + x_2)] \\ &\quad \times \int_{x_1^0}^{x_1} du_1 \int_{u_2^0}^{x_2} I_0(u_1, u_2) \exp[\sigma(u_1 + u_2)] du_2 \}. \end{aligned} \quad (3.34)$$

The diffracted power is then

$$P(\epsilon_1) = \sigma \int_v I_0(x_1, x_2) \exp(-\sigma t'_2) dv. \quad (3.35)$$

where  $t'_2$  is the distance along the diffracted beam to the crystal surface where the beam exits. Another function  $\phi(\sigma)$  is defined such that

$$P(\epsilon_1) = J_0 v \sigma \phi(\sigma) = P_k(\epsilon_1) \phi(\sigma). \quad (3.36)$$

and so

$$y = Q^{-1} \int \sigma \phi(\sigma) d\epsilon_1 \quad (3.37)$$

where

$$\phi(\sigma) = v^{-1} J_0^{-1} \int_v dv I_0(M) \exp(-\sigma t'_2). \quad (3.38)$$

When  $\phi(\sigma)$  and  $\sigma(\epsilon_1)$  are known, the extinction factor for an ideal crystal can be derived.

Iterative use of equation 3.34 can be used to calculate  $\phi(\sigma)$ . Applying it  $k$  iterative times allows for  $2k$ -fold exchange of intensity before the point  $M$  is reached. This creates a power series with terms being added where the power in  $\sigma$  is increasing by 2. For example, the first order approximation ( $k = 0$ ), which neglects the feedback term  $\sigma I$ , gives the solution:

$$I_0 = J_0 \exp(-\sigma t_1) \quad (3.39)$$

$$\phi(\sigma) = v^{-1} \int_v dv \exp[-\sigma(t_1 + t'_2)] \quad (3.40)$$

where  $t_1$  is the depth in the crystal along the incident beam. This is the expected result, with  $\sigma$  acting as an apparent absorption coefficient. However, this solution does not satisfy the conservation of energy (as represented by equation 3.32).

Having obtained solutions for perfect crystals, both theories then move on to consider mosaic crystals. When the crystallites are misaligned, the incident beam at a crystallite makes an angle  $(\epsilon_1 + \eta)$  with the ideal Bragg direction, if  $\eta$  is the misalignment angle of the crystallite. The diffracting cross section inside the crystallite is therefore  $\sigma(\epsilon_1 + \eta)$ . An angular distribution  $W(\eta)$  is defined for the crystallites. In the differential equations, outside a given crystallite,  $\sigma(\epsilon_1)$  is replaced by the convolution

$$\bar{\sigma}(\epsilon_1) = \int \sigma(\epsilon_1 + \eta) W(\eta) d\eta. \quad (3.41)$$

Zachariasen eventually determined that there were two important types of real crystals:

$$\begin{aligned} r/\lambda g &\gg 1 && \text{Type I} \\ \mathbb{P}_k &= f(gQ_0\bar{T}) \end{aligned} \quad (3.42)$$

$$\begin{aligned}
 r/\lambda g &\ll 1 && \text{Type II} \\
 \mathbb{P}_k &= f(r\lambda^{-1}Q_0\bar{T}) && (3.43)
 \end{aligned}$$

Type I crystals have a distribution function  $W$  much wider than the diffraction pattern from a single crystal and their integrated intensities depend on  $g$  (the mosaic spread), but not  $r$  (the domain radius). The reverse is true for type II crystals. Multi-wavelength measurements would be required to distinguish them.

Becker and Coppens also found two limiting cases:

- (1) The effective particle size is dominant in determining the width of the reflection curve, this corresponds to Zachariasen's type II. Because of a dependence on  $\sin 2\theta$ , for any particle size, any crystal will behave as a type II crystal for very small Bragg angles.
- (2) If the particle size is large, or mosaic spread small, the secondary extinction is dominated by the mosaic distribution. In this case it is necessary to consider the travel of the beams within a perfect crystallite. The primary and secondary extinction effects may be considered independent so that  $y \approx y_p \cdot y_s$ .

Becker and Coppens then noted that the correction could be calculated directly if the particle size and mosaic distribution could be measured, but that this is generally impossible. Furthermore,  $\sigma(\epsilon_1)$  and  $\bar{\sigma}(\epsilon_1)$  depend on the kinematical structure factor, which depends on the refinable parameters. Because of this, and because the original classification into type I and II became unclear in their theory, Becker and Coppens implemented a refinable extinction correction. Working with uncorrected intensities they included both the particle radius  $r$  and mosaic distribution coefficient  $g$  in a refinement taking account of the structural and extinction parameters.

The two theories, and some other modifications, were tested by Becker and Coppens themselves [94]. They found that their own approach was the best. Also they discovered that multi-wavelength data was indeed essential to avoid correlation between  $r$  and  $g$ , and that a Lorentzian distribution was the most useful for the mosaic spread function.

## 3.5 Diffuse Scattering

Bragg scattering contains information on the average structure of the material (in space and time) and occurs only at Brillouin zone centers. Often there are deviations from this structure, and this causes diffuse scattering. Diffuse scattering is defined by Lovesey as “all coherent scattering that is not Bragg scattering” [89]. This definition means that diffuse scattering can occur anywhere in reciprocal space. Also, because it is coherent scattering, it contains information on correlations between atoms.

The deviations from the average structure can also be described as disorder. If there were a systematic departure this would be a change in structure and there would be a change in Bragg scattering. Diffuse scattering is due to local departures from the average structure causing short ranged but non-trivial correlations. Bragg scattering is a property of fully periodic crystalline materials. Liquids and amorphous materials, in which there are short range correlations only, have only diffuse scattering. Diffuse scattering in crystalline materials is analogous to that from liquids or amorphous materials, it is due to short range correlations. The presence of Bragg scattering and diffuse scattering is indicative of the coexistence of short and long range order.

Disorder of different types can give rise to diffuse scattering, and the separation of the different origins of the diffuse scattering can be a problem. Static and dynamic disorder both occur. Static disorder is due to defects which do not involve atomic motions such as random substitutions in alloys. Dynamic disorder is time dependent and includes molecular reorientation or diffusion. Magnetic materials without long range order can also cause diffuse scattering. If they are completely disordered, i.e. paramagnetic, then the diffuse scattering will be completely featureless and so indistinguishable from any background. Only if there are non-trivial correlations does the diffuse scattering become structured.

### 3.5.1 Diffuse Scattering Analysis

Due to the variety of origins of diffuse scattering it is often difficult to analyze. Different methods are required for different materials, some are more suited to

certain experimental techniques than others. When an atomic model for the sample is available, the diffuse scattering can be calculated directly and compared to the experiment. Alternatively if the origin of the diffuse scattering is known then useful quantities can be extracted directly from the data. However, these analytical methods are limited to rather simple systems. The most productive methods for investigating diffuse scattering now seem to be computational [88].

Common methods for simulating condensed matter can be adapted to calculate diffuse scattering patterns. Molecular dynamics and Monte Carlo simulation have both been employed. Two other techniques have been developed specifically to deal with diffuse scattering, these are reverse Monte Carlo modelling (RMC), and the Pair Distribution Function Analysis method (PDF method).

RMC operates by fitting calculated structure factors to measured ones. An atomic configuration is used to calculate the structure factors. Then with each cycle, a random atom is moved a random amount, and the structure factors recalculated and fitted. If the move has improved the fit then it is accepted. If the fit has worsened then the move is accepted on the basis of a random probability, if it is rejected the atom is returned to its original position. It is this possibility of accepting detrimental moves, which can allow the structure to evolve out of a local minimum in the goodness of fit surface, which gives the technique its name. RMC can be applied to data from powders or single crystals, and to multiple data types (e.g. EXAFS or NMR, as well as diffraction data), often simultaneously. The PDF method is used for powder data. Fourier transforming the measured total scattering gives the pair correlation function  $G(r)$ . A structure is fitted to this using the smallest number of atoms possible. This makes it more suited to systems with small static distortions. RMC uses a model with a much larger number of atoms and is more useful for large deviations.

### 3.5.2 Diffuse Scattering Calculation for Single Crystals

Much work on diffuse scattering has used powder data. Far more information is obtained using a single crystal as the intensity is recorded as a function of  $\mathbf{Q}$  rather than  $|\mathbf{Q}|$ . Because diffuse scattering extends across all of reciprocal space and represents deviations from the average structure, the structure factor

equations presented above (equations 3.21 and 3.25) are no longer particularly useful. They represent the scattered intensity at a Bragg peak, any deviations are only represented as partial occupancies or thermal factors. When discussing magnetic scattering it was noted that the magnetic unit cell need not be the same size as the nuclear cell. In antiferromagnets the magnetic cell is often doubled in size compared to the nuclear cell. The antiferromagnetic Bragg peaks can be indexed at positions such as  $\frac{1}{2}\frac{1}{2}\frac{1}{2}$  when using the nuclear cell size. If the indexing was carried out using the doubled cell then this peak would be 111. By doubling the size of the unit cell the reciprocal space is compressed, inevitably since it has dimensions of  $l^{-1}$ . However, if the two reciprocal spaces are compared, the effect seems to be the calculation of Bragg peaks at fractional positions in the reciprocal space of the original small unit cell. This gives a method of calculating intensities across reciprocal space. The original unit cell is increased in size to a super-cell and the intensity is calculated at the Bragg peaks of the super-cell. The resolution of the calculation depends on the size of the super-cell, which should be made as large as possible. Essentially if an  $n \times n \times n$  super-cell is constructed  $n$  points can be calculated between two adjacent Bragg peaks along an axis of reciprocal space. The nuclear structure factor becomes

$$F(\mathbf{Q}) = \frac{1}{2\pi N} \left| \sum_{i=1}^N \bar{b}_i \exp(i\mathbf{Q} \cdot \mathbf{R}_i) \right|^2 \quad (3.44)$$

if the calculation is performed at  $\mathbf{Q}$  points which satisfy

$$\mathbf{Q} = 2\pi \left( \frac{h'}{an_a}, \frac{k'}{bn_b}, \frac{l'}{cn_c} \right) \quad (3.45)$$

for lattice parameters  $a, b, c$ , and a configuration box of  $N$  atoms with  $n_a, n_b, n_c$  unit cells in the three directions, with integer  $h', k', l'$  [95]. The same can be applied to the magnetic structure factor.

### 3.6 Summary

The aim of this chapter has been to introduce the equations and phenomena involved in the interpretation of the experimental data. Both short and long range order will be discussed, and structure factor calculations made using equations



---

and codes based on equations 3.21, 3.25, and 3.44. The reason for extinction corrections and the basis on which they can be made have also been outlined as this proves to be of great importance in analysis of data for  $\text{Ho}_2\text{Ti}_2\text{O}_7$  .

## Chapter 4

# Analysis of the Structure Factor

Before presenting the experimental data and its interpretation, it is a valuable exercise to consider the structure factors for nuclear and magnetic Bragg scattering by the rare earth titanates. This leads to some general conclusions about the scattering that might be observed. Because of the ice rules and the strong anisotropy the magnetic structures which are expected are few in number. Symmetry considerations also constrain the magnetic moment to the threefold axes [96]. In this chapter the *structure factors for the structures consistent with the applied field directions and the ice rules*, and in some cases their breakdown, are discussed.

The  $\text{Ln}_2\text{Ti}_2\text{O}_7$  materials crystallize in the cubic space group  $\text{Fd}\bar{3}\text{m}$ . The metals are divided between  $16c$  ( $\text{Ln}^{3+}$ ) and  $16d$  ( $\text{Ti}^{4+}$ ). Oxygen occupies two positions,  $48f$  and  $8a$ .  $\text{Fd}\bar{3}\text{m}$  has a choice of two origins. In this work the second choice of origin given in the International Tables was used [97]. This placed the origin at the  $16c$  site. The direct space lattice is face centered cubic and the  $16c$  positions are generated by the operation of the face centering translations on a four atom basis. Consequently the  $16c$  atoms can be divided into four groups, one of each type is found on each tetrahedron. The  $16c$  sites are illustrated in figure 4.1, with the four atom basis color-coded.

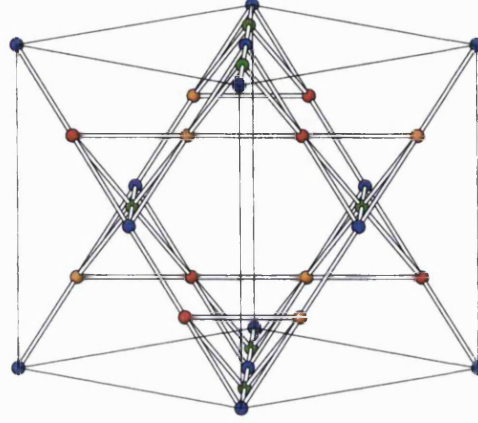


**Figure 4.1:** The pyrochlore unit cell, with the four atom basis of the 16c sites shown in color. Each color represents one atom of the basis, and its f.c.c. translation related equivalents.

## 4.1 The Nuclear Structure Factor

The nuclear structure factor for the 16c positions can be written as

$$F_N = b \left( \sum_{j=1}^4 e^{2\pi i(hx_{1j} + ky_{1j} + lz_{1j})} + \sum_{j=1}^4 e^{2\pi i(hx_{2j} + ky_{2j} + lz_{2j})} + \right. \\ \left. + \sum_{j=1}^4 e^{2\pi i(hx_{3j} + ky_{3j} + lz_{3j})} + \sum_{j=1}^4 e^{2\pi i(hx_{4j} + ky_{4j} + lz_{4j})} \right), \quad (4.1)$$

where  $b$  is the coherent scattering length of the 16c atom,  $h, k$  and  $l$  are the components of the scattering vector  $\mathbf{Q}$ , and  $x_j, y_j$  and  $z_j$  are the fractional coordinates of atom  $kj$ . In the index  $kj$ ,  $k$  denotes which part of the four atom basis is being considered, and  $j$  denotes which of the four f.c.c. translation related atoms is being considered. Attention is confined to the 16c sites as these are the only ones where magnetic scattering may occur.

Inspection of this structure factor leads, inevitably, to the reflection conditions tabulated in the International Tables of Crystallography. These state that  $h, k, l$  are permutable and that general reflections are allowed if

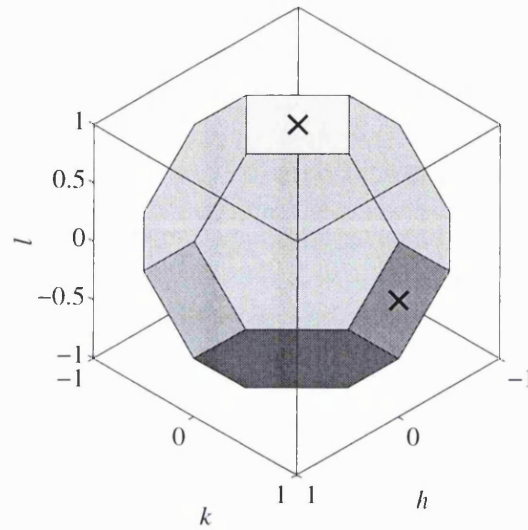


**Figure 4.2:** The first Brillouin zone of the f.c.c. lattice,  $X$  positions on the surface of the zone are marked ( $X$ ).

$$\begin{aligned}
 hkl &: h + k = 2n, h + l = 2n, k + l = 2n \\
 0kl &: k + l = 4n, k, l = 2n \\
 hhl &: h + l = 2n \\
 h00 &: h = 4n.
 \end{aligned} \tag{4.2}$$

The  $16c$  sites have the additional condition

$$\begin{aligned}
 hkl &: h = 2n + 1, \\
 \text{or } h, k, l &= 4n + 2 \\
 \text{or } h, k, l &= 4n.
 \end{aligned} \tag{4.3}$$

These conditions, combined with those for the oxygen positions, predict where nuclear Bragg peaks will occur. Of subsequent importance are the facts that 002 is disallowed while 004 is allowed, that there are both “metal only” and “oxygen only” reflections (e.g. 662 and 220 respectively) [51], and that there are no reflections with mixed odd and even indices.

The reciprocal of a face centered cubic lattice is a body centered cubic lattice [8]. The Brillouin zone is a truncated octahedron. The first zone is shown in figure 4.2. The nuclear Bragg peaks are all at zone centers, and so cannot be seen in the figure.

Other positions known as  $X$  are marked, these lie on the surface of the Brillouin zone. When a single scattering plane is studied it cuts through the surface of the Brillouin zone giving a characteristic shape. An example is shown for the plane  $hk0$  in figure 4.3, again the  $Q = X$  positions are marked. Since the zone centers are in the plane of the projection, the  $Q = 0$  peak positions can also be seen.

## 4.2 The Magnetic Structure Factor with Field Applied on $[00l]$

The configuration of either of the instruments used in this work means that applied field measurements must be made in two-axis mode (as against four-circle mode). With a vertical field magnet all scattering vectors therefore lie in a plane perpendicular to the applied field. When the field is applied on  $[00l]$  the scattering plane contains wavevectors with indices  $hk0$ . In this case it is expected that the ordered structure will be  $Q = 0$  (see figure 4.3), because all the interactions dictated by the ice rules can be satisfied, whilst the Zeeman energy is also minimized. In the  $Q = 0$  structure the four groups of atoms are unmodified (i.e. all members of each group remain in the group) by the magnetic structure, so the structure factor can therefore be expressed as

$$\begin{aligned} \mathbf{F}_M = & \mathbf{S}_{\perp 1} \sum_{j=1}^4 e^{2\pi i(hx_j + ky_j + lz_j)} + \mathbf{S}_{\perp 2} \sum_{j=1}^4 e^{2\pi i(hx_j + ky_j + lz_j)} + \\ & + \mathbf{S}_{\perp 3} \sum_{j=1}^4 e^{2\pi i(hx_j + ky_j + lz_j)} + \mathbf{S}_{\perp 4} \sum_{j=1}^4 e^{2\pi i(hx_j + ky_j + lz_j)}, \end{aligned} \quad (4.4)$$

where  $b$  has been replaced throughout by  $\mathbf{S}_{\perp n}$ , the components of the spin  $\mathbf{S}$  perpendicular to the scattering vector (given by equation 3.27). The use of  $\mathbf{S}_{\perp}$  instead of  $b$  can change the reflection conditions.

Using the atom positions and the specification of  $hk0$  scattering vectors we can

write the magnetic structure factor explicitly as

$$\begin{aligned}\mathbf{F}_M = & \mathbf{S}_{\perp 1}(1 + e^{\pi i k} + e^{\pi i h} + e^{\pi i(h+k)}) + \\ & + \mathbf{S}_{\perp 2}(e^{\frac{1}{2}\pi i(3h+k)} + e^{\frac{3}{2}\pi i(h+k)} + e^{\frac{1}{2}\pi i(h+k)} + e^{\frac{1}{2}\pi i(h+3k)}) + \\ & + \mathbf{S}_{\perp 3}(e^{\frac{1}{2}\pi i(h+2k)} + e^{\frac{1}{2}\pi i h} + e^{\frac{1}{2}\pi i(3h+2k)} + e^{\frac{3}{2}\pi i h}) + \\ & + \mathbf{S}_{\perp 4}(e^{\frac{1}{2}\pi i(2h+3k)} + e^{\frac{1}{2}\pi i(2h+k)} + e^{\frac{3}{2}\pi i k} + e^{\frac{1}{2}\pi i k}).\end{aligned}\quad (4.5)$$

Grouping the phase factors as  $A, B, C$  and  $D$  the structure factor becomes

$$\mathbf{F}_M = \mathbf{S}_{\perp 1}A + \mathbf{S}_{\perp 2}B + \mathbf{S}_{\perp 3}C + \mathbf{S}_{\perp 4}D, \quad (4.6)$$

and we can see that there will be some conditions due to the phase factors only. Firstly, any reflection for which  $A = B = C = D = 0$  will be forbidden. For  $hk0$  scattering vectors reflections with mixed odd and even  $h$  and  $k$  will be forbidden in this way. Also, one can see that combinations of the phase will not have the same additivity as they do in the nuclear structure factor. For nuclear reflections such as 200 the signs of the phases are mixed and a condition such as  $A - B - C + D$  exists, and since all are multiplied only by  $b$  these reflections are forbidden. For the magnetic structure factor this condition does not necessarily mean the reflection is forbidden since the addition of the  $\mathbf{S}_{\perp}$  components is more complicated.

For example, for 200, we can write

$$\frac{\mathbf{F}_M}{4} = \mathbf{S}_{\perp 1} - \mathbf{S}_{\perp 2} - \mathbf{S}_{\perp 3} + \mathbf{S}_{\perp 4}, \quad (4.7)$$

$$\mathbf{S}_{\perp 1} = \begin{pmatrix} 1 \\ 1 \\ 1 \end{pmatrix} - \frac{h+k+l}{\sqrt{h^2+k^2+l^2}} \hat{\mathbf{Q}}, \quad (4.8)$$

$$\frac{\mathbf{F}_M}{4} = \begin{pmatrix} 0 \\ 1 \\ 1 \end{pmatrix} - \begin{pmatrix} 0 \\ -1 \\ 1 \end{pmatrix} - \begin{pmatrix} 0 \\ -1 \\ 1 \end{pmatrix} + \begin{pmatrix} 0 \\ 1 \\ 1 \end{pmatrix}, \quad (4.9)$$

and so the intensity of this peak is finite, as

$$I_M \propto \mathbf{F}_M \cdot \mathbf{F}_M. \quad (4.10)$$

The reflection conditions for the  $Q = 0$  magnetic structure are therefore

$$\begin{aligned} hk0 : \quad & h, k = 4n, \\ \text{or} \quad & h = 4n, k = 2n \\ \text{or} \quad & h = 2n, k = 4n. \end{aligned} \tag{4.11}$$

The effect of this is to make all  $hk0$  reflections with both  $h$  and  $k$  even allowed. The nuclear structure factor does not allow either 200 or 420 which are prominently observed magnetic reflections. However, we see that all these peaks are at zone centers. This is why the structure was named  $Q = 0$  [25]. The positions of the Bragg peaks and the zone boundaries are illustrated in figure 4.3.

### 4.3 The Magnetic Structure Factor with Field Applied on $[h\bar{h}0]$

In two-axis mode this field direction means all scattering vectors lie in the  $hhl$  plane. The choice of  $[h\bar{h}0]$  as the field direction (as against  $[hh0]$ ) is a formalism to simplify subsequent calculation and discussion as it means that the scattering plane is  $hhl$ , rather than  $h\bar{h}l$ .

This field direction is interesting because half of the spins are orthogonal to the field direction (see figures 2.10 and 4.5). This separates the spins into two types. In order to gain Zeeman energy it is expected that those spins which can align with the field (as far as is permitted by the anisotropy), will do so. This produces chains of spins running parallel to the field (each chain has a ferromagnetic moment parallel to the field direction). On each tetrahedron one of the field pinned spins now points in, and one points out. For consistency with the ice rules the orthogonal spins must also have one pointing in and one out. This forms a second set of chains transverse to the field. The transverse spins must form chains; defects in the chains also cause defects in the ice rules state.

Two types of magnetic structure are allowed by this field direction. One has all the chains perpendicular to the applied field oriented in the same sense, the whole structure has a ferromagnetic moment at  $45^\circ$  to the applied field. In this case there are again four groups of spins. Consideration of the structure factor

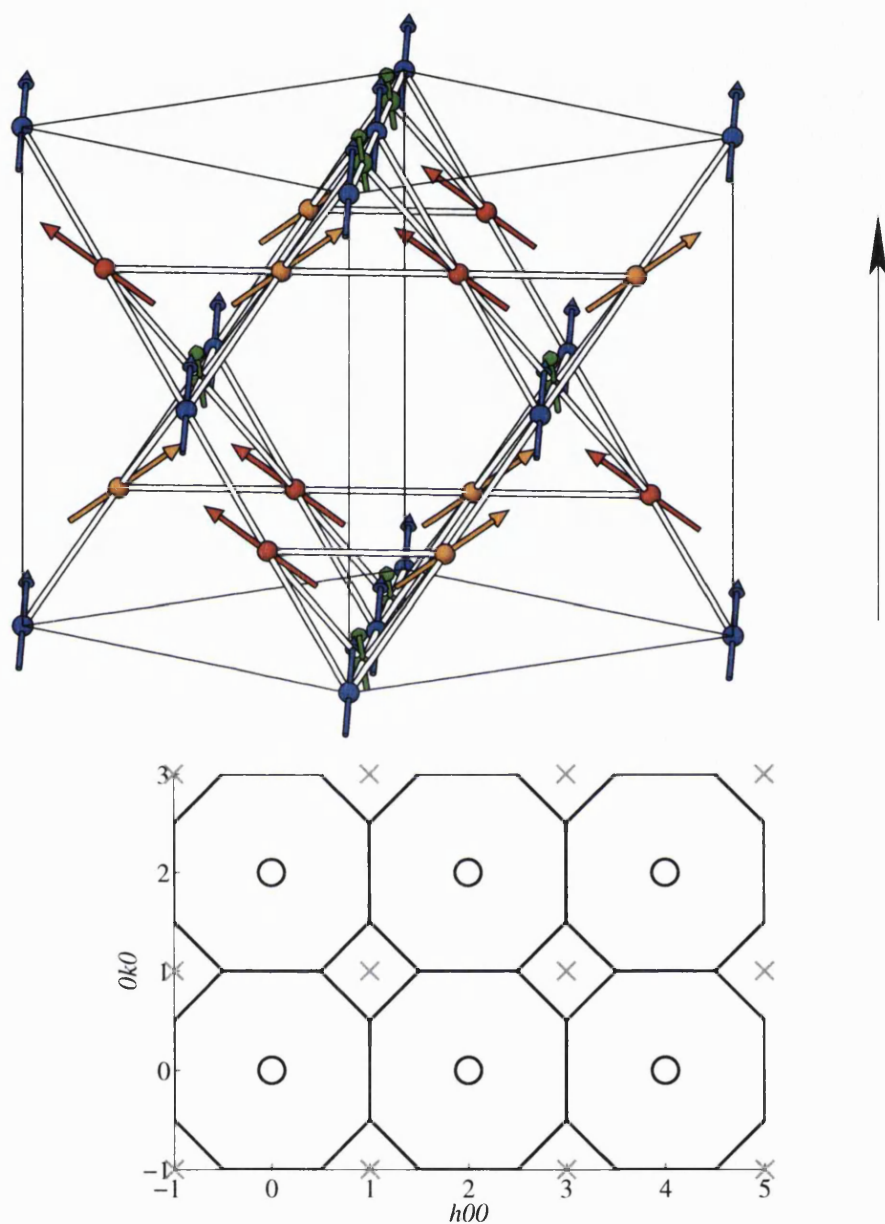


**Figure 4.3:** The  $Q = 0$  structure (top) and the  $hk0$  plane reciprocal space (bottom). In the  $Q = 0$  structure the four atom basis is preserved and all the spins on all “up” type tetrahedra are related by translations.  $Q = X$  positions are sampled in this plane, and are marked in grey, as no scattering is predicted at these positions for this structure.



gives the reflection condition as

$$hhl : h + l = 2n. \quad (4.12)$$

Again this means that the intensity occurs only at the zone centers and so this is also a  $Q = 0$  structure (see figure 4.4). There is only one structure of this type.

The second structure has alternating transverse chains. Their moments cancel so that the ferromagnetic moment of the structure is due only to the field pinned chains, and is parallel to the applied field. More than one structure of this type can be envisaged depending on how the alternating transverse chains are arranged. Within the ice rules these structures are degenerate because the ice rule only constrains near neighbors. Previously only one structure, which is named  $Q = X$ , has been discussed for this situation [25]. In this structure the chain alignment alternates in layers perpendicular to the field axis. This has magnetic and nuclear unit cells of the same size. Alternative alternation schemes require that the magnetic unit cell is doubled in size and there is no evidence to suggest that this occurs. The anti-parallel transverse chains mean the four groups of spins are no longer preserved (see figure 4.5). The perpendicular spins are split into two groups so that the structure factor is now of the form

$$\begin{aligned} \mathbf{F}_M = & \mathbf{S}_{\perp 1} \sum_{j=1}^4 e^{2\pi i(hx_j + ky_j + lz_j)} + \mathbf{S}_{\perp 2} \sum_{j=1}^4 e^{2\pi i(hx_j + ky_j + lz_j)} + \\ & + \mathbf{S}_{\perp 3} \sum_{j=1}^2 e^{2\pi i(hx_j + ky_j + lz_j)} + \mathbf{S}_{\perp 3'} \sum_{j=1}^2 e^{2\pi i(hx_j + ky_j + lz_j)} + \\ & + \mathbf{S}_{\perp 4} \sum_{j=1}^2 e^{2\pi i(hx_j + ky_j + lz_j)} + \mathbf{S}_{\perp 4'} \sum_{j=1}^2 e^{2\pi i(hx_j + ky_j + lz_j)}. \end{aligned} \quad (4.13)$$

For the  $hhl$  scattering plane the full structure factor can be written as

$$\begin{aligned} \mathbf{F}_M = & \mathbf{S}_{\perp 1}(1 + 2e^{\pi i(h+l)} + e^{2\pi i h}) + \\ & + \mathbf{S}_{\perp 2}(2e^{\pi i(2h+l)} + e^{3\pi i h} + e^{\pi i h}) + \\ & + \mathbf{S}_{\perp 3}(2e^{\frac{3}{2}\pi i(h+l)} + \mathbf{S}_{\perp 3'}(e^{\frac{1}{2}\pi i(h+l)} + e^{\frac{1}{2}\pi i(5h+l)}) + \\ & + \mathbf{S}_{\perp 4}(e^{\frac{1}{2}\pi i(5h+l)} + e^{\frac{1}{2}\pi i(h+l)}) + \mathbf{S}_{\perp 4'}(2e^{\frac{3}{2}\pi i(h+l)}). \end{aligned} \quad (4.14)$$

This structure factor has two properties that the others do not. The reflection conditions are now

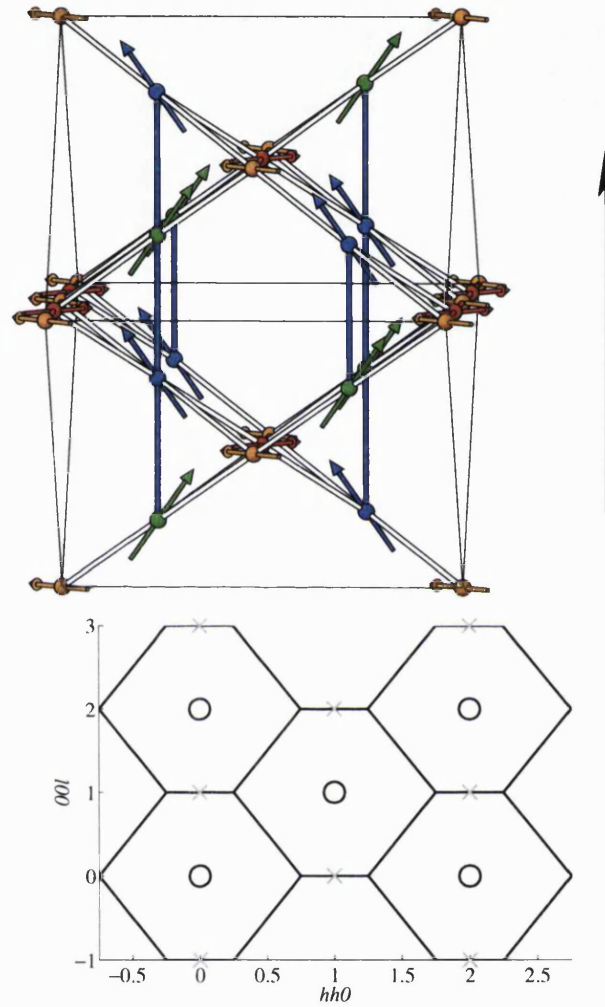


**Figure 4.4:** The  $Q = 0$   $45^\circ$  structure (top), and the reciprocal lattice in the  $hhl$  plane (bottom). In the illustration the field is applied on  $[h\bar{h}0]$  (which is vertical). The four atom basis and f.c.c. translations alone can describe this magnetic structure as the transverse chains are all aligned, so it is a  $Q = 0$  structure. The color code of the previous figures has been permuted as atoms 3 and 4 of the basis are pinned by the field and atoms 1 and 2 make up the free chains. The magnetic structure has a ferromagnetic moment at  $45^\circ$  to the magnetic field. No scattering is expected at the  $Q = X$  positions which are shown in grey.

$$\begin{aligned}
hhl : \quad h + l &= 2n, \\
\text{or} \quad h &= 2n, l = n \\
\text{or} \quad h &= n, l = 2n.
\end{aligned} \tag{4.15}$$

Reflections can occur at all the zone centers and also at positions on zone edges such as 001 or 110. These are the  $X$  points of the Brillouin zone, hence the structure has been called  $Q = X$ . The other property of the structure factor is that the magnetic scattering can be separated into two types. The spin chains pinned by the field (i.e. terms 1 and 2 in the structure factor) give rise only to the scattering at the  $Q = 0$  or zone center positions. The perpendicular spin chains (terms 3, 3', 4 and 4') cause the scattering at the  $Q = X$  positions.

### 4.3.1 The Niitaka Models

Niitaka *et al.* studied  $\text{Ca}_3\text{CoRhO}_6$ , a material in which the dominant interaction forms ferromagnetic Ising spin chains. The chains are arranged on a triangular lattice and the weaker inter-chain interaction is antiferromagnetic [98]. Monte Carlo simulations of such a system predict a partially disordered antiferromagnetic (PDA) state in which 2/3 of the chains are ordered antiferromagnetically and the rest remain incoherent [99]. At lower temperatures the model orders fully into a ferrimagnetic structure (FR).

As described previously, upon application of a field on  $[h\bar{h}0]$ , a spin ice is separated into a series of chains. In a first approximation these chains are also arranged on a triangular lattice (see figure 4.6) and will be coupled antiferromagnetically by dipolar interactions. In the case of the applied field creating the chains, two phases might be expected. At low fields where the exchange interaction competes with the field a frustrated triangular antiferromagnet (of chains) will be produced. At higher fields, when the exchange interaction is overwhelmed by the field, a ferromagnet will be produced, with all the chains aligned in the same sense.

It was expected that a situation similar to the models used by Niitaka would arise. This thinking was particularly encouraged by the presence of a step in the magnetization curve (see chapters on neutron scattering results). The suggestion being that in low fields a triangular antiferromagnet of chains would be formed.

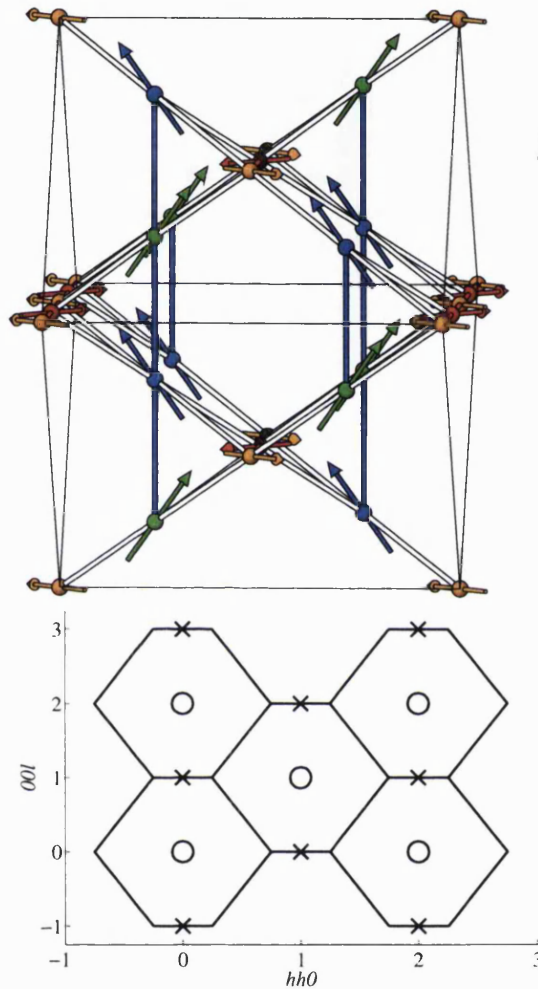


**Figure 4.5:** The  $Q = X$  structure again (top), and the reciprocal lattice in the  $hhl$  plane (bottom). Here the atoms are divided into the four atom basis, and again according to spin orientation. The color code has been permuted as atoms 3 and 4 of the basis have spins pinned by the field and atoms 1 and 2 make up the free chains. The field is vertical, and the free chains lie parallel to the scattering plane in the direction  $[hh0]$ . The four atom basis and f.c.c. translations alone cannot describe this magnetic structure. The hatched atoms are indistinguishable from the unhatched atoms of the same color in the nuclear or  $Q = 0$  structure factors. This lowering of symmetry in this structure allows the extra peaks at  $Q = X$  as well as at the  $Q = 0$  positions.

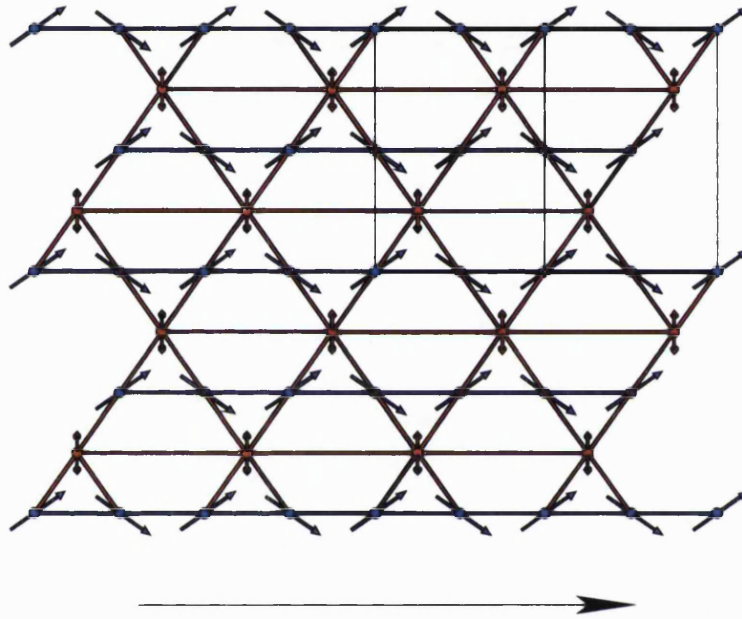


**Figure 4.6:** With the field applied on  $[h\bar{h}0]$  two types of spin chain are formed. Those spins with a component on the field are represented here as blue chains. The field is in the plane of the page, parallel to the blue bonds. The perpendicular chains can be seen to form a triangular lattice of chains. Both the perpendicular and parallel chains are forming similar triangular lattices. The triangular lattice is not quite perfect, though this is not clear in this picture.

In higher fields which could overwhelm the interchain coupling the ferromagnet would be formed.

The phases expected were first a spin ice state, then a PDA and/or FR state, and then a ferromagnet. The simplest system which could capture models of this type is a  $2 \times 2 \times 2$  supercell of the pyrochlore unit-cell. Careful counting of the atoms confirms that both parallel and perpendicular spins are equally represented. Different configurations were investigated.

The chief finding was that the  $Q = X$  peaks such as 110 can be produced by antiparallel spin chains either parallel or perpendicular to the field.

## 4.4 The Melko Model

The loop-move simulations of Melko *et al.* predict an ordered groundstate [64]. This was illustrated in figure 2.11, and is shown again in figure 4.7, for clarity. Compared to the  $Q = X$  structure (figure 4.5), the symmetry has been lowered even further as both sets of chains are now anti-parallel. This modifies the reflection condition again. In this structure the pairs of anti-parallel spins cancel and so all the  $Q = 0$  magnetic Bragg peaks become disallowed. Only the  $X$  positions are allowed to have a finite magnetic intensity. In the  $hhl$  scattering plane this corresponds to Bragg peaks at all the mixed index positions.

## 4.5 The Magnetic Structure Factor with Field Applied on $[hhh]$

The  $[hhh]$  direction is one of the three fold axes of the cubic unit cell, and of a tetrahedron. This direction is of particular interest for the study of the competition between field induced order and the preservation of degenerate ice rule states. With the field applied on this direction the lowest energy structure for high fields is no longer an ice rules state (see figure 4.8). At some point there must be a cross over from the entropically stabilized low field state to the energetically stabilized high field state.

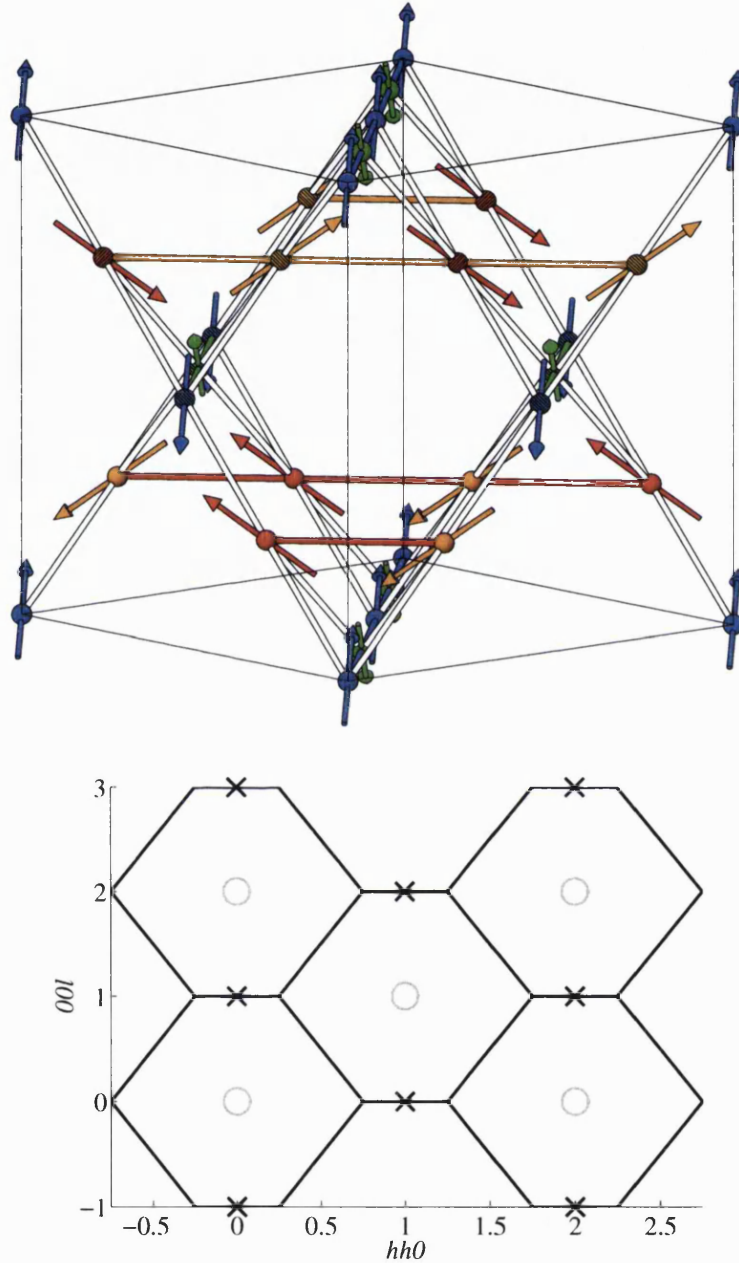


**Figure 4.7:** The loop-move groundstate structure again (top) and the reciprocal space in the  $hhl$  plane. Compared to the  $Q = X$  structure in figure 4.5, the symmetry has been lowered even further. Anti-parallel chains run in two directions so that all four sites of the four atom basis are divided into pairs. This means that magnetic Bragg scattering now occurs only at the  $Q = X$  positions, and the  $Q = 0$  positions are now shown in grey.

In low fields the balance between entropic and energetic stabilization can be struck by ordering only the spins which are actually on the axis on which the field is applied. This leaves three spins on every tetrahedron which can still form a disordered phase. This is a realization of the kagomé ice phase [81, 78, 79].

With the field applied on  $[hhh]$  the scattering plane has a threefold symmetry and it is no longer possible to define it conveniently with two independent vectors. Two vectors which lie in the plane are  $[\bar{h}0h]$  and  $[0h\bar{h}]$ , scattering vectors can be obtained using combinations of them. Some general conditions apply to the combination of the vectors. If they are treated as the addition of vectors consisting of zero and either  $n, 2n, 3n$ , or  $4n$  numbers it can be seen that the addition of  $n$  or  $3n$  numbers gives a scattering vector with mixed indices, as does the addition of  $n$  or  $3n$  to either  $2n$  or  $4n$ . The only way to obtain a scattering vector without mixed indices is to add  $2n$  and/or  $4n$  numbers. Previously mixed indices have lead to forbidden reflections for both magnetic and nuclear scattering, except in the  $Q = X$  structure where the symmetry was lowered by the anti-parallel chains. However,  $Q = X$  is the only situation in which the symmetry of the four atom basis is reduced.

The four atom basis retains its identity in both the high and the low field phases. In the low field phase only one of the spins in each four spin unit is expected to be ordered by the field. This simplifies the structure factor to a single term:

$$\mathbf{F}_M = \mathbf{S}_{\perp 1} \sum_{j=1}^4 e^{2\pi i(hx_j + ky_j + lz_j)}. \quad (4.16)$$

If the spin is represented as a vector of ones then the term  $\mathbf{S}_{\perp 1}$  can be reduced to

$$\mathbf{S}_{\perp 1} = \begin{pmatrix} 1 \\ 1 \\ 1 \end{pmatrix} - \frac{h+k+l}{\sqrt{h^2+k^2+l^2}} \hat{\mathbf{Q}}. \quad (4.17)$$

Given that the field is parallel to  $[hhh]$ , the ordered spin is exactly and entirely in this direction, and that the scattering plane contains vectors perpendicular to this, it is clear that the spin is entirely perpendicular to the scattering vector. Equally it can be seen that combining the two plane defining vectors as described above will always lead to the condition  $h+k+l=0$  and so  $\mathbf{S}_{\perp 1} = \mathbf{S}$ . The presence or absence



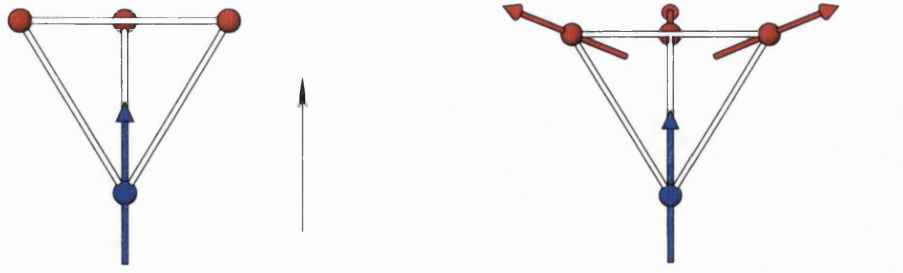


**Figure 4.8:** Two possible spin structures are expected when the field is applied on  $[hhh]$ . The first is in low fields, when only the spins exactly parallel to the field is ordered (left), the remainder can form a kagomé ice phase. The second is a non-ice rules phase expected when the field overwhelms the spin-spin interactions (right). Both have  $Q = 0$  reflection conditions as the spin structure is the same on each tetrahedron.

of a reflection is determined by the phase factor and the reflection condition is

$$hkl : h + k = 2n, h + l = 2n, k + l = 2n. \quad (4.18)$$

Since the full structure factor can be written as

$$\mathbf{F}_M = \mathbf{S}_{\perp 1} \left( 1 + e^{\pi i(h+k)} + e^{\pi i(h+l)} + e^{2\pi i(k+l)} \right), \quad (4.19)$$

out of plane reflections such as  $0, 0, 2$  or  $1, 1, \bar{1}$  are observable with the condition

$$hkl : h + k = 2n, h + l = 2n, k + l = 2n. \quad (4.20)$$

The reflection conditions for the high field structure for this scattering plane are identical, though the actual values of the structure factor will differ.

## 4.6 The Magnetic Structure Factor with Field Applied on $[hh2h]$

This direction was studied using a horizontal field magnet. This means that for magnetic scattering some equivalent peaks may become inequivalent. For example, in a cubic ferromagnet a vertical field aligning the spins on  $[00l]$  will leave reflections  $h00$  and  $0k0$  identical as the spin component perpendicular to both

scattering vectors is the same. However, if the field is applied on a vector in the scattering plane, say  $[h00]$  these two reflections become inequivalent. Because the spins have been aligned on  $[h00]$  the  $h00$  magnetic peaks disappear as there is no perpendicular spin component, but  $0k0$  remain. Of course in the vertical field  $00l$  would be absent if the detector could be brought to that position. The novelty is in the fact that peaks in the scattering plane can be made inequivalent by the field.

The real space direction corresponding to  $[hh2h]$  is a bisector of one face of a tetrahedron. This means that three spins on the corners of this face have a component on the field direction (see figure 4.9). The remaining spin is perpendicular to the field. This situation is somewhere in between the two previous directions in terms of constraint. There is clearly a high field groundstate in which three spins are ordered by the field and the fourth is ordered by the ice rules. Two of the three will point out and one points in, the ice rules will force the fourth spin to point into the tetrahedron.

Because of the extremely low symmetry of the scattering geometry in the horizontal field magnet the only reflection conditions to be investigated are for the  $hhl$  type peaks actually accessible. These are  $11\bar{1}$ ,  $22\bar{2}$ ,  $111$ , and  $224$ . If the four atom basis is regarded as a single tetrahedron at the origin of the unit cell, then the coordinates of these atoms are  $1 = (0, 0, 0)$ ,  $2 = (1/4, 1/4, 0)$ ,  $3 = (1/4, 0, 1/4)$  and  $4 = (0, 1/4, 1/4)$ . The scattering plane is  $hhl$  and so the field axis  $[hh2h]$  bisects the triangular face containing atoms 1,3 and 4 of the basis. The free spin is 2 and for each peak the structure factor will either have no contribution from this spin (disordered models) or from all four (ordered models).

Three different behaviors are observed for the peaks.  $11\bar{1}$  and  $22\bar{2}$  are parallel to the axis of spin 2, and so since there is no perpendicular component they are only sensitive to the magnetization of the three field-pinned spins and will show no change if/when the fourth spin orders.  $111$  is sensitive to both types of spin and an increase in structure factor is expected in the fully ordered structure compared to the partially ordered structure.  $224$  is also sensitive to both types of spin, but with equal ordered moments on all sublattices, it should disappear. In the partially ordered structure, the structure factor is finite and will depend on the

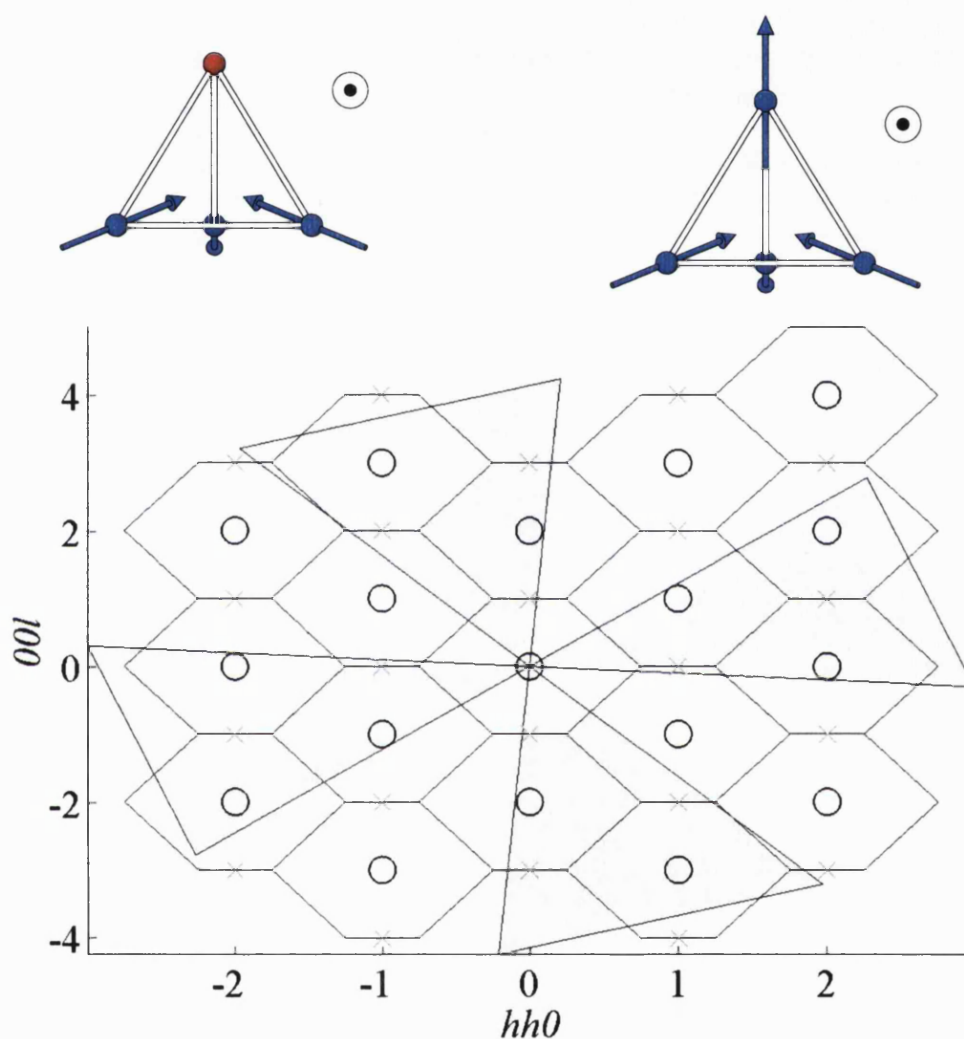


**Figure 4.9:** Two possible spin structures expected when the field is applied on  $[hh2h]$ . The first is in low fields, when only the three spins with a component on the field are ordered (top left). The second is a  $Q=0$  ice rules phase expected when the interactions are strong enough to draw the fourth spin in the ordered structure.  $Q = X$  peaks are not expected so are shown in grey. The shading represents the dark angles of the horizontal field cryomagnet required to access this field direction.

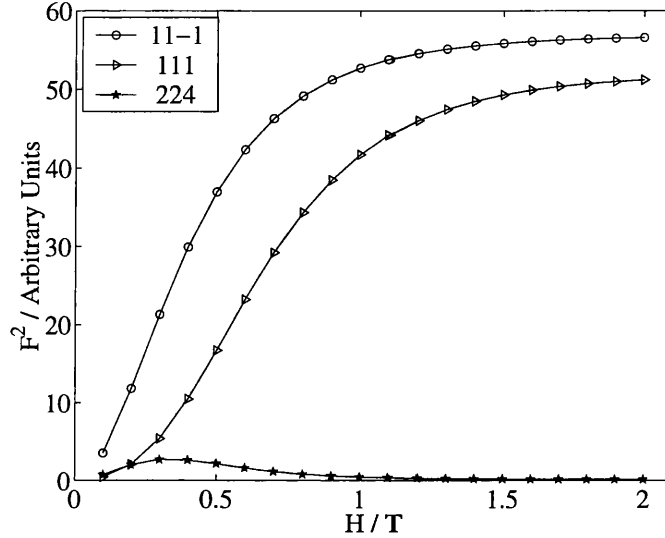


**Figure 4.10:** Calculated peak behavior for a nearest neighbor spin ice model with field applied on  $[hh2h]$ . The intensity changes are calculated by enumerating all  $2^{16}$  states of the pyrochlore unit cell and taking a Boltzmann factor weighted average of the structure factor of each. The model parameters are chosen to place the system in the ice rules regime.

size of the three field-pinned moments. As the fourth moment orders this peak should decrease in intensity, eventually returning to exactly zero magnetic intensity when all four ordered moments are the same size. An illustration of the behavior of the three peak types is shown in figure 4.10.

## 4.7 Summary

The object of this chapter was to present some of the general features of the magnetic structure factors of the spin structures that might be expected in the experiments reported in the following chapters. The general conclusions to be drawn from this exercise are that when the ordering is simple, i.e the symmetry of the four atom basis is preserved, then intensity will appear at the nuclear positions. This is the case for the  $Q = 0$  structure obtained when the field is applied on  $[00l]$ , and for the partial and fully ordered structures when the field is applied on  $[hhh]$

and  $[hh2h]$ . In the case of transitions from partial to full order it is possible for the structure factors of some peaks to decrease, whilst others increase.

When the symmetry of the four atom basis is reduced, extra peaks may appear. This symmetry breaking can be due to antiferromagnetic ordering, in which case extra peaks occur at  $X$  positions.

Structure	Field Direction	1	1'	2	2'	3	3'	4	4'	Peaks
$Q = 0$	$[00l]$	111		$\bar{1}\bar{1}1$		$1\bar{1}1$		$\bar{1}\bar{1}1$		$Q = 0$ only
$Q = 0(45^\circ)$	$[110]$	111		$11\bar{1}$		$1\bar{1}1$		$1\bar{1}\bar{1}$		$Q = 0$ only
$Q = X$	$[110]$	111	$\bar{1}\bar{1}\bar{1}$	$11\bar{1}$	$\bar{1}\bar{1}1$	$1\bar{1}1$		$1\bar{1}\bar{1}$		$Q = 0$ and $Q = X$
Melko		111	$\bar{1}\bar{1}\bar{1}$	$11\bar{1}$	$\bar{1}\bar{1}1$	$1\bar{1}1$	$\bar{1}\bar{1}\bar{1}$	$1\bar{1}\bar{1}$	$\bar{1}11$	$Q = X$ only
partial order	$[hhh]$	111								$Q = 0$ only
full order	$[hhh]$	111		$11\bar{1}$		$1\bar{1}1$		$\bar{1}\bar{1}1$		$Q = 0$ only
partial order	$[hh2h]$	111				$1\bar{1}1$		$\bar{1}\bar{1}1$		$Q = 0$ only
full order	$[hh2h]$	111		$\bar{1}\bar{1}1$		$1\bar{1}1$		$\bar{1}\bar{1}1$		$Q = 0$ only

Table 4.1: Spin directions in different spin structure models for the tetrahedron at the unit cell origin. If atoms  $j'$  exist they are located on other tetrahedra in the unit cell related to the first by an f.c.c. translation. However, the spin reversal means that atoms  $j$  and  $j'$  can no longer be related directly by such a translation. If neither  $j$  or  $j'$  is present the model is partially disordered and no ordered component is attributed to this spin.

## Chapter 5

# The Field Induced Phases of Holmium Titanate

In this chapter the details of four neutron scattering experiments on  $\text{Ho}_2\text{Ti}_2\text{O}_7$  are presented (one on POLARIS at ISIS, three on D10 at the ILL), followed by the results and analysis of the data. The data presented in this chapter were not collected in the sequence in which they are presented. For example, the need for a detailed extinction correction only became apparent after the second experiment (examining field and temperature dependence with field applied on  $[\bar{h}\bar{h}0]$  and  $[00l]$ ). Consequently this measurement was made in the third experiment.

### 5.1 Experimental details

#### 5.1.1 POLARIS

POLARIS is a medium resolution, time of flight powder diffractometer at ISIS. Data is collected by three detector banks at low angle ( $30^\circ$ ),  $90^\circ$  and backscattering ( $145^\circ$ ) positions. The low angle bank allows the data to be collected for very large d-spacings and the backscattering bank provides high resolution at smaller d-spacings. The data were normalized to vanadium to correct for detector efficiency, and then time-focussed. The diffraction pattern of  $\text{Ho}_2\text{Ti}_2\text{O}_7$  was collected at 1.8 K.

### 5.1.2 D10

D10 is a highly adaptable single crystal diffractometer at the ILL. Three experiments were carried out on D10 using three different crystals and a variety of sample environments.

D10 can be used with full four circle diffractometer capability or the Eulerian cradle can be replaced by a tilt stage with much more restricted tilts. The tilt stage can be used to mount large cryostats. Three cryomagnets were used successfully. The first was a small vertical field superconducting magnet with a maximum field of 2.5 T and dilution refrigerator insert. The second was a larger Oxford Instruments vertical field superconducting magnet with a maximum field of 6 T and a dilution refrigerator insert. The third was a small horizontal field magnet with a maximum field of 2 T. Dilution refrigerator capability was sacrificed in favor of a rotating sample stick. This cryomagnet has particularly restrictive dark angles. There are four windows at  $90^\circ$ , each having an opening angle of  $45^\circ$ .

The crystals were all grown by evaporation of a lead fluoride flux [100]. To simplify demagnetization corrections spherical crystals were used wherever possible.  $\text{Ho}_2\text{Ti}_2\text{O}_7$  is a hard material and so to make a spherical crystal (“sphericalization”) requires time and a harsh abrasive. The crystal to be sphericalized was placed in a boron carbide lined chamber, high pressure compressed air was forced in at one end and out through a finely perforated seal at the other end. The crystals were small enough to be carried on the turbulent airflow and after a period of days emerged approximately spherical.

Three crystals were used in these experiments, two sphericalized and one not. The characteristics of these crystals were as follows:

- A small regular octahedral crystal which was sphericalized, the remnants of distinct faces can still be seen. It is  $\approx 2 \times 2 \times 2$  mm;
- A larger regular octahedral crystal, also sphericalized but with clear faces remaining. It is  $\approx 3 \times 3 \times 3$  mm;
- A larger irregular crystal, the regular octahedral shape has been compressed to give two large triangular faces. It is  $\approx 3 \times 3 \times 2$  mm;



They will be referred to as “the small crystal”, “the large crystal”, and “the flat crystal” respectively. All the crystals are a dark amber color and prior to sphericalization they had shiny flat faces. The faces are known to be  $\langle 111 \rangle$  planes and this greatly assists the alignment process. When a specific alignment was required a neutron Laue camera was used to locate the axis. The crystals were attached to a copper pin with stycast.

The following measurements were made<sup>a</sup>:

- Using the large crystal and the full four circle capability a large number of Bragg peaks were measured at wavelengths of 2.36 and 1.26 Å at room temperature. This was for the extinction correction (third experiment).
- Using the small crystal with the field applied on  $[h\bar{h}0]$ , field, temperature and history dependence were investigated. The small cryomagnet was used so the parameter space available was  $T \approx 0.05 - 1.2$  K and  $-2.5 - 2.5$  T (second experiment).
- Using the large crystal with the field applied on  $[00l]$ , field, temperature and history dependence were investigated. In particular field dependent magnetization was studied in a search for the postulated liquid-gas critical point [55]. Again the parameter space available was  $T \approx 0.05 - 1.2$  K and  $-2.5 - 2.5$  T (second experiment).
- Using the flat crystal with  $[hhh]$  vertical a more limited study of field and temperature dependent magnetization was made. In anticipation of the higher field required to access the non-ice rules high field phase, the large cryomagnet was used (third experiment).
- Using the small crystal with the  $[h\bar{h}0]$  vertical and the horizontal field magnet a brief investigation of the field and temperature dependence of magnetic structures induced by a field applied on  $[hh2h]$  was made (fourth experiment).

---

<sup>a</sup>The experiments were carried out beginning on 12<sup>th</sup> April 2001 (by S. T. Bramwell, J. S. Gardner, T. Fennell and B. Ouladdiaf), 21<sup>st</sup> May 2002 (by T. Fennell and B. Ouladdiaf) and 14<sup>th</sup> November 2002 (by T. Fennell, B. Ouladdiaf, S. T. Bramwell and M. Shirai)

## 5.2 Crystal Structure and Extinction Correction

The crystal structure of  $\text{Ho}_2\text{Ti}_2\text{O}_7$  is important as a set of parameters describing the nuclear contribution to diffracted intensity. Because of the complicated sample environments and high symmetry of the crystals, the number of inequivalent peaks that can be measured is always rather small. The need to survey a phase diagram also restricts the number of peaks that can be measured at any point in the phase space. Consequently the crystal structure must be reduced to a model which can be fitted to the restricted set of peaks measured in these experiments, before the field is applied (because no magnetic order is observed in zero field, all transitions to ordered spin structures described below occur as a function of field, rather than temperature). Ideally a single scale parameter should be sufficient to achieve this fit.

The need for an extinction correction became clear during initial attempts to refine the crystal structure published by Knop [51] against the zero-field data from the first D10 experiment. Extinction is treated differently in different structure refinement packages. The two packages which are most useful for single crystal studies of magnetic structures are FullProf [101] and the Cambridge Crystallographic Subroutine Library (CCSL) [102]. In Fullprof, the extinction correction is an empirical correction with a refinable parameter, originally used in SHELX for large XRD diffraction data sets [101, 103]. This was found to be insufficient in early attempts to use FullProf in this problem. The extinction correction in the CCSL is an implementation of the Becker and Coppens treatment of extinction described in section 3.4 [93]. The correction includes the crystal shape and diffraction geometry and proved much more successful after some initial difficulties. However, it does constrain the user to the subsequent use of the CCSL for all structure refinement as the corrected output cannot be input into any other package.

Another problem in crystal structure refinement is to be realistic about where the data can actually give meaningful information. The data measured for the extinction correction does contain a very much larger number of Bragg peaks than a typical measurement made in a cryomagnet. However, because of time pressures it was not possible to cover an especially wide range in reciprocal space at both

wavelengths. Data at both 1.26 and 2.36 Å are concentrated at rather low- $|Q|$ . This means that the data are inappropriate for accurate determination of thermal displacement parameters. This was clear in initial attempts to refine the thermal parameters, these were wildly unstable and inevitably lead to unrealistic answers.

As the aim was to produce a realistic set of crystal structure parameters the way to solve this problem seemed to be to introduce thermal parameters which had been accurately determined. Powder diffraction is a much more efficient way to access structural details at high  $|Q|$ .  $\text{Ho}_2\text{Ti}_2\text{O}_7$  had previously been investigated on the POLARIS powder diffractometer at ISIS by Harris and Bramwell [70]. This data had remained untreated for several years.

The crystal structure according to Knop [51] has few refinable parameters, as it must with such high symmetry. Using the Fullprof package it was simple to obtain a satisfactory fit to the data from the back-scattering/high resolution detector bank by Rietveld refinement [101]. The fit is illustrated in figure 5.1 and the derived parameters of the crystal structure in table 5.1. Other parameters required for the fit are the lineshape, an absorption correction, diffractometer parameters and a fitted background.

The lineshape used was a pseudo-Voigt function for typical sample broadening effects, convoluted with back to back exponential decays representing the pulse shape of the moderator. The parameters for this function were obtained from the instrument parameter file for the cycle in question and come originally from the measurement of a standard sample. Only the sample dependent pseudo-Voigt parameters were adjusted in the refinement. The zero offset of the sample was allowed to vary as in principle the measured sample may have been slightly offset from the standard. The absorption correction is often important on POLARIS and chiefly corrects intensity mismatch at low- $|Q|$  where absorption is indeed expected to be more significant in time-of flight neutron scattering. Only small changes from original values were noted for these parameters. The background was modelled by a four term polynomial.

The crystal structure obtained was used in the refinement of the extinction parameters. The CCTL program ARRNGE was used to group the reflections for processing. AVEAR was used to calculate coefficients for the Becker and Cop-

Phase	Refinement Parameters	Atom Positions	Displacement Parameters $8\pi^2\langle u^2 \rangle / \text{\AA}^2$
$\text{Ho}_2\text{Ti}_2\text{O}_7$	$a = 10.0947(1) \text{ \AA}$ $\chi^2 = 11.530$ $R_p = 0.091$ $R_{wp} = 0.0746$ $R_{Bragg} = 0.026$ $R_F = 0.022$	Ho	0.0000000
			0.27(1)
			0.0000000
			0.0000000
		Ti	0.5000000
			0.26(2)
			0.5000000
			0.5000000
		O1	0.1250000
			0.21(1)
			0.1250000
			0.1250000
		O2	0.42104(5)
			0.36(1)
			0.1250000
			0.1250000

**Table 5.1:** Crystal structure parameters for  $\text{Ho}_2\text{Ti}_2\text{O}_7$  from Rietveld refinements of POLARIS data.

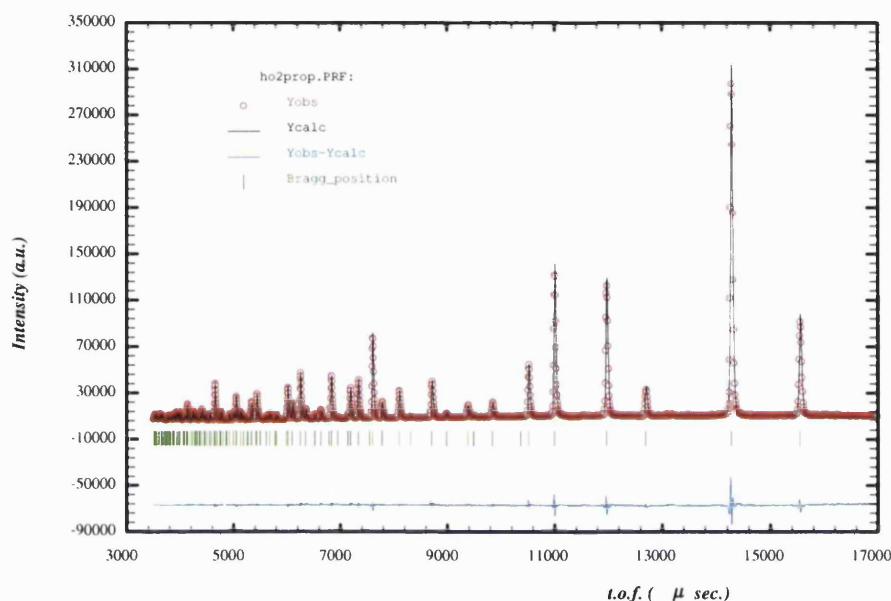


**Figure 5.1:** Rietveld refinement of powder diffraction data for  $\text{Ho}_2\text{Ti}_2\text{O}_7$  collected on the backscattering detector bank of POLARIS .

pens extinction corrections. The extinction correction can operate with either a Gaussian or Lorentzian distribution of mosaic spread. The Lorentzian distribution was generally found to be more realistic by Becker and Coppens. Both were tested and it was found that the Gaussian model lead to completely unstable refinements. Using the Lorentzian distribution the refinement converged rapidly.

The two parameters associated with the extinction (domain radius and mosaic spread) were strongly correlated in the refinement (-70%). Also they can be strongly influenced by their starting values and those of the scale parameters (one for each wavelength). Arbitrary starting values lead to divergence or non-physical values. However, alternating refinement of the scale and domain radius parameters caused the solution to evolve towards the previously obtained answer, and a situation was reached in which the four parameters would refine stably to the original answer. Consequently this model was accepted as one which would adequately represent the nuclear intensities in subsequent data analysis. An overall temperature factor was introduced to take account of the difference in temperature between the two measurements (the powder data was recorded at 1.8 K, the single

crystal data at room temperature). The effect of this was to cause very strong correlations with the extinction parameters. This inevitably drove the extinction parameters to nonsensical values. Consequently this parameter was abandoned in the refinement of the extinction correction. For subsequent scaling of the applied field data sets the temperature factor could be used as the extinction parameters were fixed. Presumably any differences between the thermal parameters at 1.8 K, measured on POLARIS, and those at room temperature, appropriate for this data set, are absorbed by the extinction parameters. The final parameters are listed in table 5.2.

The extinction parameters obtained are assumed to apply to all three crystals as they are all grown by the same method and are of closely comparable quality. This assumption was confirmed by comparing the width of a 220 type peak measured in all the different experimental configurations (see figure 5.2).

To summarize briefly, a model crystal structure to represent the nuclear intensities has been obtained. Severe extinction effects have been corrected for using the CCSL implementation of the Becker and Coppens extinction correction. In doing this, and applying the model subsequently, a series of approximations have been made. These are

- Thermal parameters were obtained from powder data, it is assumed that the ratio of thermal displacements does not change for refinements at different temperatures. Data from different temperatures is then related by an overall temperature factor.
- The different measurement temperatures of the powder and single crystal data were absorbed by the extinction correction, as no account can be taken of them during the refinement of the extinction parameters. It is further assumed that this does not compromise the extinction parameters for other refinements.
- The previous assumption implies that extinction is temperature independent. This appears the worst approximation, since it is common crystallographic practice to reduce the temperature as far as possible to alleviate extinction.
- The extinction parameters can be applied to all three crystals.

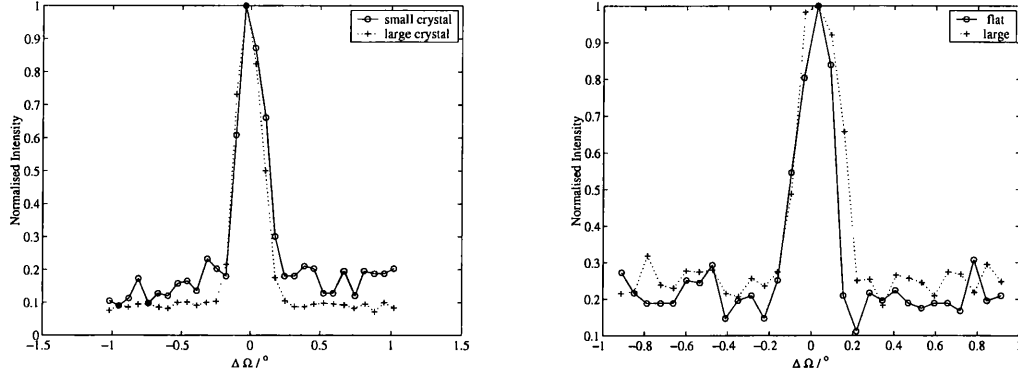


**Figure 5.2:** Comparison of the 220 peaks in the large and small crystals at 2.36 Å and the large and flat crystals at 1.26 Å.

- The extinction parameters can be applied to the magnetic intensity.

These assumptions must be born in mind whenever conclusions are drawn about the physics underlying the data. However, the thread of reasoning behind each successive approximation is the only way available to proceed through the data analysis at present. Extinction is a very complicated problem. Examples exist where comparable quantities of experimental time have been dedicated to determining a single magnetic structure, in the presence of severe extinction [104], and that is not the type of study which is being described here. We note the philosophy of Watkin [105] as to completeness of a refinement and use these models on the basis that they accurately represent the nuclear intensity within the framework of the CCSL structure factor calculation.

### 5.3 Field Applied on $[00l]$

In this orientation complete degeneracy removal by the field, and the formation of the  $Q = 0$  structure was expected. A novel critical point was predicted in the  $H - T$  phase diagram [55]. Other workers have hypothesized that a suitable field and temperature cycle would encourage the magnet into its true groundstate [106], currently assumed to be that predicted by Melko *et al.* [64], and so  $Q = X$  Bragg peaks would appear.

The sample was cooled to base temperature ( $T \approx 0.05$  K) in zero field, and

Phase	Refinement Parameters	Atom Positions	Displacement Parameters $8\pi^2\langle u^2 \rangle / \text{\AA}^2$	
Ho <sub>2</sub> Ti <sub>2</sub> O <sub>7</sub>	$a = 10.0947(1) \text{ \AA}$	Ho	0.0000000	0.27
	$\chi^2 = 11.530$		0.0000000	
	$R_1 = 4.43$		0.0000000	
	$R_2 = 8.53$	Ti	0.5000000	0.26
	$R_3 = 4.0$		0.5000000	
	$R_4 = 7.58$		0.5000000	
	$\chi^2 = 45.6$	O1	0.1250000	0.21
	Domain radius =		0.1250000	
	$34.0(11.0)(\times 10^{-7} \text{ cm})$		0.1250000	
	Mosaic spread =	O2	0.42100(2)	0.36
	$2.15(1) (10 \text{ radians}^{-1})$		0.1250000	
	Scale(1) = 15.2(1)		0.1250000	
Scale(2) = 41.6(4.8)				

**Table 5.2:** Crystal structure and extinction parameters for Ho<sub>2</sub>Ti<sub>2</sub>O<sub>7</sub> from the refinement of dual wavelength data collected on D10. The thermal factors were fixed and are the same as those determined on POLARIS. The refinable parameters of the extinction correction are the domain radius and the mosaic spread. The O2  $x$  position was allowed to refine but it has remained identical to that previously determined on POLARIS. A scale parameter is required for each wavelength (scale(1) is for  $\lambda = 1.26 \text{ \AA}$  and scale(2) is for  $\lambda = 2.36 \text{ \AA}$ ).



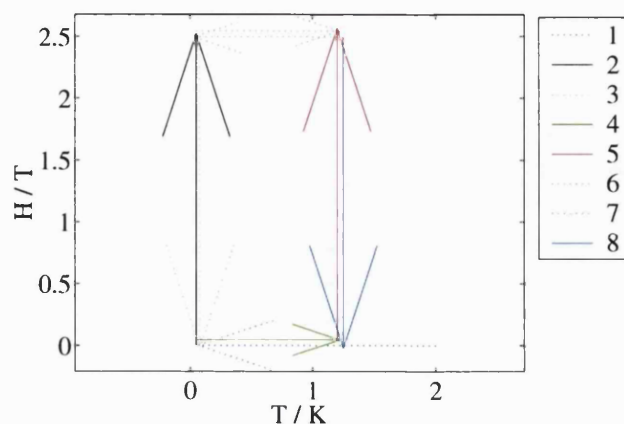


**Figure 5.3:** Path through  $H/T$ -space with the field applied on  $[00l]$  during early part of experiment prior to field cycles at intermediate temperatures.

then the field was scanned to 2.5 T and back to zero. The temperature was then raised (in zero field) to 1.2 K where the field was scanned to 2.5 T. In 2.5 T the temperature was reduced to base temperature and then warmed again to 1.2 K before the field was scanned back to zero again (the path through  $T/H$ -space for this part of the experiment is illustrated in figure 5.3). This field and temperature cycling was designed to produce a  $Q = X$  phase, but none was observed.

Subsequently field scans were measured at intermediate temperatures from zero to 2.5 T and back. The temperatures were 0.15, 0.3, 0.5, 0.7 and 1.2 K. Between each field scan the temperature was raised to 1.2 K to destroy any remnant magnetization. These field scans were used to search for the postulated liquid gas critical point. This was not irrefutably observed. Also, an increasingly strong hysteresis appears in the loops as the temperature is lowered.

The data was treated by refining model magnetic structures using the CCSL program MAGLSQ. The crystal structure and extinction parameters were taken from the fit to the room temperature data described above. In this case the measurements were made on the same crystal and so the smallest number of approximations are being employed. A set of peaks collected in zero field was used to establish a new scale factor and an overall temperature factor was included since the data for scaling was collected at a much lower temperature than that used for refinement of thermal or extinction parameters. The scale and temperature fac-

tors were strongly correlated but the refinement converged rapidly at reasonable values of both. If the temperature factor is not included then fits of the magnetic structures have a strongly reduced magnetic moment, and there is a  $|Q|$  dependent misfit.

The obvious model for the magnetic structure in this configuration is the  $Q = 0$  structure. The ferromagnetic moment of the structure can align with the field. This structure gives rise to Bragg peaks at nuclear positions and also some forbidden positions such as 200. The loops at variable, intermediate temperatures can all be shown to be consistent with the development and saturation of this magnetization (figure 5.4). In all cases  $R_3 < 10\%$  ( $R_3$  is the weighted  $R$ -factor  $\sum_i W_i(I_i^{\text{obs}} - I_i^{\text{calc}})/\sum_i W_i(I_i^{\text{obs}})$ , where  $W_i = 1/\sigma_i^2$  is the weight of observation  $i$ ), and this indicates an acceptable model in conventional crystallographic terms.

Scans at six temperatures are shown in figure 5.4. At temperatures of 0.7 and 1.2 K no hysteresis was detected so simple magnetization curves were obtained. Where data points were measured at the same value of rising and falling field, the measurements were combined to improve statistics. This was not possible for the loops recorded at 0.5 K and below. The number of peaks monitored in these measurements is necessarily small. In the loops above base temperature four or five peaks were monitored, magnetic intensity developed on two, the 200 and 420. The others, which are associated with  $Q = X$  type ordering, remained absent. Although the fit of the  $Q = 0$  structure to these peaks is good, a systematic difference between the calculated and observed intensities is observed for all the temperatures. For all these loops the results of the fitting is very good at low field, with observed and calculated intensities essentially matching exactly. As the field increases the model becomes less satisfactory. An example of this is shown in figure 5.5 where the calculated and observed intensities of 200 and 420 are plotted for the loop at 0.7 K. This mismatch is attributed to a field dependent extinction effect discussed below.

For the loop at base temperature more information is available, as in addition to having recorded 200 and 420 and an equivalent of each, 400 and 220 were also recorded, as well as a collection of  $Q = X$  peaks which remained absent. The fits shown in figure 5.4 did not include 400 as it behaves very differently to the

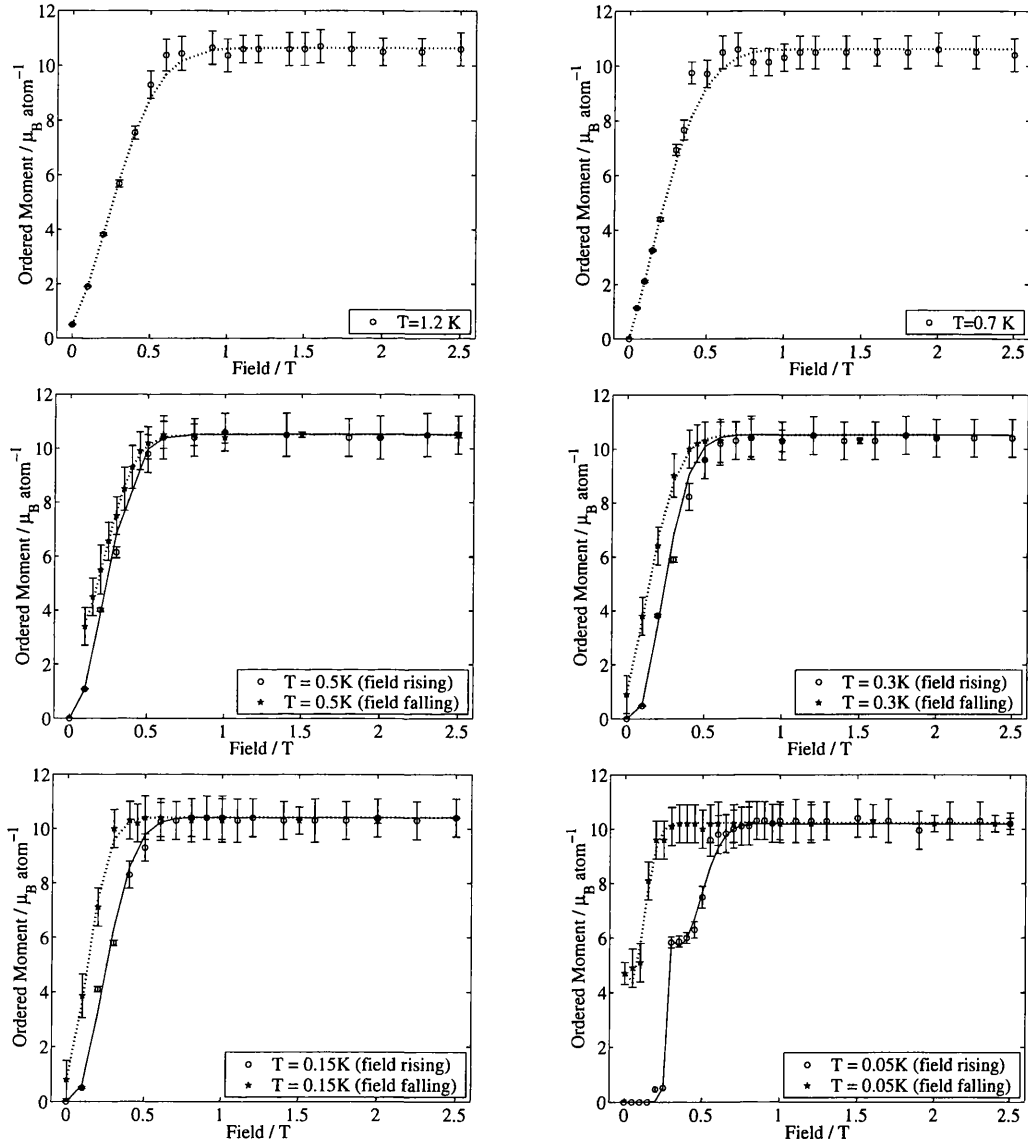


**Figure 5.4:** Development of  $Q = 0$  magnetization at different temperatures, with field applied on  $[00l]$ . Lines are to guide the eye only.

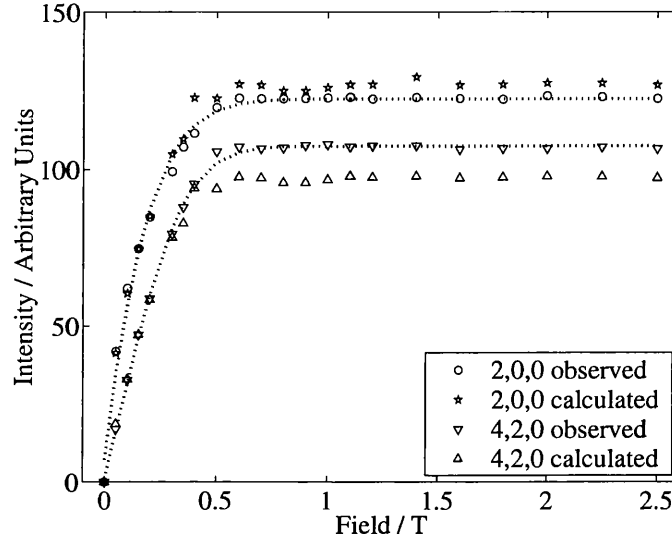


**Figure 5.5:** Field dependence of the mismatch between calculated and observed intensities for  $T=0.7$  K.

other peaks. This behavior prevents the fitting of a  $Q = 0$  model to the intensities measured in this loop if this peak is included.

The behavior of the 400 peak is rather bizarre, it is shown in figure 5.6. Whilst all the other peaks are indicative of field induced ordering and increase in intensity, 400 decreases. The decrease tracks the stepwise increase of peaks such as 200. The fact that the intensity of this peak falls below its zerofield nuclear level is suggestive that this stepwise decrease is completely spurious. A possible explanation is double scattering or simultaneous diffraction. The coincidence of a second reflection on the Ewald sphere can lead to spurious reduction or increase in intensity.

The classic investigations of double scattering involve holding the crystal in the diffracting condition and rotating it around the scattering vector. As the reciprocal lattice is swept through the Ewald sphere peaks can appear and disappear, even when the crystal has been held at a forbidden position. This is known as the Renninger effect [107, 108]. It is envisaged that the coincidence of a strongly field dependent peak on the Ewald sphere could lead to a field dependent Renninger effect.

The simplest way to discover if any other reflection could have been on the

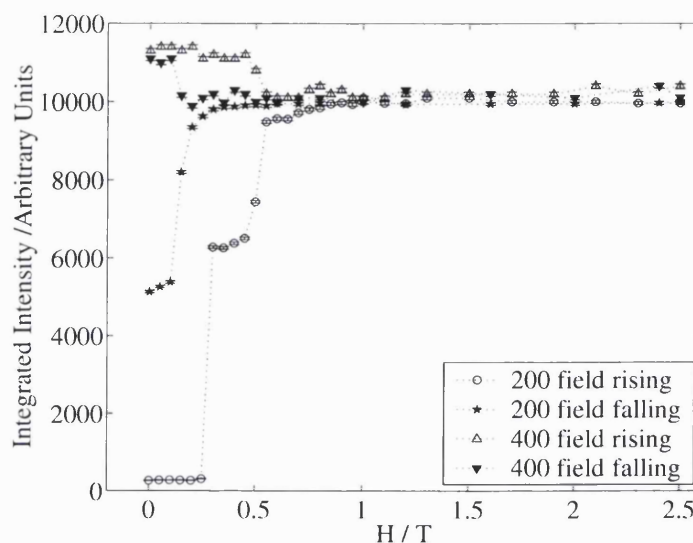


**Figure 5.6:** Field dependence of the 400 and 200 peaks at 0.05 K. Note that the 400 actually falls below its zero field, i.e. pure nuclear, intensity congruently with the growth of magnetic intensity, here exemplified by 200.

Ewald sphere is to construct the reciprocal lattice and the sphere and see what was where. Because the crystal orientation was specified with scattering vectors in the  $hk0$  plane the construction is greatly simplified. Two possible constructions can be made, corresponding to  $\psi = 0 \pm 180^\circ$  ( $\psi$  is the rotation about the scattering vector and is the only movement in a Renninger experiment, but is not an independent movement on a four-circle diffractometer). The construction can be examined by looking at successive layers of the reciprocal lattice. Planes above and below  $hk0$  are symmetrical because the sphere is centered in  $hk0$ . Successive layers with the ever shrinking Ewald sphere are shown in figure 5.7.

There are several peaks very close to the Ewald sphere. Multiple scattering involves three reflections, the primary, operative (the second reflection on the Ewald sphere), and cooperative reflections. The primary and operative reflections must have  $\mathbf{Q} = \mathbf{G}$ , and so the difference between the two is also a reciprocal lattice vector. The indices of the cooperative reflection can be obtained by subtracting the indices of the operative reflection from the primary. For a field dependent multiple scattering we must require three reflections with finite magnetic struc-

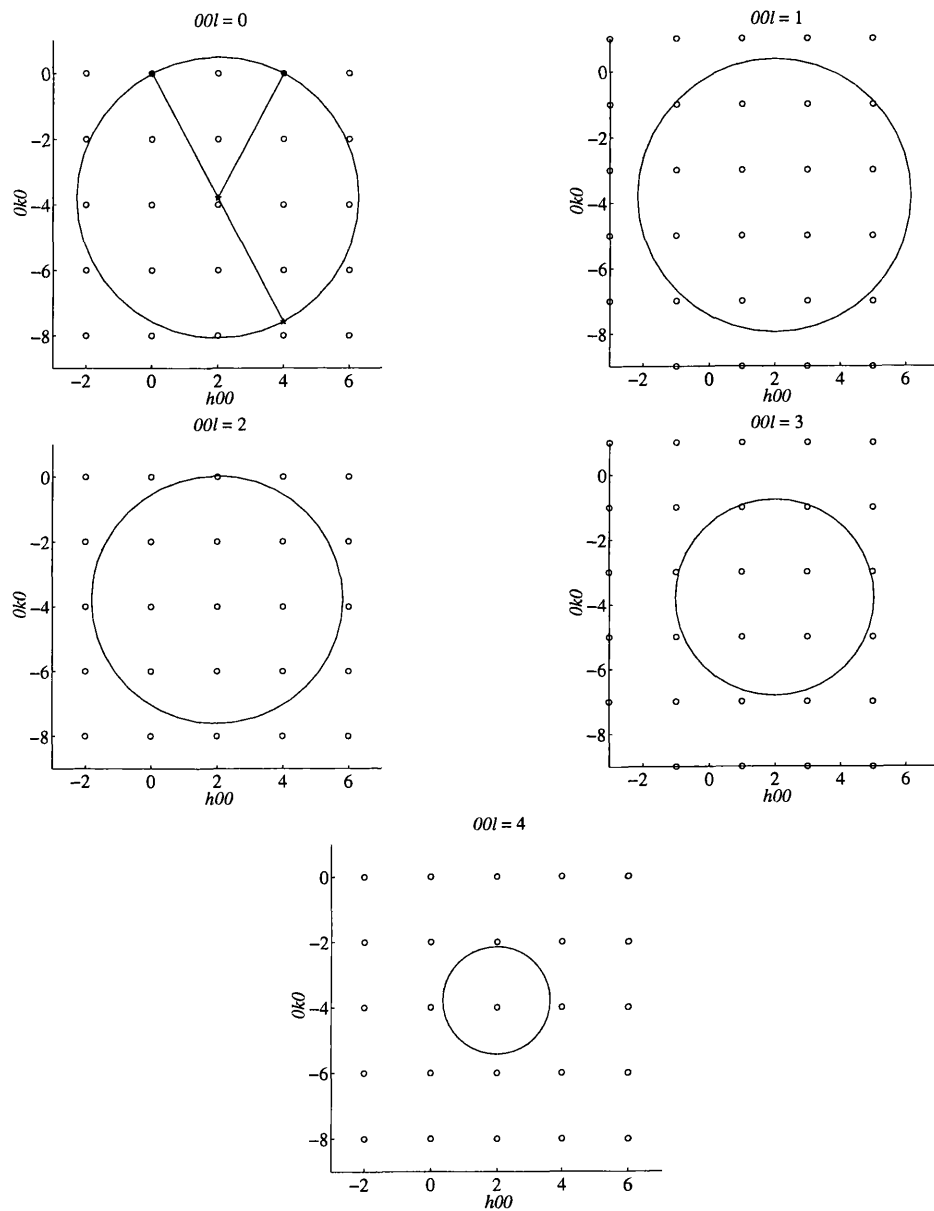


**Figure 5.7:** The Ewald sphere cutting through the reciprocal lattice for the 400 reflection. Possible simultaneous reflections can be seen in several layers.

ture factors. All but two of the cooperative reflections obtained from 400 and the possible multiple scatters in figure 5.7 have strong magnetic structure factors and so could be involved. To determine whether any of the potential operative reflections are responsible, further detailed constructions would be required. The experimental **UB** matrix could be used to determine the exact orientation of the reciprocal lattice during the  $\omega$ -scan. Then it could be seen whether any of the potential operative reflections cross the Ewald sphere during the part of the scan when there is strong scattered intensity from the primary reflection.

The question of field dependent extinction has absorbed a considerable part of the effort expended on this section of the work. Originally it was postulated as a solution to the 400 problem discussed above. Ultimately no quantitative argument has yet been produced. However, I will note some points about the processes that must be involved. In a detailed study of the magnetic structure  $\text{TbAlO}_3$  using a “rather good” crystal, Brown *et al.* encountered a complicated extinction effect [104]. They discovered that the magnetic intensity was much less severely extinguished than the nuclear intensity. They argued that the magnetic domains must be smaller than the mosaic blocks of the crystal. A successful model was developed to account for this and fit the intensities and polarization data. Apparently it is possible for nuclear and magnetic scattering to be affected differently by extinction. Since the magnetic structures in this work are field dependent, it must be possible for the extinction to also become field dependent.

In this case it appears that as the field, and therefore the magnetic intensity, increases, the extinction correction becomes less and less applicable. The reflection 200 is more intense than 240 and so is more severely extinguished. Therefore, as the extinction correction begins to fail, the calculated 200 intensity rises above the observed intensity and 240 exceeds its calculated intensity, as the least squares routine attempts to minimize the misfit to the two.

Considerable efforts were made to overcome the extinction problem. It seems they were not entirely successful. In the rest of the chapter it appears that the extinction effects become compounded as the parameters are used for the other crystals. The original philosophy was to produce a robust model of the crystal structure which could be easily scaled to fit the data. An even greater simplifying

step would be to carry out this scaling, and then simply subtract the nuclear intensities. This would avoid the problem of mixed extinction, and if sufficient reflections were available might enable an entirely magnetic extinction correction to be obtained. Even to do this, more data would be needed. Although Brown *et al.* did not use multi-wavelength data this seems the weakest part of their ingenious and exhaustive work [104]. Two wavelengths were sufficient here, but ideally a third would be used, in any case insufficient reflections are available to attempt to produce a magnetic extinction correction for this dataset.

Although the  $Q = X$  peaks remained absent throughout the experiment, this does not rule out any action at all at these positions. Looking at the map of diffuse scattering made previously (figure 2.4) shows that strong diffuse scattering associated with the spin ice state is expected at these positions. Because this experiment was focused on measuring Bragg peaks all the measurements made were  $\omega$ -scans. These are unsuited to measuring diffuse scattering, as is discussed further in the next section, and the appendix. However very broad features may appear as a high, flat background in such a scan, and some insight into their behavior can be obtained by tracking the field and temperature dependence of this background. To this end, the intensity at 100 and 110 was fitted as a straight line. For the base temperature hysteresis loop this is compared to the intensity of 200 in figure 5.8.

After the hysteresis loop was completed, the temperature was raised in zero field. It can be seen in figure 5.4 that there is a remnant magnetization at the point where the hysteresis loop returns to zero field. As the temperature is raised the remnant magnetization was destroyed. By extracting the diffuse scattering intensity during the temperature increase, it can be seen that as the remaining long range order is destroyed, the original state with zero Bragg intensity and diffuse scattering is re-established (see figure 5.9).

### 5.3.1 Summary of the $[00l]$ Experiment

Clearly experimental problems have been encountered, and to some extent surmounted. Despite the multitude of difficulties plenty of insight into the physical processes in the sample can still be obtained. First of all it is clear that the



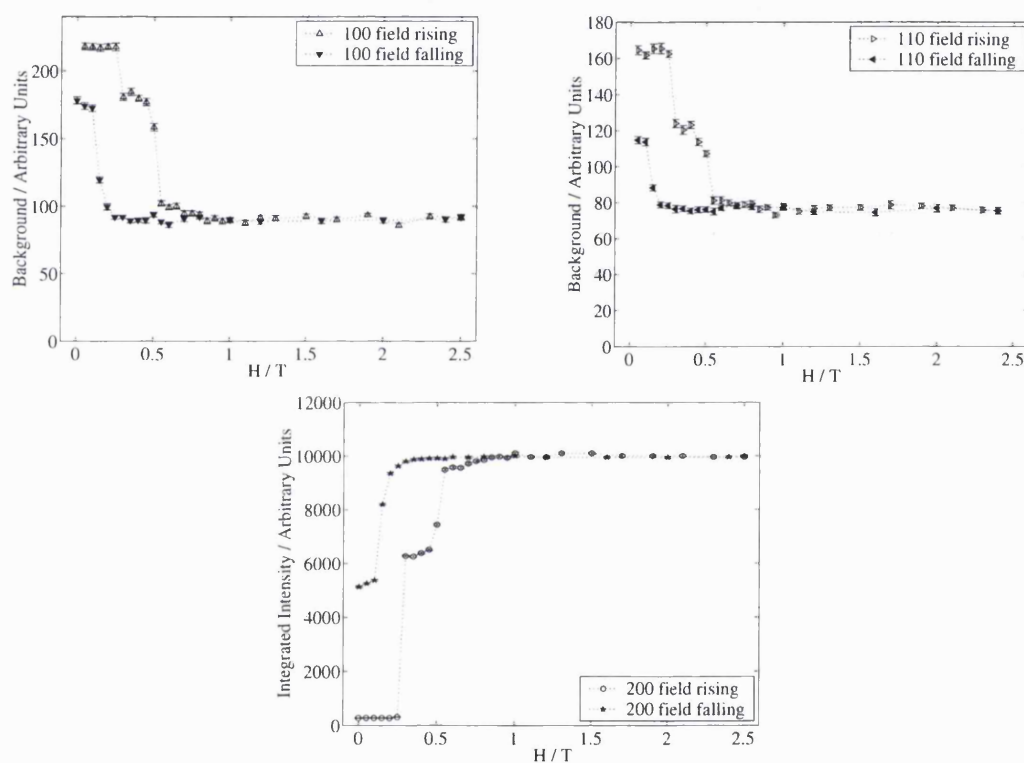


**Figure 5.8:** The intensity of the flat background, or diffuse scattering, at the 100 and 110 positions with field applied on  $[00l]$ , at 0.05 K. The 200 peak intensity is shown as a comparison.

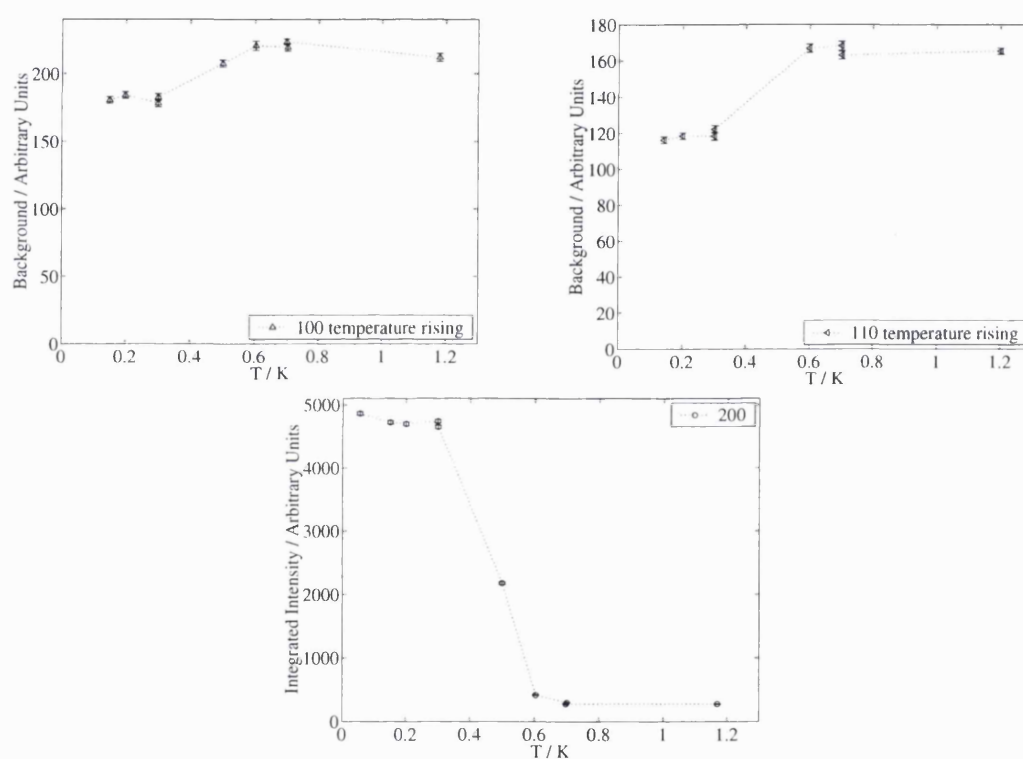


**Figure 5.9:** The intensity of the flat background, or diffuse scattering, at the 100 and 110 positions as a function of temperature, after completion of a hysteresis loop at 0.05 K (the field is zero). The 200 peak intensity is shown as a comparison.

magnetic intensities observed are consistent with the development of the  $Q = 0$  structure. The value of the ordered moment obtained ( $10.3 \pm 0.7 \mu_B \text{ atom}^{-1}$ ) agrees well with that expected for  $\text{Ho}^{3+}$  ( $10.6 \mu_B \text{ atom}^{-1}$ ). Whilst the precision of the ordered moment obtained may be debated, the relative intensity changes show that this structure is developing and saturating. As expected the degeneracy is removed by the application of the field in this direction. The suggestion that a field and temperature cycle would drive the magnet into an antiferromagnetic state with  $Q = X$  peaks was shown to be unfounded.

The postulated liquid-gas critical point was not irrefutably absent. The prediction of Harris *et al.* can be cast as first order phase transition in finite field [55]. This is observed at base temperature, but not at 0.15 K. The critical point may lie in this temperature range, if it does exist.

The system becomes hysteretic at  $T \approx 0.5$  K, and the hysteresis becomes increasingly strong on cooling. When measuring  $\text{Ho}_2\text{GaSbO}_7$ , Blöte *et al.* noted that below  $T \approx 0.3$  K it appeared that the spin system was apparently no longer in good thermal contact with the thermometer [49]. Similar effects were observed by Orendac in more recent heat capacity measurements on  $\text{Ho}_2\text{Ti}_2\text{O}_7$ , below a temperature of  $T \approx 0.6$  K the heat capacity became time dependent [109]. The neutron scattering data is comparable with this as the hysteresis develops in field scans at 0.5 K and below. The dynamics of  $\text{Ho}_2\text{Ti}_2\text{O}_7$  are slowed to the longest timescales in these temperature ranges: no dynamics have been detected by neutron scattering or neutron spin echo. Matsuhira *et al.* found that the susceptibility of  $\text{Ho}_2\text{Ti}_2\text{O}_7$  was virtually zero below 0.5 K [66]. This loss of dynamics explains the increasing hysteresis as the temperature was lowered. The liquid-gas critical point is a property of thoroughly equilibrated simulated systems, it may very well be obscured in the real materials by the lack of dynamics in the temperature range of interest. Whether or not the spin interactions could ever compete with the fields involved is another question, but the lack of dynamics will also explain why the  $Q = X$  type groundstate was not observed. When the system was cooled in a field it simply became trapped in a  $Q = 0$  state.

The form of the hysteresis loop at 0.05 K is particularly interesting. A plateau is observed. It is interesting to speculate about the origin of this plateau. Hysteresis

is not a property of magnetization plateaux of the type described in section 1.10.2 (i.e. a plateau due to a quantum mechanical mechanism). The temperature dependence of the hysteresis suggests that this is not a magnetization plateau of that type, but is also due to the very slow dynamics. It appears that the hysteresis is due to the reluctance of the system to move out of a stable state. That is to say, as the field is ramped up the spin ice state persists to finite fields, and the growth of the magnetization lags behind the higher temperature examples. Then, as the field is removed the system does not relax as readily out of the ordered state back toward the zero magnetization spin ice when the temperature is below 0.5 K. At 0.05 K the persistence of the spin ice state in finite field is most noticeable, zero magnetization persists in finite fields. However, in theory an infinitesimally small field in this orientation will remove the degeneracy [110].

The hysteresis observed here must be the first example of the field regulated dynamics that will be exemplified much more strikingly later on. In this case the system is almost completely frozen and must be driven into the ordered state by the field, in an almost mechanical fashion. An alternative way of looking at this is to ask why the plateau is at  $\approx 6 \mu_B \text{ atom}^{-1}$ ? I am proposing that because the dynamics are so slow, and the thermal fluctuations so weak, that the system is barely able to relax. Therefore the plateau does not represent some partially ordered structure with a magnetization of 6/10, or fluctuating moments contributing 6/10 of the saturated magnetization. It represents a partially ordered spin ice, in which 6/10 of the moments have been driven into their ordered orientation by the field and pinned there. Somehow the remaining 4/10 require higher fields to reorient them. To extend this conjecture to the limit I suggest that there must be loops, chains and clusters of spins that can be oriented relatively easily. Meanwhile some spins are left on branches, or in regions not reached by a percolating cluster. In the absence of thermal fluctuations these spins become trapped as defects in the  $Q = 0$  state and only high fields can remove them. This is similar to work hardening in alloys. The material is stressed, and at first responds. Some defects are removed by this process, eventually the remaining defects become entangled or locked together, and the material no longer responds to the stress. Eventually it fails.

The diffuse scattering provides some support for this hypothesis. The system begins in a disordered spin ice state, with diffuse scattering and no Bragg scattering. As the field is raised the Bragg scattering increases as the ordered structure forms. Simultaneously the diffuse scattering decreases. However, in the plateau region both Bragg and diffuse scattering are present, suggesting that the system has both regions of long and short range order, as suggested above (see figure 5.8).

The rate of the field scan in the hysteresis loop has not been discussed, and indeed there is no data available for this quantity. However, it is shown to be important for  $\text{Dy}_2\text{Ti}_2\text{O}_7$  in a different orientation in the next chapter. More careful investigations of this would cast light on the origin of the plateau.

The extremely slow dynamics are able to hold the system in an ordered state even when the field cycle was completed. Only as the temperature is raised above 0.5 K does the system begin to relax. Once this occurs, it relaxes back into the disordered spin ice manifold, away from the low weighted ordered structure.

## 5.4 Field Applied on $[h\bar{h}0]$

In this orientation, as with  $\text{Dy}_2\text{Ti}_2\text{O}_7$ , both Bragg and diffuse scattering is observed. Throughout this experiment  $\omega$ -scans were measured, which are extremely limited in reciprocal space. Different manifestations of the diffuse scattering are seen in the  $\omega$ -scans. Evidently a very narrow  $\omega$ -scan is extremely unsuitable for measuring broad diffuse features. However, information on the diffuse scattering can be extracted from these  $\omega$ -scans. For diffuse scattering attention is entirely focussed on the 001 and 110 positions which were measured at all the points in phase space that were visited.

At some points the diffuse scattering is so broad that no shape can be seen in the  $\omega$ -scan at all, giving the appearance of a flat background. If this flat background is fitted and compared to the flat background found around Bragg peaks it can be seen to be significantly higher. The background around various Bragg peaks in zero field is compared with that at the  $Q = X$  positions in figure 5.10. There is no obvious  $\theta$  dependent functional form of the background, but it is evidently lower than that at the two  $Q = X$  positions. Furthermore, the background at

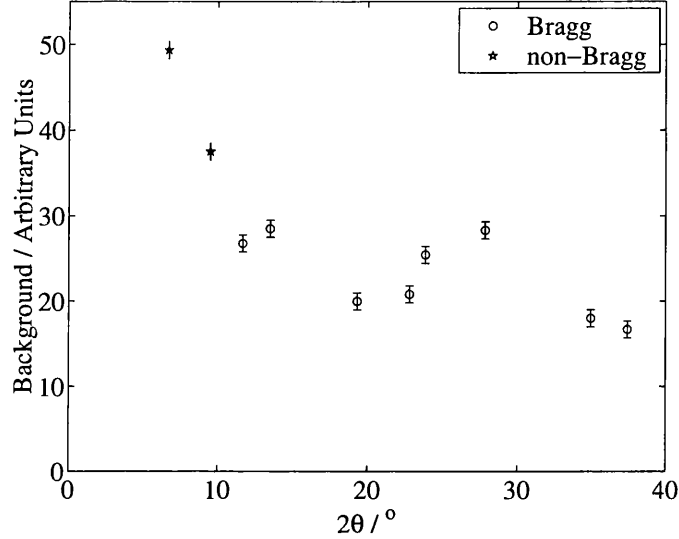


**Figure 5.10:** Dependence of the background around Bragg peaks on the  $\theta$  angle using a wavelength of 2.36 Å on D10. The two  $Q = X$  peak positions where diffuse scattering is expected are also shown (“non-Bragg” positions).

the  $Q = X$  positions then proves to be field dependent. This is attributed to a growing, but still very diffuse, feature which is outside the width of the scan (the limited scope of the  $\omega$ -scan in reciprocal space is discussed in the appendix).

Subsequently the features grow into peaks, at first with widths which still easily exceed the  $\omega$ -scan, and then sharpening to lie within the scan width. Efforts were made to quantitatively extract correlation lengths and to take account of the instrumental resolution when sharp features developed. These were ultimately foiled by the shape of the features which were not amenable to resolution convolution. The details of the width extraction and resolution are contained in the appendices. The diffuse features are compared in terms of amplitude (i.e. wavevector dependent susceptibility,  $\chi_Q$ ). The amplitude was extracted by fitting to a functional form appropriate to the peak shape. These were straight lines, a single Gaussian, or triangular functions.

The behavior of the Bragg peaks is different to the  $Q = X$  features. Ideally a magnetic structure would be fitted to the peak intensities and the field/temperature dependence of the sublattice magnetization determined. During analysis of the

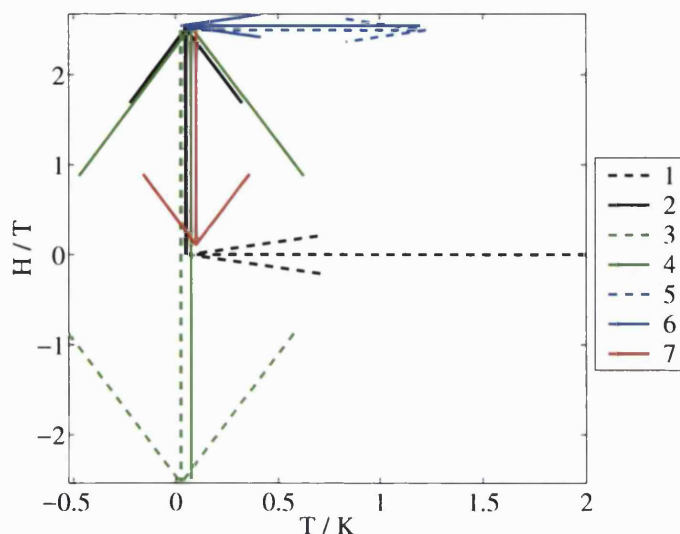


**Figure 5.11:** Path through  $H/T$ -space with the field applied on  $[h\bar{h}0]$ .

Bragg scattering it transpired that this could not be done particularly precisely. A plot of intensity versus field shows features which are outside the error associated with the measurement of an intensity. However, the magnetic moments of the postulated structures cannot be determined with sufficient precision to see the difference between the two states outside of the error-bar. Consequently, in the following description of the results the evolution of the Bragg peaks is discussed in terms of integrated intensity, and not the growth or loss of sublattice magnetization. However, the probable reasons for the intensity changes and the associated evolution of spin correlations must be discussed. Therefore some comparisons of magnetic structures at important points in phase space are made.

#### 5.4.1 Hysteresis Loop at Base Temperature

The first section of the experiment was a full hysteresis loop (the path through  $H/T$ -space is illustrated in figure 5.11). The field was scanned up to 2.5 T, back to -2.5 T, and then back up to 2.5 T. During some parts of the loop an expanded collection of peaks was measured, particularly if it seemed that a magnetic structure might be determined for that point. At most points only five peaks were measured, these being 110, 001,  $11\bar{1}$ ,  $11\bar{3}$  and 002. As discussed above, the scat-

tering at the  $Q = X$  positions 110 and 001 is diffuse. During the cycling of the field at base temperature these features never evolve into a peak-shape within the bounds of the  $\omega$ -scan (this occurs during the temperature scan described below). The behavior of the diffuse features can only be described by fitting the formless intensity in the  $\omega$ -scan with a flat line. The two features are shown in figure 5.12. Their field dependance is extraordinary.

Three Bragg peaks were routinely measured during the rising field stage of the hysteresis loop. They are compared in figure 5.13. It can be seen that they gain intensity congruently. A single magnetization process is occurring. All the peaks show the same complicated sequence of jumps. The entire hysteresis loop is shown for the 002 peak in figure 5.14.

Possible magnetic structures in this orientation have been discussed in the analysis of structure factors and the introduction to spin ice properties in applied fields. Two magnetic structures were used in the work of Harris *et al.* [25]. One was a  $Q = 0$  structure with all chains transverse to the field aligned in the same sense. The other was a  $Q = X$  structure with the transverse spin chains alternating. The first one was used to account for the intensity seen at this point (i.e. saturated magnetization at base temperature). Apparently Harris *et al.* chose to ignore the growing intensity at the  $Q = X$  positions at this point. A  $Q = 0$  structure therefore can explain their observed intensity distribution. However, it seems impossible to invoke it here when  $Q = X$  features are evident. Apart from the long range ordered structure which is giving the magnetic Bragg scattering, there must be some other type of spin correlation causing the appearance of  $Q = X$  features. Because of this, and also the continued separated development of the  $Q = X$  features during the temperature scan, it seems most likely that the spin system is indeed separated into two types of spin with respect to the field. Long and short range order can therefore coexist. The application of the field is required to restrict the degeneracy to states with chains of spins.

The point of all this is that neither model used by Harris *et al.* seems appropriate here. As the  $Q = X$  features are not Bragg peaks the transverse chains must still be disordered to some degree. The Bragg intensity would then be due to the chains of spins which have been pinned by the field. A magnetic structure



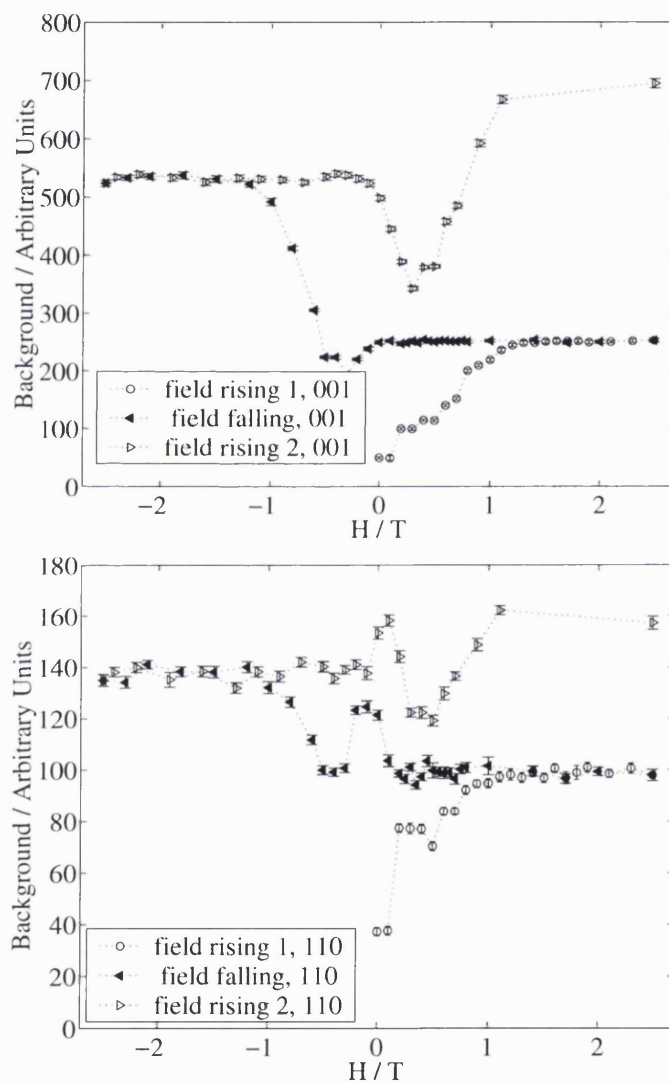


**Figure 5.12:** Hysteresis loop,  $T \approx 0.05$  K, field applied on  $[h\bar{h}0]$ . Amplitude of diffuse features at 001 or 110 fitted as a flat background.

with zero (i.e. disordered) moments on the transverse spins and ferromagnetic chains parallel to the field was used. The fitted moment obtained was  $6.5 \pm 0.3 \mu_B$  atom<sup>-1</sup>. This moment is very much reduced below what is expected. This was also a feature of the structure refinements of Harris *et al.* and will be discussed later.

The intensity saturates identically on both sides of the loop showing that the spin structure giving rise to Bragg scattering is indistinguishable each time. This implies that the same long range ordered state is eventually reached in a high field, regardless of history, and independent of the short range ordered state. This is assumed to be the state with all parallel spin chains pinned in the same sense by the field.

The central region of the hysteresis measurement is expanded in figure 5.15. This shows that on removal of the field there is a remnant order which is not destroyed. Normally hysteresis loops show a negative magnetization as the field sweeps below zero. Because we are observing the square of the magnetization, this does not happen. Presumably the remaining ferromagnetic order is reversed by the oppositely polarized field. Given the very slow dynamics of spin ices it seems most likely that at this point there are remaining regions of frozen order, and other regions in which the long range order has been lost. At this point it is envisaged that the remaining ordered regions are flipped over.

The field falling and rising curves are essentially symmetric suggesting that after the initial evolution out of the disordered spin ice state recorded in the pristine curve, the subsequent field dependence of this set of spins is always much the same. The pristine curve lies outside the hysteresis loop and this is also very unusual.

The  $Q = X$  features present an even greater mystery. It is clear that the development of these correlations requires the establishment of the  $Q = 0$  structure simultaneously. Also it is evident that when the  $Q = 0$  order is not changing, neither are these. This part of the experiment provides the clearest example of the field regulated dynamics alluded to in section 5.3. At this temperature the spin system is almost completely frozen, though some very slow dynamics must remain as the magnetization does relax when the field is removed. This means

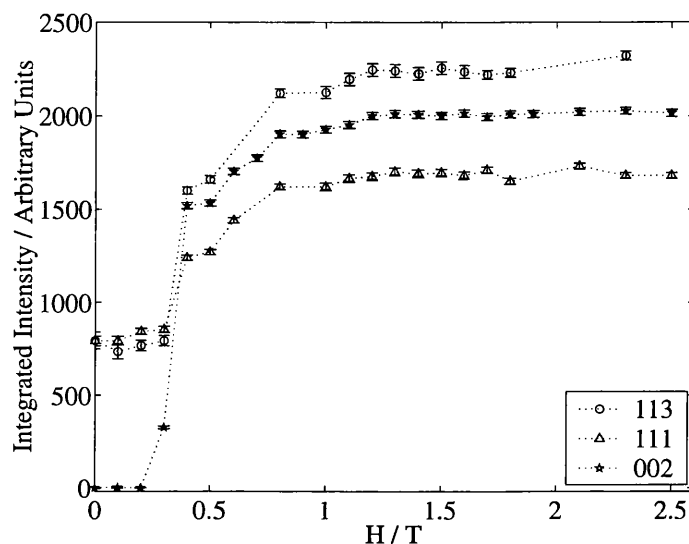


**Figure 5.13:** Field dependence of the three Bragg peaks measured during the rising field section of the hysteresis loop. Their congruent development shows that all the spins contributing to the Bragg scattering are being driven into the magnetic structure in the same manner.

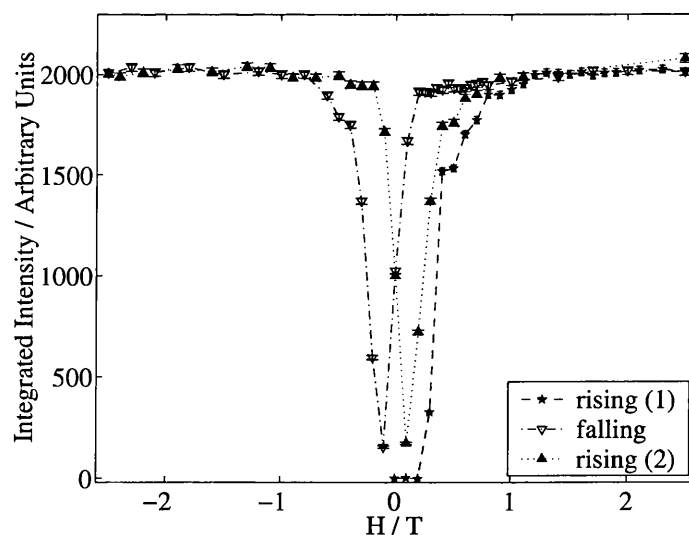


**Figure 5.14:** Field dependence of the 002 peak at 0.05 K during cycling of the field.

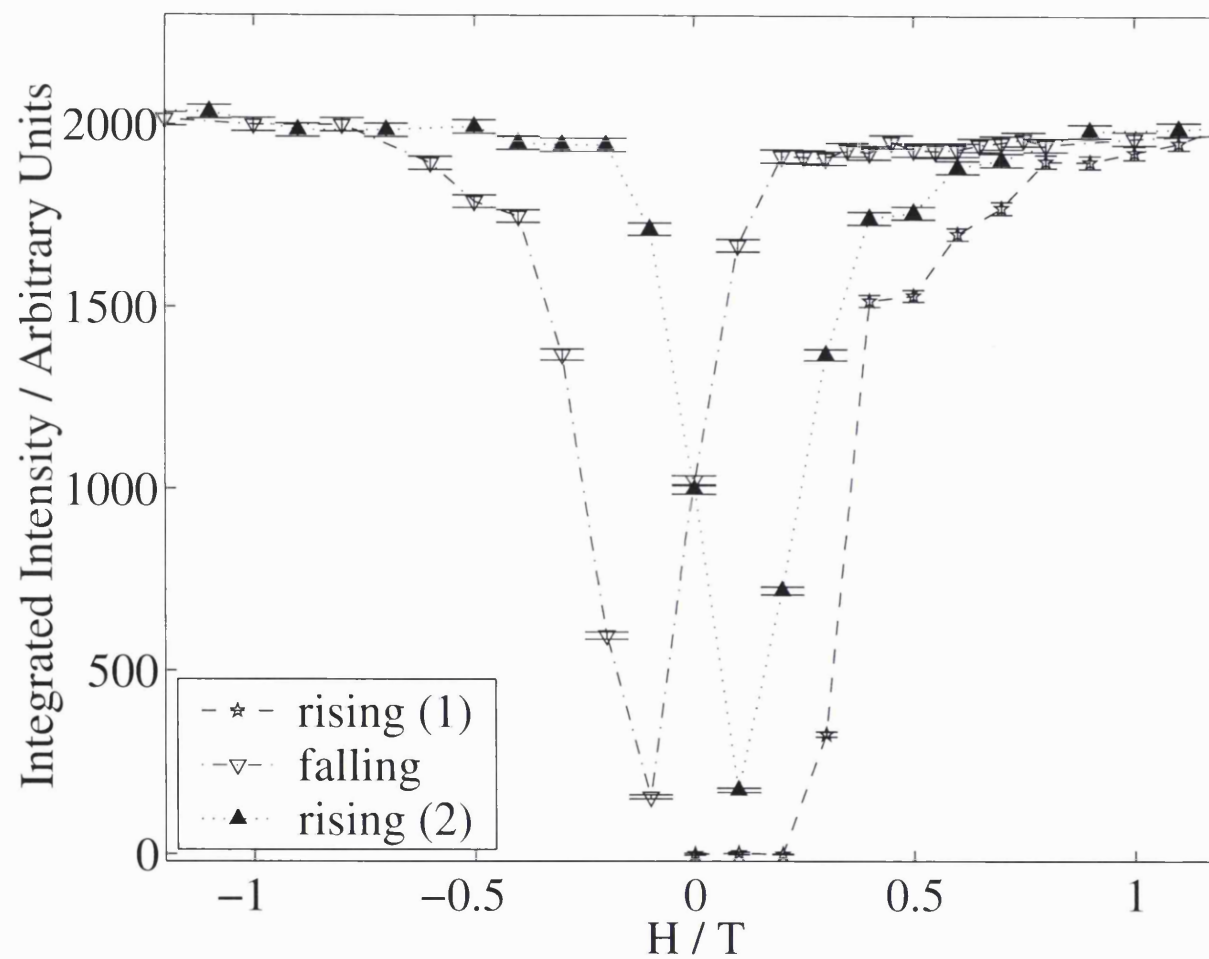


Figure 5.15: Central region of the hysteresis loop measured at 0.05 K. The peak shown is 002.

that by promoting spin reorientation the field can induce dynamics, this occurs when the field is rising. The field can also suppress the dynamics, as in large fields which pin the spins. Finally the field can “allow” dynamics, i.e. when the field is reduced, intrinsic dynamical processes are re-established allowing the magnetization to decrease. In this orientation this is especially clear because of the two spin systems. Only when the field is inducing or allowing dynamics in one spin system are there any dynamics in the other. This is illustrated in figure 5.16 where the three sections of the hysteresis loop are plotted separately.

The set of spins with a component on the field is driven into order by the field, as evidenced by the repeated saturation of the  $Q = 0$  Bragg peaks. Unlike the  $Q = 0$  peaks, the  $Q = X$  correlations continue to evolve throughout the hysteresis loop, e.g. two different states are seen when the field reaches 2.5 T for the first and second times. When the degeneracy is initially restricted and the  $Q = 0$  peaks begin to grow, some level of correlation is developed in the transverse chains. Once the pinned spin system is saturated no further change can occur and both types of correlations are frozen. As the field is scanned back down, the pinned spin system is able to relax into a less ordered state by whatever slow dynamical process remains operative, and is then driven back to order. When this occurs the  $Q = X$  correlations are somewhat reduced but subsequently are increased, as the long range order is re-established. This happens again as the field is scanned back up. For much of the hysteresis loop the field holds the parallel spin system frozen. During these periods, the transverse spin system is also static. It is trapped in a state of short range order, the nature of which is discussed below. When the field induces dynamics in the parallel spin system the transverse chains also become dynamic again, and the extent of order in the transverse system continues to increase again.

The shape of the  $Q = X$  features in reciprocal space is of great interest. Sheets or rods of scattering are indicative of one or two dimensional ordered structures. The perfection of order in the transverse chains must be low at this stage (i.e. throughout the hysteresis loop), because subsequently during the temperature scan the  $Q = X$  features become much stronger and sharper showing there is still great scope for increased order). Given this subsequent further ordering, the state at this

stage might be expected to consist of ordered chains with no significant interchain correlation. The later ordering would then be the ordering of chains. During the hysteresis loop the ratchet-like development of intensity at the  $Q = X$  positions would have to correspond to increasing intrachain correlations. Therefore during these stages the partially ordered spin ice state must be defective. Each time the  $Q = 0$  peaks saturate the transverse chains are differently correlated and where the  $Q = X$  features are below their maximal intensities this must mean that there are imperfections in the chains and therefore frozen defects in the spin ice state.

This scenario should generate first of all a sheet of scattering perpendicular to the chain structure. Subsequent interchain ordering will lead to a localized feature in reciprocal space which contracts to a Bragg peak in the limit of perfect long range order. With the field applied on  $[h\bar{h}0]$  the transverse chains are along  $[hh0]$ . A sheet of scattering would then be expected to extend along  $[00l]$  for a structure with order within chains and no intrachain correlations.  $\omega$ -scans at an  $00l$  position should scan across this sheet and at  $hh0$  the scan will be in the sheet. Entirely fortuitously, our collection of peaks allows us to check this possibility. First, the fact that the  $001$  feature is flat/outside the width of the  $\omega$ -scan means that any such sheet is rather thick. It would be expected as a flat background contribution at  $002$  as well. The form factor of  $\text{Ho}^{3+}$  will reduce the intensity. However, both positions are quite close to the maximum in the form factor, so since the eventual intensity maximum for  $001$  in the hysteresis loop is 600 counts it should also be clearly visible at  $002$ . Likewise the presence of  $110$  as a flat feature would imply another sheet extending up  $[11l]$  which would be visible in the background of  $11\bar{1}$ . The backgrounds of both Bragg peaks are field independent. This rules out the possibility of extended sheets of scattering parallel to either  $00l$  or  $hh0$ , or rods of scattering parallel to these positions.

As a result of this discussion, the two-stage scenario of ordering first in chains and then between chains seems to be excluded. In the analysis of the structure factors it was shown that the presence of  $Q = X$  peaks was due to antiferromagnetic arrangements of chains. Therefore it seems that the transverse chains must be evolving into a three dimensional structure with antiferromagnetic chains. This occurs in stages and during the hysteresis loop does not proceed to a particularly

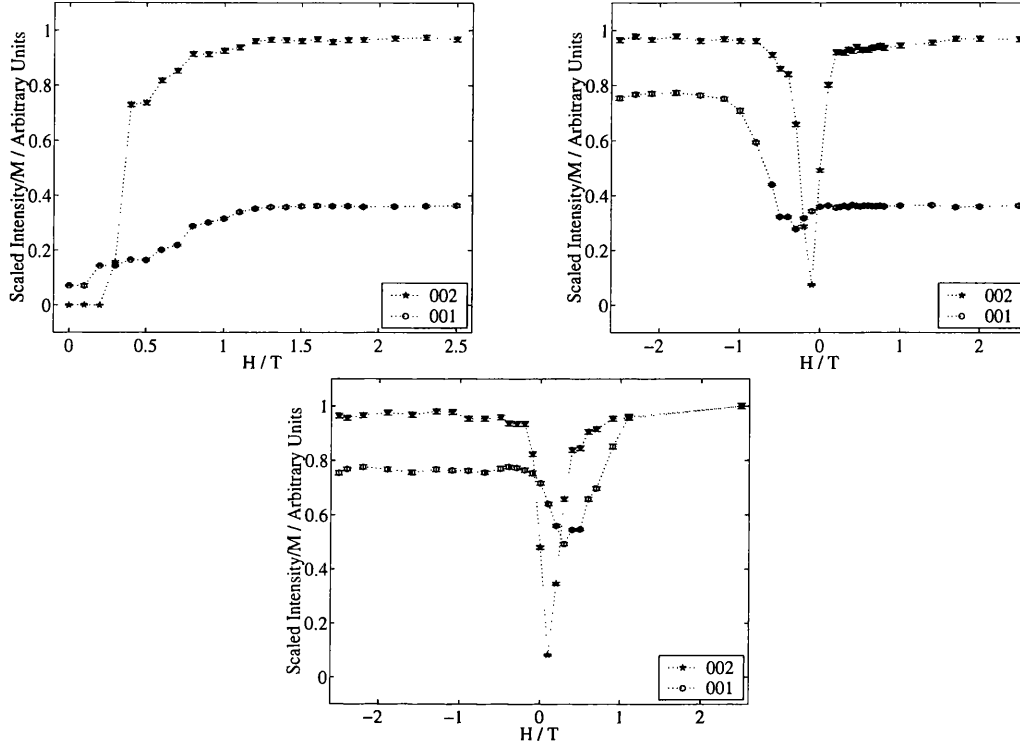


**Figure 5.16:** Comparison of evolution of  $Q = 0$  and  $Q = X$  features during the three stages of the hysteresis loop (field rising from pristine, top left, field falling, top right, field rising, bottom). The 002 intensities were scaled to the maximum value which occurs during the hysteresis loop.  $\chi_{001}$  was treated in the same way. During the field scans it seems that the spins giving the  $Q = X$  features can only move significantly while the spins causing the  $Q = 0$  feature are being driven by the field.

advanced stage as the features remain so broad. There must be small domains of antiferromagnetic chains separated by defects and/or disordered regions. Each time the pinned spins are driven through a hysteresis cycle by the field, the field induced dynamics allow spin flips in the transverse spin system. Each time this occurs, the order is somewhat increased in the transverse spin system.

#### 5.4.2 Temperature Scan in Applied Field

After the hysteresis cycle had returned to 2.5 T the temperature was raised to 1.2 K, and then lowered back to base temperature. During this temperature scan an

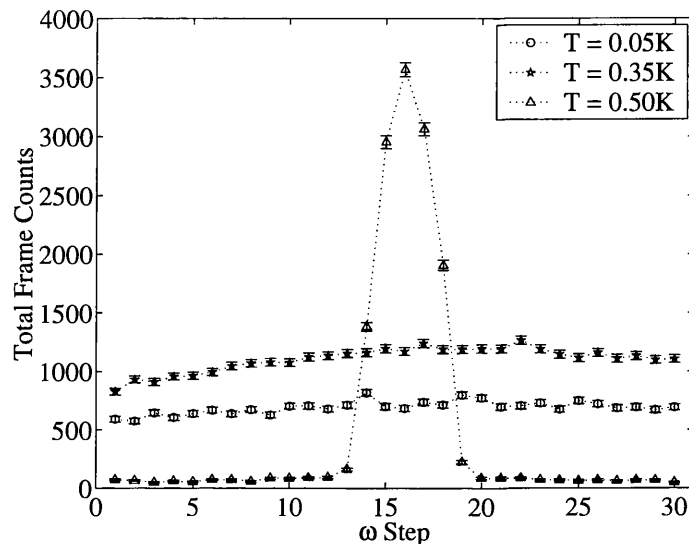


**Figure 5.17:** Sharpening of the 001 feature as a function of temperature.

enormous gain in intensity is seen on the  $Q = X$  peaks, in particular 001. These sharpen from features which are flat in the  $\omega$ -scan to quite sharp peaks. However, it was not possible to fit these and take sensible account of the width. Instead the amplitude, i.e.  $\chi_Q$ , was extracted by fitting to a functional form appropriate to the peak shape. These were straight lines, a single Gaussian, or a triangular function. Three examples of the evolution of the form of the scattering are shown in figure 5.17. The triangular function was of particular use for the 001 feature which was not amenable to fitting with a Gaussian, or convolution of Gaussians. The temperature dependence is shown in figure 5.18. The Bragg peaks contrast strongly with the  $Q = X$  features because no change in the Bragg peaks was seen during this temperature scan. They remained at the values seen in the saturated regions of the hysteresis loop. Again it was established that no extensive diffuse scattering is present, the backgrounds of the Bragg peaks were unchanging with temperature.

These observations are also very supportive of the suggestion that there are two spin systems. The pinned spin system is apparently held so strongly by the field that the rise in temperature has no effect on it. Meanwhile the transverse spin system is able to undergo a very marked transition to a much greater degree



of order. Apparently the increase in temperature is sufficient to restore dynamics. However, the temperature remains low enough that the interactions are still important and so the order increases. This is not exactly an order-by-disorder situation but an analogy can be seen. Thermal fluctuations are required to overcome the energy barriers and select the more ordered states. True order by disorder has entirely entropic selection of a groundstate from a manifold of degenerate groundstates. Here the thermal fluctuations are required for accessing states which are presumably energetically favorable but kinetically inaccessible. Again this can be regarded as some sort of annealing process where defects are preserved when the dynamics are frozen, but can then be eliminated when dynamics are induced. Increasing temperature seems to be a much more effective way to activate this process than the field scan.

As far as they are known, the measured dynamics of spin ices are consistent with this part of the experiment. During the temperature rise  $\chi_Q$  begins to fall again above  $T \approx 1$  K. This is roughly consistent with the peak in the susceptibility seen at around 1 K. Lowering the temperature again then freezes these correlations.

### 5.4.3 Field Removal After the Temperature Scan

After the temperature had returned to base temperature the field was ramped back down to zero. Then it was driven to a small negative value to try to remove the  $Q = 0$  peaks. The field was then returned to zero. The 002 peak did not disappear, and the  $Q = X$  features remained as intense and relatively sharp features, albeit not as intense as in stronger applied fields (figure 5.19). The strong history dependence of the sample is clearly evidenced by the fact that this is the fourth state in which the sample has been observed, at this point in phase space (zero field cooled, field falling during hysteresis loop, field rising during hysteresis loop, field removed). The intensity of the  $Q = 0$  Bragg peaks is always similar each time the experiment reaches this point, but the  $Q = X$  features have differed strongly each time.

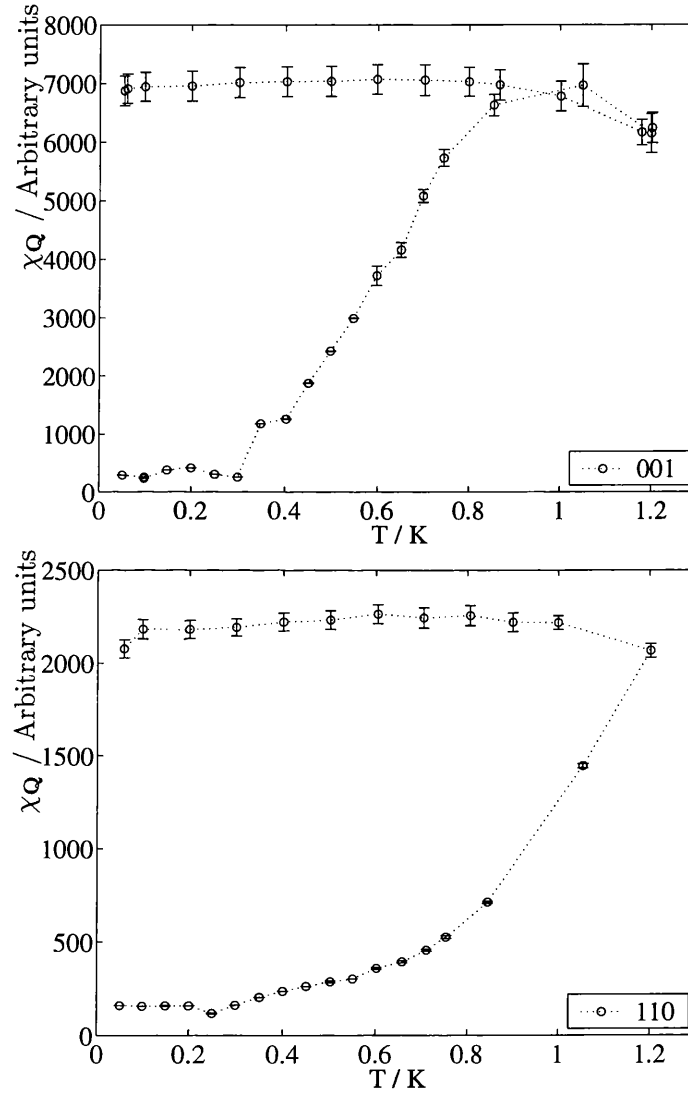


**Figure 5.18:** Temperature scan,  $H = 2.5$  T, field applied on  $[h\bar{h}0]$ . Amplitude of diffuse features at 001 or 110 fitted as a flat background (0.05-0.3 K), single gaussian (0.3-0.6 K) or triangular peak (0.6-1.2 K and all points on the falling  $T$  scan).

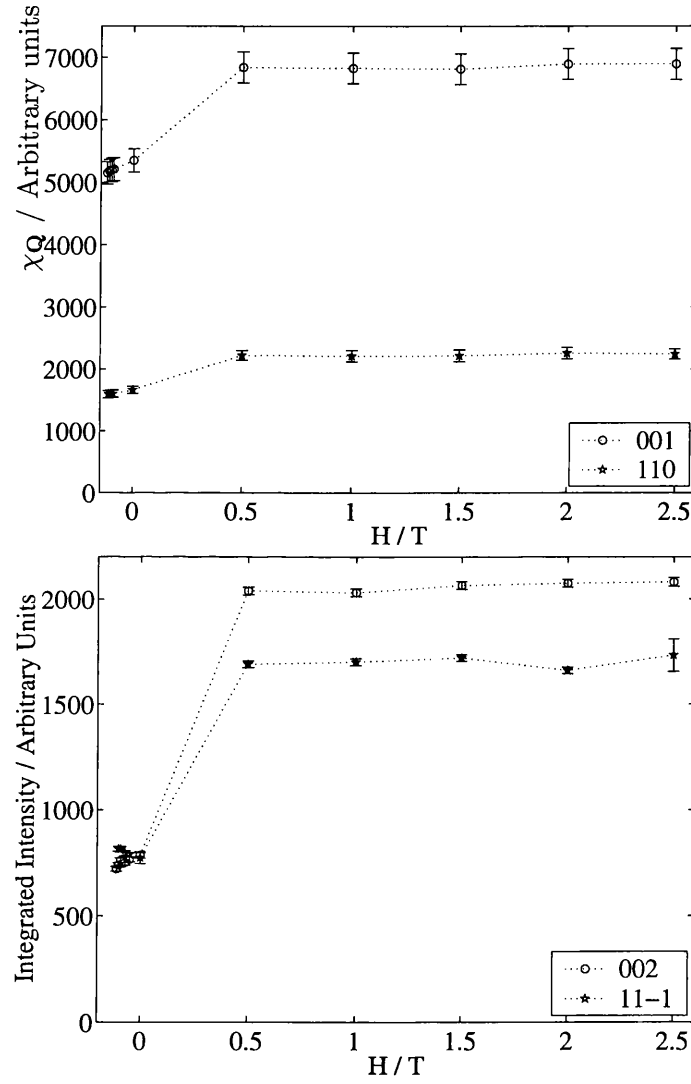


**Figure 5.19:** Field removal after temperature scan,  $T = 0.05$  K, field applied on  $[h\bar{h}0]$ . Amplitude of diffuse features at 001 or 110 fitted as a triangular peak (top), Bragg peak intensity (bottom).

#### 5.4.4 Summary of the $[h\bar{h}0]$ Experiment

The observations and deductions of this part of the experiment are a central part of this study. To recapitulate briefly what I believe has been learnt, the spin system is separated into parallel and transverse sub-systems, field regulated dynamics are seen in both at base temperature. At higher temperatures the dynamics of the transverse system can be activated independently of the parallel spin system which is still pinned by the field. The transverse spin system is undergoing some continual evolution toward a three dimensional ordered state.

The three dimensional ordering takes place by an annealing process. Whenever dynamics are activated or allowed by the field or temperature this process continues. The diffuse scattering takes the form of weak localized features (no background at adjacent positions throughout hysteresis loop), giving way to much stronger, sharply localized features (during the temperature increase). Because of this, the ordering must be in domains of three dimensional order, with the annealing increasing the size of domains. An alternative scenario involving order in chains, and then between chains can be discounted because of the absence of spatially extended diffuse features. The ordering is being controlled by long range interactions, as the chains are not coupled by nearest neighbor interactions. The continual evolution toward order does suggest that there is a definite groundstate for the system in this situation, and this appears to be the  $Q = X$  structure. Ultimately this part of the experiment suggests that the spin ice manifold does contain favored groundstates. The dynamics of the system, and therefore its ability to move through the manifold of states, are the controlling factors in the realization of these states. Indirectly this lends support to the hypothesis of Melko and Gingras [64] that there is a true groundstate.

This section of the work also requires close comparison with the work of Harris *et al.* [25]. The first comparable section of both experiments is the field scan at base temperature. In this experiment the temperature was  $T \approx 0.05$  K and in their experiment it was 0.35 K. Their data is shown in figure 2.13, and compares most closely with figure 5.16 (top left). The two are quite different. There is no sign of the steps at 0.35 K. This same behavior is later shown for  $\text{Dy}_2\text{Ti}_2\text{O}_7$  under conditions which are more readily comparable. The other part of the experiment

that is similar is the heating in applied field (2.5 T here, 2.0 T by Harris *et al.*). The history of the two samples before the temperature was raised is different, theirs was subject to field cooling experiments and some field scans, here only the full hysteresis loop was performed. Despite this, the effect of the temperature rise is the same in both cases. The  $Q = 0$  peaks are constant, and both 2.0 and 2.5 T are well within the region of the hysteresis loop where the magnetization is saturated so are both strong enough fields to completely pin the parallel spin chains. The  $Q = X$  peaks show a dramatic increase in intensity and sharpness. Higher temperatures could be accessed in their experiment than in ours and they were able to see the  $Q = X$  peaks collapse again at  $T \approx 2$  K. They did not then cool down, so neither study shows what happens if the correlations are completely destroyed before cooling. In this work the maximum temperature was 1.2 K and the  $Q = X$  peaks were just beginning to decrease, but on cooling grew to a greater maximum. However, cooling was from a state which was still very strongly correlated compared to almost all points in the history. It remains an open question as to whether the  $Q = X$  correlations can spontaneously form in and around the existing  $Q = 0$  parallel chain ordered structure.

Harris *et al.* also observed a strongly reduced moment. At the end of their base temperature field scan they attribute the Bragg intensity to a  $Q = 0$  structure with ordered moment  $4.6(5) \mu_B \text{ atom}^{-1}$ . As explained above, in the presence of  $Q = X$  features, it does not seem correct to attribute the Bragg intensity to a fully ordered magnetic structure. I have used a structure with ordered chains parallel to the field and obtained an ordered moment of  $6.5(3) \mu_B \text{ atom}^{-1}$ . No explanation for their reduced moment was actually advanced by Harris *et al.* who moved swiftly on to other issues. I would suggest that had they fitted the size of only two moments (out of four on the tetrahedron), i.e. the same structure I used, that their moment would have been much larger and they would not have had this problem. The reduced moment obtained in this study can only be attributed to the compounded effects of applying an extinction correction obtained for nuclear intensities measured at high temperature to magnetic intensities measured at very low temperature in a different crystal.

Returning to the question of field dependent extinction again, a possible mech-

anism might be suggested. Brown *et al.* found that since the magnetic intensity was less extinguished, initial fits of the magnetic structure using the nuclear extinction parameters produced a moment of  $17 \mu_B \text{ atom}^{-1}$  [104]. In their case, the magnetic domains were smaller than the mosaic blocks of the crystal. In this case, the situation would have to be reversed. For the magnetic extinction to be more severe, resulting in a reduced moment size, the magnetic structure would have to be completely coherent over longer distances than the mosaic blocks. If the anisotropy were finite and the spins could become a tiny bit canted off axis, the magnetic structure could become coherent across small angular displacements at the block boundaries. This would render the magnetic crystal more perfect than the nuclear, and make the magnetic extinction more severe, serving to reduce the fitted moment.

## 5.5 Field Applied on $[h\bar{h}\bar{h}]$

When the field is applied on a direction such as  $[h\bar{h}\bar{h}]$  previous work shows that there is a competition between the field and the exchange. At high fields the exchange is overwhelmed and the ice rules broken. Theory and bulk measurement are in agreement that this occurs [55, 77, 78, 79]. No measurement of the change in spin structure during these transitions had been made before this part of the experiment. The scope of this section was very limited. A small collection of peaks were measured as the magnetic field was cycled in a hysteresis loop up to 5.5 T. Only two temperatures were measured, 0.05 K and 1.8 K. The peaks measured were 002, 422, 110, 220, 440, and 240. The tilting detector was employed and this allowed access to the out of plane reflections 002 and 240.

Three field dependent behaviors were seen. 220 and 422 showed a strong field dependence. At 0.05 K they were hysteretic, at 1.8 K they were not. The intensity of 440 remained virtually constant. The other three peaks are absent nuclear reflections and no magnetic intensity appeared at any of their positions. When significant magnetic intensity had appeared on 220 equivalent reflections to 002 were also checked, but were also found to have zero intensity. The field dependence of the intensities at 1.8 K is shown in figure 5.20.

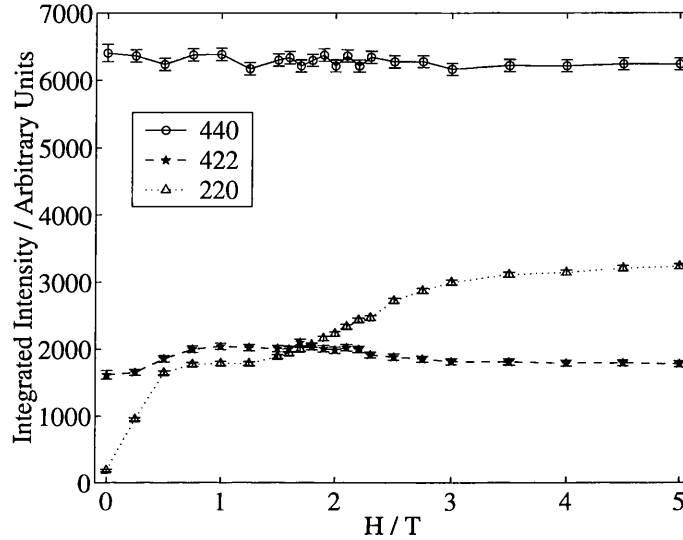


**Figure 5.20:** The field dependence of Bragg peaks with field on  $[h\bar{h}\bar{h}]$  at 1.8 K. The 002, 110, and 240 peaks were also measured and all maintained zero intensity throughout.

The pattern of field induced intensity is problematic for interpretation in terms of spin ice and other simple field induced structures with the spins constrained to  $\langle 111 \rangle$  directions. The main reason for this problem is the absence of 002 and 240. Both of these peaks are expected for the types of structure proposed for this direction, indeed 002 is expected for any of the field induced spin ice structures. The constancy of 440 is also problematic. For the present it is assumed that the absence of 002 and 240 is an artefact. Possible reasons could be that they are out of plane reflections and conceivably the windows of the cryostat were insufficient, or the “flat” shape of the crystal meant it scattered anisotropically and was particularly weak in this direction. More probable explanations are that either incoherent scattering from the abundance of stycast used to fix the crystal to the sample rod, or absorption by the cadmium foil masking the tip of the sample rod was the cause of complete loss of the scattered beam.

The consequence of these absences/non-observations is that the magnetic structures are being fitted using just two peaks, the 422 and the 220. For models with only one variable to be fitted (the size of the magnetic moment), the fit is con-

strained, albeit marginally, with minimal leverage. Two models can be used in this way. The first is expected to apply to low field data and has a magnetic moment assigned only to the spin which is on the axis where the field is applied. The other three spins are given zero moment to represent the disordered kagomé ice phase. The second model has all four spins constrained to be the same size and might be expected to apply in the highest field situations when the sample is fully magnetized (these are referred to as model A and B, respectively).

However, there is no reason to suppose that the system will cross neatly from one to the other. The magnetization of the field pinned sublattice develops to a greater extent than the kagomé ice sublattices in the plateau phase [78, 79]. To change directly from the first model to the other would require a sudden increase in the magnetization of the kagomé ice spins to reach the same level of order as the pinned spins, in effect saturating the system in a single step. Alternatively a mechanism in which the cost of decreasing the magnetization of the pinned spin system to the same level as the incipient magnetization of the kagomé ice part would be offset by the overall increase in order is required. Ideally a model in which the two spin systems can evolve separately is required. This means that the size of two moments must be refined simultaneously and at least one extra peak is required. Already it is clear that 002 and 240 are required for all these structures and so their inclusion would lead to wild misfits. Therefore persisting with the view that their absence is spurious, and that 440 is also behaving problematically, all that can be included is 110, which is also absent throughout. In doing this it is assumed that 110 is a genuine absence. The model with a variable moment size for both spin systems is referred to as model C.

One other model can be tested. The low field data could be fitted using a model with a single pinned spin (model A). The value of the magnetization on this sublattice in the plateau phase would then be fixed and the high field data fitted by varying the moment size on the kagomé spins. This assumes that the on-field spins are fully saturated both in and above the plateau phase. This is model D (all four models are illustrated and described in table 5.3 at the end of this chapter).

The extinction correction is slightly more complicated for this crystal. In the CCSL extinction correction routines the crystal faces must be specified using a



vector equation for a plane. With the sphericalized crystals this remains a simple task. All the faces are the same distance from the origin of the axis system, and so all that is required is a list of the face normals, i.e. the  $\langle hhh \rangle$  directions. When working with the “flat” crystal, different distances for the different planes are required. Also, it is important to relate the axis system of the CCSL routines to the actual orientation of the crystal. In practice this part is quite simple. The scattering plane is specified by the setting of the diffractometer. Because the face normal is one of  $\langle hhh \rangle$ , and the field is applied on one of  $\langle hhh \rangle$ , the crystal is attached to the pin, by one face. From the reflections in the plane it is easy to determine that  $[h\bar{h}\bar{h}]$  and  $[\bar{h}hh]$  were vertical. Using trigonometry and vector analysis a host of angles and distances to these two plane faces can be determined, including the positions of their corners. The simplest way to determine the other faces proved to be to consider the orientations of the remaining faces on a regular octahedron, and compare this to the distorted shape of the crystal. The positions of the corner points and the normal vectors then give sufficient information to specify the face. As before the nuclear peaks in zero field were used to fix the scale parameter so that subsequently magnetic structures could be fitted by varying just the moment sizes.

### 5.5.1 Hysteresis Loop at 1.8 K

The actual measurement was a hysteresis loop but no hysteresis was observed so all the peaks for a given field have been grouped to improve statistics. The magnetic structure models discussed above have been fitted to the data. Because the number of degrees of freedom is so small the fits are all at the very limit of meaningfulness. Some general features of all of them are low  $R$ -factors and reduced moment size. Their different behavior will be outlined below. Somehow they must be distinguished.

The simplest model was the one with the single on-field spin becoming pinned by the field (model A). In this case the only way for the model to fit the higher intensities at higher fields is to keep increasing the size of the fitted moment. The fit at low fields up to and in the plateau phase is good. It can be seen that the error in the magnetic moment determination suddenly begins to increase greatly

as the plateau phase is left (see figure 5.21).

Model B, in which all four spins are constrained to be the same size, is also simple to fit. In this case the fit is always good, in both the plateau phase and the high field phase. The  $R$ -factor is lower than that in the single spin model throughout. This is unexpected since there is a clear crossover in the behavior of the system when the 422 peak actually decreases in intensity and so it seems unlikely that only one spin structure can be applied at all fields (see figure 5.21).

When the moment size of the two spin systems is allowed to vary separately (model C) two new problems appear. First in the plateau phase the two moment sizes become strongly and negatively correlated. Previously models with correlations were accepted when the nuclear intensities were being fitted for the extinction correction. Here the policy cannot be the same. The difference between the two situations is that in the description of the crystal structure the values of the parameters were deemed relatively unimportant, only an accurate calculation of the nuclear structure factors was required. If two parameters were correlated this was ultimately not a problem as their final values were fixed and accepted as the most useful description of the crystal structure which could simply be scaled for other data sets. In this case correlated parameters will distort the values being obtained. The second problem is one of constraint. There are two parameters and three peaks, yet the peaks can be calculated exactly for every field (provided that no noisy intensity was assigned to 110 by Racer). This gives  $R$ -factors of zero. This is similar to using a single peak to fit a single parameter, the answer is always right. It appears that the fit is under-constrained. Because of this model C must be rejected.

The final model (D) also fits well. The crossover from a single free spin to one fixed and three free spins was taken to be at 1.7 T. This is where the error on the moment size begins to increase rapidly for the single spin model (see figure 5.21).

The question of how to distinguish these models and therefore what is actually happening in the spin system has to be addressed. Simply accepting the lowest  $R$ -factors seems a poor criterion. All the models have  $R$ -factors which are acceptable in crystallographic terms. In this sense each is a valid representation of the magnetic structure. How then to proceed?

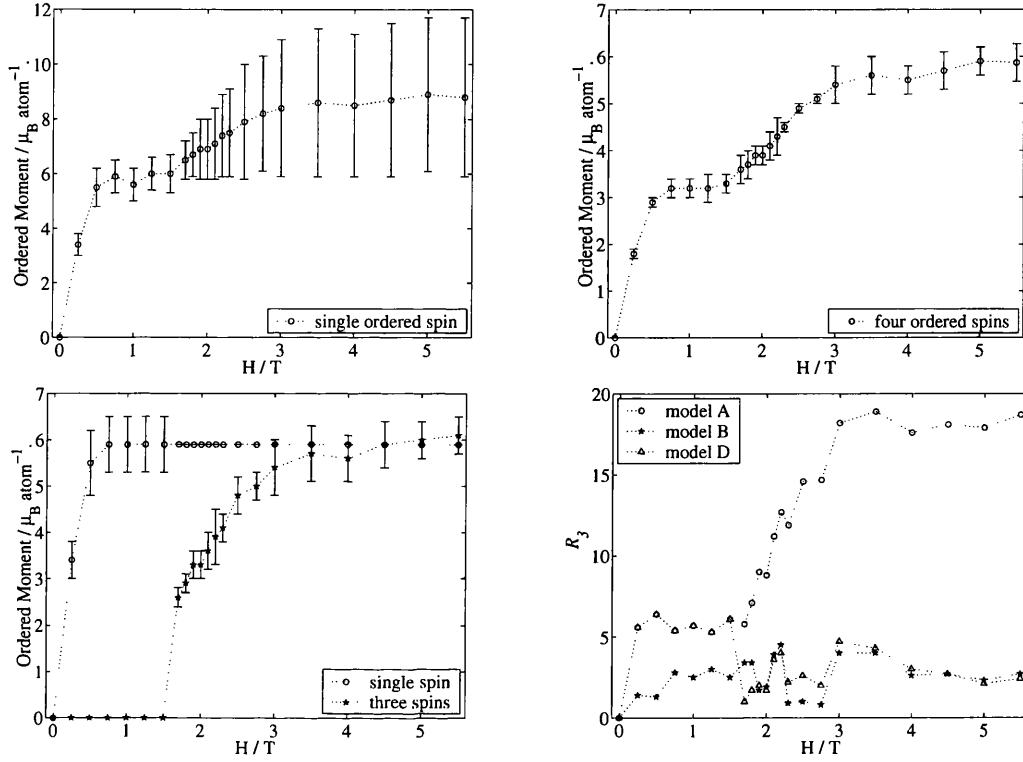


**Figure 5.21: Hysteresis loop,  $T = 1.8$  K, field applied on  $[h\bar{h}h]$ .** Development of sublattice magnetizations in different models fitted to the data. If a single spin (per tetrahedron) is used, the fit is good up to the plateau region, then the error becomes very large (model A, top left). If four spins constrained to be the same size are used the model fits well at all fields (model B, top right). If the single spin is used up to the plateau and then fixed, and the remaining three spins allowed to vary, two sublattice magnetizations are obtained, both with good fits (model D, bottom left). The  $R$ -factors of the three models are compared (bottom right). Model D is the same as model A up to the end of the plateau, after that it fits as well as model B. The fluctuations in the  $R$ -factor for models B and D above the plateau are almost entirely due to noise assigned to 110.

Previously in the situation of partial degeneracy removal with the field on  $[h\bar{h}0]$  it was possible to see diffuse features evolving simultaneously with Bragg scattering. This was interpreted as the coexistence of long and short range order. In this orientation the same effect is expected. The sample starts as a spin ice and should have distinctive diffuse scattering. Subsequently it is expected to become a kagomé ice and the disordered spins of the kagomé planes might be expected to give rise to some new pattern of diffuse scattering which would then disappear on the formation of the ordered structure (this diffuse scattering has been calculated by Moessner and Sondhi [111]). Examination of the form and evolution of any scattering in the absent peak positions is inconclusive. The scattering at 110 is suggestive of such an effect but the counting statistics are poor (the counting time in this experiment was one quarter of that being used in the  $[h\bar{h}0]$  experiment). The background intensity at 110 is shown in figure 5.22 for the high temperature loop, with the field rising and falling points combined and averaged. It does appear that initial spin ice diffuse scattering decreases in two stages, with field values appropriate for the plateau. With better statistics this could provide a way to reject the fully ordered spin model (B) on the grounds that it cannot represent a sample with long and short range order.

The main criterion for rejecting the fully ordered model (B) seems to be the fact that it cannot be true. In crystallography it is usual to invoke “soft constraints,” to include knowledge about the problem from other sources to guide the structure determination. In this case the existing data about the kagomé ice phase cannot be ignored [78, 79]. Already it is known that a partially disordered phase is formed in the plateau region. Our data confirms this interpretation by showing that the Bragg scattering can indeed be fitted using a single ordered spin on each tetrahedron with the remaining three disordered (model A). Subsequently the model in which the single ordered spin is pinned and the other three spins are varied (model D) can be seen to fit as well as the four spin model (model B). The description of the magnetization curve in terms of the pinning of a single spin, followed by the breaking of the ice rule and the magnetization of the remaining spins seems to be the most acceptable solution. Again the moment sizes are much reduced and again this can only be explained by a deficiency in the extinction corrections.

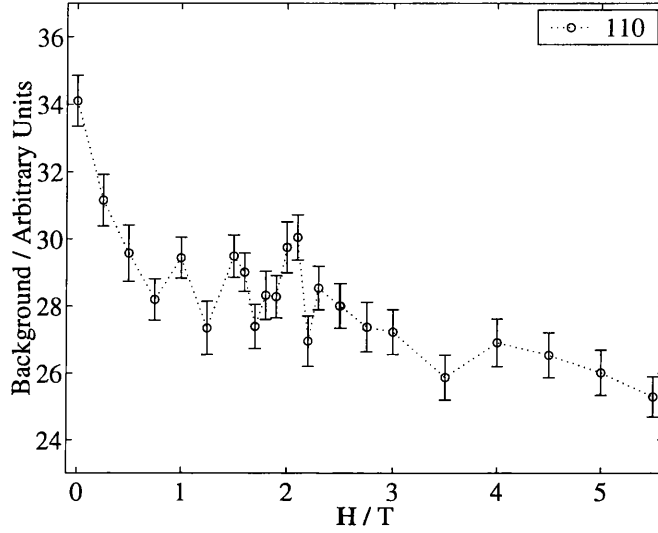


**Figure 5.22:** Field dependence of the background at the 110 position with field applied on  $[h\bar{h}h]$ .

### 5.5.2 Hysteresis Loop at 0.05 K

The same series of measurements were made at 0.05 K. At this temperature the field dependence of the peaks is similar but a strong hysteresis is observed. The integrated intensities are shown in figure 5.23. Again 002 and 240 were absent and no field dependent diffuse features could be discerned on either the rising or falling field scans.

Models A,B and D were fitted to the data. The field dependence of the ordered moments is shown in figure 5.24. Again the single spin model fits well up to and in the plateau phase. At higher fields the error on the moment size, and the  $R$ -factor both become unacceptably large. Not only is the beginning and end of the plateau hysteretic, but also the ordered moment within it. This represents a problem in the context of model D which is discussed below. Very surprisingly, the ordered moment is lower on the falling field scan. Given that the dynamics are so effectively frozen at this temperature, and that the field reaches 5.5 T it might be expected that if the on-field spins were not saturated in the plateau phase, this would be seen on the rising field scan.

Model B shows the same reduced moment in the plateau phase for the field

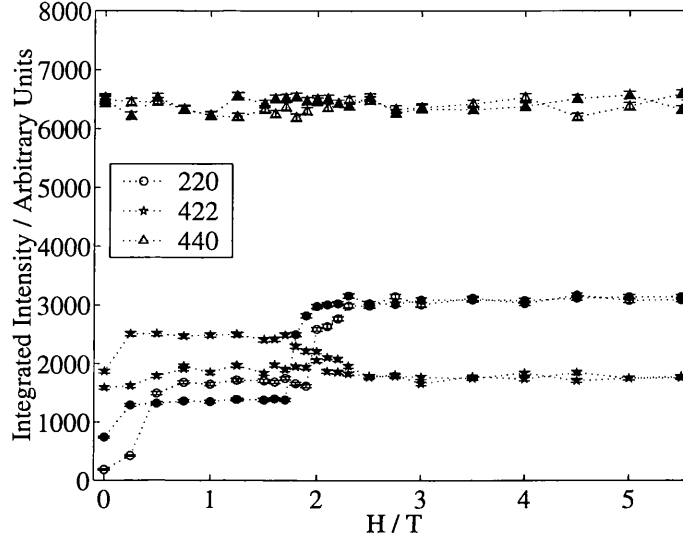


**Figure 5.23:** The field dependence of Bragg peaks with field on  $[1\bar{1}\bar{1}]$  at 0.05 K. The 002, 110, and 240 peaks were also measured and all maintained zero intensity throughout. Open symbols are for rising fields.

falling scan, compared to the rising field scan. Unlike 1.8 K, the  $R$ -factor does actually rise above that of model A. The  $R$ -factors have been plotted against point number rather than field to disentangle the rising and falling fields (see figure 5.24). Points 1-22 are the field rising points and 23-44 the field falling points. Model D is the same as model A up to the end of the plateau phase. Then it has similar  $R$ -factors to model B. However, in the plateau phase of the falling field scan model A, and therefore also D, become considerably better fits than model B. The error on the size of the moment in model B is also increased in this plateau region, compared to the rest of the loop.

Model D requires a value for the fixed moment. At 1.8 K this is simple as the moment size in the plateau is not hysteretic. At 0.05 K the question arises as to what value to use. The fits shown in figure 5.24 were obtained by using the rising field plateau moment for the rising field data points ( $5.6 \mu_B \text{ atom}^{-1}$ ), and the falling field plateau moment for the falling field data points ( $5.3 \mu_B \text{ atom}^{-1}$ ). This does not have any actual effect on the moment size of the kagomé spins, which is the same in the high field saturated phase on field rising and falling legs of the

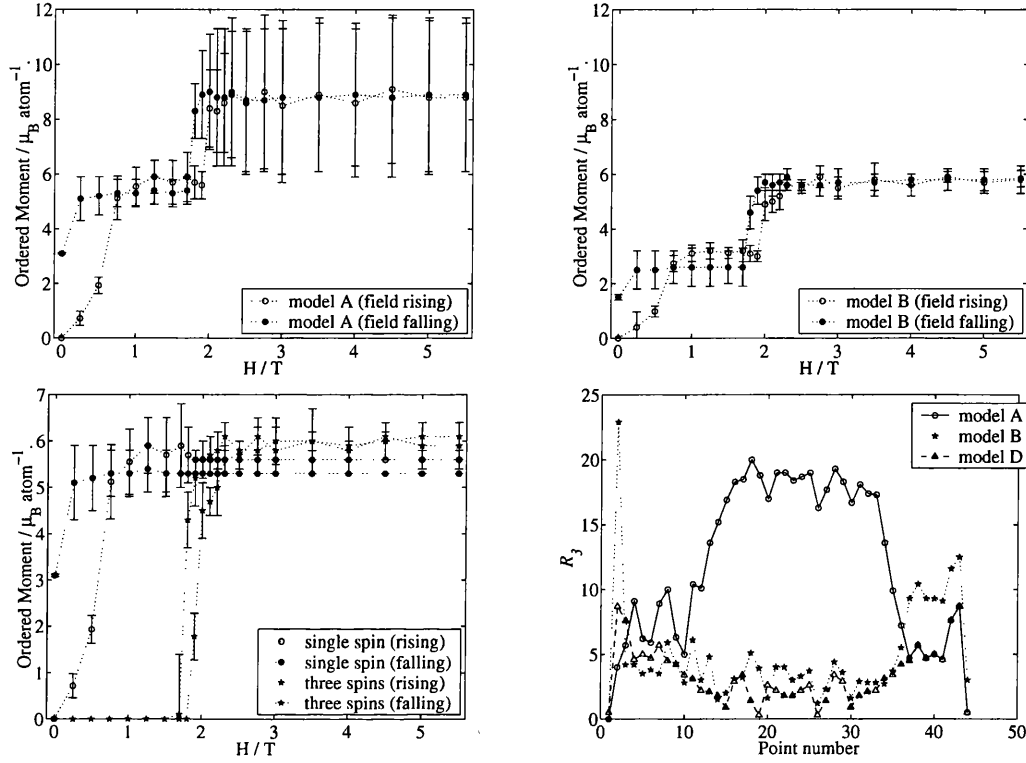


**Figure 5.24: Hysteresis loop,  $T = 0.05$  K, field applied on  $[h\bar{h}\bar{h}]$ .** Development of sublattice magnetizations in different models fitted to the data. If a single spin (per tetrahedron) is used the fit is good up to the plateau region, then the error becomes very large (model A, top left). If four spins constrained to be the same size are used the model fits well at all fields (model B, top right). If the single spin is used up to the plateau and then fixed, and the remaining three spins allowed to vary two sublattice magnetizations are obtained, both with good fits (model D, bottom left). The  $R$ -factors of the three models are compared (bottom right). Rather than plotting against field these have been plotted against point number, the rising field sweep ends at point 22, and the field is then falling. Model D is the same as model A up to the end of the plateau, after that it fits as well as model B. The fluctuations in the  $R$ -factor for models B and D above the plateau are almost entirely due to noise assigned to 110.

loop.

Again the data is consistent with the pinning of the on-field spins with persistent disorder in the kagomé spins, until the field is strong enough to break the ice rules. At this lower temperature the transition from partial order to full order has become hysteretic. This may be taken to indicate that it is first order. This is in agreement with the latest findings of Matsuhira *et al.* who also found that the ice-rule breaking transition became first order at a critical temperature  $T_c = 0.36 \pm 0.02$  K [112].

### 5.5.3 Summary of $[h\bar{h}\bar{h}]$ Experiment

This section of the work was not strikingly successful. It seems to involve a condensation of spurions into the same dataset. Two expected peaks are absent, another shows no change, and then another absence is treated as such, but what a priori reason is there for this, when two other absences are treated as spurious? If the background is examined at 240 and 002 an intensity loss almost as strong as that at 110 is found for 002 (240 is constant). This is a disconcerting surprise. Within a  $\sqrt{I}$  error appropriate for counting statistics no significant change occurs at any of these positions, as compared to earlier examples of this treatment of diffuse scattering where very real changes in intensity are observed. Nonetheless, the pattern of intensity change at 110 and 002 appears systematic (the errors in figure 5.22 come from the fit, not the counts). Improved statistics are required to show what actually happens. Diffuse scattering is expected at 110 so the question is what happens at 002, and whether this is also spurious. The only way to interpret this data which agrees with the bulk measurements (performed now by four groups, and agreeing in three cases [65, 77, 76, 78, 79]) is to assume that the behavior of 002, 440 and 240 is indeed spurious, and to say that what remains is consistent with the bulk measurements.

## 5.6 Field Applied on $[hh2h]$

Recently there has been no interest in the application of a magnetic field on the  $[hh2h]$  direction. A brief investigation into this mysteriously neglected direction



was made when the search for a postulated incommensurate structure foundered. This direction bisects one face of the tetrahedron, again it is a situation in which different spins must experience different field environments. The groundstate of a single tetrahedron in a strong field will have three spins pinned by the field, either one in and two out, or two in and one out. The fourth spin is perpendicular to the field. The ice rule will dictate the orientation of this spin when the coupling is effective.

Again a very small number of peaks were measured.  $11\bar{1}$  and  $22\bar{2}$ , which were nearly transverse to the applied field,  $111$ , which was close to the applied field, and  $224$  which is parallel to the applied field. Because of the restricted geometry of the horizontal field magnet, the incident beam for  $111$  is in one of the dark angles. It is close to the edge of the window however, and the incident beam is sufficiently strong to observe the field dependence of this reflection, though its absolute integrated intensity is attenuated. Because no dilution refrigerator was available during this experiment the minimum temperature was 1.9 K. These measurements therefore probe the onset of the ice rule regime.

Some measurements were made as a function of field and some as a function of temperature. If the field and temperature dependence of the  $11\bar{1}$  and  $224$  are compared (figure 5.25), it can be seen that there is a definite crossover in behavior. This is evident in the behavior of  $224$ . This is expected to be due to the fourth spin. At high temperatures the coupling is overwhelmed by thermal fluctuations. The application of the field magnetizes the three spins but, without strong coupling, the fourth spin remains disordered. At low temperatures as the three spins are pinned into the ordered structure, the coupling draws in the fourth spin as well. The crossover in behavior of the  $224$  peak is due to the change from an uncoupled to a coupled regime, and consequent change in behavior of one sub-lattice.

Previously with the field applied on  $[h\bar{h}h]$  several spin structures and field dependencies could be envisaged. The situation and aim here is the same. Somehow the field dependence of the Bragg peaks must be explained and interpreted using model spin structures which can be fitted to the observed intensities. Three more models are introduced, different to those of the previous section. They will be numbered sequentially and are illustrated in table 5.3, at the end of the chapter.

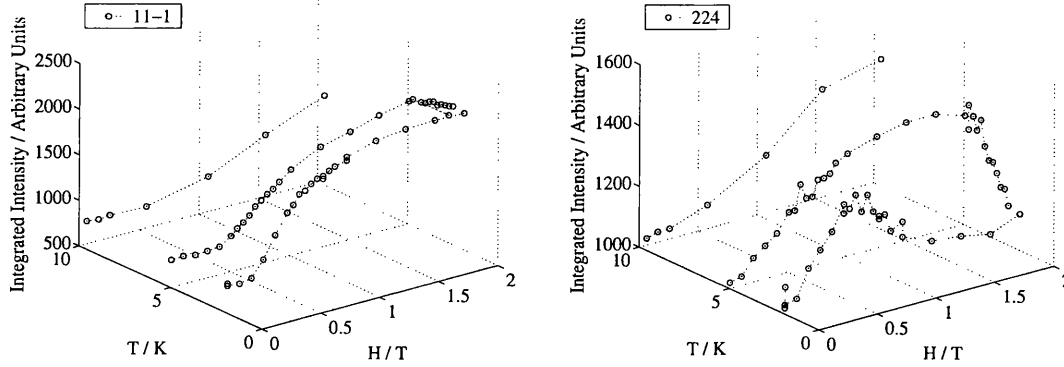


**Figure 5.25: Horizontal field applied on  $[hh2h]$ .** Comparison of intensities of  $11\bar{1}$  (left) and  $224$  (right) as function of field and temperature. Clearly a crossover in ordering behavior occurs between 1.9 and 5 K. This is shown predominantly by the  $224$  peak.

Model E has three moments, constrained to be the same size, these are the three spins on which the field is effective. They are oriented with one in and two out. Model F has four moments, all the same size, the three on which the field is effective are oriented as in model E. The fourth points in to complete the ice rules groundstate of the tetrahedron. Model G has separate moment sizes for the three pinned spins and the fourth free spin.

Fitting of the structures was again carried out using the CCSL program MAGLSQ. The particular problem in these fits, apart from the small number of peaks, was the attenuation of  $111$ . This was easily solved by the use of a second scale factor for this peak. Extinction corrections were applied as with the other data sets, and scale parameters redefined for each temperature using zero field nuclear Bragg peaks.

The experiment consisted of detailed field scans at temperatures of 1.9, 3.6 and 5 K (0-2 T), two limited field scans at 2.7 (0-1 T, few points) and 10 K (0-2 T, few points), and a temperature scan at 2 T (1.9-10 K). The three models described above can all be fitted to all the points with varying goodness of fit. The results of this fitting procedure are presented in figures 5.26-5.31. Subsequently the different models will be discussed again.

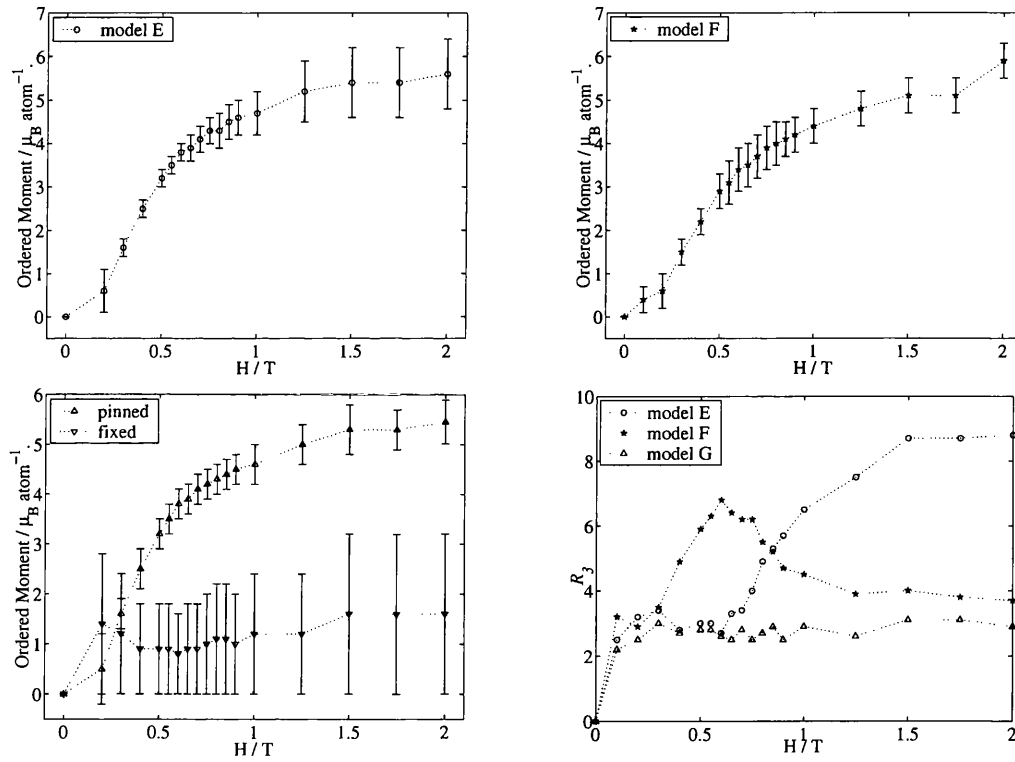


**Figure 5.26:** Horizontal field applied on  $[hh2h]$ ,  $T = 1.9 \text{ K}$ , field applied on  $[hh2h]$ . Development of sublattice magnetization in different models fitted to the data (E, top left, F, top right, G, bottom left).

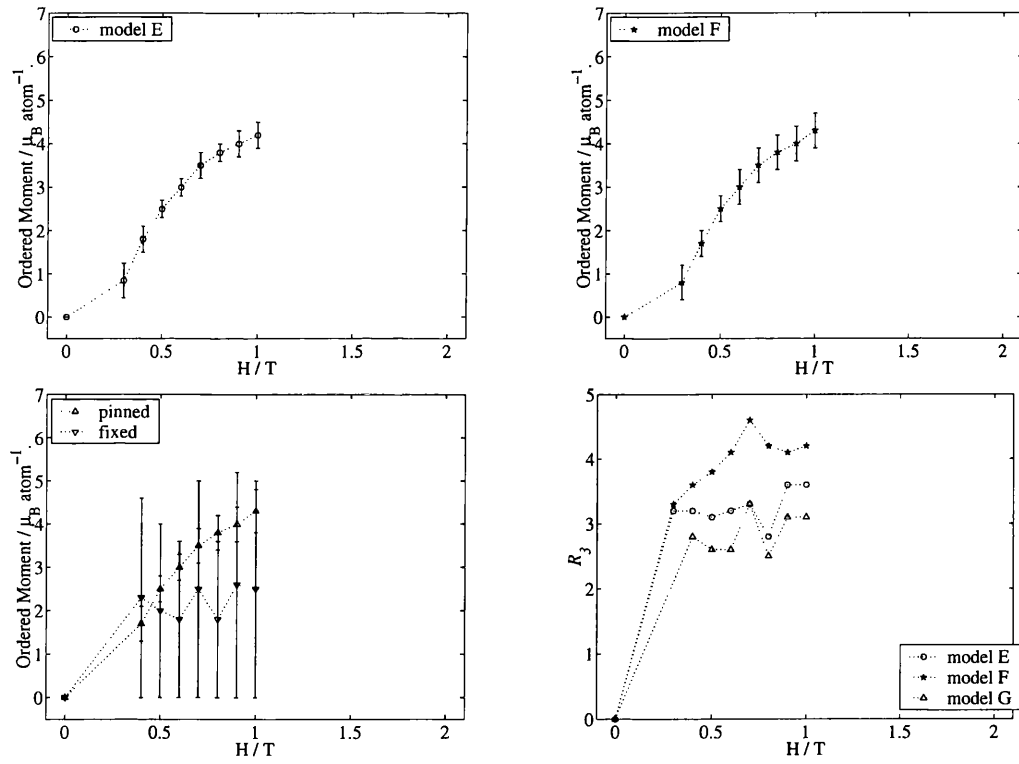


**Figure 5.27: Horizontal field applied on  $[hh2h]$ ,  $T = 2.7$  K.** Development of sublattice magnetization in different models fitted to the data (E, top left, F, top right, G, bottom left).

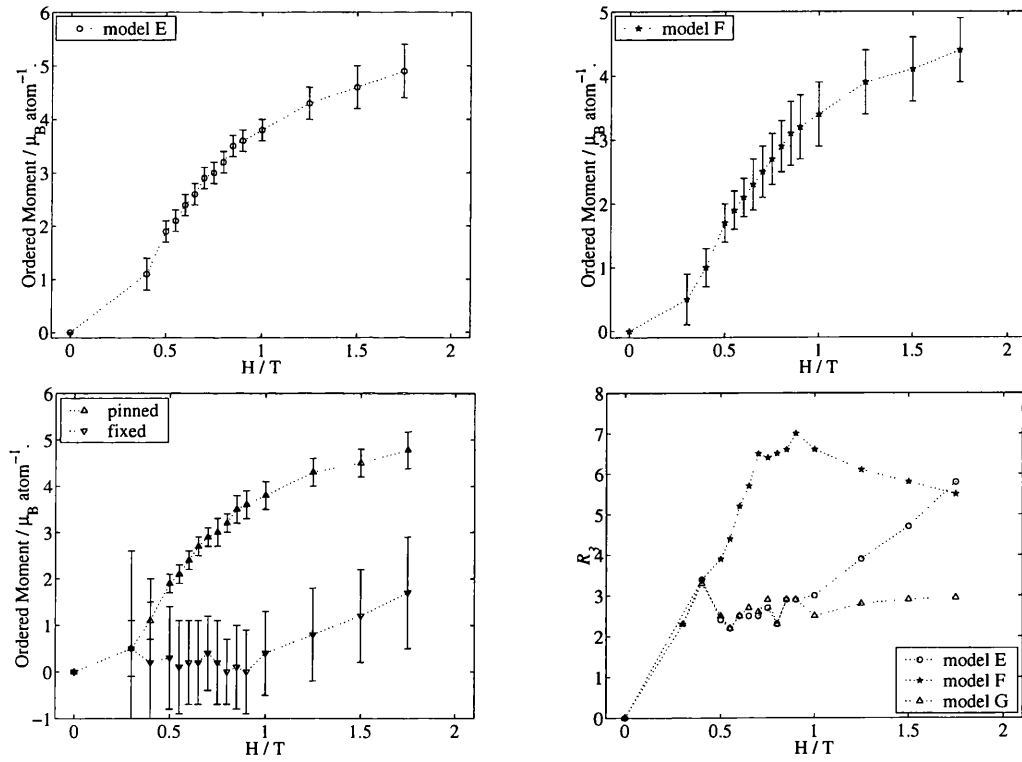


**Figure 5.28:** Horizontal field applied on  $[hh2h]$ ,  $T = 3.6$  K. Development of sublattice magnetization in different models fitted to the data (E, top left, F, top right, G, bottom left).

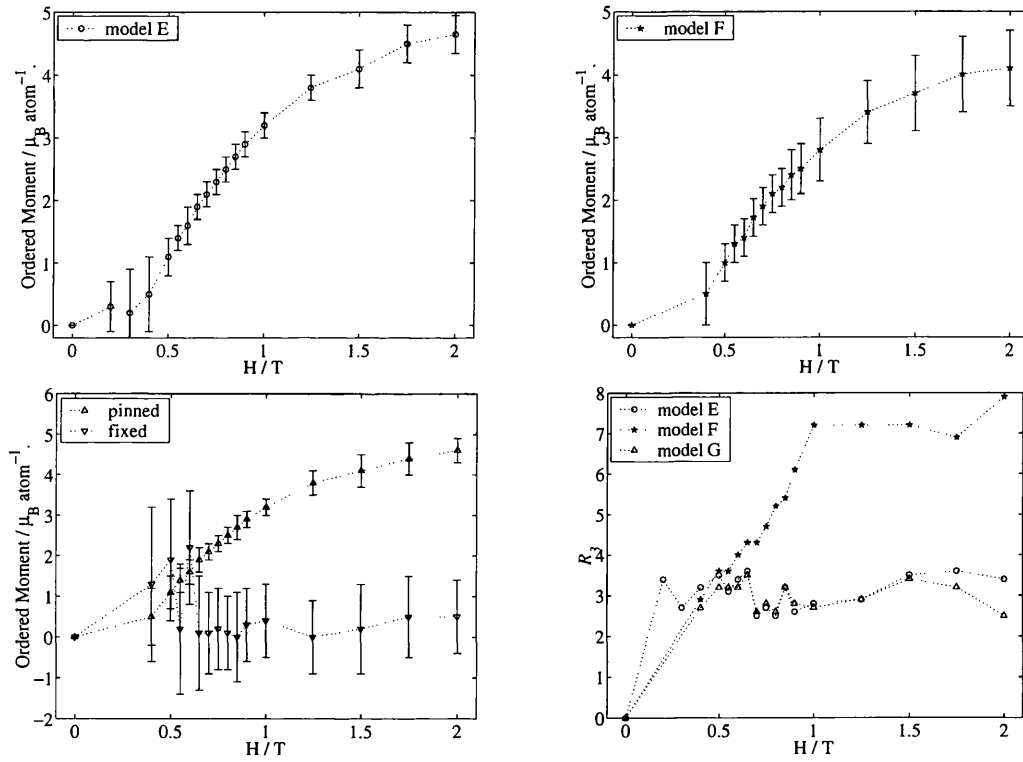


**Figure 5.29:** Horizontal field applied on  $[hh2h]$ ,  $T = 5.0$  K. Development of sublattice magnetization in different models fitted to the data (E, top left, F, top right, G, bottom left).

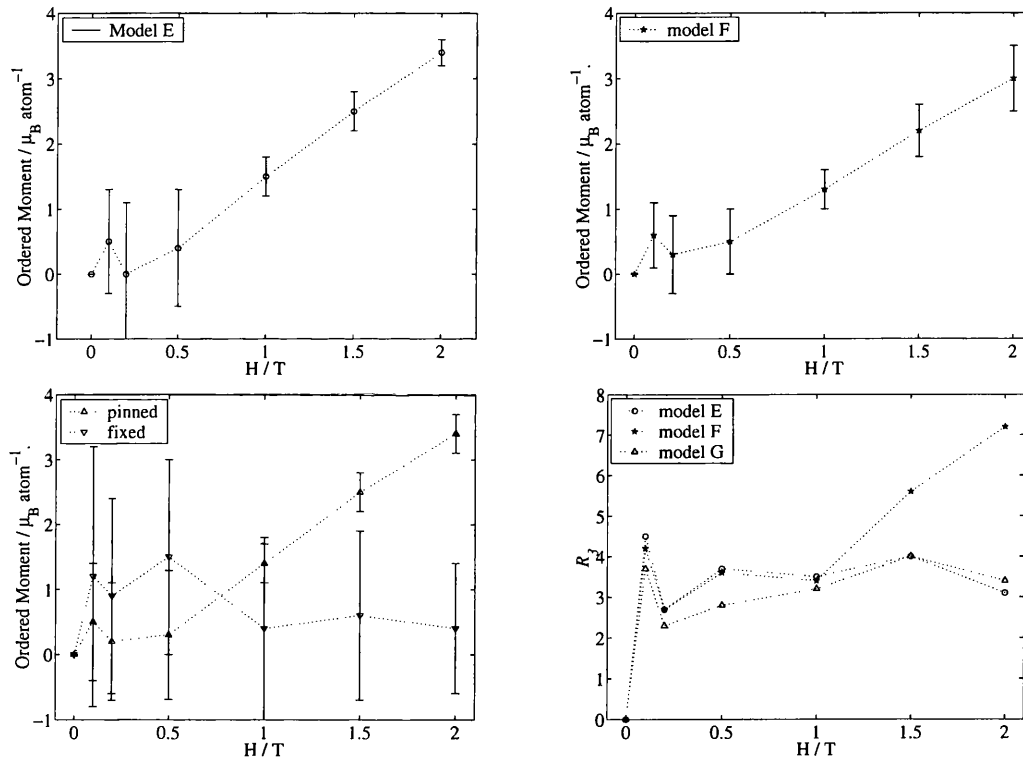


**Figure 5.30:** Horizontal field applied on  $[hh2h]$ ,  $T = 10.0$  K. Development of sublattice magnetization in different models fitted to the data (E, top left, F, top right, G, bottom left).

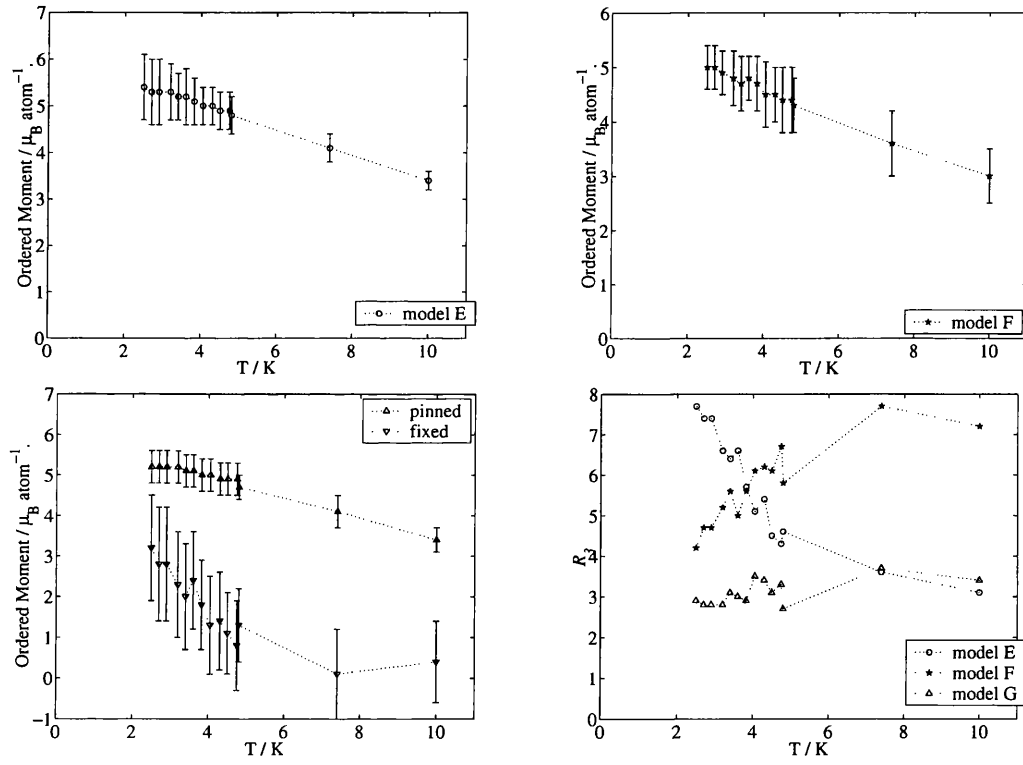


Figure 5.31: Temperature scan,  $H = 2.0$  T, horizontal field applied on  $[hh2h]$ . Development of sublattice magnetization in different models fitted to the data (E, top left, F, top right, G, bottom left).



Again there are some general features of the fits. The maximum observed moment is strongly reduced from  $10.6$  to  $5.5 \pm 0.4 \mu_B \text{ atom}^{-1}$ . Large errors are often found for the fitted parameters, particularly for the free spin in model G.  $R_3$  is almost always low enough to be acceptable in a conventional crystallographic sense. For some points particularly large errors were observed, and these points have been excluded. They were all for low fields ( $0.1 - 0.3 \text{ T}$ ) where the magnetic intensity is small. Although the  $R$ -factors are acceptable the large errors in moment size makes concrete interpretation of the situation difficult. A particular example of this problem is seen in figure 5.26. The fit using model G shows an unexpected peak in the size of the free moment at low fields, where none is expected from the physical formulation of the model. Subsequently the moment grows, but the error bar is so large that any imaginable field dependence could be fitted to these points with very low residuals. One other feature common to all points is that the four spin model (F) always calculates zero magnetic intensity for 224. Magnetic intensity does clearly appear on this peak position, and at low temperatures (e.g.  $1.9 \text{ K}$ ) it then disappears. Each field/temperature scan will be discussed individually.

### 5.6.1 Field Scan at $1.9 \text{ K}$

At this temperature the Bragg peaks show two field dependencies. The Bragg reflections  $22\bar{2}$ ,  $11\bar{1}$  and  $111$  grow smoothly with field.  $224$  grows in low fields, and then falls in higher fields (see figure 5.25). The three spin model (E) fits well in low field, but in higher field (above the peak in  $224$ ) the  $R$ -factor suddenly grows (see figure 5.26). The four spin model (F) fits well in very low field when the magnetic intensity is small. It also fits well in high field when the  $224$  intensity has peaked and fallen close to its original level. When there is significant intensity on  $224$  the fit is poor. This gives the field dependence of the  $R$ -factor a similar appearance to the field dependence of the  $224$  peak intensity. As noted previously, the structure factor of  $224$  for this model is zero. Consequently when the magnetic intensity at this position becomes large this model does not fit well. Model G, which has a variable moment size for both the three on-field spins, and the single free spin shows a very similar field dependence for the size of the on-field spins to the other models. The presence of the variable free spin means that it can fit with a lower

$R$ -factor than model E at high fields or model F at low fields.

The peak in the  $R$ -factor for model F (four spins) and the improved fit of model G (three spins + one free spin), compared to model E (three spins), both suggest that the fourth spin is drawn into the ordered structure at this temperature. Unfortunately the huge error on the moment size of that spin in model G means it is impossible to quantify directly how and when this occurs.

### 5.6.2 Field Scan at 2.7 K

This was the final section of the experiment, recorded with time pressing. The intention was to collect one more field scan in the crossover region. Because of this the 111 peak was sacrificed. It was chosen because the attenuation by the cryostat was felt to render it less reliable than the unaffected peaks. In fact the 111 peak adds particular leverage to the fitting. The errors on the free spin in model G have become so large in this data that it is practically useless. The field dependencies of the model E and F  $R$ -factors are not sufficiently developed to see if there seems to be a crossover at this temperature (see figure 5.27).

### 5.6.3 Field Scan at 3.6 K

The 224 peak again shows a maximum in its field dependence, but it does not fall as low as it did at 1.9 K. Consequently model F (four spins/zero 224 structure factor) does not have such a pronounced maximum in the  $R$ -factor (see figure 5.28) as at 1.9 K. The quality of the fits to model G is higher, the errors are smaller and a definite field dependence of the free spin can be seen. Its size apparently refines to zero in low fields. Then in higher fields when the fit to model F improves and model E deteriorates, the ordered moment on the free spin begins to grow.

### 5.6.4 Field Scan at 5 K

Figure 5.25 shows that when the temperature has reached 5 K the regime has definitely changed (see figure 5.29). There is no longer a maximum in the field dependence of 224. Model F becomes a progressively poorer fit as the field rises, and the 224 peak is ever increasing. Conversely, model E does not suffer this

deterioration in goodness of fit. Model G shows zero refined moment on the free spin, except at very low fields where a peak appears, as at 1.9 K. When the moment of the free spin is zero, model G is identical to model E. This clearly indicates that the ordering of the fourth/free spin does depend on whether the sample is in the ice rules regime or not. Here it is not, and no ordered moment can reasonably be assigned to this sub-lattice.

### 5.6.5 Field Scan at 10 K

Identical conclusions can be drawn from this scan as from the field scan at 5 K. The magnetization curves have straightened considerably as  $\text{Ho}_2\text{Ti}_2\text{O}_7$  is essentially a paramagnet at this temperature (see figure 5.30).

### 5.6.6 Temperature Scan at 2 T

This represents an alternative way to investigate the same phenomenon (see figure 5.31). Again it can be seen that as the sample was cooled into the ice rules regime the three spin model (E) becomes much less suited and the four spin model (F) improves, i.e. the ordered moment on the free spin is increasing and the system is crossing over from partial order, as described by the three spin model, to full order, as described by the four spin model. This can be seen in the fitting of model G where the free spin moment size refines to zero at high temperature and then grows at lower temperature. Temperature scans were not employed further in this experiment as stability was rather poor and so field scans were faster.

### 5.6.7 Summary of $[hh2h]$ Experiment

Different patterns of field dependence in the Bragg peaks have been highlighted. This has been interpreted in terms of a crossover from an uncoupled regime, to a coupled ice rules regime. Although the data is limited, it has been shown that the associated model spin structures are consistent with this picture. However, this has been achieved by qualitative arguments based on changes in  $R$ -factor. The theory of linear hypothesis tests has been applied to crystallographic problems by Hamilton [113]. This provides a way to test the significance of  $R$ -factors, or

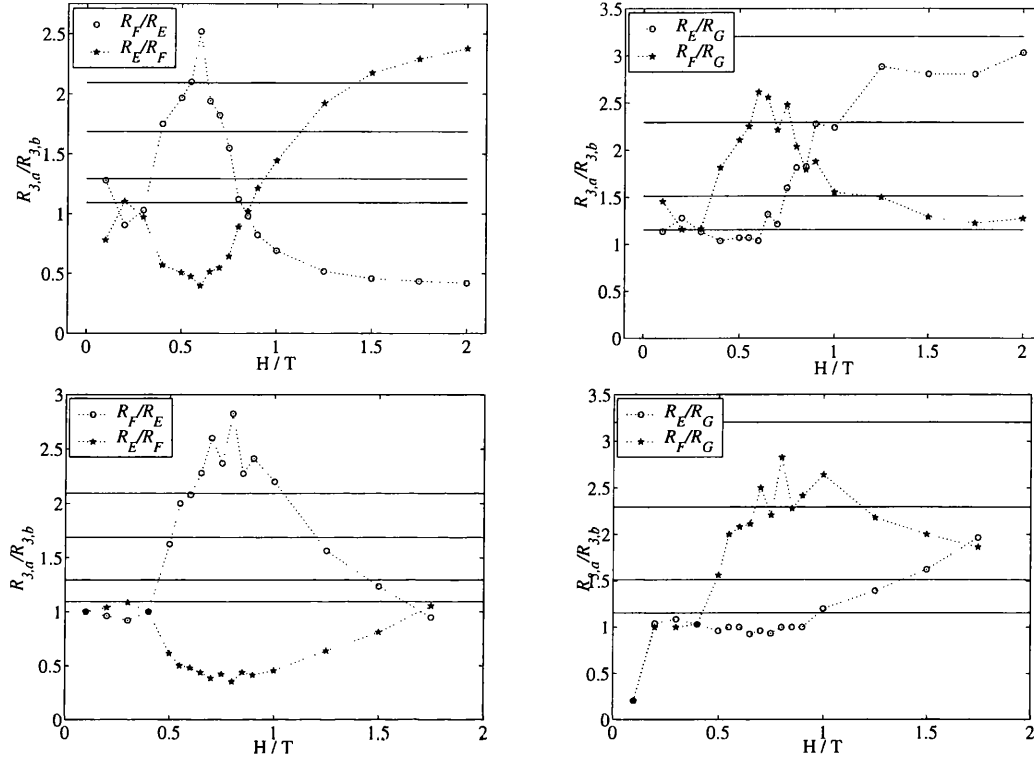


**Figure 5.32: Field Scans,  $T = 1.9$  K and  $T = 3.6$  K, horizontal field applied on  $[hh2h]$ .** Significance testing of  $R$ -factor ratios. The ratios are of  $R_3$  for models E and F (top left at 1.9 K, bottom left at 3.6 K), and models E and G and F and G (top right at 1.9 K, bottom right at 3.6 K). Significance thresholds for 50, 25, 10 and 5% confidence levels are shown as ascending flat lines.

more correctly, whether an improved  $R$ -factor results from a significantly improved model, as compared to the original model.

The significance test employs a ratio of  $R$ -factors. The ratio is compared to tables of significance levels which depend upon the number of parameters and observations. The ratio must exceed the relevant significance level if one model is to be regarded as more significant. The smaller  $R$ -factor is the divisor and if the threshold is exceeded by the ratio then the model with the smaller  $R$ -factor is the more significant. Significance testing of this type was used to try to clarify the acceptability of the models, and the crossover scenario. It has been applied to the field scans at 1.9, 3.6, and 5.0 K, and the temperature scan at 2.0 T.

The results of the significance testing are disappointingly non-definitive. Ideally

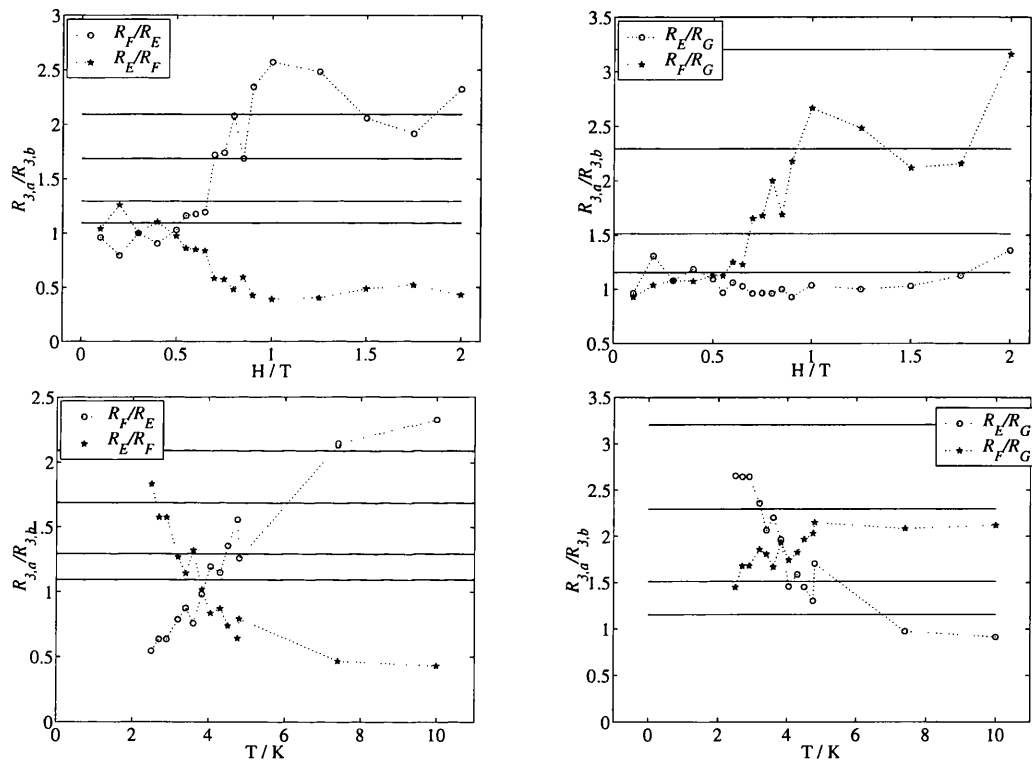


**Figure 5.33:** Field ( $T = 5$  K) and temperature ( $H = 2$  T) scans, horizontal field applied on  $[hh2h]$ . Significance testing of  $R$ -factor ratios. The ratios are of  $R_3$  for models E and F (top left at 5 K, bottom left at 2 T) and E and G and F and G (top right at 5 K, bottom right at 2 T). Significance thresholds for 50, 25, 10 and 5% confidence levels are shown as ascending flat lines.

one of two answers is obtained. Either the hypothesis cannot be accepted at the 50 % level, or it can be accepted with a high level of confidence. In the first instance this means that neither model is more satisfactory, or that they are indistinguishable. In the second situation the new model is an improvement on the old, and this can be stated to the appropriate confidence. With this data, the highest confidence was 5 %, accepting a model at this level of confidence implies that in 95 % of the times it is chosen, it will be correct. When examining these figures it must be noted that in some cases the ratio falls below 1.0. This happens when comparing model E and F for example. Both  $R$  factor ratios have been computed and plotted and where one falls below 1.0 the other must be examined. The thresholds are higher for the comparison with model G as it has two variable moment sizes and so fewer degrees of freedom.

A clear crossover in model significance can be seen in figure 5.32. For the field scan at 1.9 K model E (three spins) can be accepted with much greater confidence (i.e. at the 5 or 10% levels) than model F (four spins) for fields of 0.4-0.7 T and vice versa for fields of 1.25-2 T. Model G offers some improvement over both where they are expected to fail, but only at the 10 % level and for few points. Between 0.7 and 1.25 T the three spins become sufficiently strongly pinned to draw the fourth spin into the ordered structure

At 3.6 K model E is superior to model F at fields of 0.6-1.0 T. The expected crossover in model applicability at higher fields does not occur. Although the  $R$ -factor ratios are crossing, high levels of confidence for rejection or indistinguishability are not reached. Again model G does not offer highly significant improvements and in fact cannot be distinguished from model E below 1 T.

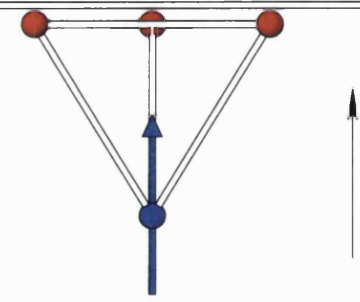
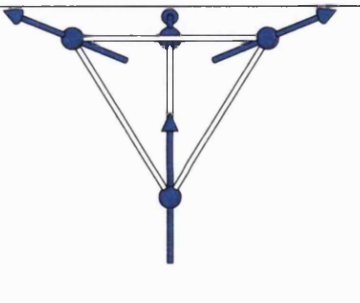
At 5 K models E and F are indistinguishable at low field (up to 0.6 T, figure 5.33). Then model F becomes significantly worse and model E can be accepted with 5 or 10% confidence levels. Model G does offer improvement over model F, but not at high levels of significance, it is indistinguishable from model E. The acceptance of model E over model F shows that the fourth spin remains disordered at this temperature.

Although the fitted points from the temperature scan look to provide a clearer support for the crossover hypothesis, in fact little can be drawn from them with

confidence. It can be seen however that model E is definitely superior to model F at high temperature and the converse is true at low temperature (at 1.9 K and 2 T model F can be accepted over model E at 5% confidence).

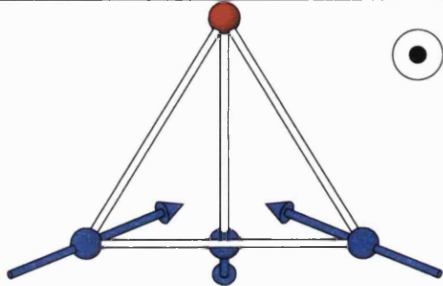
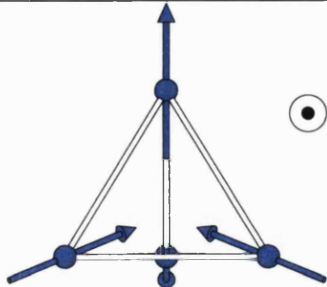
To summarize, the confidence testing supports the crossover hypothesis. Within the parameter space investigated there are transitions to or from the ice rules regime as a function of either field or temperature. The most successful model changes from one in which the free spin is disordered, presumably by thermal fluctuations, to one in which it is coupled to the other spins and orders in an ice rules groundstate.

This part of the experiment takes place in a different dynamical regime to the experiments with the field on  $[00l]$  or  $[h\bar{h}0]$ . In those, the very low temperatures ensured that the field regulated the dynamics. Here the dynamics are faster and so the free spin can fluctuate even when there is an applied field. At 5 K the fluctuations are strong enough to overcome the spin-spin interactions at all fields. The magnet is being magnetized as a paramagnet. In contrast at 1.9 K the interactions become important. When a field of sufficient strength is applied to stop the on-field moments fluctuating very strongly, the free moment is also unable to fluctuate strongly and is drawn into the ordered structure.

Model	Field Direction	Description	
A	$[h\bar{h}\bar{h}]$	Single moment to be fitted which lies on the axis parallel to the field. Expected to apply to the low field and plateau regions of a field scan.	
B	$[h\bar{h}\bar{h}]$	All four moments on the tetrahedron are fitted, they are constrained to be the same size. Expected to apply above the plateau region of a field scan.	



Model	Field Direction	Description	
C	$[h\bar{h}\bar{h}]$	Two moment sizes fitted, one for the spin on the field axis, and one for the other three spins which are constrained the same size. This model should fit the entire field scan and the variable spin sizes should cross over between models one and two.	
D	$[h\bar{h}\bar{h}]$	The spin on the field axis is used to fit the low field data (with zero moments on the other spins) and then its moment size is fixed, and the other three spins are used to fit the high field data.	

Model	Field Direction	Description	
E	$[hh2h]$	Three spins pinned by the field are used to fit the data. Expected to be applicable at low fields and/or high temperatures.	
F	$[hh2h]$	Four spins forming an ice rules tetrahedron are used to fit the data. Expected to be applicable at high fields and/or low temperatures.	

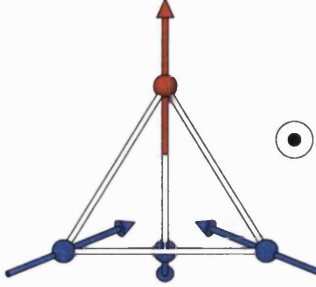
Model	Field Direction	Description	
G	$[hh2h]$	Two moment sizes are fitted, one for the three pinned spins and one for the free spin. Expected to follow the crossover from model E to F.	

Table 5.3: Spin structure models used in fitting data from  $[h\bar{h}\bar{h}]$  and  $[hh2h]$  experiments. The field is vertical in the  $[h\bar{h}\bar{h}]$  models, and perpendicular to the plane of the page for the  $[hh2h]$  models, as shown by the arrows or arrow projections.

## Chapter 6

# The Field Induced Phases of Dysprosium Titanate

In this chapter the details of three neutron scattering experiments on  $\text{Dy}_2\text{Ti}_2\text{O}_7$  are presented, followed by the analysis of the data. All the experiments on  $\text{Dy}_2\text{Ti}_2\text{O}_7$  discussed below were carried out on the PRISMA instrument at ISIS. The very different mode of operation of this instrument to D10 means that the information available from the results in this chapter often contrasts quite strongly with the type of information presented in the previous chapter.

### 6.1 Experimental Details

PRISMA is a unique instrument designed to provide the  $(Q, \omega)$ -space access of a triple axis spectrometer at a pulsed source. This is achieved using a movable bank of detectors with individual analyzers, and a white beam. However, in these experiments, PRISMA was configured with no analyzers, in which case it becomes a “time-sorted Laue diffractometer”. The available tilts on the goniometer are very limited so all measurements are constrained to the two axes situation. Typically these measurements are made by choosing a detector angle which will optimize flux in the  $Q$  range of interest without incurring a severe air scattering background, and then the crystal is rotated.

Natural Dysprosium contains several isotopes, several are quite strongly neu-

tron absorbing. This can make the detection of weaker effects like diffuse scattering difficult or impossible. To reduce this an isotopically enriched sample was used. The natural abundances and scattering lengths/cross sections for Dysprosium are given in table 6.1. The composition of the  $\text{Dy}_2\text{O}_3$  used for the growth of the crystal and the modified values of the scattering lengths/cross sections are also given. The isotopic  $\text{Dy}_2\text{O}_3$  was produced by Goss Scientific Instruments Ltd. The enrichment pattern was chosen to satisfy cost and efficiency. The least absorbing isotopes are the extremely rare light ones such as  $^{156}\text{Dy}$ . A crystal grown using these would be outrageously expensive. Therefore one of the moderately absorbing heavier isotopes was chosen. Although  $^{163}\text{Dy}$  has a slightly lower absorption cross section than  $^{162}\text{Dy}$ , the dominant impurity would have been the strongly absorbing  $^{164}\text{Dy}$  had  $^{163}\text{Dy}$  been chosen. The absorption cross section  $\sigma_a$  is reduced by a factor of 4.8, but since absorption typically attenuates scattered intensity by a factor of the form  $\exp(-\sigma_a x)$  (with the absorption cross section  $\sigma_a \propto \lambda$  and  $x$  the sample thickness) this makes a significant difference at long wavelengths. The cost of the crystal was the same as the nominal cost of a day of beam time at ISIS at that time. More than one day of data collection is saved by the expenditure!

Isotope	Natural Abundance (%)	Sample Content (%)	$b_{coh}$ (Fm)	$b_{inc}$ (Fm)	$\sigma_{coh}$ (barn)	$\sigma_{inc}$ (barn)	$\sigma_s$ (barn)	$\sigma_a$ (barn)
Dy	—	—	$16.9 - 0.276i$	—	35.9	54.4(1.2)	90.3	994.(13.)
$^{156}\text{Dy}$	0.06	< 0.01	6.1	0	4.7	0	4.7	33.(3.)
$^{158}\text{Dy}$	0.1	< 0.01	6.(4.)	0	5.(6.)	0	5.(6.)	43.(6.)
$^{160}\text{Dy}$	2.34	0.02	6.7	0	5.6	0	5.6	56.(5.)
$^{161}\text{Dy}$	19	0.47	10.3	(+/-)4.9	13.3	3.(1.)	16.(1.)	600.(25.)
$^{162}\text{Dy}$	25.5	96.8	-1.4	0	0.25	0	0.25	194.(10.)
$^{163}\text{Dy}$	24.9	2.21	5.0	1.3	3.1	0.21	3.3	124.(7.)
$^{164}\text{Dy}$	28.1	0.5	$49.4 - 0.79i$	0	307.(3.)	0	307.(3.)	2840.(40.)
sample	—	—	$-0.95 - 0.004i$	0.05	1.91	0.019	1.93	207.6

**Table 6.1:** Isotopic abundances and scattering lengths of natural Dysprosium and the enriched sample used in these experiments.

A single crystal was grown in Warwick by Dr G Balakrishnan, using an infra-red double mirror image furnace [114]. The crystal has a diameter of  $\approx 0.4$  cm, a length of  $\approx 2$  cm, and is translucent red in color. It has a cylindrical form typical of image furnace grown crystals. Initial alignments were performed using an x-ray Laue camera and subsequently refined on PRISMA [115]. Realignments were carried out entirely on PRISMA. The crystal was glued into a large copper support to ensure good thermal contact and immobility in the field.

Again more than one experiment was performed. This time they can be reported more or less in the order in which they were carried out<sup>a</sup>. The measurements were made as follows:

- Using a  $^3\text{He}$  sorption refrigerator insert in an Orange cryostat the  $hhl$  plane was mapped in zero field at 0.3 K using the scattering angle  $\phi = -48^\circ$ . The same plane was mapped at 0.3 K, 1.3 K and 20 K using the scattering angle  $\phi = -32^\circ$  (first experiment).
- Using a dilution refrigerator insert in an Oxford Instruments cryomagnet the  $hk0$  plane was mapped in zerofield at 0.05 K, a hysteresis loop was measured and the plane mapped in 1.0 and 2.0 T (second experiment).
- Using the same equipment the  $hhl$  plane was mapped in zerofield at 0.05 K, a hysteresis loop was measured and the plane mapped in 1.5 T, the temperature was raised to 0.9 K and then lowered in an applied field of 1.5 T (second experiment, see figure 6.1).
- In a separate experiment with the same sample environment the magnetization curve was re-measured in much greater detail, the effects of field warming and cooling were further investigated, two hysteresis loops were measured at 0.3 K and one at 1.8 K (third experiment, see figure 6.1).

---

<sup>a</sup>The experiments were carried out beginning on 13<sup>th</sup> July 2000 (by O. A. Petrenko, B. Fåk and J. D. M. Champion, I was not a member of the experimental team on this experiment), 4<sup>th</sup> June 2001 (by O. A. Petrenko, B. Fåk and T. Fennell), and 29<sup>th</sup> July 2002 (by O. A. Petrenko, B. Fåk and T. Fennell.)

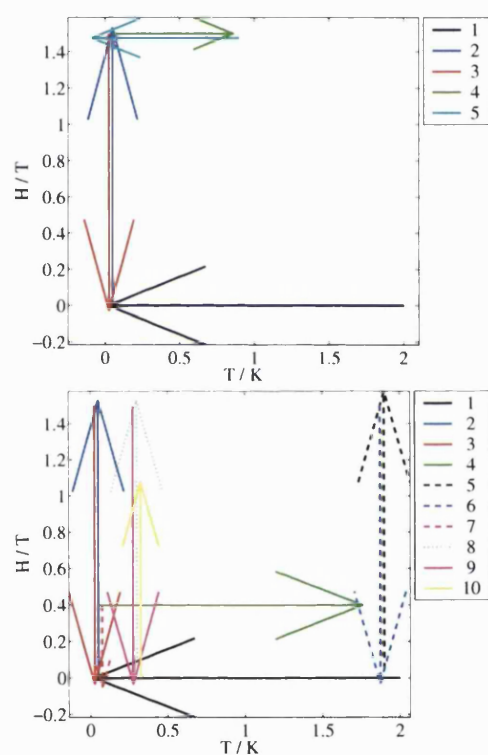


**Figure 6.1:** Paths through  $H/T$  space for the second ( $hhl$  part only) and third PRISMA experiments. Between steps 9 and 10 of the third experiment the temperature was raised to 0.7 K.



All the sample environments used have aluminium tails. This is because Aluminium is an extremely weak incoherent scatterer and so the contributions of the sample environment to the background is confined to powder lines. Vanadium tails do not produce these powder lines but can lead to a rather large background from the incoherent scattering by Vanadium. Generally the information required lies within the first powder line so the data is only displayed to this particular  $|Q|$ .

The data was reduced using VCRS, a macro written for the ISIS data display software Genie. The VCRS macro has been updated several times during this work [116]. The current version performs the following functions:

- Correction of a dataset for Vanadium for absorption;
- Optional smoothing of the Vanadium data;
- Normalization of the measured data to the Vanadium;
- Correction of the normalized data for absorption.;
- Transformation of the data from time-of-flight to reciprocal space.

The essential function of this process is the normalization. The scattering from Vanadium is incoherent and so is expected to be identical regardless of time-of-flight and diffractometer angles. This means it can be used to divide out the flux profile of the moderator and scale for detector efficiency. Although the absorption cross section of our sample has been reduced by the use of isotopic enrichment, it is still significant and so the absorption correction must be applied. The absorption correction was made by calculating an absorption coefficient by which the data could be divided. The coefficient for a cylinder of radius  $R$  was originally derived by Sears [117] and is

$$A(s, \phi) = [1 + 4bs^2 - 0.5s^2 \cos^2(\phi/2)] \times \exp(-2as), \quad (6.1)$$

where  $a = 8/3\pi$ ,  $b = (1 - a^2)/2$ ,  $s = \mu R$  and  $\phi$  is the scattering angle. This correction was added to the VCRS macro with the additional assumption that  $\mu$  depends on both the scattering cross section, and the wavevector dependent absorption cross section [116, 118].

Subsequent data manipulation was performed on the normalized data using the *tslice* package for MatLab [119]. The data structure obtained on PRISMA consists of radial detector trajectories in the scattering plane. For each detector the data is recorded as a function of time and subsequently converted to  $h, k, l$ , and  $|Q|$ . These are stored in *tslice* as the columns of a group of matrices. In manipulating this data certain directions are particularly simple to work with. It is easy to extract information as a function of  $|Q|$  in an arbitrary radial direction, moving in a straight line in reciprocal space. This is equivalent to working with a single detector trajectory, or one column of each of the group of matrices. It is also easy to extract information at a constant value of  $|Q|$ . Locally this will be approximately perpendicular to a detector trajectory but correctly this is a curve in reciprocal space. One row of the group of matrices is being manipulated. Arbitrary directions in reciprocal space are harder to achieve as they cut across the data structure.

### 6.1.1 Peak Integration on PRISMA

Three strategies for peak integration have been used; each has different merits. The first method is to make a cut through the data and sum the counts in the cut between the limits of the integral required. The second method is to sum counts within a box. The box is an arbitrary rectangular enclosure of points in the scattering plane. A second larger box can be used to estimate the average background around the region of interest which can then be subtracted. The third method is a two dimensional generalization of the Lehmann-Larsen  $\sigma/I$  method [120]. The advantages of the first two methods are that they are very simple and robust. Their major disadvantages are the possible inclusion of background counts, and the rigid specification of the area of integration. For one dimensional data the Lehmann-Larsen method is a systematic and proven way of integrating peaks with optimal background subtraction. The major disadvantage here seems to be that on generalization to two dimensions it becomes less robust and reliable.

The two dimensional implementation of the Lehmann-Larsen method works by first performing a  $\sigma/I$  search across the peak at a constant value of  $|Q|$  to define a peak width [119]. For PRISMA data this corresponds to searching across detectors

to see which detectors recorded intensity from the peak. A  $\sigma/I$  search is then performed outward along each detector trajectory included by the first transverse search. It is unsurprising that this procedure is sensitive to the transverse peak shape and resolution. The Lehmann-Larsen routine is used successfully throughout the section with the field aligned on  $[00l]$ . Apart from a scaling, the integrals agree with those previously performed with the simple slicing method. In that part of the experiment single point scans were measured and the transverse resolution was poor, all the intensity was essentially contained in a single detector. This means that the transverse search which defines the width is easy and reliable. In the work with the crystal aligned on  $[h\bar{h}0]$  the resolution was improved by measuring a five-point rocking scan. This resolved a second crystallite and lead to a spread of intensity across detector trajectories. In this more complicated situation it seemed that the Lehmann-Larsen method became susceptible to error. Previously the integrations had been performed with the slice method and a distinct plateau in the integrated intensity of 0,0,2 as a function of field was observed. Using the Lehmann-Larsen routine this plateau mysteriously disappeared. Obviously the presence or absence of a step at this point is very important.

To establish whether the integral of the two peaks should be similar, and the plateau real, comparisons were made using cuts (figure 6.2). Cuts along and across the peaks at the center and through the tails show that they are very closely comparable and therefore the Lehmann-Larsen routine is at fault. The area over which it integrates is very similar for both peaks, however it rejects part of the peak where there is significant intensity. The difference in intensity must accumulate in the detailed differences in integration of the tails of the peaks. This problem and the rejection of intensity from some parts of the peak meant that the box integrator was adopted for integration of intensities from these scans. Using the box integral method the form of the magnetization curve agrees with that originally produced by the slice method.

### 6.1.2 Resolution Convolution on PRISMA

Because of the nature of neutron sources and optics, neutron scattering instruments set to measure at a particular momentum and energy transfer ( $\mathbf{Q}_0, \omega_0$ ), are actually

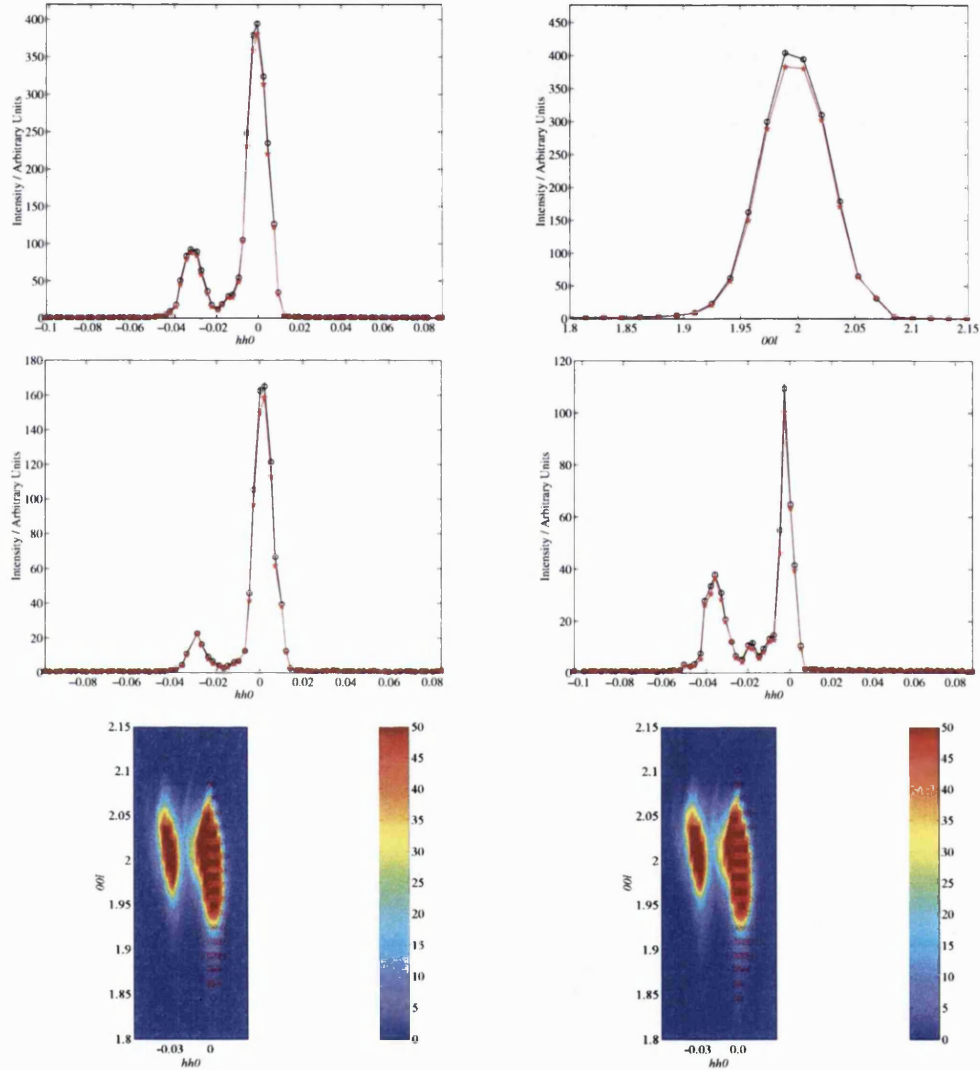


**Figure 6.2:** Comparison of integration process for 002 peaks measured at 0.25 and 0.3 T. Previous integrations suggested they should have equal intensity but the Lehmann-Larsen method suggests they do not. The cuts are at 002 (top left), radially through the peak center (top right), at 001.95 (middle left), and at 002.05 (middle right). The areas of integration are shown for 0.25 T (bottom left) and 0.3 T (bottom right).

measuring within a small volume of  $(\mathbf{Q}, \omega)$  space around  $(\mathbf{Q}_0, \omega_0)$ . To take account of this it is necessary to perform a resolution convolution in which the measured signal is described as a convolution of the spectrometer resolution function  $R(\mathbf{Q} - \mathbf{Q}_0, \omega - \omega_0)$  and the scattering function  $S(\mathbf{Q}, \omega)$ . The resolution function is peaked at  $(\mathbf{Q}_0, \omega_0)$  and decreases for deviations  $(\Delta\mathbf{Q}, \Delta\omega)$  from  $(\mathbf{Q}_0, \omega_0)$  [121].

One implication of the spread of momentum transfers being measured is that a feature which in theory is a  $\delta$ -function, such as a Bragg peak, becomes a feature with finite width. In this work all energy transfers were integrated/ignored so only resolution in  $\mathbf{Q}$  is important. The finite width of the resolution function means that all features will have an intrinsic width due only to the resolution of the instrument. When a feature becomes particularly sharp a situation can be reached in which the actual width of the feature is less than the resolution of the instrument and all that is being measured is the resolution function. In this case spurious conclusions would be reached about the behaviour of this width if the resolution function was ignored. Resolution convolution is employed in just such a situation in this work. A feature showing field dependent narrowing has been studied. At some fields it becomes very sharp and the instrumental contribution to the width must be accounted for.

The original resolution convolution described by Cooper and Nathans is usually associated with the study of excitations on triple axis spectrometers [122]. Their basic assumption is that the probability of transmission of neutrons through elements of the spectrometer such as the collimation or the monochromator can be represented by Gaussian functions. This assumption has turned out to be entirely justified and their approach has been widely adopted. For instruments such as PRISMA their method can be adapted, but Gaussian functions cannot be used for all spectrometer components. The resolution function of PRISMA has been formulated and discussed by Hagen and Steigenberger (HS) [123]. The non-Gaussian part is the lineshape of the initial neutron pulse.

In this work the feature of interest lies on the  $[00l]$  direction of reciprocal space. There is a detector trajectory which passes directly along this axis. This means that the correlation lengths of interest are to be extracted parallel and perpendicular to the detector trajectory. Scattering from two crystallites can be

distinguished. Their scattering is separated perpendicular to the  $[00l]$  detector trajectory. HS discuss only the parallel contribution to the resolution of PRISMA. For this work this will give the intrinsic instrumental lineshape along the  $[00l]$  axis. This function is derived as

$$I(E_i^0) = I_0 \exp \left[ \left( \frac{\chi_0}{\tau} \right) \left( \frac{Q^0 - Q_B}{Q^0} \right) \right] \times \operatorname{erfc} \left( \frac{1}{\sqrt{2}} \left[ \frac{\sigma_0}{\tau} + \left( \frac{\chi_0}{\sigma_0} \right) \left( \frac{Q^0 - Q_B}{Q^0} \right) \right] \right). \quad (6.2)$$

Conveniently the transverse resolution can be represented by a Gaussian [118].

The cuts through the features are one dimensional and so is the resolution convolution. A full four-dimensional Cooper-Nathans [122] type resolution convolution is unnecessary and inappropriate. The form of convolution appropriate here is

$$I(Q_0) \approx \delta(Q^* - Q_0) \times \int R'(Q^* - Q) S(Q) dQ, \quad (6.3)$$

The calculation being employed is a convolution by integration. In the equation  $R'$  is the resolution function, centered at  $Q^*$ , and  $S(Q)$  is the scattering function. The resolution function is “scanned” through the scattering function (i.e.  $Q^*$  shifts) and the product integrated at each point. The intensity is then attributed only to the point where the resolution function was centered. This means that the intensity at  $Q_0$  contains contributions from surrounding  $Q$ -points, depending on the width of  $R$ . The calculated profile represents the sample and instrumental effects. The parameters of the scattering function are adjusted by least squares until the convoluted profile matches the data. The resolution calculations were all performed using new functions written for the least squares package *Mfit* [124, 125].

Two sets of resolution convolutions are required, one for the longitudinal resolution function and one for the transverse. The resolution for the transverse direction is of particular importance since it is in this direction that the features become sharpest. The scattering function used was a double Lorentzian, one for each crystallite.

The resolution function employed was a normalized, parameterized gaussian. The only parameter to be chosen was the width. This is because the amplitude

is fixed by the normalization, the center is determined by the point for which the calculation is being made and the background is zero. The width is the resolution limit at this value of  $|Q|$ . Ideally the width could vary across a cut but this is not at all practical to treat so it is assumed that the width is fixed for a given  $|Q|$ . This is not strictly true as the cut is straight and constant- $|Q|$  is an arc, however the cut is short and so a significant difference between the arc and the line does not accumulate over their length. The width was obtained by fitting the widths of successive  $00l$  Bragg peaks as a function of  $[hh0]$ ; an example is shown in figure 6.3. Data from a high field was used as this means that 002 and 006 are present giving a meaningful number of peaks to fit. It is assumed that magnetic and nuclear Bragg peak widths have identical  $|Q|$  dependence. The fitting of the resolution convolution was further constrained since the separation of the two Lorentzians can be obtained by fitting the separation of the Bragg peaks due to the two crystallites and interpolating for the correct  $|Q|$ . The fit of the separation of the Bragg peaks from each crystallite and the widths are also shown in figure 6.3. The  $[00l]$  dependence of the width of the main Bragg peak was used to interpolate the width of the resolution at 003 for the convolution.

For the parallel direction a single crystallite is contributing as the scans were fine enough to distinguish the crystallites and individual detector trajectories pass through one or other. Therefore a single Lorentzian could be used for the scattering function. This was to be convoluted with a normalized, parameterized function of the type given in equation 6.2. The resolution function was fitted to the Bragg peaks from 002 to 0010 (the main grain contribution to 0010 falls just on the scattering map but the minor does not so it can be used for longitudinal but not transverse resolution fitting). Again high field data was required to give sufficient Bragg peaks. An example of the fit is shown for 002 in figure 6.4. Two parameters are required to fit equation 6.2. These are  $\tau$ , the cutoff time, and  $\sigma_0$ , the width. The peak position and height, and the background were all also able to vary. Their fitted values were small adjustments to the initial guess parameters.

The peak parameters should be a smooth function of time of flight or wavelength (or energy, as in the original work of HS). It does not follow that they will be a smooth function of  $|Q|$  because of the possible angle dependence of  $|Q|$  [118].

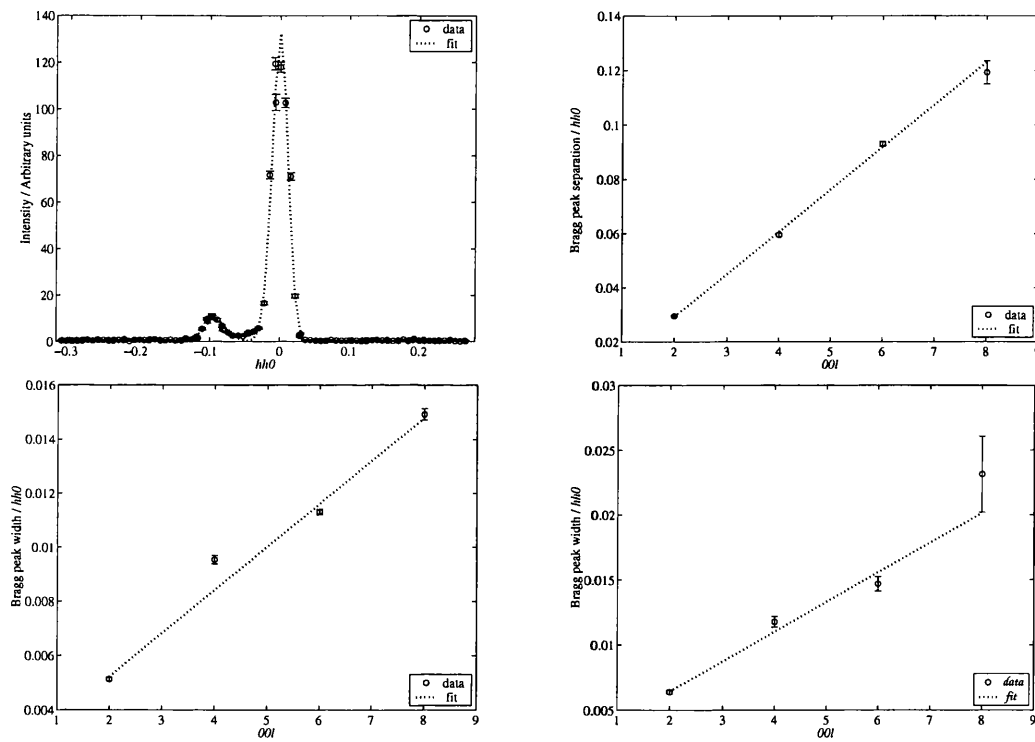


**Figure 6.3:** Fits involved in the resolution convolution: Example of the Gaussian fits used for Bragg peak width and separation in the transverse resolution convolution (top left), width of major Bragg peak as function of  $[00l]$  (top right), width of minor Bragg peak (bottom left), and Bragg peak separation as function of  $[00l]$ .



In this case however, since the data is collected in a single detector at a constant scattering angle the parameters should also be a smooth function of  $|Q|$ . The most useful function for interpolating the fitted parameters proved to be an exponential decay and these interpolations are shown in figures 6.5 and 6.6. The interpolated parameters for 003 were  $\sigma_0 = 1.0 \pm 2 \times 10^{-4}$  s and  $\tau = 7.2 \pm 9 \times 10^{-5}$  s. These are of the same order of magnitude as the values obtained by HS for these parameters for different materials (such as Cu and Ge).

## 6.2 Zero Field Scattering

The first comparison that can be made is between the two scattering angles used in the first experiment. Clearly  $\phi = -32^\circ$  (figure 6.10) is considerably more useful than  $\phi = -48^\circ$  (figure 6.9) as it provides more information at low  $|Q|$  without apparently compromising the quality of the pattern. Consequently, after the first experiment all measurements were made with  $\phi = -32^\circ$ .

The temperature dependence of the diffuse scattering due to the freezing of the spins is sampled at four points only for the  $hhl$  plane. These are widely separated. An important point that can be obtained from these three measurements is that the diffuse scattering does evolve with temperature. The four temperatures are shown in figure 6.7 (20 K), 6.8 (1.3 K), 6.10 (0.3 K) and 6.11 (0.05 K). Evidently no spin correlations have built up at 20 K. This is entirely expected as the susceptibility shows that  $\text{Dy}_2\text{Ti}_2\text{O}_7$  is paramagnetic at this temperature. At 1.3 K strong diffuse scattering has appeared. The form is closely similar to that of the near-neighbour spin ice as simulated by Bramwell *et al.* (see figure 2.4) [57]. Between 1.3 and 0.3 K the spin correlations evolve and additional features appear in the scattering pattern. The additional scattering is localized around the Brillouin zone boundaries. For the  $hk0$  plane data has only been collected at 0.05 K (figure 6.12).

Monte Carlo simulations of the dipolar spin ice model with parameters appropriate for Dysprosium Titanate have been made [126]. The scattering pattern has been calculated for both the  $hhl$  and  $hk0$  planes. For the  $hk0$  plane the simulation and the experiment seem to agree very well indeed. The two scattering maps are

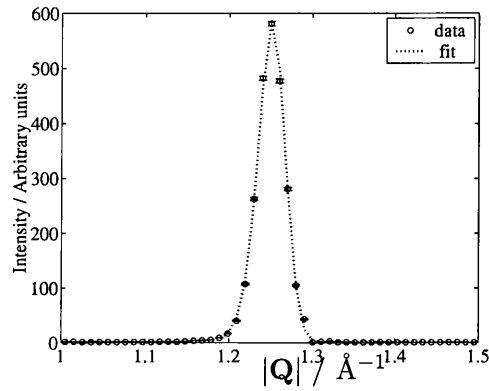


**Figure 6.4:** 0,0,2 Bragg peak (magnetic) fitted using equation 6.2.

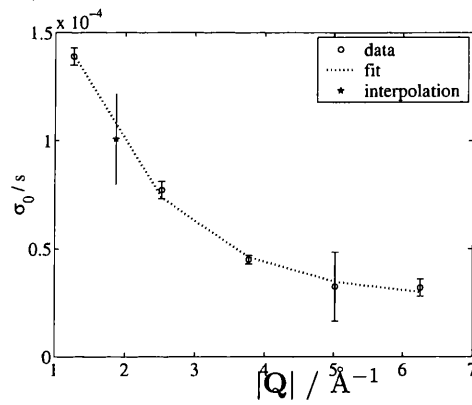


**Figure 6.5:** Exponential decay used to interpolate the fitted values of  $\sigma_0$ .

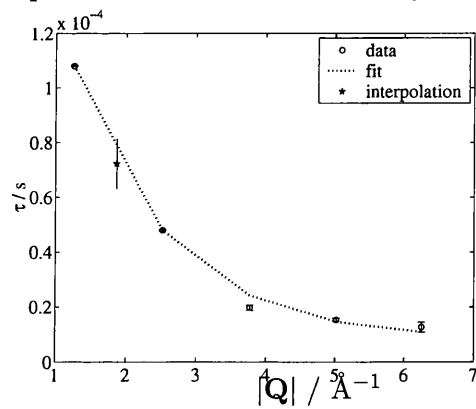


**Figure 6.6:** Exponential decay used to interpolate the fitted values of  $\tau$ .

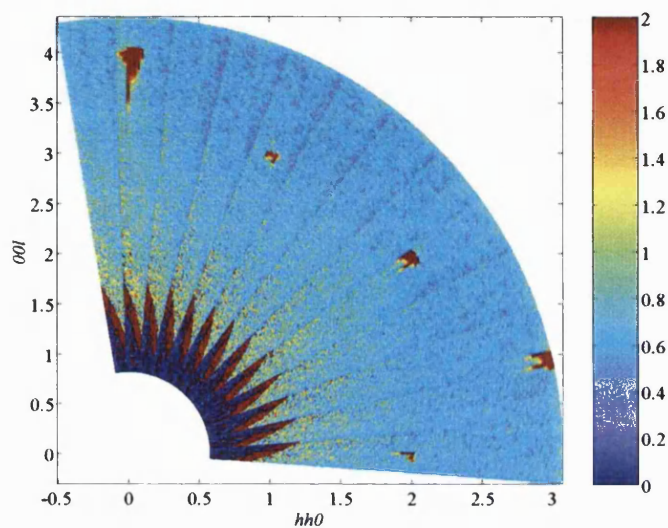


**Figure 6.7:** Scattering intensity in the  $hhl$  plane recorded on PRISMA at 20 K.

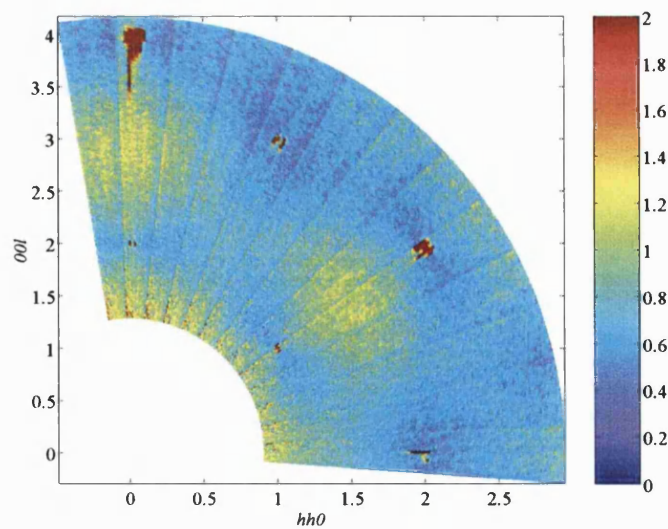


**Figure 6.8:** Scattering intensity in the  $hhl$  plane recorded on PRISMA at 1.3 K.

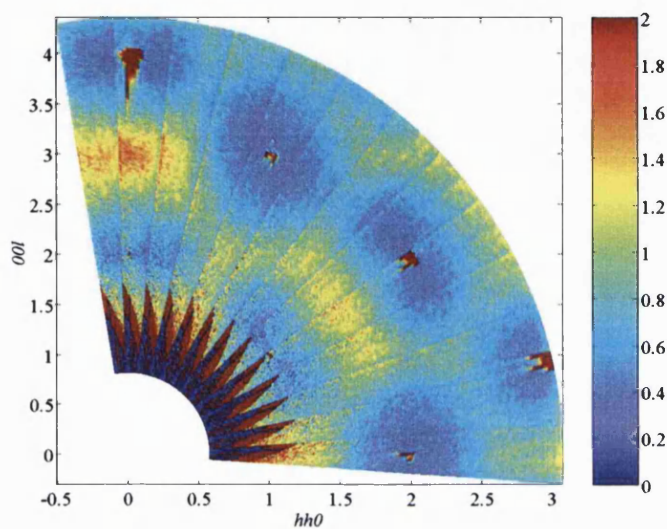


**Figure 6.9:** Scattering intensity in the  $hhl$  plane recorded on PRISMA at 0.3 K with  $\phi = -48^\circ$ .

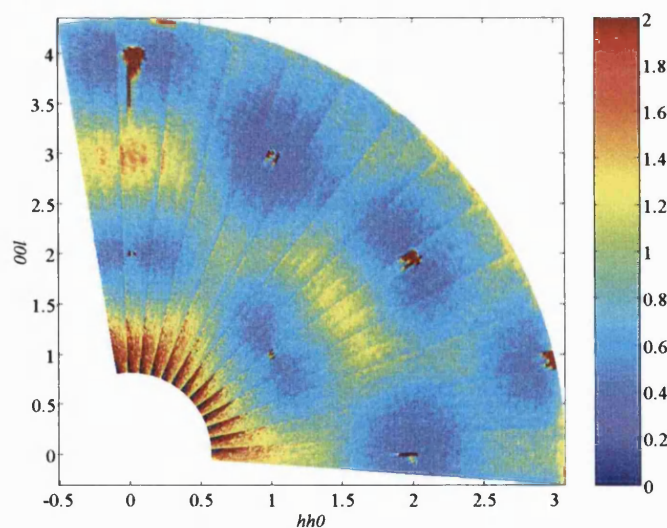


**Figure 6.10:** Scattering intensity in the  $hhl$  plane recorded on PRISMA at 0.3 K with  $\phi = -32^\circ$ .

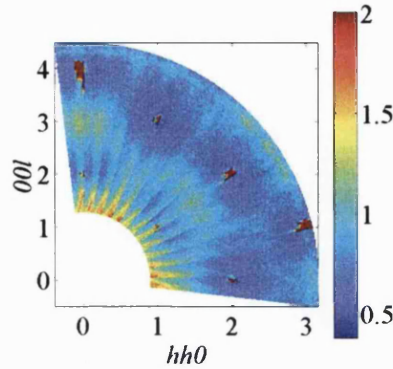


**Figure 6.11:** Scattering intensity in the  $hhl$  plane recorded on PRISMA at 0.05 K.

shown in figure 6.12. A comparison by a cut through the data is shown in fig 6.13. The Monte Carlo pattern has been corrected for the magnetic form factor of Dysprosium and fitted to the experimental diffuse scattering using a flat background and a scaling parameter.

For the  $hhl$  plane direct comparison of the two scattering maps shows that there are significant differences. There are also close similarities which are somewhat obscured by the unexpected features. In figures 6.14 and 6.15 the two scattering patterns are shown. It is apparent in these maps that the difference is that whilst the experimental pattern does contain the features of the spin ice scattering (for example the large diffuse feature at 003) it also contains the zone boundary features which are not reproduced by the simulation.

The similarities of the two patterns are more clearly emphasized in figure 6.16. Here slices through the data have been made. The agreement along the  $[00l]$  and  $[hh0]$  is actually very good. However, the slice along  $[hh0]$  at  $[00l] = 2.3$  is chosen to highlight the differences and it can be seen that where the slice crosses the zone boundary the form of the calculated and experimental intensities is completely different.

One possible explanation for the zone boundary features is that they are due to phonons [118, 127]. However, the following facts suggest that the intensity is magnetic:

- The fact that the scattering appears/intensifies as temperature is decreased,

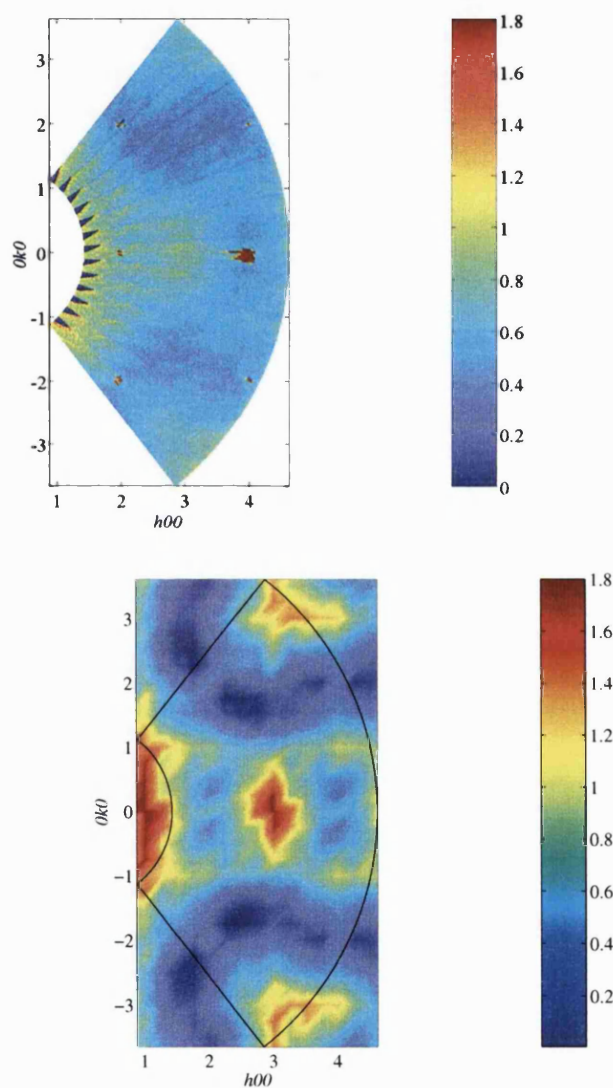


**Figure 6.12:** Scattering intensity in the  $hk0$  plane recorded on PRISMA at 0.05 K (top), and calculated from Monte Carlo simulations (bottom).



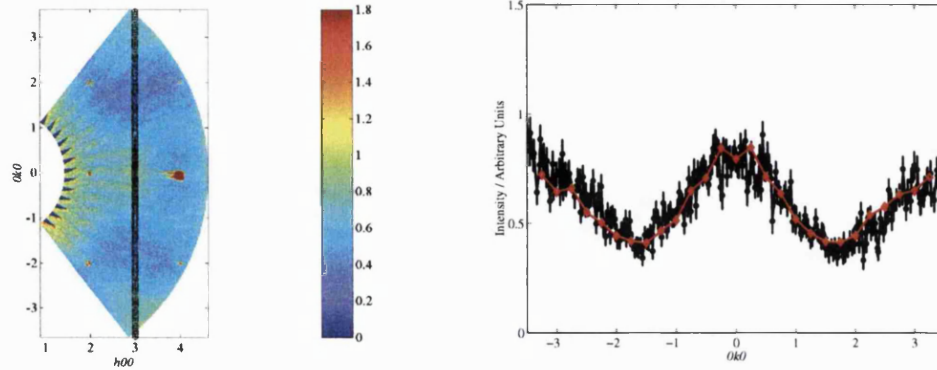


**Figure 6.13:** Slice position in the  $hk0$  scattering plane, and the slices along  $[0k0]$  at  $[h00] = 3$  (Black circles = data, red diamonds = Monte Carlo.)

the converse would be expected for a phonon;

- For a phonon  $I_{|Q|} \propto |Q|^2$  whereas these features fall off with  $|Q|$ .

The second point can be demonstrated by comparison of the intensity of the feature with the magnetic form factor of  $\text{Dy}^{3+}$ . If the intensity at equivalent points on successive zone boundaries is compared it would be expected to follow the form factor if the scattering process is magnetic. This comparison is made and illustrated in figure 6.17 for data at 0.3 K with the scattering angle either  $\phi = 32^\circ$  or  $\phi = 48^\circ$ .

The comparison is made by taking a cut through the data in the direction indicated in figure 6.17. The choice of zone boundaries to consider in this comparison may seem odd. First, the data contains relatively few equivalent zone boundary points. Secondly, assuming that the pattern is made up of “spin ice + zone-boundary features” various zone boundaries become inadmissible in such a comparison as they appear to be overlain by spin ice scattering. In the direction chosen there is a distinctive absence of spin ice scattering in the simulated pattern, as seen in figure 6.17.

The cuts are shown in figure 6.17. Each zone boundary feature was fitted with a gaussian. The background from each individual fit was used to estimate a sloping background across the cut. The form factor was scaled by least squares to the amplitudes of the Gaussians. On the basis of this comparison it seems entirely reasonable to attribute the zone boundary features to a magnetic correlation.

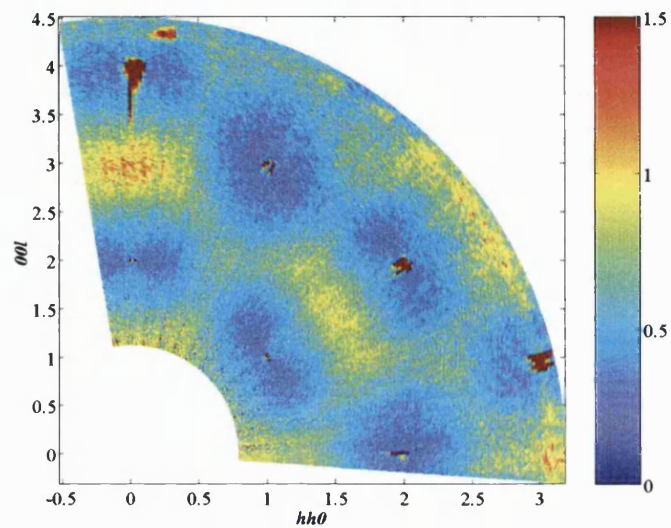


**Figure 6.14:** Scattering intensity in the  $hhl$  plane recorded on PRISMA at 0.3 K.

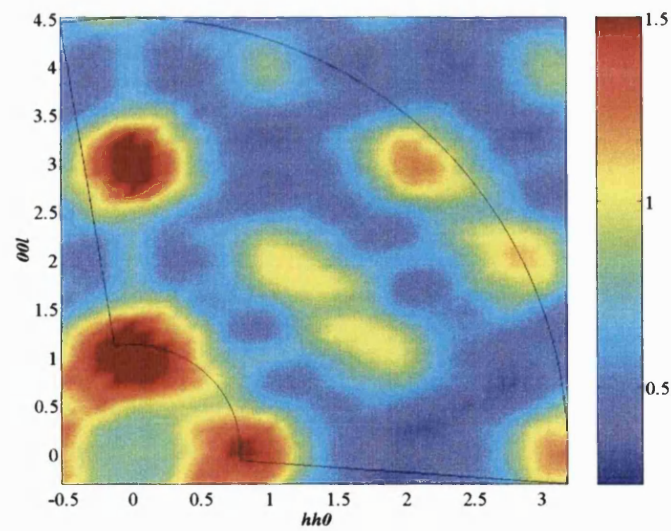


**Figure 6.15:** Scattering intensity for the  $hhl$  plane calculated by Monte Carlo simulation of the dipolar spin ice model.



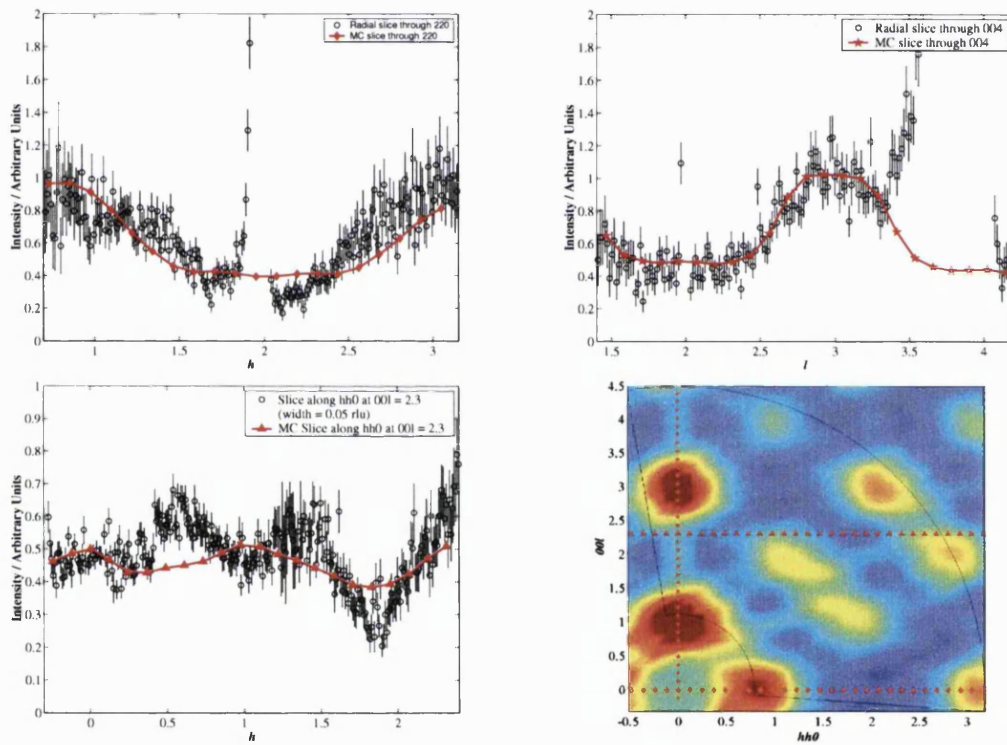


**Figure 6.16:** Comparison of experimental and Monte Carlo data for the  $hhl$  plane using slices along  $[hh0]$  (top left),  $[00l]$  (top right), along  $[hh0]$  at  $[00l] = 2.3$  (bottom left) and the slice positions in the scattering plane (bottom right).

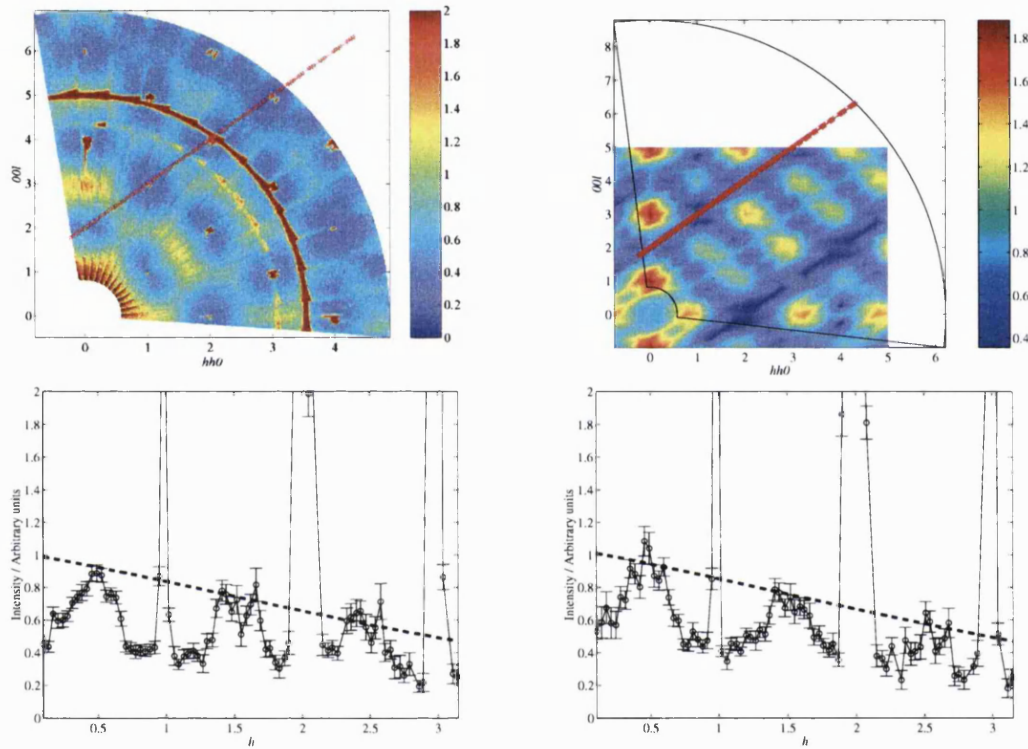


**Figure 6.17:** Comparison of zone boundary features with the magnetic form factor of  $\text{Dy}^{3+}$  showing the direction of the cut across zone boundary features in the data (top left); direction of the cut across zone boundary features indicating absence of expected spin ice scattering in the Monte Carlo data (top right); the cut across zone boundary features for data with  $\phi = 32^\circ$  (bottom left), the dashed line is the form factor of  $\text{Dy}^{3+}$  fitted with a scale and sloping background; and the cut across zone boundary features for data with  $\phi = 48^\circ$  (bottom right).

The dipolar spin ice model apparently provides a very successful model for the spin correlations in  $\text{Dy}_2\text{Ti}_2\text{O}_7$ . However, some additional correlations do occur which are not captured by the model. The model is very successful in describing the bulk and microscopic data for  $\text{Ho}_2\text{Ti}_2\text{O}_7$  [57], and the bulk data for  $\text{Dy}_2\text{Ti}_2\text{O}_7$  [59]. One might therefore ask how these correlations appear, and how this further restriction of the dipolar spin ice manifold is not manifested in the fit to the heat capacity.

Firstly, the fit to the heat capacity is not perfect, the experiment and simulation differ in details. The zone boundary features are not due to a very high degree of spin correlation, since they are still very diffuse in reciprocal space. Also the fact that they run all around the zone boundaries is suggestive that the correlations are rather ubiquitous and symmetric. This implies that they are only short ranged. A large difference between the experimental and theoretical heat capacities is therefore not expected since it does not appear that the extra correlations would make a major contribution to the entropy. The entropic contribution of the zone boundary features could be contained in the detailed differences of the experimental and theoretical heat capacities.

Secondly, it is not clear that these correlations are absent in  $\text{Ho}_2\text{Ti}_2\text{O}_7$ . If the diffuse scattering data for  $\text{Ho}_2\text{Ti}_2\text{O}_7$  is examined with the zone boundary features in mind then some may be discernible (see figure 2.4) [57]. PRISMA has been considerably upgraded since that data was collected and so they may have been missed. Also the crystal was not aligned perfectly in that experiment, as evidenced by occurrence of Bragg peaks at unexpected positions. If the zone boundary features are confined to the  $hhl$  plane then they may have been weakened relative to the other diffuse scattering processes by the misalignment.

Thirdly, the simulations are for samples which are thoroughly equilibrated by single spin flips. The calculated pattern is for a sample which is strictly in states of the dipolar spin ice manifold plus associated excited states. No data exists for the effect of the rate of cooling on these materials. However since the dynamics evidently become very slow below  $T \approx 0.5$  K it is also possible that the sample has in fact been quenched and has frozen into a defective spin ice state. Defects might include local breaking of the ice rules, which cannot be relaxed, due to

the the frozen dynamics. These could cause the departure of the data from the experimental pattern.

### 6.3 Field Applied on $[00l]$

With the crystal oriented with the field applied on  $[00l]$  two magnetization curves were recorded and the scattering plane mapped in the saturation field (at 0.05 K).

The map of the scattering plane made in 1.0 T is shown in figure 6.18. It can be seen on comparison with the zero-field map (figure 6.12) that the diffuse scattering disappears and that all that remains are Bragg peaks and background. This suggests that the system is fully ordered by this applied field. This is the expected outcome. Other outcomes that might also be consistent with the data are that the order is partial and the disordered parts of the system do not give rise to strong diffuse scattering as they are insufficiently correlated, or that the correlations give rise to diffuse scattering that lies on a different plane of reciprocal space. For disorder to persist it must surely overcome the energetic favorability of a field aligned ice rules state so it seems unreasonable to suppose that this happens.

The pattern of Bragg peaks observed is distinctive. Each occurs at a zone center, though some occur at the center of zones previously lacking a peak. This is entirely consistent with the development of a  $Q = 0$  structure. The pattern of integrated intensities across the map does not seem to be reliable enough for structure factor calculations.

The first magnetization curve was recorded with the detectors arranged to collect data points around the  $[h00]$  axis. The scattering was observed as field dependent Bragg peaks at the positions 200, 400, 600, and 800. The field dependence of integrated intensities is shown in figure 6.19. The 800 peak lies on a powder line and this allowed the Lehmann-Larsen integration routine to include spurious intensities. It proved most practical to integrate this peak by summing intensity in a single detector which effectively contains all the scattered intensity for this peak. The second loop was recorded on the peak position  $4\bar{2}0$ . No other Bragg peaks are included at this position. Because it lies very close to the edge of the measured section of reciprocal space it was again impossible to use the Lehmann-

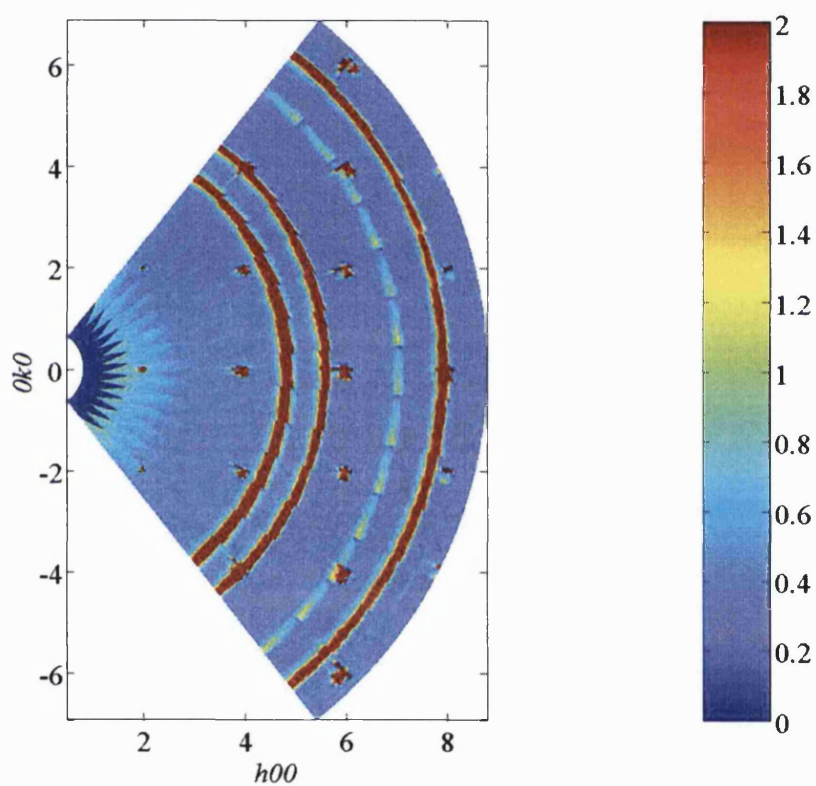


**Figure 6.18:** Scattering intensity in the  $hk0$  plane recorded on PRISMA at 0.05 K and 1 T.

Larsen routine as it could not search across the peak width correctly to determine the width. This peak was also integrated by summing counts in a single detector between appropriate limits. The field dependence of this Bragg peak is also shown in figure 6.19. The reflection conditions are the same for 200 and  $4\bar{2}0$ . The 200 from the first loop is compared with the  $4\bar{2}0$  by normalizing both to their maximal intensities. The comparison is also shown in figure 6.19.

The magnetization develops in a series of steps. This is a feature of many of the field dependent measurements described. Some reasons for stepped magnetization curves were discussed in the introduction. As with the other steps observed it seems most sensible to attribute these to metastable states accessed as the field promotes the reorientation of spins into the ordered structure. The pattern of steps on the second loop is similar (figure 6.19) but not identical. This history dependence is also suggestive that the steps are due to the very slow dynamics, rather than a mechanism such as tunnelling. As with  $\text{Ho}_2\text{Ti}_2\text{O}_7$ , discussed in section 5.3, the step is attributed to reorientation of a fraction of the spins, followed by those which require higher fields to drive them into the ordered structure. Again it is possible that there could be a first order phase transition in finite field, as predicted by Harris *et al.* [55] and described in section 2.5. The different step positions on successive cycles suggests that this is not the case.

## 6.4 Field Applied on $[h\bar{h}0]$

This orientation has been investigated in two separate experiments (i.e. the second and third). During these experiments field and temperature dependencies of the magnetic scattering have been measured. Both experiments had a similar plan. This was basically to measure a magnetization curve at base temperature, and then a temperature scan. Additional field scans at intermediate and high temperatures were performed in the third experiment. As with  $\text{Ho}_2\text{Ti}_2\text{O}_7$  in this orientation short and long range correlations are expected to coexist.

The magnetization curves were measured on the  $[00l]$  axis of the  $hhl$  plane. Bragg peaks were observed at positions 002 and 004. Non-resolution limited features were observed at positions such as 003. A five point omega scan was used to

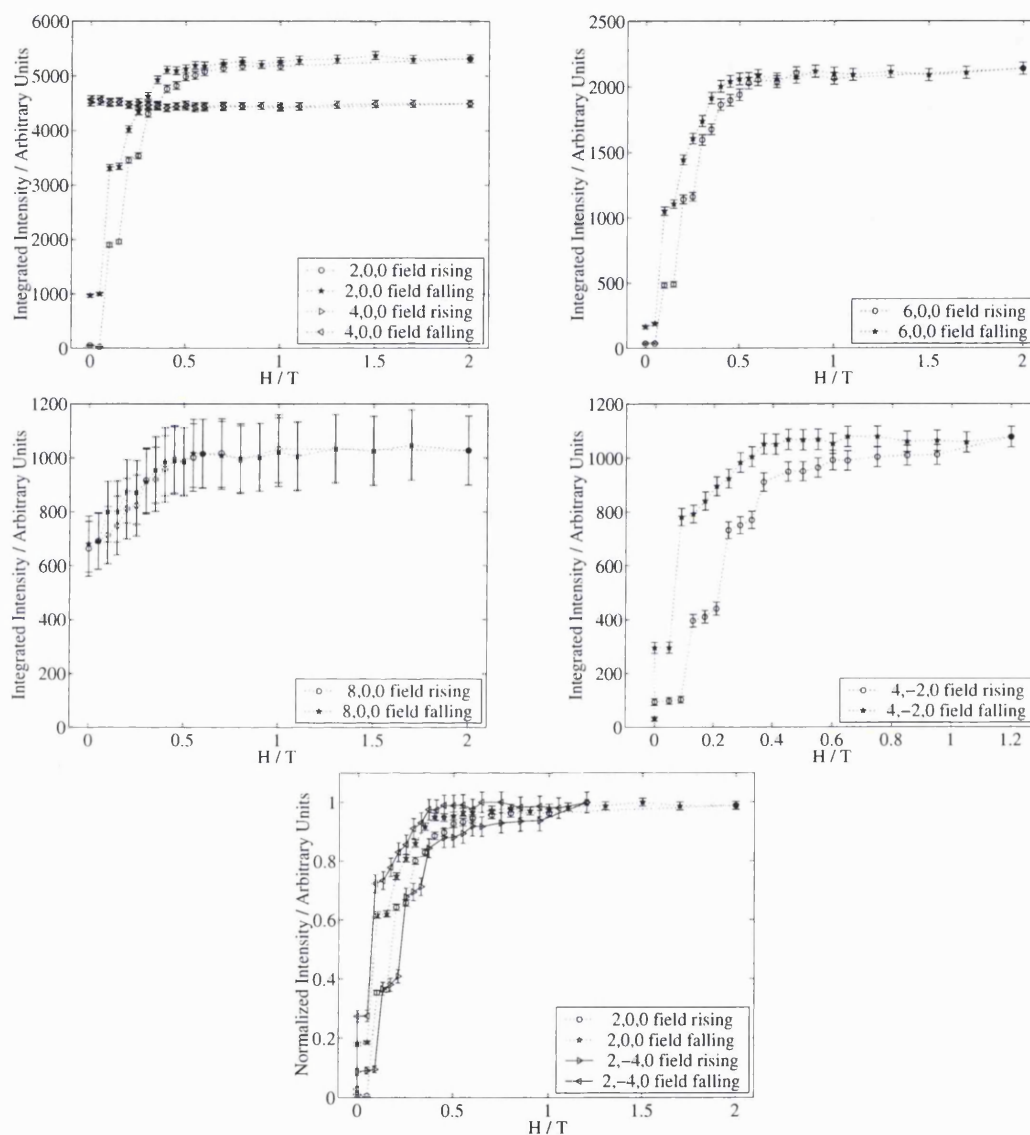


**Figure 6.19:** Hysteresis loop, second experiment,  $T \approx 0.05$  K, field applied on  $[00l]$ . Field dependance of 200 and 400 peaks (top left), 600 (top right), 800 (middle left),  $4\bar{2}0$  on the second hysteresis cycle (middle right), and the normalized intensities of 200 and  $4\bar{2}0$  on the first and second hysteresis cycles respectively (bottom).

improve the resolution. This allows two grains to be distinguished in the crystal. One is misaligned and the most intense scattering comes from the well aligned one. The non-resolution limited features are field dependent and become sharper with increasing field (their field dependence is discussed further below). The width, at least in one direction, does approach that of a Bragg peak and so a resolution convolution was performed to take account of instrumental resolution in the extraction of correlation lengths from these features.

### 6.4.1 Results of the Second Experiment

#### Hysteresis Loop at Base Temperature

The first part of the experiment was a hysteresis loop at base temperature, starting in the zero field cooled state. The magnetic scattering does not develop smoothly as a function of field. Both Bragg peak integrated intensities and quantities derived from the non-resolution limited features have steps. Data points from each of the stages of the development of the scattering are shown in figure 6.20. Initially the 003 feature is broader than the five point scan. This is the same feature which can be seen in the zero field spin ice scattering. At low fields a rather more elongated and intense feature appears. This in turn gives way to a considerably sharper and more intense feature. The full scattering plane was mapped at 1.5 T and it can be seen that these elongated features appear at all the  $Q = X$  positions in the scattering plane (figure 6.21). Two correlation lengths have been extracted from the feature at 003. One was extracted from the data parallel to  $[00l]$ , where the feature is broad; the other was extracted perpendicular to  $[00l]$ , where the feature is sharp. These are known as the “interchain” and “intrachain” correlation lengths respectively. This is because the features are due to the formation of domains of ordered chain sections (this is justified below). In this case, the correlation length along  $[hh0]$  (i.e. intrachain) corresponds to the length of the chain sections in the domain. The correlation length parallel to  $[00l]$  (interchain) characterizes the size of the domains perpendicular to the chain direction. The interchain correlation length is therefore a measure of the correlation between chains, hence its name.

Some of the fits obtained during the extraction of the intrachain correlation



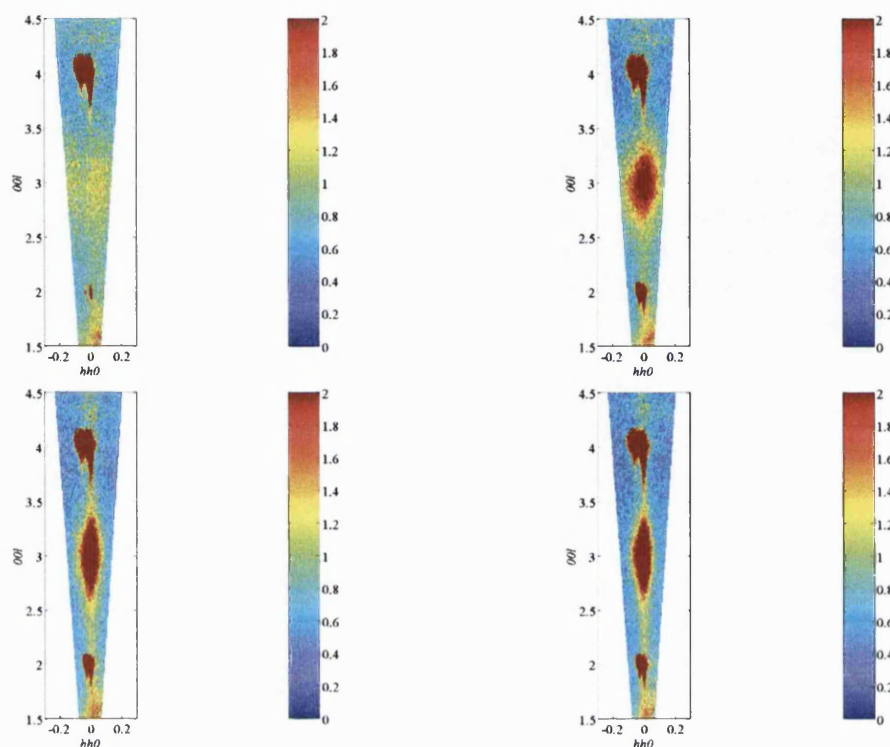


**Figure 6.20:** 002 and 003 in zero field, 0.3, 0.5 and 1.0 T applied on  $[h\bar{h}0]$ .

lengths are illustrated in figures 6.22. The initial broadest features were not amenable to the resolution convolution approach described above. In zero field the full extent of the feature can only be obtained from a full scattering map, and even then only half of it is available. Considerable intensity differences were apparent between adjacent detectors and so a coarse binning was used in making the cut to smooth this effect somewhat. Even so it proved necessary to exclude some of the spuriously low points from the data (these can be seen in figure 6.22 as triangles). Also, a Lorentzian was a very poor fit to this feature so a Gaussian was used. The next feature to appear at 003 is also not quite captured by the five point scan. Because of this the profile is not well defined and so the resolution convolution fails. Because the feature is still very broad and so well outside the instrumental resolution it was fitted with a single Lorentzian, with the background constrained to the value seen in higher field data points where the background is accessed. All of the sharper features at fields above 0.4 T were successfully fitted by the resolution convolution procedure, two examples are shown in figure 6.22.

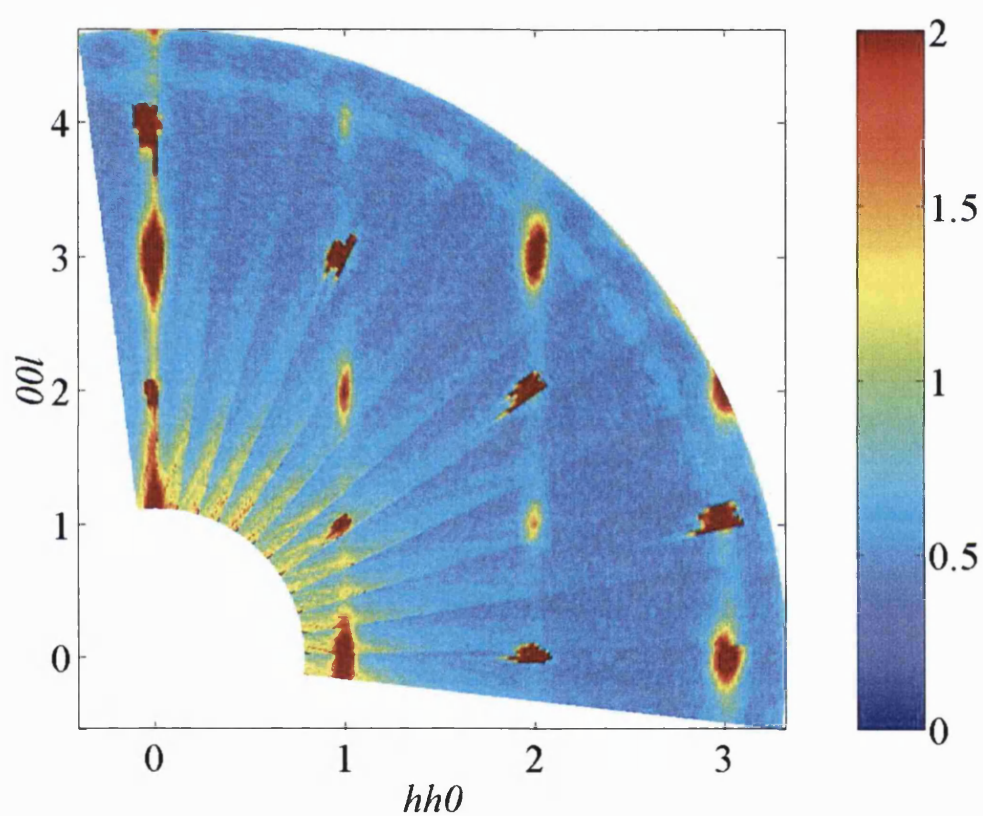


**Figure 6.21:** Scattering intensity in the  $hhl$  plane recorded on PRISMA at 0.05 K and 1.5 T.

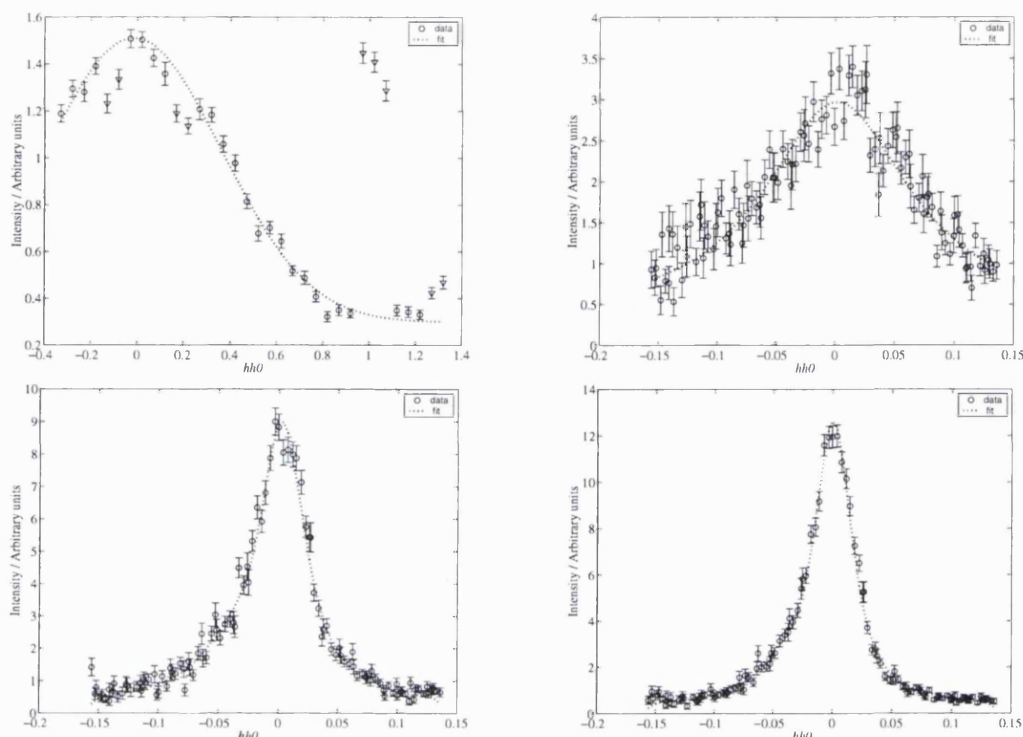


**Figure 6.22:** Fits used in the extraction of intrachain correlation lengths from the 003 feature. In zero field a single Gaussian was used, in small fields ( $< 0.4$  T) a single Lorentzian, in larger fields a double Lorentzian was convoluted with the instrumental resolution.

The field dependence of the intrachain correlation length is shown in figure 6.23. The correlation length is given in angstroms although the fitting was carried out in units of  $hh0$  since this is the most convenient way to work with the data. The experimental resolution limit in this direction is estimated to be  $\approx 2100 \pm 210$  Å.

The extraction of the interchain correlation length raised similar problems to the intrachain. The broadest feature at low field is visible in the scattering map, but statistics are insufficient to distinguish it in a single detector trajectory in the rocking scan. Consequently the correlation length was obtained from the map data and the same value was used for all similar features. The correlation lengths are shown in figure 6.23.

The intensities of the Bragg peaks 002, 004, 006 and 008 were integrated using the box method described above. The integrated intensities as a function of field

are plotted in figure 6.23. The 004 peak is not shown as it does not change in intensity.

There are three major steps in the Bragg intensities which occur at fields of 0.1, 0.25 and 0.4 T. The 003 feature has two steps in its development at 0.25 and 0.4 T, and then the wavevector dependent susceptibility and correlation lengths continue to grow as the field rises, and while the field falls, until it reaches  $\approx 0.25$  T when the intensity of the feature collapses and it disappears. The long range correlations responsible for the Bragg scattering, and the shorter range correlations causing the  $Q = X$  features apparently grow synchronously. This simultaneous long and short range ordering is understood in the same way as for  $\text{Ho}_2\text{Ti}_2\text{O}_7$ . The field is pinning spins which have a component parallel to the field, into a long range ordered structure. This restricts the degeneracy of states considerably and so also causes the transverse spins to become more correlated than before. The transverse spins must order into domains of three dimensional order as the  $Q = X$  features are all localized in reciprocal space. There are some complications of this statement. A very weak but continuous intensity can be seen on  $[00l]$ . This could be a rod (in which case there is a two-dimensional structure parallel to  $[hh0]$ ) or the intersection of a sheet of scattering with the measured scattering plane (due to a one-dimensional feature parallel to  $[hh0]$ ).

The restriction of the degeneracy ideally produces chains parallel to  $[hh0]$  and so the non-Bragg scattering must be due to domains with three-dimensionally ordered short chains, giving the localized features, and in addition some chains which are ordered over much longer lengths causing the quasi-1d scattering pattern. The shape of the  $Q = X$  features means that the domains are highly anisotropic. The correlations are longer ranged parallel to  $[hh0]$  (intrachain correlation length) than they are parallel to  $[00l]$  (interchain correlation length). A single domain is therefore a collection of a few chains (with a maximum interchain correlation length  $\zeta = 16 \text{ \AA}$  this is 1.5 unit cells and so 4-6 chains), each extending up to  $1200 \text{ \AA}$  (maximum intrachain correlation length) and ordered antiparallel (required to put the features at the  $Q = X$  positions).

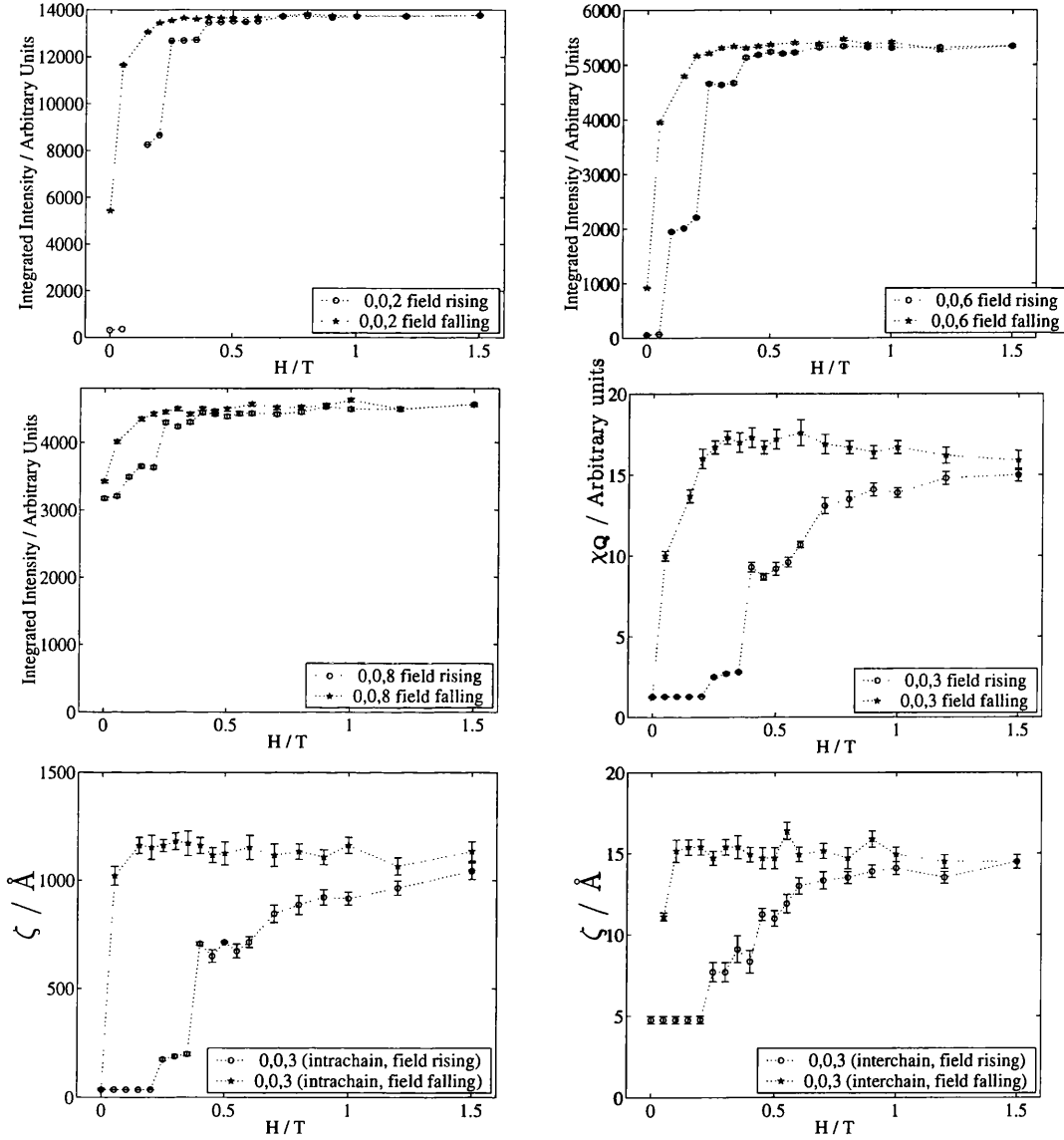


**Figure 6.23:** Hysteresis loop, second experiment,  $T \approx 0.05$  K, field applied on  $[h\bar{h}0]$ . Integrated intensities of 002 and 006 (top left and right), and 008 as a function of field, 004 maintained a constant intensity of  $\approx 20000$  counts. The amplitude (middle right) of the 003 feature, and the correlation lengths extracted from it are also shown (intrachain bottom left, interchain bottom right).

### Warming and Cooling in an Applied Field

After the hysteresis loop had been measured a brief investigation of the temperature dependence of the spin correlations was made. The temperature was raised from  $T \approx 0.05$  K to 0.9 K in a field of 1.5 T. Because time was short the fine scans in omega could not be used and so a single point was collected at each temperature. This means that the resolution is considerably compromised. The  $0, 0, l$  features now fall in a single detector trajectory so that the correlation length, at least in the transverse sense (intrachain), is meaningless. The shape of the feature is still fully defined in the longitudinal sense and so the interchain correlation length can still be extracted.

The  $00l$  Bragg peaks all maintained constant intensity. A complicated temperature dependence was observed for the longitudinal correlation length and wavevector dependent susceptibility at 003. These are shown in figure 6.24. In such a high field the temperature scan is unable to affect the field pinned spins. Therefore the Bragg intensities remain constant. The same effect was observed for  $\text{Ho}_2\text{Ti}_2\text{O}_7$  on D10. The behavior of the 003 feature is also similar to  $\text{Ho}_2\text{Ti}_2\text{O}_7$ . As the temperature increases the correlation lengths grow, so the system is becoming more ordered. This must mean that the transverse chains are becoming more ordered, since the parallel chains are unchanging (constant Bragg intensity). This process sharpens the feature parallel to  $[00l]$  (lengthening the interchain correlation length) showing that number of chains in the domain is increasing. Without the intrachain correlation length no information about the chain length in the domain is available. The growth of the domains is thermally activated. Raising the temperature increases the dynamics allowing more ready chain reorientation. This is followed by a thermal disordering and the correlation length begins to fall. However, on cooling the correlations are re-established and the system is cooled into a more correlated state than before the temperature scan.

#### 6.4.2 Results of the Third Experiment

Similar measurements were carried out in the third experiment. The path through the field and temperature history was quite complicated, so in this section each

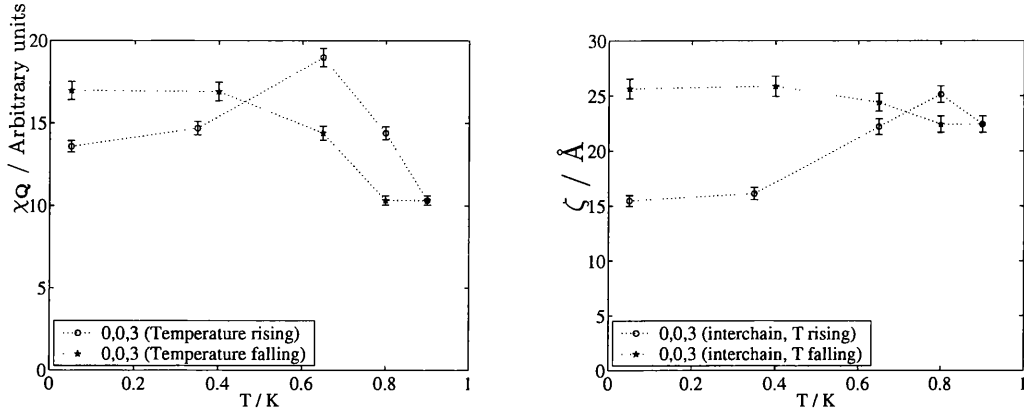


**Figure 6.24: Temperature scans, second experiment,  $H= 1.5$  T on  $[h\bar{h}0]$ .**  $\chi_Q$  at 003, and the interchain correlation lengths extracted from the 003 feature are shown (002 – 8 maintained constant intensities, the intrachain correlation length is not available due to the low resolution scan employed).

segment of this path is described and the results presented. Comparisons are made in the next section. All the data has been reduced in the same way as for the second experiment, by integration or resolution convolution. New parameters were obtained for the resolution functions.

### Hysteresis Loop at Base Temperature

After cooling in zero field a hysteresis curve was measured. In this experiment considerably more field points were used. This has defined the steps in the curves much more clearly (figure 6.25). Also it demonstrates their reproducibility. This time the steps come at 0.15 and 0.3, and there is a minor one at 0.5 T. There are two steps in the wavevector dependent susceptibility at 0.325 and 0.5 T. These are followed by smooth and continued growth during both the field rising and falling sections of the loop until the field has fallen back down to  $\approx 0.3$  T.

### Warming in Applied Field

After the hysteresis loop was completed the field was raised to 0.4 T again and the temperature scanned (figure 6.26). The temperature was raised to 0.9 K, at which point temperature control was lost so the next measured data point occurs at 1.9 K. This time a marked effect can be seen on the Bragg peaks, most clearly

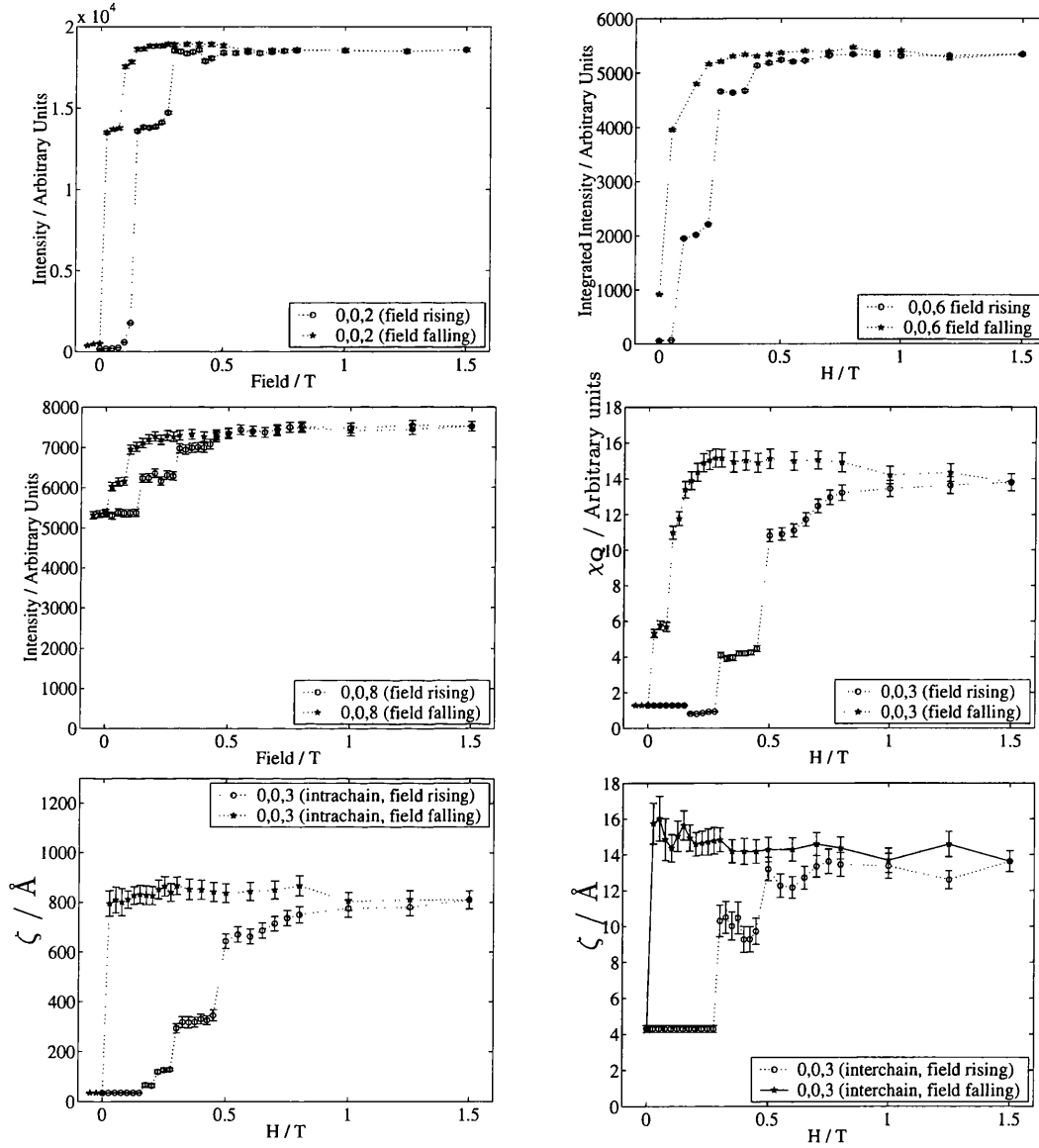


**Figure 6.25: Hysteresis loop, third experiment,  $T \approx 0.05$  K, field applied on  $[h h 0]$ .** Integrated intensities of 002 and 006 (top left and right), and 008 as a function of field, 004 maintained a constant intensity of  $\approx 20000$  counts. The amplitude (middle right) of the 003 feature, and the correlation lengths extracted from it are also shown (intrachain bottom left, interchain bottom right).



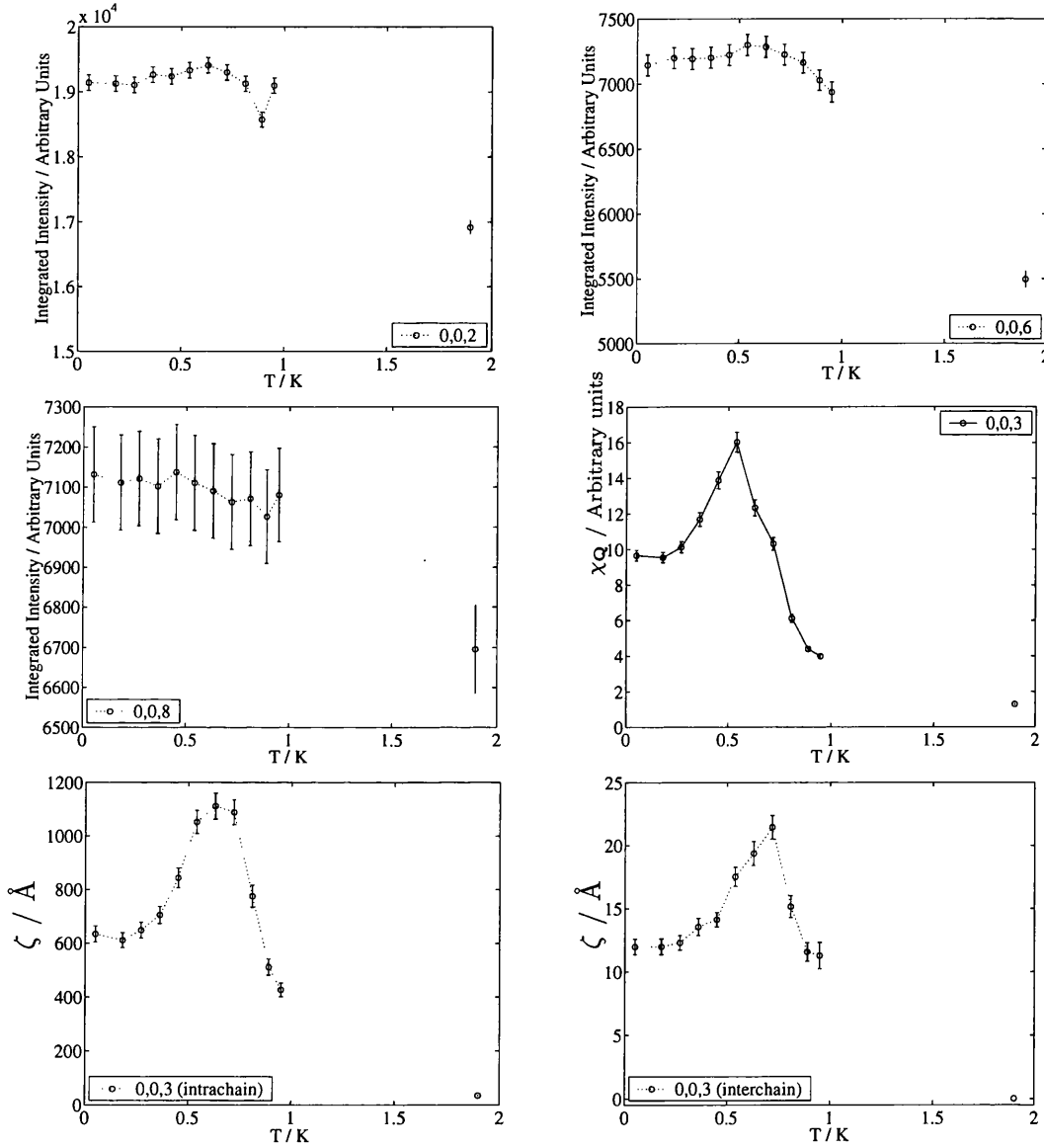


**Figure 6.26:** Rising temperature in applied field, second experiment,  $H = 0.4$  T on  $[h\bar{h}0]$ . Integrated intensities of 002 and 006 (top left and right), and 008 as a function of field, 004 maintained a constant intensity of  $\approx 20000$  counts. The amplitude (middle right) of the 003 feature, and the correlation lengths extracted from it are also shown (intrachain bottom left, interchain bottom right).

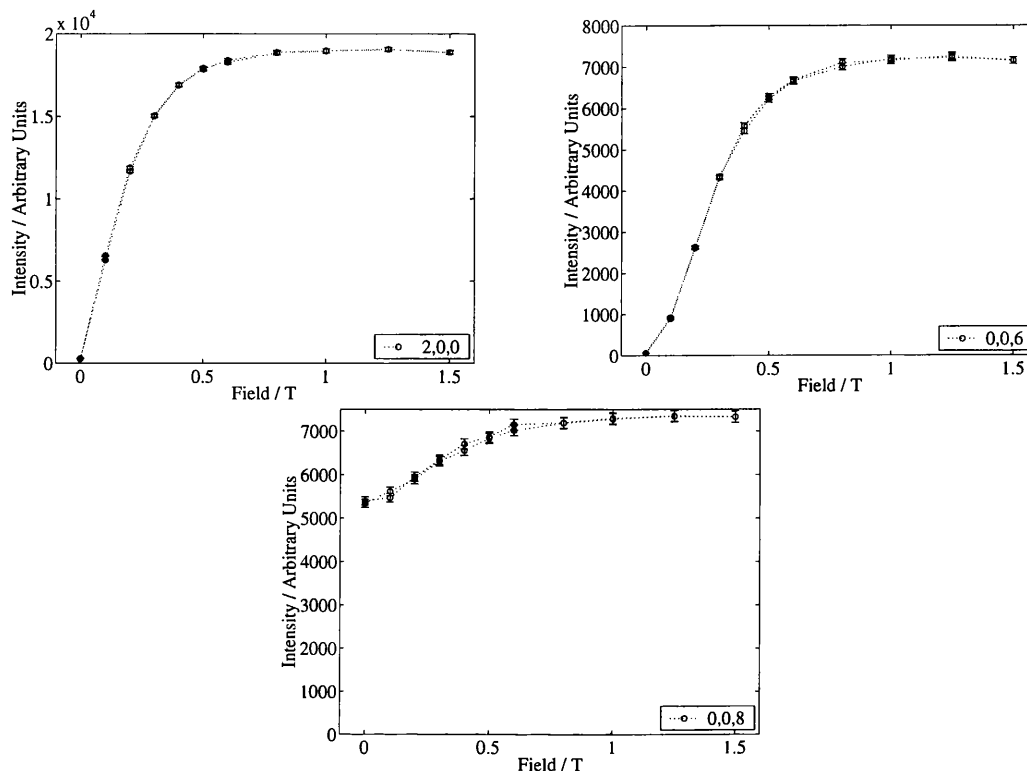


**Figure 6.27: Hysteresis loop, third experiment,  $T = 1.9$  K, field applied on  $[h\bar{h}0]$ .** Integrated intensities of 002 and 006 (top left and right), and 008 as a function of field, 004 maintained a constant intensity of  $\approx 20000$  counts.

006 which does begin to decrease significantly. The behavior of the 003 feature is remarkable. As the temperature is increased  $\chi_Q$  passes through a clear maximum, as do the correlation lengths.

### Hysteresis Loop at 1.9 K

At 1.9 K the field was removed and then a hysteresis loop recorded (figure 6.27). However, no actual hysteresis was observed. The Bragg peaks show smoothly developing long range order. No correlation lengths were extracted as the 003 feature does not grow into a peak at this temperature. Scattering above the background is evidently present at these positions but is too broad to be captured by the five point scan.

### Field Removal After Field Cooling

The sample was then cooled in 0.4 T (figure 6.28). Temperature control was not possible so no intermediate data points could be measured. This part of the measurement sequence therefore begins at 0.05 K and 0.4 T. The field was then lowered to zero. Cooling in a field establishes both long and short range correlations. The Bragg peaks have reappeared, showing that the parallel chains have been re-established by the field. The  $Q = X$  features have reappeared, showing that the transverse chains have become correlated into domains of ordered chain sections again.

### First Hysteresis Loop at 0.3 K

The temperature was then raised to 0.3 K and a hysteresis loop was recorded (figure 6.29). This loop features rather coarse field stepping and so compares most readily with the base temperature loop from the second experiment. Proper steps are not really developed in the growth of the Bragg peaks. Instead the hysteresis curve has several inflexions.  $\chi_Q$  develops almost completely smoothly and again continues to grow, even while the field is falling.

### Second Hysteresis Loop at 0.3 K

After the first loop a remnant magnetization remained, the temperature was raised to 0.7 K (above the susceptibility peak of Fukuzawa and Matsuhira [65, 67]) and this proved sufficient to remove the remnant. The sample was cooled back to 0.3 K and a second loop begun with much finer field stepping (figure 6.30). This loop compares with the base temperature loop from this experiment. The intention was to measure a full hysteresis loop in this way, but time was insufficient and so only a magnetization curve for the rising field was actually obtained. The development of both the Bragg peaks and  $\chi_Q$  was completely smooth.

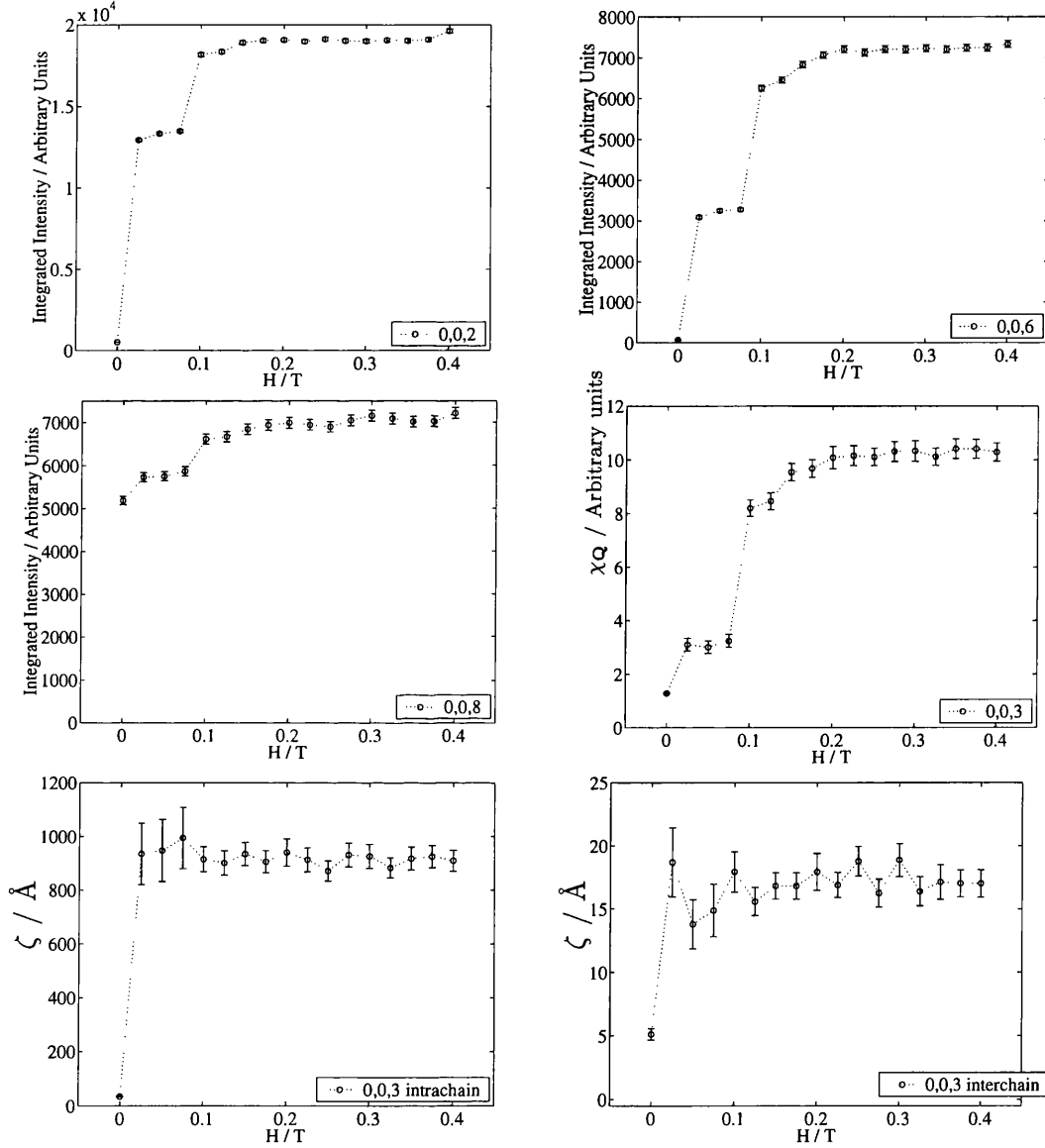


**Figure 6.28: Field Removal after field cooling, third experiment,  $T \approx 0.05$  K, field applied on  $[h\bar{h}0]$ .** Integrated intensities of 002 and 006 (top left and right), and 008 as a function of field, 004 maintained a constant intensity of  $\approx 20000$  counts. The amplitude (middle right) of the 003 feature, and the correlation lengths extracted from it are also shown (intrachain bottom left, interchain bottom right).

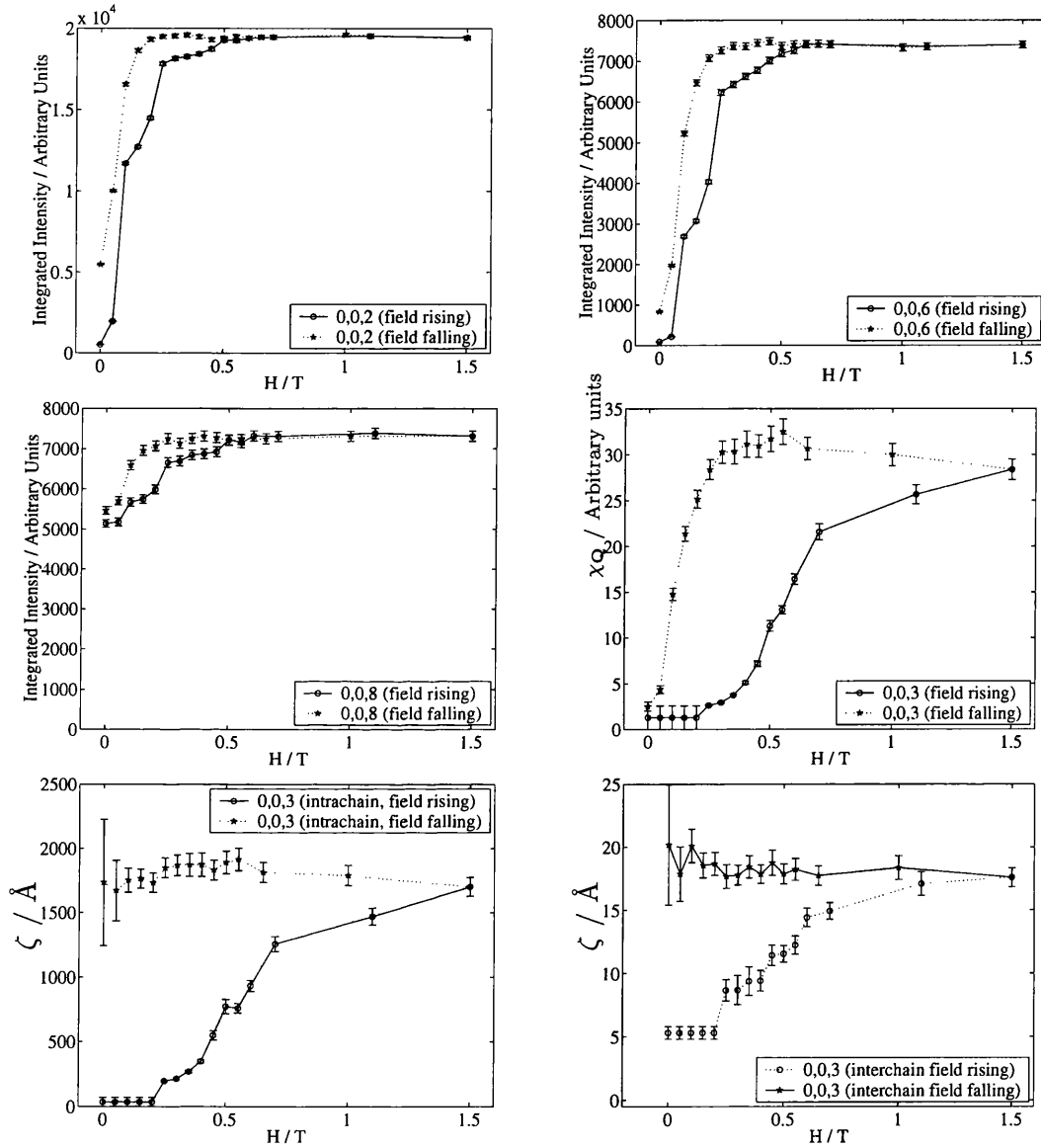


**Figure 6.29:** First Hysteresis loop, third experiment,  $T = 0.3$  K, field applied on  $[h\bar{h}0]$ . Integrated intensities of 002 and 006 (top left and right), and 008 as a function of field, 004 maintained a constant intensity of  $\approx 20000$  counts. The amplitude (middle right) of the 003 feature, and the correlation lengths extracted from it are also shown (intrachain bottom left, interchain bottom right).

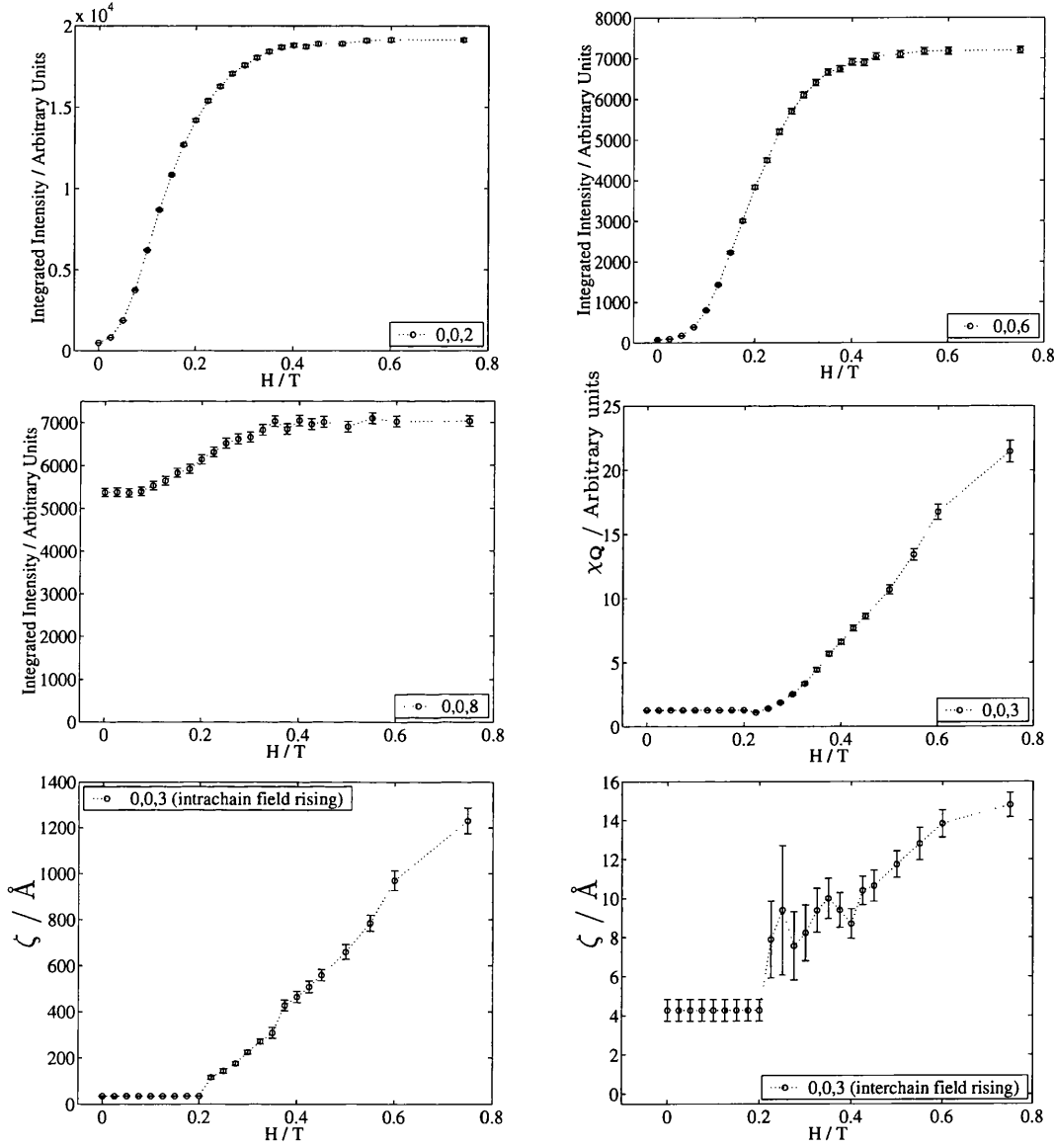


**Figure 6.30:** Second Hysteresis loop, third experiment,  $T = 0.3$  K, field applied on  $[h\bar{h}0]$ . Integrated intensities of 002 and 006 (top left and right), and 008 as a function of field, 004 maintained a constant intensity of  $\approx 20000$  counts. The amplitude (middle right) of the 003 feature, and the correlation lengths extracted from it are also shown (intrachain bottom left, interchain bottom right).

### 6.4.3 Computational Investigations of Model Systems

Two approaches have been followed in attempts to model this data. The first was an attempt to understand the step in the magnetization curve. The second was an investigation of the diffuse scattering in high fields.

The step in the magnetization curve (e.g. figure 6.25, top left) was hypothesized to be due to the formation of a triangular antiferromagnet of chains. It was envisaged that the field would separate the spin system into chains. At first the interaction between chains would compete with the field. This would lead to some chains being opposed to the field, and the  $0,0,2$  intensity would not be fully developed. Then the field would overwhelm this interaction and align all the chains, saturating the Bragg intensity. This was why the structure factor of models based on the Niitaka models for  $\text{Ca}_3\text{CoRhO}_6$  were studied [98]. Because  $Q = X$  peaks appeared when chains were aligned antiparallel, regardless of whether they were parallel or perpendicular to the scattering plane, this model for the developing magnetization was discounted.

The second type of study was the calculation of diffuse scattering from a variety of systems, to try to reproduce the pattern of diffuse scattering shown in figure 6.21. All the calculations proceeded in the same way. A fully ordered supercell was constructed with size up to  $20 \times 20 \times 20$  unit cells. The ordered structure would either be  $Q = 0\ 45^\circ$ , or  $Q = X$ . The system would then be “adjusted” to give a partially disordered structure. The structure factor for appropriate points in the  $hhl$  plane was then calculated.

The crucial stage is the adjustment. A series of algorithms ( $a - n$ ) were produced, each of increasing complexity. All the adjustment algorithms rely on an entirely mechanical mechanism. The orientation of a chain is determined by comparison to a random number and a threshold, it is then flipped over or not, depending on the criteria.

The simplest model is to flip chains at random, in this case the system becomes a set of chains parallel to the field, with completely disordered perpendicular chains. No scattering is calculated at the  $Q = X$  positions. The more complicated models involve attempts to produce domains of chains. The most complicated model involves a growing front of tested chains spreading across the system, with

the flipper sign preserved between successive moves in a specific direction (this is clarified somewhat in figure 6.31).

It is difficult to produce a system with some degree of correlation, but no extra correlations, using only such a mechanical process. An alternative scheme for producing suitable correlations is to use spin configurations from a Monte Carlo simulation of a 2-dimensional Ising model [128]. This approach has not been extended very far, two examples are shown in figure 6.32. Extra work is required to characterize the Ising model itself, these examples are simply taken near  $T_c$  when the correlation is finite, but there appears to be a system size dependence on the type of domains formed. Also it appears that better resolution is required in the scattering calculation, and so a faster code to operate with larger systems is required. This could be achieved quite simply by rewriting the existing code (in MatLab) in a compiled language such as C++.

The calculations lend support to the hypothesis that the system contains parallel ordered chains, and transverse partially ordered chains. Currently the chains are system spanning, introduction of disorder within the transverse chains is expected to make the model even more realistic.

#### 6.4.4 Summary of the Third Experiment and Comparison with the Second

The path through the field and temperature history taken in the third experiment was quite complicated. Individual sections have been described above. However, it is also essential to compare some of these sections. Also during both the second and third experiments a hysteresis loop was measured at 0.05 K, and the temperature was raised in an applied field so these sections can also be compared.

Comparison of hysteresis loops measured at the same temperature reveals that the form of the curve depends on the field stepping regime used to record the loop. For both 0.05 K and 0.3 K two different hysteresis loops have been measured. At each temperature one loop was recorded with a coarse field stepping regime. Subsequent investigations used a finer stepping regime to investigate the pattern of steps in greater detail. These are shown in figures 6.23 and 6.25 for 0.05 K, and 6.29 and 6.30 for 0.3 K. The effect of changing to fine field stepping has been



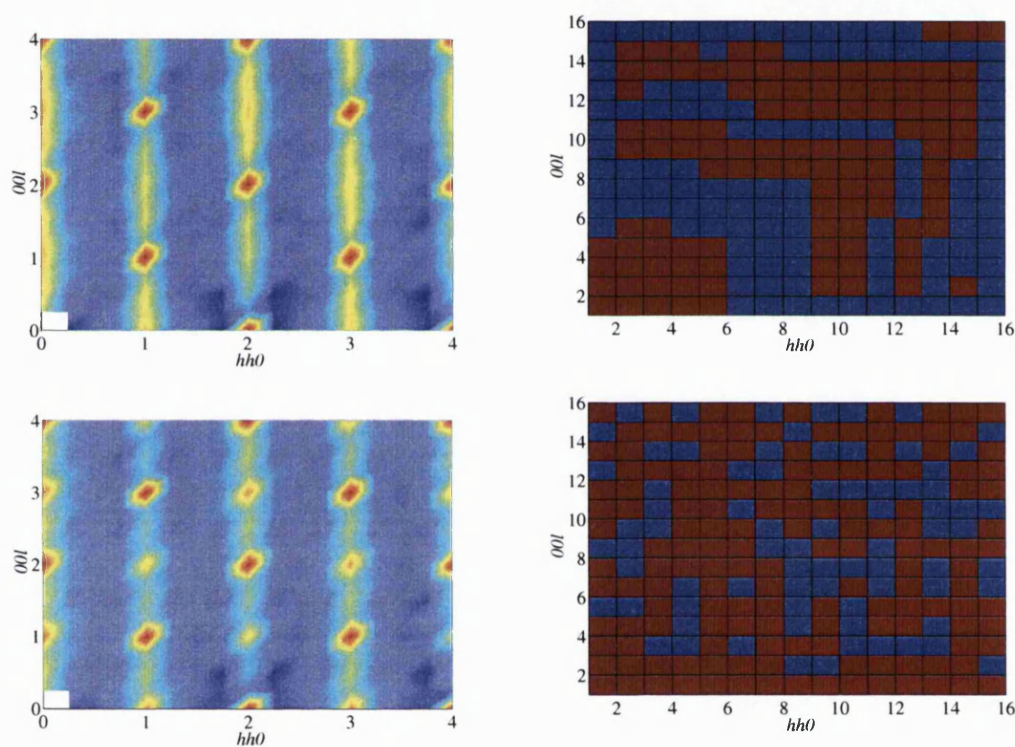


**Figure 6.31:** Calculated diffuse scattering patterns for application of field on  $[hh0]$  (top and bottom left). The logarithm of the calculated intensity is shown, as the Bragg scattering is extremely intense. The supercell size is  $8 \times 8 \times 8$  and ten successive calculations have been averaged. The pattern of chains in a single configuration is represented at top and bottom right. It can be seen that the less sophisticated adjustment routine (top) has very artificial domain shapes.

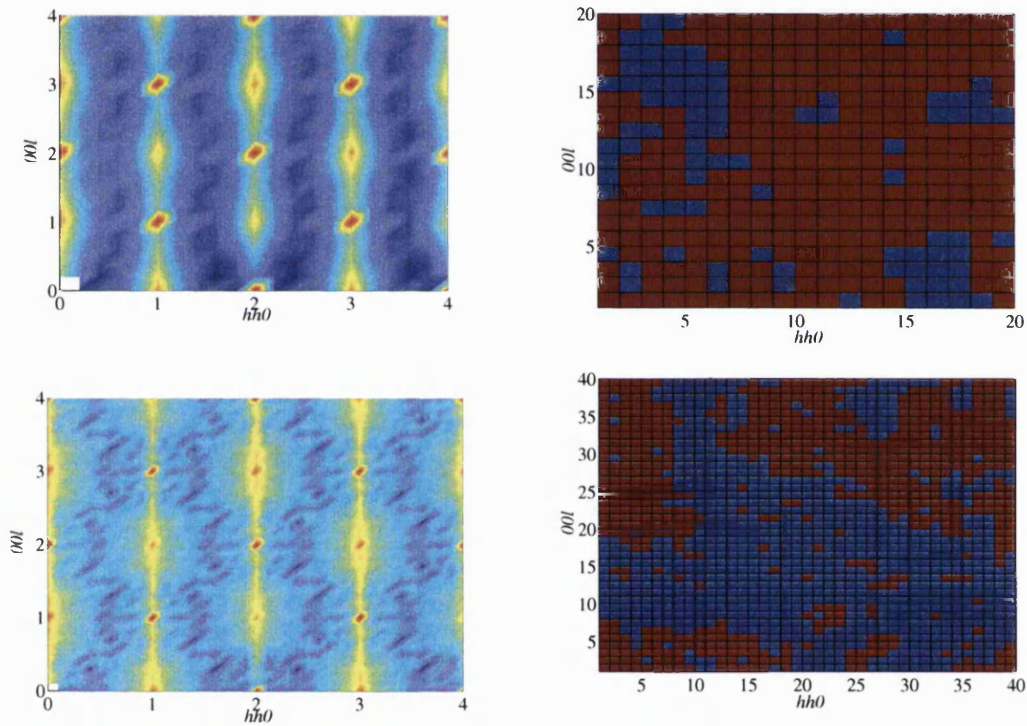


**Figure 6.32:** Calculated diffuse scattering patterns for application of field on  $[hh0]$  (top and bottom left). The logarithm of the calculated intensity is shown, as the Bragg scattering is extremely intense. The transverse chains have been organized according to spin configurations of a 2-d Ising model. Averaging the scattering using ten randomly chosen configurations (from 1000 Metropolis steps) such as the one at top right gives scattering as at top left ( $L = 10$ ). Bottom right shows a calculation using a single configuration and a system size of  $L = 20$  (pyrochlore unit cells, the 2-d Ising is  $40 \times 40$ ).

to smooth the changes in intensity, to reduce the apparent number of steps and to define others more clearly. Also, there is a clear difference between 0.05 K and 0.3 K, particularly with fine field stepping. With fine field stepping at 0.3 K the steps are completely lost and a very smooth increase in intensity is observed (compare figures 6.25 and 6.30). At 1.9 K no hysteresis was observed. At this temperature the sample is not in the history dependent regime. The comparisons are also illustrated in figure 6.35.

Since the sample is in some kind of frozen, non-equilibrium state, the rate of field change compared to the relaxation of the magnetization becomes an important variable. Apparently the timescale for relaxation is of the same order as the time taken for field steps (this is very surprising as the count rate on PRISMA means the field was being stepped approximately hourly making the dynamics astonishingly slow). With coarse stepping the magnetization is unable to relax sufficiently rapidly and more metastable states are accessed. With the fine stepping the relaxation keeps pace with the field scan. Between 0.03 and 0.3 K an energy scale must be crossed since even with fine field stepping at 0.05 K a step is clearly observed. At 0.3 K this step is barely visible with fast stepping and not at all with slow stepping.

These experiments were not conducted with the consideration of the rate of field change foremost in their planning. In order to access information on this quantity the time of data collection for each point must be used. The time dependence of the applied field is shown in figure 6.33. The disparity in the fine and coarse field stepping regimes is further illustrated in figure 6.34. Clearly the rate at which the field was swept is an important parameter. Also the behavior of the 003 feature with its continual sharpening above some field (see figure 6.37) suggests that the total length of time for which the field was applied is important, in terms of the aging of the system.

Four temperature scans were made. In the second experiment the temperature was raised and lowered in 2 T (figure 6.24), in the third experiment the temperature was raised and lowered in 0.4 T (figure 6.26). The Bragg peak intensity is attributed to the field pinned chains. The two fields studied contrast. In 2 T the field is sufficient to maintain these chains without any decrease in order up to the

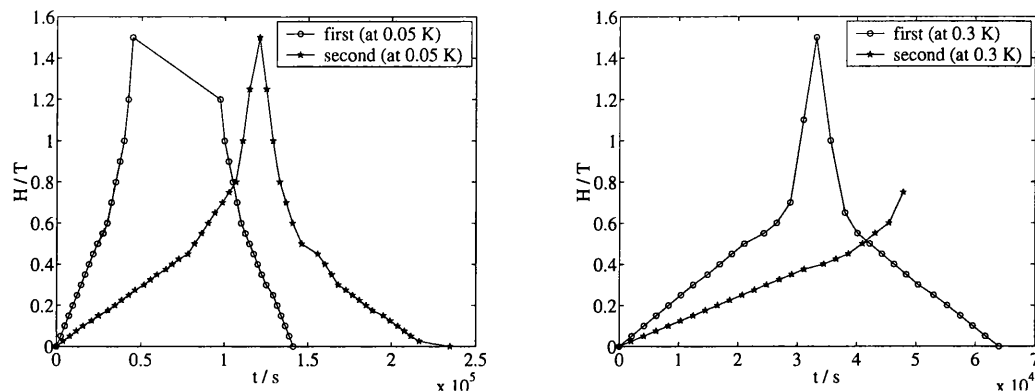


**Figure 6.33:** The time dependence of the applied magnetic field in the four hysteresis loop measurements. The large gap in the first experiment at 0.05 K is due to a long wait whilst a map was made.

highest temperature studied (0.9 K). In 0.4 T the Bragg peaks begin to decrease at higher temperatures showing that thermal fluctuations are able to compete with the smaller field at temperatures of order 0.5 – 0.75 K.

During the hysteresis loops at base temperature the field of 0.4 T has two different states, depending on the history of the sample. After cooling in a field of 0.4 T the sample accesses the second state seen in the hysteresis loop. On removal of the field the falling intensity tracks that observed in the hysteresis loop (figure 6.36). When ramping the field from the spin ice state the dynamics are not sufficiently fast to allow the parallel chains to reach their maximum potential magnetization and a metastable state is observed. Cooling in the field means that at higher temperatures faster dynamics allow spin reorientation and so the parallel chains reach base temperature fully magnetized. An interesting point about this measurement is that while the parallel chains cool into their saturated state, the transverse part of the system is still only short range ordered. Despite going to a high temperature of 1.9 K the transverse chains do not cool into an ordered state. It may be that the rate of cooling represents a quench and disorder is frozen into this part of the spin system.

The Bragg peak intensities always saturate at the same value. This must be due to the field completely ordering these chains. Once this happens no further increase in intensity is expected. The 003 feature is more complicated. A single

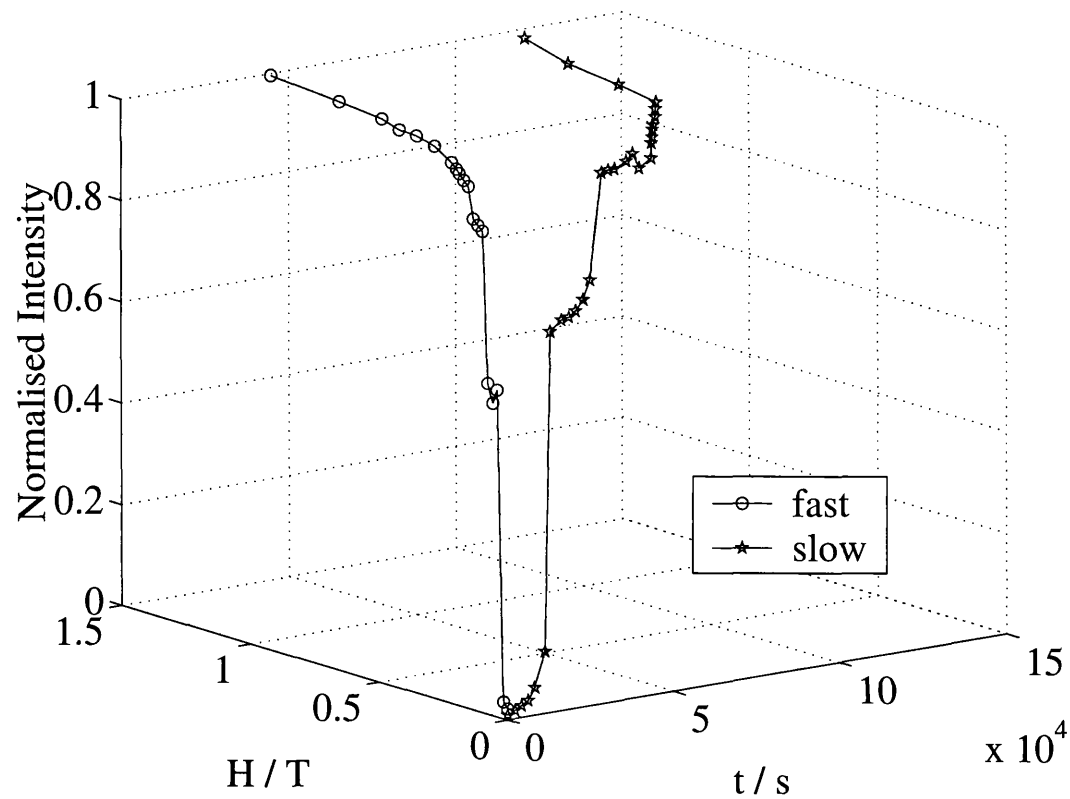


**Figure 6.34:** Time and field dependence of the 002 peak during the rising field section of hysteresis loops measured at 0.05 K in the second and third experiments.

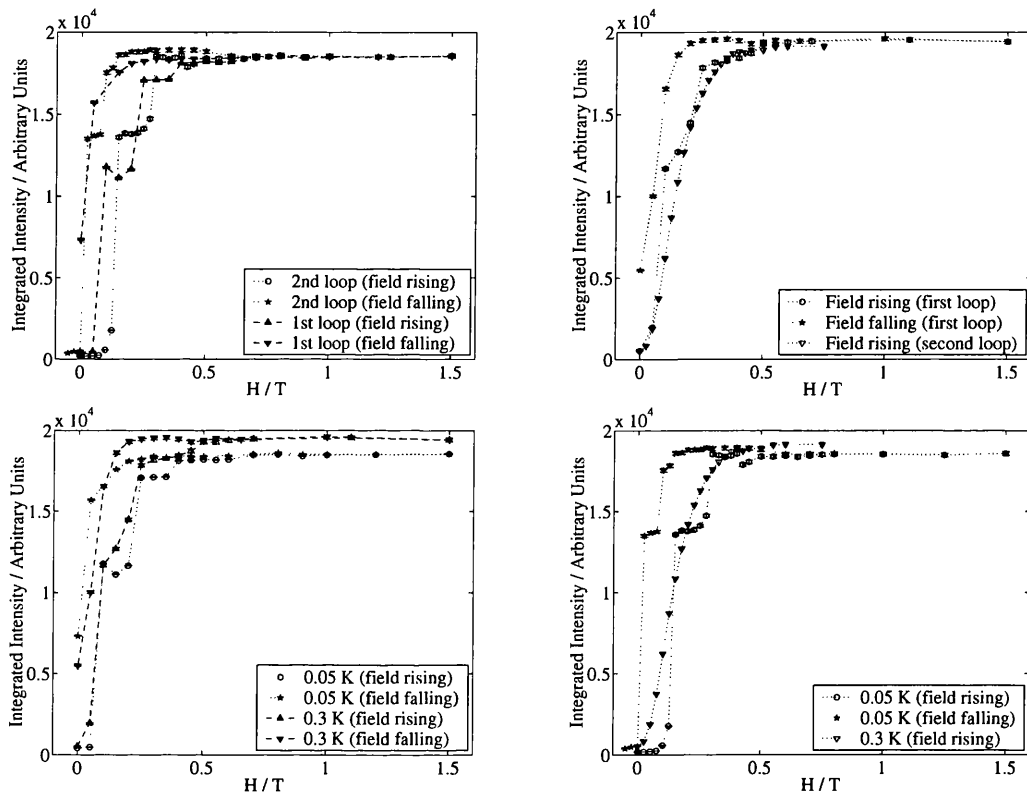


**Figure 6.35:** Comparison of hysteresis loops at different temperatures or with different field stepping regimes. At 0.05 K the change of field stepping smooths the curve (top left, the first loop is from the first experiment and has been scaled to match the second). At 0.3 K finer field stepping entirely removes the steps (top right). The bottom left figure shows the coarse field stepping loops at 0.05 K (scaled to the 0.05 K loop of the second experiment) and 0.3 K. The bottom right shows the fine field stepping loops at 0.05 and 0.3 K.

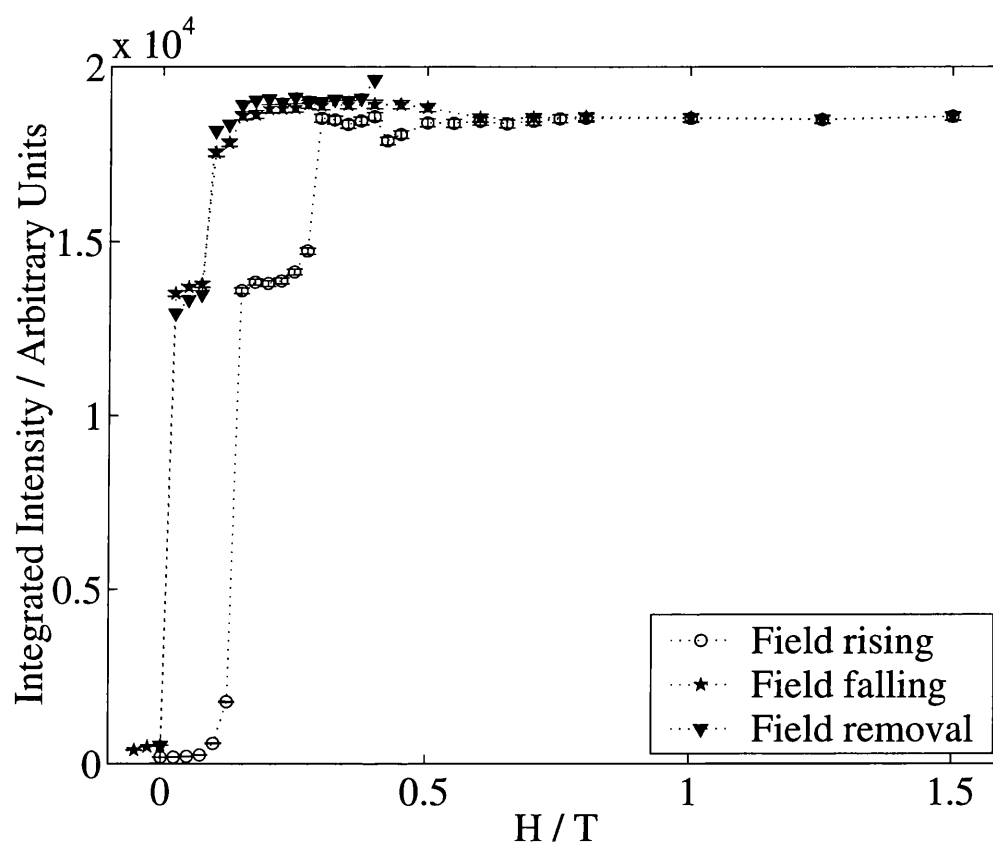


**Figure 6.36:** Field dependence of the 002 peak during a hysteresis loop at 0.05 K and after cooling to the same temperature in 0.4 T.

representation of its amplitude during certain sections of the third experiment is shown in figure 6.37. The three chief observations to be made about this figure are that during the field warming the feature grows and then falls (rather than just falling), that at 0.3 K the feature grows much more intense than it does at 0.05 K, and that above a “threshold field” of  $\approx 0.3$  T the feature is continually sharpening. The field cooling section of the experiment is not shown in this picture as the lack of temperature control means it is represented by a single data point lying on the return branch of the hysteresis loop at base temperature. The fact that the 003 feature still exists after this process and is not a Bragg peak is also important.

These facts suggest that there is a definite selection of a subset of states. This selection is inhibited at base temperature and is accelerated at higher temperatures. Increasing the temperature promotes the sampling of states in the manifold by accelerating the spin reorientation dynamics. Below the peak in  $\chi_{003}$  at 0.6 K (in the field warming scan) the system is in a regime where the energetics of increasing correlations outweigh the randomizing effect of thermal fluctuations. Therefore increasing the temperature supplies more rapid dynamics allowing greater relaxation into the favored states. Higher fields, as accessed in a hysteresis loop at 0.3 K, constrain the parallel spin chains more rigidly and this also reduces disorder in the transverse spins which are coupled to them. However, despite the fact that there appear to be favored states, it seems that the degeneracy either cannot be completely removed, or that the dynamics are still controlling the access to the ordered state. Field cooling from the dynamically free regime at 1.9 K, which results in order in the parallel chains, would be expected to produce the long range ordered  $Q = X$  type structure. After all, the system has the degeneracy restricted by the field, the temperature lowered so that interactions will overcome the thermal fluctuations, and yet dynamics should have been preserved to fully anneal the transverse chains. The fact that this does not occur may be due to quenched magnetic disorder in the chains due to a rapid cooling, as suggested above, or because the degeneracy removing energetics are still frustrated [62].



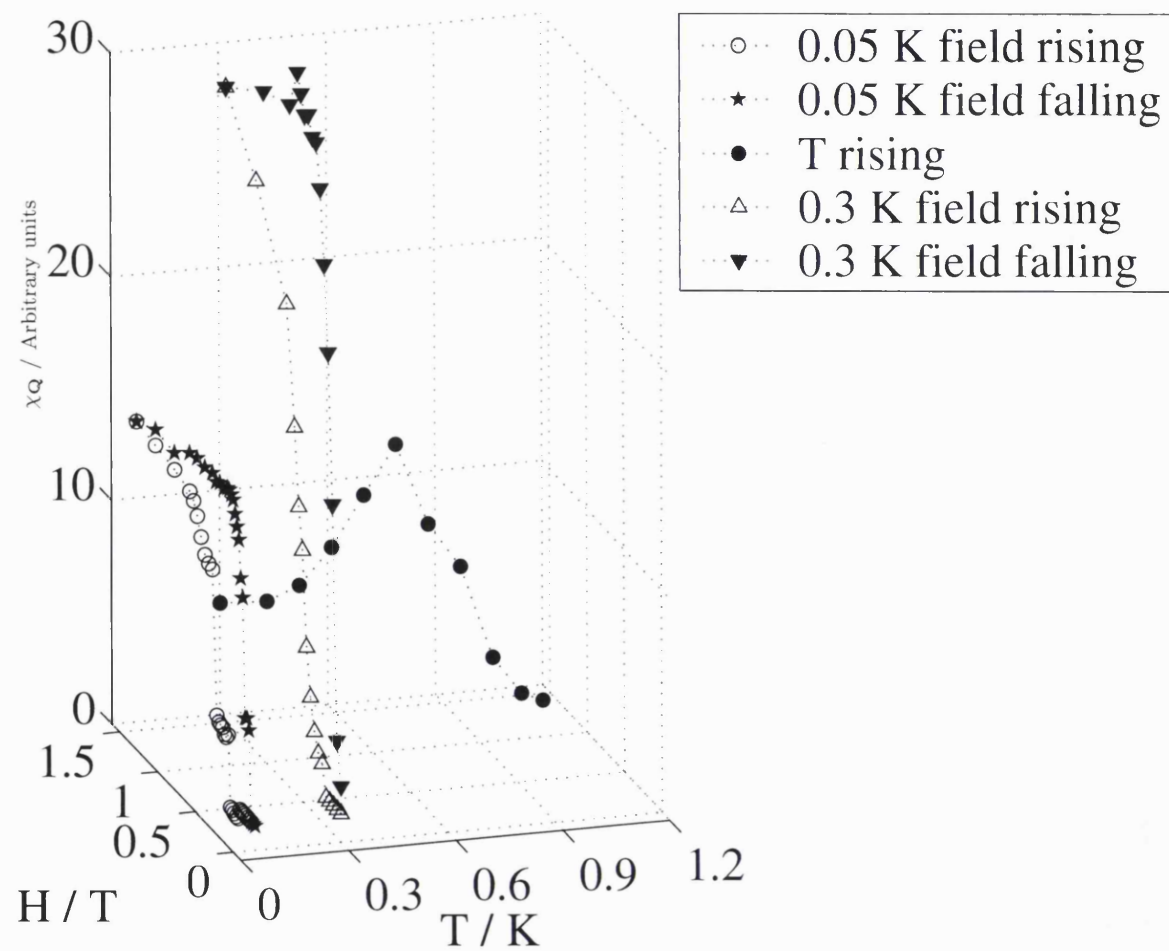


**Figure 6.37:** Field and temperature dependence of the amplitude of the 003 feature.

# Chapter 7

## Discussion and Conclusions

Over the course of the two preceding chapters, a large amount of neutron scattering data has been presented, and often explanations have been advanced for the features of each data set. Here I wish to draw together all that has been learnt about the two compounds, and spin ice physics during this work.

These comparisons can be difficult to make, because the two compounds were studied on different instruments. The type of information available from D10 and PRISMA is rather different, and the time scale of the experiments is also different. On PRISMA a single detailed scan such as those used in the  $[h\bar{h}0]$  experiment takes around an hour. On D10 the equivalent measurement, which was a small collection of Bragg reflections, takes around 10 minutes. This is partly why a much greater part of the phase space of  $\text{Ho}_2\text{Ti}_2\text{O}_7$  was covered on D10. The division of the two materials between the two instruments is essentially historic.

### 7.1 Dysprosium Titanate and the Dipolar Spin Ice Model

The measurements presented here are the first microscopic measurements of the properties of  $\text{Dy}_2\text{Ti}_2\text{O}_7$ . Previously only the heat capacity [56], susceptibility [65, 66] and kagomé ice studies [78, 79] have been published. Owing to the more complicated heat capacity of  $\text{Ho}_2\text{Ti}_2\text{O}_7$ ,  $\text{Dy}_2\text{Ti}_2\text{O}_7$  has been advanced as the more ideal spin ice [56, 80]. Comparison of the neutron scattering data with the predictions

of the nearest neighbor and dipolar spin ice models represents a new and detailed test of the theories of spin ice. No formal comparison to the nearest neighbor spin ice model was made, as simulation data specifically for  $\text{Dy}_2\text{Ti}_2\text{O}_7$  does not exist. It can be seen by comparing the appropriate simulation for  $\text{Ho}_2\text{Ti}_2\text{O}_7$  (figure 2.4) with the experimental data at 1.3 K (figure 6.8) that there is a qualitative match at this temperature. More detailed comparisons of the dipolar spin ice model and the experimental data were made, these are shown in figures 6.14, 6.15 and 6.16. It was concluded that the dipolar spin ice model provides a successful basis for understanding  $\text{Dy}_2\text{Ti}_2\text{O}_7$ , but that there are issues which remain to be clarified. The mismatch between theory and experiment at the zone boundaries in the  $hhl$  plane remains unexplained.

## 7.2 Dynamical Regimes in Spin Ices

Both sets of experiments show that there are distinctive dynamical regimes in spin ices. This was particularly evident for  $\text{Ho}_2\text{Ti}_2\text{O}_7$  over the course of the three experiments, but can also be extracted from the  $\text{Dy}_2\text{Ti}_2\text{O}_7$  data. Paramagnetic  $\text{Dy}_2\text{Ti}_2\text{O}_7$  at 20 K exhibits no structured diffuse scattering (figure 6.7). At 1.3 K the diffuse scattering resembles the nearest neighbor spin ice model (figure 6.8). As the sample is cooled into the strongly history dependent temperature range, these correlations evolve further to give the diffuse scattering pattern which strongly resembles the dipolar spin ice model (figures 6.14 and 6.15).

The experiments on  $\text{Ho}_2\text{Ti}_2\text{O}_7$  showed that in the sub-5 K temperature range, there are at least three distinctive dynamical regimes. The first is not tremendously interesting in this study as it cannot be effectively probed using these instruments. It is paramagnetic, but known to have non-trivial dynamics (the “hot spin ice” phase is discussed in section 2.4 and by Ehlers *et al.* [69]). The second is found around 1.9 K for  $\text{Ho}_2\text{Ti}_2\text{O}_7$  and in this situation the spins are strongly interacting, but the dynamics are still fast enough to keep the system in equilibrium on the experimental timescale, no history dependence is seen. This is evidenced by the lack of hysteresis in the magnetization curve at 1.8 K, with field applied on  $[h\bar{h}\bar{h}]$ ; and the experiment with field applied on  $[hh2h]$ . The importance of the  $[hh2h]$

data is the crossover into the ice rule regime which occurs between 1.9 and 5 K. At 5 K thermal fluctuations can overwhelm the spin-spin interactions, but at 1.9 K the free spin is clearly drawn into the ordered structure by its interactions with the field pinned spins.

These dynamical regimes account for the different appearance of the diffuse scattering in  $\text{Dy}_2\text{Ti}_2\text{O}_7$  at 0.3 and 1.3 K. At 1.3 K  $\text{Dy}_2\text{Ti}_2\text{O}_7$  is in the regime in which the spins are interacting, but still dynamic. It is captured by the nearest neighbor model. As it is cooled further, the longer range interactions and correlations of the dipolar spin ice model become important.

Ramirez distinguishes between systems such as ice, where the “symmetry-incompatibility is established at a lower energy scale than the interaction of the dynamical entities”, and systems such as metal oxides, where the global symmetry is established at a very high temperature compared to the interaction of the degrees of freedom [129]. In this respect the systems might differ, but there is a parallel in the sequence of dynamical regimes. In ice the liquid solidifies into a disordered solid, the protons are still dynamic. On cooling further the protons become frozen, and no ordered state has been realized. In a spin ice, if one considers only the spin degrees of freedom, as one does when drawing an analogy between ideal gases and paramagnets, the effect is the same. The system cools from a liquid like state of very short range correlations into the strongly interacting but disordered nearest neighbor spin ice phase. Then on further cooling the spins freeze before the ordered state can be selected.

### 7.3 Magnetization Plateaux

Both materials were studied with the field applied on  $[00l]$  at  $T \approx 0.05$  K. In both cases strong hysteresis and magnetization plateaux were observed. The pattern of steps is quite different.  $\text{Ho}_2\text{Ti}_2\text{O}_7$  has a step at 6/10 of saturation, whereas  $\text{Dy}_2\text{Ti}_2\text{O}_7$  has steps at 4/10 and 8/10 (figure 7.1). They were also both studied with the field applied on  $[h\bar{h}0]$  at  $T \approx 0.05$  K. Again clear plateaux developed in the magnetization curves. The importance of the rate of field scanning in this dynamical regime was highlighted in the study of  $\text{Dy}_2\text{Ti}_2\text{O}_7$  with the field applied

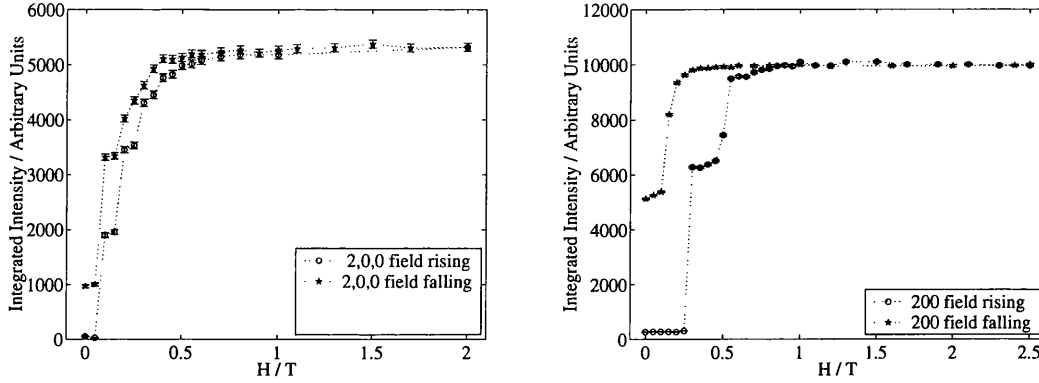


**Figure 7.1:** Comparison of hysteresis loops with field applied on  $[00l]$  for  $\text{Dy}_2\text{Ti}_2\text{O}_7$  (left) and  $\text{Ho}_2\text{Ti}_2\text{O}_7$  (right). The different pattern of steps may be due to intrinsic differences between the two materials, or different field sweeping regimes in a spin ice.

on  $[h\bar{h}0]$ , but no data exists to quantify its effect in the other orientation, or in  $\text{Ho}_2\text{Ti}_2\text{O}_7$ .

The observation of these steps is extremely interesting in itself. The fact that the two spin ices appear to differ, when in all other respects they are the same (or the differences can be clearly accounted for and are not central to the spin ice properties, e.g. the nuclear spin contribution in  $\text{Ho}_2\text{Ti}_2\text{O}_7$ ), is also very interesting. The question is whether the steps are intrinsic to the materials, or are a general property of a spin ice. If they are due to the properties of a spin ice, as is the plateau with the field applied on  $[h\bar{h}\bar{h}]$ , it would be expected that if the two materials could be made to follow the same  $H/T$  history, the curves would be the same. Herein lies a problem. Although data for the magnetization from the zero field spin ice state into the fully or partially ordered  $Q = 0$  and  $Q = X$  states is reported for both materials in this work, it does not fulfil this criterion. The rate of field sweeping on D10 is much faster than on PRISMA and so the histories are different. This is a great shame, as the presence of the plateaux must offer some key insight into the two materials.

A mechanism based on Macroscopic Quantum Tunneling of the magnetic moment (MQT) is very appealing. The very large magnetic moments and strong anisotropy could create a situation where such an effect could be observed for a

single moment. In other frustrated magnets fundamental spin dynamics have been shown to depend on coupled units of spins<sup>a</sup>, and such a unit might also relax by a MQT mechanism in this frozen regime<sup>b</sup>. This type of mechanism could produce a simple difference between the two spin ices due to different crystal field schemes. However, without detailed investigation of the dependence on field sweeping rate, it is overextending the data to conclude that because the two materials are different, the steps are intrinsic.

The steps may also be due to the magnetization processes of a spin ice. In this case the different measurements could be envisaged as different data points measured on some general spin ice. To put them on the same scale would require consideration of the energy scales of each compound, which are slightly different. Eventually the result would be hysteresis loops of the “general spin ice” measured at different rates and different temperatures, which would still be insufficient for examining the details of the process.

During the hysteresis measurements the  $Q = X$  positions were often monitored. It was found that in  $\text{Ho}_2\text{Ti}_2\text{O}_7$  with field applied on  $[00l]$ , that these features remained broad, and decreased coincidentally with the steps (see figure 5.8). Statistics on PRISMA in this section of the experiment were insufficient to follow the process. This shows that regions of short range order persist in the step phase. This was attributed to a process similar to work hardening in alloys in section 5.3.1.

Regardless of the relaxation process operating, the steps are a fascinating observation. They represent an interesting departure for new investigations into spin ice, and history dependent systems in general.

## 7.4 Field Regulated Dynamics

The longest continuous sequence of measurements was the entire hysteresis loop measured on  $\text{Ho}_2\text{Ti}_2\text{O}_7$  with the field applied on  $[h\bar{h}0]$ . It was in this part of

---

<sup>a</sup>For example in  $\text{ZnCr}_2\text{O}_4$ , where groups of six spins organize into weakly interacting antiferromagnetic loops, whose directors govern the low temperature dynamics [130].

<sup>b</sup>It is possible for a MQT mechanism to exhibit rate dependence, as the form of the hysteresis loop will depend on the balance between thermal and quantum relaxation [45].

the work that one of the most striking results of all was observed. This was the complicated field regulated dynamics. The data is shown in figures 5.12 and 5.16. Again the histories of the two samples were not identical. Disappointingly the full hysteresis loop, which was required to reveal the field regulated dynamics in  $\text{Ho}_2\text{Ti}_2\text{O}_7$ , could not be repeated for  $\text{Dy}_2\text{Ti}_2\text{O}_7$ . It would have been particularly interesting to see this process with the reciprocal space coverage of PRISMA.

The remarkable aspects of this sequence of measurements are the slowness of the dynamics, and the clear signature of a complicated, collective process in a strongly interacting system. The dynamics are extremely slow indeed. When the hysteresis loop is complete, the  $Q = X$  features are still flat within the  $\omega$ -scan, and the potential for order is still great (the features become very much sharper and more intense when the temperature is raised). Even when the parallel spin chains are being driven by the field, and dynamics are induced in the transverse system, they are not fast enough to produce order. The collective nature of the process is evidenced by the fact that the dynamics of the transverse chains are controlled by their interactions with the parallel chains. Only when the parallel chains are driven by the field are there any dynamics in the transverse chain. It is only because the transverse chains are coupled to the parallel chains that there are any dynamics at all.

Again this result motivates a question about the relaxation processes in a spin ice. Clearly these are also collective. Simple spin flips in the transverse spin system could be activated by temperature but not by the orthogonal field. Field induced flipping of parallel spins must propagate relaxation dynamics into the transverse system.

The other aspect of the collective behavior is the trend toward order in the transverse spin system. Each time the system passes through a field range where the dynamics of the transverse system are unfrozen, the level of order increases after some randomization. This is important in terms of the groundstate question discussed further below.

There is known to be a slight difference in energy scale between the two compounds. This is manifested in this work as the continued aging of  $\text{Dy}_2\text{Ti}_2\text{O}_7$  during the base temperature hysteresis loop. The dynamics in  $\text{Ho}_2\text{Ti}_2\text{O}_7$  are so

completely frozen that during the hysteresis loop they are entirely field regulated, and the  $Q = X$  features maintain identical intensities for the parts of the hysteresis loop when the field is maintaining the parallel chains static. In the same situation in  $\text{Dy}_2\text{Ti}_2\text{O}_7$  the  $Q = X$  features continue to grow, independently of the parallel spin chains, which are frozen. The energy scale of  $\text{Dy}_2\text{Ti}_2\text{O}_7$  is slightly lower than  $\text{Ho}_2\text{Ti}_2\text{O}_7$  and so some dynamics are preserved to lower temperatures.

## 7.5 Temperature Activated Dynamics

When the field is applied on  $[h\bar{h}0]$  to either system, the effect of increasing temperature is most striking. Like the field regulated dynamics, the temperature dependent measurements provide evidence of a complicated collective effect. With the parallel chains pinned by the field the dynamics of the transverse chains are regulated by the field. However, while the Bragg peaks due to the parallel chains are unchanged by temperature scans in fields of 1.5 T for  $\text{Dy}_2\text{Ti}_2\text{O}_7$  and 2.5 T for  $\text{Ho}_2\text{Ti}_2\text{O}_7$ , the  $Q = X$  features are radically altered. Increasing the temperature from 0.05 K activates the dynamics of the transverse spin system. However, it still remains strongly correlated. Not until the temperature is above 1 K do the  $Q = X$  features begin to decline. In the intervening temperature range the activated dynamics and strong correlations further increase the order of the system.

When the dynamics are induced by the field, the relaxation process must involve correlated motions of spins in both chain systems. Here only the transverse chains are changing, and so a new relaxation process is operative. Evidently with sufficient thermal energy it is possible for entire sections of chain to flip, or that the interactions are strong enough to propagate a spin flip along a chain section.

## 7.6 The $Q = X$ State and the True Groundstate

By far the most extensive part of the work is the study of the two materials with the field applied on  $[h\bar{h}0]$ . Although some of the data and quantities derived from it require conservative handling and interpretation, the value of neutron scattering is uncontrovertible for this work. The central conclusion in both studies was that



the spin system is separated into two subsystems. One is influenced directly by the field, and the other only feels the effect of the field by way of the first system to which it is coupled. Bulk techniques will currently say nothing about the second spin system. By employing neutron scattering we have learnt that highly anisotropic correlations build up in the transverse spin system as the parallel one is manipulated by the field.

As the degeneracy is restricted by applying the field and separating the spin sub-systems, the ordering of the parallel spin chains drives the formation of medium ranged correlations in the transverse system. Although the transverse system seems to evolve into favored states (for example if the temperature is increased so that its dynamics are freed from the parallel spin system then the correlations increase further), it does not ever fully order in the  $Q = X$  structure. The suggestions made earlier were just that the system was tending toward this structure. However, both systems were subject to high temperatures where the susceptibility is large, and so the dynamics should be relatively free, with degeneracy restricting applied fields. This seems like strong encouragement to the system to work its way through the manifold into the  $Q = X$  state, and yet it does not. The arrest of the system apparently so close to order is another key result of this work.

The nature of the partially ordered state was deduced for both compounds from the form of the scattering. It was concluded in both cases that there was no diffuse scattering which extended widely across reciprocal space, such as a rod or sheet would do (except for one weak feature in  $\text{Dy}_2\text{Ti}_2\text{O}_7$ ). Because of this the spins must be correlated in three dimensional domains. This is also supported by diffuse scattering calculations of such systems where models with three dimensional domains agree qualitatively with the observed scattering pattern. The domains are known to be highly anisotropic in  $\text{Dy}_2\text{Ti}_2\text{O}_7$  where the reciprocal space access of PRISMA gives two correlation lengths. The same is believed to be true for  $\text{Ho}_2\text{Ti}_2\text{O}_7$  but establishing the shape of these features in reciprocal space, using D10 data, is much harder. This points to a situation similar to the one described by Wannier for the triangular lattice Ising antiferromagnet [23]. In that case there was no energetic advantage to long range order and the triangular lattice Ising antiferromagnet has a manifold of disordered states which are favored due to their

greater weight. Here it is presumed that there is an energetic groundstate since one exists for zero field [64]. However, as with the zero field groundstate, it could well be weakly favored. Consequently the system is envisaged to be in a quasi-degenerate situation, where the energetic gain of long range order amongst these chains is not sufficient to drive the ordering before the dynamics become frozen instead.

The weak favoring of the ordered state and the anisotropic nature of the ordered domains can be conjectured to be due to two effects. Because the transverse chains are not coupled by nearest neighbor interactions the ordering of the system relies on the further neighbor dipolar interactions and these are relatively weak, and will have a complicated energy surface [59]. This could account for the small size of the domain in terms of number of chains. The order along the chains is much stronger as it is produced by nearest neighbor interactions. However, defects must remain, perhaps this is not surprising, we are discussing some of the most basic models of magnetism and the classical result predicting no order in an Ising chain at finite temperature should not be forgotten.

## 7.7 Contact with Other Experimental Work

The neutron scattering data casts some light on an experimental observation made by Ramirez *et al.* [56]. When measuring the heat capacity in an applied field, they noted three sharp peaks at field independent temperatures. These contributed a small fraction of the total spin entropy. They were attributed to ordering of the transverse chains. The small contribution to the entropy was because they measured a powder and so said only a very small proportion of grains would have the correct orientation. None of our temperature scans in applied field are consistent with three sharp temperature independent features. The explanation of these features by Ramirez is apparently not correct as long range order is not established in the transverse spin system.

The work in this thesis builds on and extends the work of Harris *et al.* [25]. Their interpretation of the  $Q = 0$   $45^\circ$  structure as the saturation field structure in their hysteresis loop was shown to be incorrect. The system remains partially

disordered. Their approximation of a fully ordered  $Q = X$  structure was shown to be insufficient, again because the system is only partially ordered.

The kagomé ice studies of Matsuhira *et al.* were supported. The data for the application of a field on  $[h\bar{h}\bar{h}]$  were consistent with the formation of a partially ordered structure, with only one spin on each tetrahedron ordering. In higher fields the data were consistent with the breaking of the ice rules and formation of a fully ordered structure.

The most recent work of Fukazawa *et al.* involves the measurement of the heat capacity in all four applied field directions discussed in this thesis<sup>c</sup> [131]. The main finding of this work was that in high fields the entropy was fully recovered for all directions. For intermediate fields the  $[hhh]$  direction has a residual entropy, but the other directions do not. The residual entropy is due to the kagomé ice state, a partially ordered state in finite field. Other such states have been identified in this thesis. It seems that no residual entropy has been detected. The most likely explanation for this is the same as that of Wannier [3], partly outlined on the first page of the introduction. Because the entropy is measured per spin, and not per chain, the residual entropy of the  $Q = X$  state is not detected. If their data was re-analyzed in terms of chains, Fukazawa *et al.* might reach another conclusion.

## 7.8 Future Work: Theoretical

Theoretical developments are often motivated by experiments. These experiments should offer several exciting problems for theorists to tackle.

First there are the zone boundary features in  $\text{Dy}_2\text{Ti}_2\text{O}_7$ . These might be investigated in two ways. First, further neighbor interactions might introduce some additional correlations. If they are weak, they will not necessarily be sufficient perturbation to cause a departure from the quasi-degenerate dipolar spin ice manifold. Alternatively attempts to produce defective spin ice states might be made. Short range correlations around the defects might explain the zone boundary features.

The processes operating in applied fields are very interesting, and are another open question for theorists. These may be tackled by simulating spin ices using

---

<sup>c</sup>Recently there has been a great deal of interest in the former mysteriously neglected direction!

different cooling and field cycling regimes [132].

The Reverse Monte Carlo technique is a way to model short range order. It would be ideal to apply to these systems. Indeed a whole RMC code was written, but there has been insufficient time to debug, run and optimize it; so this work has not been undertaken. Because of the the high level of constraint available (i.e. the well ordered crystal structure, and Ising spins), the Monte Carlo algorithm would only have to operate on Ising spin orientations. The method could be equally applied to zero field or applied field data. The application to zero field data, in parallel with ordinary Monte Carlo, could shed light on the origin of the zone boundary features. The difference between the spin configurations obtained should contain this information. PRISMA data is not ideal for RMC, and so it seems most sensible to await SXD data (see below). SXD data for ice has previously been investigated by RMC [88].

## 7.9 Future Work: Experimental

The next study of a spin ice by neutron scattering will be the investigation of the temperature dependence of the diffuse scattering in  $\text{Dy}_2\text{Ti}_2\text{O}_7$  using the SXD instrument at ISIS. This will provide a wealth of data about the spatial extent of diffuse features in reciprocal space. Currently data is limited to the two planes described here. It is of particular interest to see what happens to the zone boundary features, both as a function of space and temperature, especially to see if they evolve at the same time as the dipolar spin ice pattern emerges from the nearest-neighbor spin ice pattern. Gingras *et al.* propose that diffuse scattering data from higher temperatures could be used to parameterize further neighbor exchange interactions [132].

Bulk measurements represent a much more efficient way to operate in this history dependent regime. Major insight has come from the work of Matsuhira *et al.* in terms of dynamics [66, 67] and the kagomé ice observations [78, 79]. In the future it would be very interesting to map the phase diagrams as a function of parameters such as field stepping rate. For the  $[00l]$  orientation where the magnetization and the spin structure are simply related, a detailed magnetization

study could be used to suggest whether the steps are intrinsic or due to the rate of field scanning. It would be very interesting to extend the work of Ramirez *et al.* [56] and measure the heat capacity of a single crystal with a field applied on  $[hh0]$  to further investigate the sharp features. The kagomé ice studies have shown that heat capacity in an applied field is a useful way to characterize the spin ice states with coexisting long and short range order, as the entropy can be used to quantify the behavior of the partially ordered part.

SXD is unsuitable for use with a cryomagnet. Therefore it seems that RMC is unlikely to be a realistic prospect for applied field data. Another way to investigate the spin correlations in a field would be to use a horizontal field magnet. We have seen the shape of the  $Q = X$  features in the  $hhl$  plane with the field applied on  $[h\bar{h}0]$ . If the same crystal is mounted in a horizontal field magnet the field can be applied on  $[hh0]$  and the scattering plane remains  $hhl$ . However, the features will have changed orientation. Scans along  $[hh0]$  will now give information which is currently missing as it is perpendicular to the scattering plane.

The recent work of Moessner and Sondhi [111] has predicted the diffuse scattering pattern of the partially ordered kagomé ice phase. This represents an obvious and accessible experimental test of theory.

A final pet future project is the question of dynamics in the chains, especially perpendicular to the field. It seems likely that interesting soliton type dynamics could be investigated using inelastic neutron scattering.

## 7.10 Conclusions

To conclude, application of a field to a spin ice leads to partial or full removal of the degeneracy, depending upon the direction in which it is applied. The question of the true groundstate of a spin ice seems to be governed entirely by the dynamics. It appears that there are energetically favored states, but that they are at most weakly favored. The very slow dynamics and entropic weight of less ordered states prevents their ultimate selection. Spin ice remains an intriguing subject for further research with many experimental and theoretical avenues open.

# Appendix A

## Resolution Calculations for D10

Originally it was hoped to extract more information about the correlation lengths in  $\text{Ho}_2\text{Ti}_2\text{O}_7$  when the field is applied on  $[h\bar{h}0]$ . It turned out that the shape of the features were not amenable to resolution convolution. This may be due to the incompleteness of the following work. The method envisaged was to express the area detector pixel points as individual scattering vectors and so obtain the shape of the  $Q = X$  features in reciprocal space. An empirical resolution curve was then obtained to use in the convolutions.

### A.1 Inversion of the UB Matrix

On single crystal diffractometers such as D10 the orientation of the reciprocal lattice is determined during a set of preliminary measurements. Knowing the relation between the real space and the reciprocal space allows any Bragg peak to be driven into a diffracting condition. The matrix manipulations necessary were originally described by Busing and Levy [133]. At the heart of their method is the **UB**-matrix, which essentially describes the orientation of the reciprocal lattice on the diffractometer.

The crystal orientation is achieved by considering a hierarchial set of frames of reference (this treatment is slightly simpler than that of Busing and Levy as the details of the choice of instrument axes are not included, it is based on the Busing and Levy paper and is described by Azaroff [134]). The first frame of reference is

the reciprocal lattice. The reciprocal lattice is “attached” to the crystal which is attached quite firmly to a pin. Bragg scattering occurs when the scattering vector  $\mathbf{Q}$  is equal to a reciprocal lattice vector and the instrument settings bring  $\mathbf{Q}$  to the surface of the Ewald sphere. Consider a reciprocal lattice vector  $\mathbf{v}$  which may be defined in terms of the basis vectors of the reciprocal lattice  $\mathbf{b}_i$  as

$$\mathbf{v} = \sum_{i=1}^3 v_i \mathbf{b}_i. \quad (\text{A.1})$$

This is the scattering vector and the four circles of the diffractometer can be used to bring it into the diffracting condition.

A second frame of reference is specified in cartesian coordinates. This is the “crystal” frame. It is simply a cartesian frame considered to be rigidly attached to the crystal in a convenient orientation. A matrix is required to express  $\mathbf{v}$  as  $\mathbf{v}_c$ , a vector in the crystal frame, i.e.

$$\mathbf{v}_c = \mathbf{B}\mathbf{v}, \quad (\text{A.2})$$

where

$$\mathbf{B} = \begin{pmatrix} b_1 & b_2 \cos \beta_3 & b_3 \cos \beta_2 \\ 0 & b_2 \sin \beta_3 & -b_3 \sin \beta_2 \cos \alpha_1 \\ 0 & 0 & 1/a_3 \end{pmatrix} \quad (\text{A.3})$$

and the  $as/\alpha s$  and  $bs/\beta s$  refer to the crystal and reciprocal lattice parameters respectively.

Again another cartesian frame of reference is defined, now attached to the  $\phi$  axis of the diffractometer so that

$$\mathbf{v}_\phi = \mathbf{U}\mathbf{v}_c. \quad (\text{A.4})$$

The process is repeated for the other circles of the diffractometer  $\omega, \chi$  and  $2\theta$ . A frame of reference is defined attached to each of the axes and a matrix used to rotate from one to the next, such that

$$\mathbf{v}_\chi = \mathbf{\Phi}\mathbf{v}_\phi, \quad (\text{A.5})$$

$$\mathbf{v}_\omega = \mathbf{\chi}\mathbf{v}_\chi, \quad (\text{A.6})$$

$$\mathbf{v}_\theta = \mathbf{\Omega} \mathbf{v}_\omega, \quad (\text{A.7})$$

where

$$\mathbf{\Phi} = \begin{pmatrix} \cos \phi & \sin \phi & 0 \\ -\sin \phi & \cos \phi & 0 \\ 0 & 0 & 1 \end{pmatrix}, \quad (\text{A.8})$$

$$\chi = \begin{pmatrix} \cos \chi & 0 & \sin \chi \\ 0 & 1 & 0 \\ -\sin \chi & 0 & \cos \chi \end{pmatrix} \quad (\text{A.9})$$

and

$$\mathbf{\Omega} = \begin{pmatrix} \cos \omega & \sin \omega & 0 \\ -\sin \omega & \cos \omega & 0 \\ 0 & 0 & 1 \end{pmatrix}. \quad (\text{A.10})$$

The original reciprocal lattice vector of interest  $\mathbf{v}$  has the form

$$\mathbf{v} = \begin{pmatrix} h \\ k \\ l \end{pmatrix}. \quad (\text{A.11})$$

The normal to the selected planes has the correct orientation for diffraction if

$$\mathbf{h}_\theta = \mathbf{\Omega} \chi \mathbf{\Phi} \mathbf{U} \mathbf{B} \mathbf{v} \quad (\text{A.12})$$

has the form

$$\mathbf{h}_\theta = \begin{pmatrix} q \\ 0 \\ 0 \end{pmatrix}. \quad (\text{A.13})$$

where  $q = v_{c1}^2 + v_{c2}^2 + v_{c3}^2$  and  $\mathbf{h}_c = \mathbf{B} \mathbf{v}$ .

Equation A.13 depends on the axis system which has been defined for the  $2\theta$  circle. Here it is assumed that the  $2\theta$  frame has  $x$  and  $y$  in the horizontal plane of the laboratory,  $z$  is vertical and parallel to the main axis of the instrument. Also, the form of A.13 is only correct if the detector is confined to this plane. Some detectors (including the one on D10) can be tilted, in this case an extra frame of reference must be added to allow for the  $\nu$  circle.  $\mathbf{U}$  is determined from



the observation of the angle settings at three indexable reflections. All the other matrices are determined either from the angle settings or from the cell parameters.

The reason for this exposition of a standard piece of crystallographic mathematics follows. Usually an instrument such as D10 is used to produce a single integrated intensity for the scattering measured as a particular Bragg peak is scanned through the Ewald sphere. A conventional single tube detector samples a line in reciprocal space that crosses the Ewald sphere. However, since D10 is fitted with a small area detector, a volume of reciprocal space is measured. Using the geometry of the area detector, the **UB** matrix, and the angle settings of a measurement, it is possible to work backwards through the above treatment to obtain the individual scattering vectors (i.e.  $\mathbf{v}$  above) which are included in the volume of reciprocal space measured.

Let the laboratory frame of reference, which is right handed and has  $x$  parallel to the incident beam and  $z$  vertical, be  $L$ . When the scattering angle is zero the detector lies on the  $x$  axis. The vector from the sample to the center of the detector can then be written as

$$\mathbf{v}_{L0} = \begin{pmatrix} l \\ 0 \\ 0 \end{pmatrix}, \quad (\text{A.14})$$

where  $l$  is the distance from the sample to the detector. Knowing the size of the pixels a family of vectors can be written from the sample to each pixel. They have the form

$$\mathbf{v}_L = \begin{pmatrix} l \\ n_y y \\ n_z z \end{pmatrix}, \quad (\text{A.15})$$

where  $n_y$  is the number of pixels moved from the detector center, and  $y$  is the pixel width across the horizontal face of the detector and  $n_z$  and  $z$  are the equivalent quantities for vertical movements on the detector. These vectors all have different lengths so they are converted to unit vectors and then to vectors of length  $2\pi/\lambda$ . One of these vectors  $\mathbf{v}_L$  will be considered further.

The matrix product  $\mathbf{M} = \mathbf{UB}$  is available from the experiment. An extra term

is easily added to equation A.12 such that

$$\mathbf{v}_L = \mathbf{\Theta}\mathbf{\Omega}\mathbf{\chi}\mathbf{\Phi}\mathbf{U}\mathbf{B}\mathbf{v}. \quad (\text{A.16})$$

To obtain the identity of an arbitrary scattering vector from its laboratory frame equivalent and the angle settings it is simply required to invert equation A.16:

$$\mathbf{v} = \mathbf{M}^{-1}\mathbf{\Phi}^{-1}\mathbf{\chi}^{-1}\mathbf{\Omega}^{-1}\mathbf{\Theta}^{-1}\mathbf{v}_L. \quad (\text{A.17})$$

In practice this is achieved by creating a bundle of vectors at the  $2\theta = 0$  position and rotating them by  $2\theta^\circ$ . Then each of the matrices is calculated for the angle settings of the point in the omega scan and inverted numerically. At the end of this process each individual measured intensity (for a pixel point) can be related to an individual vector in the reciprocal lattice. A three dimensional data structure is obtained with dimensions  $32 \times 32 \times 30$  for the  $32^2$  pixel area detector and a 30 point scan.

The simplest way to analyze this three dimensional data set seemed to be to make cuts. The most sensible place to start was with three perpendicular cuts, each passing through the center of the data volume. To improve statistics four pixels surrounding each point were averaged (also since there is an even number of pixels/points cuts passing through the center of the data volume must consist of averages of surrounding points). The first cut contains the four central pixels from each frame. This cut therefore tracks the omega scan in reciprocal space. The second cut contains the central two columns of pixels from the area detector, in the central two frames of the scan. This is the vertical cut through the data volume. The final cut contains the central two rows of pixels from the area detector in the central two frames of the scan. This is another horizontal cut in the scattering plane. Whilst it is perpendicular to the first cut in the data volume, it follows the same trajectory in reciprocal space. The cuts through the data volume are illustrated schematically in figure A.1.

Because the first cut type tracks the omega scan in reciprocal space, the coordinates can be used in conjunction with the total counts in the frame. If the points measured by the central pixels are plotted in the reciprocal space it can be seen that the omega scan at a  $00l$  point is an arc. The tangent to the arc is

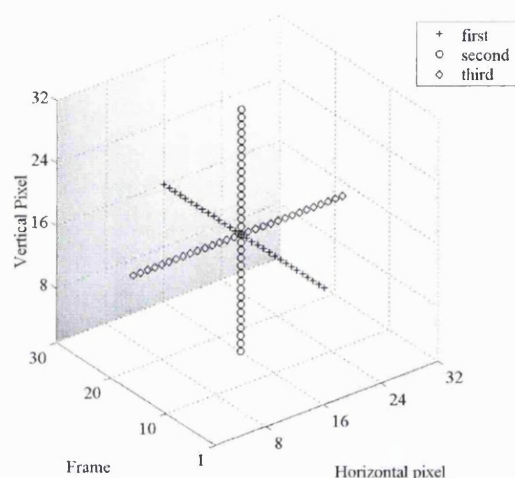


**Figure A.1:** Illustration of the three simplest slices through the D10 data volume. The first slice type corresponds to the omega scan, the second is perpendicular to the scattering plane, the third also follows the omega scan in the scattering plane. The shaded plane represents a single frame of data (the thirtieth) in an  $\omega$  scan.

perpendicular to  $[00l]$ . A typical omega scan is a very short distance in reciprocal space and barely deviates from a straight line. Similarly omega scans about  $hh0$  points are essentially perpendicular to  $[hh0]$ . The omega scans about 001 and 110 measured in this experiment are shown in figure A.2. The importance of the **UB**-matrix inversion is that it allows the investigation of non-resolution limited features in specific directions in reciprocal space. Typically an  $\omega$ -scan would only provide an integrated intensity from a Bragg reflection and non-resolution limited features could only be investigated as a function of the  $\omega$ -rotation of the crystal.

## A.2 Resolution on D10

Because the point of the inversion of the **UB** matrix is to investigate in detail the non-Bragg features it becomes important to understand the resolution of the instrument. An empirical method was used to estimate the resolution of D10 when measuring at the 001 and 110 positions. The largest set of data for the appropriate wavelength comes from the extinction correction measurement on the

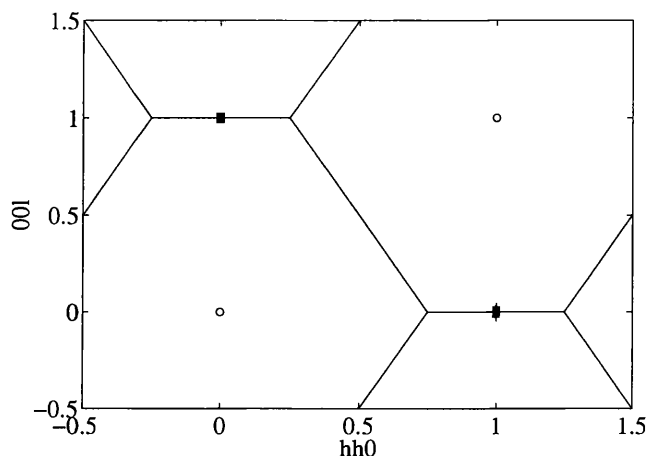


**Figure A.2:** Illustration of the reciprocal space points sampled by  $\omega$  scans at 110 and 001 on D10. Evidently an  $\omega$  scan covers a very small volume of reciprocal space and is effectively perpendicular to the axis of the Bragg peak at which it is measured.

large crystal. The full width of the peak at half maximum height is output by the peak integrating program Racer. The widths were extracted from the output and used to estimate the peak width dependence on  $2\theta$ . After rejection of spurious widths due to weak peaks all data points at a particular  $2\theta$  were averaged. No estimate of the error of this width is provided by Racer so it was estimated as the standard deviation of the measured widths from the average width at given  $2\theta$ . The angle dependence of the peak width was fitted with a five term polynomial. Five terms were found to provide a suitably smooth function and good fit without meaningless addition of terms. This polynomial was used to calculate the expected width of a Bragg peak for the 001 and 110 positions where the non-Bragg features occur. The fit and the extrapolation are shown in figure A.3. The calculated widths were  $0.38 \pm 3^\circ$  and  $0.34 \pm 5^\circ$  respectively. This gives a resolution of  $0.0024 \pm 0.0002$   $00l$  at 001 and  $0.0042 \pm 0.0006$   $hh0$  at 110. The resolution information can be used to convolute a gaussian effective resolution function with a single Lorentzian or Gaussian to obtain the correlation lengths parallel to  $[hh0]$  (from 001) and to  $[00l]$  (from 110).

It proved most effective to fit a gaussian to the peak, convoluted with a gaussian

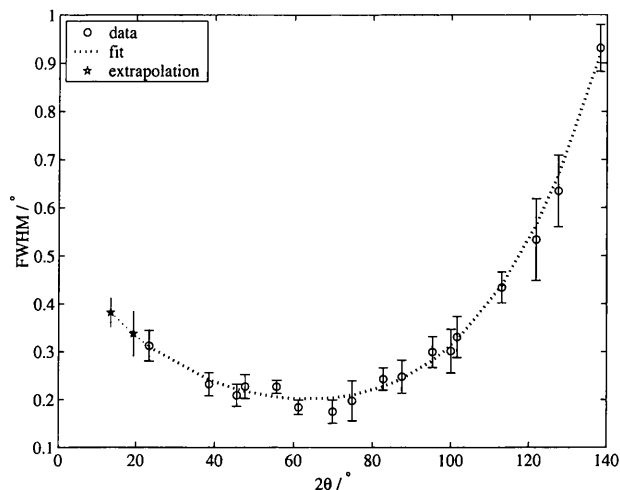


**Figure A.3:** Dependence of the width of Bragg peaks on the  $2\theta$  angle using a wavelength of 2.36 Å on D10.

representing the resolution. The widths of the resolution function were calculated previously. The background was fixed at the average for the Bragg peaks shown in figure 5.10. The width of the fitted feature must be converted from degrees in omega into a proper correlation length. The **UB**-matrix inversion code was used to convert two points  $\omega_0$  and  $\omega_0 + \Delta\omega$  into the reciprocal lattice points at which they would have been measured. The width in units of  $hh0$  or  $00l$  can be easily converted to a correlation length in angstroms.

Another important issue is the vertical resolution. The vertical extent of the type of features under investigation is very interesting. With the empirical approach to the quantification of the resolution taken here, we have no information about the vertical resolution. The only resolution function available is the width of a Bragg peak, in the scattering plane (i.e, during an  $\Omega$ -scan). Any study of the vertical shape of these features would therefore be qualitative. It can be seen, from comparison with Bragg peaks that they are outside the resolution. However, the vertical resolution of an instrument like D10 is often rather poorly optimized. In order to complete this work a rather arduous process of fitting the widths of Bragg peaks, from raw data files, would be required to generate a similar curve.

# Bibliography

- [1] C. Dickens, *A Tale of Two Cities* (Wordsworth Editions Ltd., Ware, 1993).
- [2] W. G. V. Rosser, *An Introduction to Statistical Physics* (Ellis Horwood Limited, Chichester, 1982).
- [3] G. H. Wannier, *Statistical Physics* (Dover Publications, Inc., New York, 1966).
- [4] W. F. Giaque and J. W. Stout, J. A., Chem. Soc. **58**, 1144 (1936).
- [5] L. Pauling, J. Am. Chem. Soc. **57**, 2680 (1935).
- [6] V. F. Petrenko and R. W. Whitworth, *The Physics of Ice* (Oxford University Press, Oxford, 1999).
- [7] H. E. Stanley, *Introduction to Phase Transitions and Critical Phenomena* (Oxford University Press, Oxford, 1971).
- [8] C. Kittel, *Introduction to Solid State Physics* (John Wiley and Sons, Inc., Chichester, 1996).
- [9] R. L. Carlin, *Magnetochemistry* (Springer, Berlin, 1986).
- [10] J. A. Mydosh, *Spin Glasses: an experimental introduction* (Taylor and Francis, London, 1993).
- [11] J. Rossat-Mignot, *Magnetic Structures in "Methods of Experimental Physics, volume 23, Part C, ed. K Sköld, D. L. Price* (Academic Press, London, 1987).

- [12] A. S. Wills, Magnetic Structures and Representational Analysis, (ftp://ftp.ill/wills/transit, 2000).
- [13] Y. A. Izyumov, V. E. Naish, and R. P. Ozerov, *Neutron Diffraction of Magnetic Materials* (Consultants Bureau, New York, 1991).
- [14] W. Opechowski and R. Guccione, *Magnetism, vol. 2, ed. G. T. Rado, H. Suhl* (Academic Press, London, 1965).
- [15] K. Stephens, *Magnetism, vol. 1, ed. G. T. Rado, H. Suhl* (Academic Press, London, 1963).
- [16] C. Domb, *Magnetism, vol. 2a, ed. G. T. Rado, H. Suhl* (Academic Press, London, 1965).
- [17] J. J. Binney, N. J. Dowrick, A. J. Fisher, and M. E. J. Newman, *The Theory of Critical Phenomena: An Introduction to the Renormalization Group* (Clarendon, Oxford, 1992).
- [18] S. T. Bramwell, M. N. Field, M. J. Harris, and I. P. Parkin, J. Phys.: Condens. Mat. **12**, 483 (2000).
- [19] M. J. P. Gingras, B. C. den Hertog, M. Faucher, J. S. Gardner, S. Dunsiger, L. J. Chang, B. D. Gaulin, N. Raju, and J. E. Greedan, Phys. Rev. B **62**, 6496 (2000).
- [20] L. J. de Jongh and A. R. Miedema, *Experiments on Simple Magnetic Model Systems* (Taylor & Francis, London, 1974).
- [21] M. P. Zinkin, M. J. Harris, and T. Zeiske, Phys. Rev. B **56**, 11786 (1997).
- [22] A. P. Ramirez, Annu. Rev. Mater. Sci. **24**, 453 (1994).
- [23] G. H. Wannier, Phys. Rev. **79**, 357 (1950).
- [24] P. W. Anderson, Phys. Rev. **102**, 1008 (1956).
- [25] M. J. Harris, S. T. Bramwell, D. F. McMorrow, T. Zeiske, and K. W. Godfrey, Phys. Rev. Lett. **79**, 2554 (1997).

- [26] G. Ferey, R. de Pape, M. Leblanc, and J. Pannetier, *Rev. Chem. Miner.* **23**, 474 (1986).
- [27] J. C. Maxwell, *Phil. Mag.* **27**, 294 (1864).
- [28] R. Moessner, *Can. J. Phys.* **79**, 1283 (2001).
- [29] R. Moessner and J. T. Chalker, *Phys. Rev. Lett.* **80**, 2929 (1998).
- [30] J. Villain, *Z. Phys. B* **33**, 31 (1979).
- [31] S. T. Bramwell, M. J. P. Gingras, and J. N. Reimers, *J. Appl. Phys.* **75**, 5523 (1994).
- [32] J. T. Chalker, P. C. W. Holdsworth, and E. F. Shender, *Phys. Rev. Lett.* **68**, 855 (1992).
- [33] J. D. M. Champion, M. J. Harris, P. C. W. Holdsworth, A. S. Wills, G. Balakrishnan, S. T. Bramwell, E. Cizmar, T. Fennell, J. S. Gardner, J. Lago, D. F. McMorrow, M. Orendac, A. Orendacova, D. M. Paul, R. I. Smith, M. T. F. Telling, and A. Wildes, *Phys. Rev. B*, 2003.
- [34] J. N. Reimers, *Phys. Rev. B* **45**, 7287 (1992).
- [35] N. Raju, M. Dion, M. J. P. Gingras, T. E. Mason, and J. E. Greedan, *Phys. Rev. B* **59**, 14489 (1999).
- [36] S. E. Palmer and J. T. Chalker, *Phys. Rev. B* **62**, 488 (2000).
- [37] J. N. Reimers, A. J. Berlinsky, and A. C. Shi, *Phys. Rev. B* **43**, 865 (1991).
- [38] S. T. Bramwell and M. J. P. Gingras, *Science* **294**, 1495 (2001).
- [39] G. Bertotti, *Hysteresis in Magnetism* (Academic Press, London, 1998).
- [40] J. P. Sethna, O. Perković, and K. Dahmen, *Hysteresis, Avalanches, and Barkhausen Noise in "Scale Invariance and Beyond: Les Houches Workshop, March 10-14, 1997"* (Springer, Berlin, 1997).
- [41] O. Perković, K. Dahmen, and J. Sethna, *Phys. Rev. Lett.* **75**, 4528 (1995).



- [42] H. J. Jensen, *Self-Organized Criticality* (Cambridge University Press, Cambridge, 1998).
- [43] D. Sornette, J. Phys. I **4**, 209 (1994).
- [44] J. R. Friedman, M. P. Sarachik, J. Tejada, and R. Ziolo, Phys. Rev. Lett. **76**, 3830 (1996).
- [45] E. M. Chudnovsky and J. Tejada, *Macroscopic Quantum Tunneling of the Magnetic Moment* (Cambridge University Press, Cambridge, 1998).
- [46] T. M. Rice, Science **298**, 760 (2002).
- [47] K. Kodama, M. Takigawa, M. Horvatic, C. Berthier, H. Kageyama, Y. Ueda, S. Miyahara, F. Becca, and F. Mila, Science **298**, 395 (2002).
- [48] E. Müller-Hartmann, R. R. P. Singh, C. Knetter, and G. S. Uhrig, Phys. Rev. Lett. **84**, 1808 (2000).
- [49] H. W. J. Blöte, R. F. Weilinga, and H. Huiskamp, Physica **43**, 549 (1969).
- [50] R. D. Roth, J. Res. Nat. Bur. Std. **56**, 17 (1956).
- [51] O. Knop, F. Brisse, and L. Castelliz and Sutarno, Can. J. Chem. **43**, 2812 (1965).
- [52] S. Rosenkranz, A. P. Ramirez, A. Hayashi, R. J. Cava, R. Siddharthan, and B. S. Shastry, J. Appl. Phys. **68**, 855 (1992).
- [53] Y. M. Jana and D. Ghosh, Phys. Rev. B **61**, 9657 (2000).
- [54] M. J. Harris, S. T. Bramwell, T. Zeiske, D. F. McMorrow, and P. J. C. King, J. Magn. Magn. Mater. **177**, 757 (1998).
- [55] M. J. Harris, S. T. Bramwell, P. C. W. Holdsworth, and J. D. M. Champion, Phys. Rev. Lett. **81**, 4496 (1998).
- [56] A. P. Ramirez, A. Hayashi, R. J. Cava, R. Siddharthan, and B. S. Shastry, Nature **399**, 333 (1999).

- [57] S. T. Bramwell, M. J. Harris, B. C. den Hertog, M. J. P. Gingras, J. S. Gardner, D. F. McMorrow, A. R. Wildes, A. L. Cornelius, J. D. M. Champion, R. G. Melko, and T. Fennell, *Phys. Rev. Lett.* **87**, 047205 (2001).
- [58] J. D. M. Champion, S. T. Bramwell, P. C. Holdsworth, and M. J. Harris, *Europhys. Lett.* **57**, 93 (2002).
- [59] B. C. den Hertog and M. J. P. Gingras, *Phys. Rev. Lett.* **84**, 3430 (2000).
- [60] R. Siddharthan, B. S. Shastry, A. P. Ramirez, A. Hayashi, R. J. Cava, and S. Rosenkranz, *Phys. Rev. Lett.* **83**, 1854 (1999).
- [61] S. T. Bramwell and M. J. Harris, preprint .
- [62] M. J. P. Gingras and B. C. den Hertog, *Can. J. Phys* **79**, 1339 (2001).
- [63] R. Moessner, *Phys. Rev. B* **57**, R5587 (1998).
- [64] R. G. Melko, B. C. den Hertog, and M. J. P. Gingras, *Phys. Rev. Lett.* **87**, 067203 (2001).
- [65] H. Fukazawa, R. G. Melko, R. Higashinaka, Y. Maeno, and M. J. P. Gingras, *Phys. Rev. B* **65**, 054410 (2002).
- [66] K. Matsuhira, Y. Hinatsu, K. Tenya, and T. Sakakibara, *J. Phys.: Condens. Mat.* **12**, L649 (2000).
- [67] K. Matsuhira, Y. Hinatsu, and T. Sakakibara, *J. Phys.: Condens. Mat.* **13**, L737 (2001).
- [68] J. Snyder, J. S. Slusky, R. J. Cava, and P. Schiffer, *Nature* **413**, 48 (2001).
- [69] G. Ehlers, A. L. Cornelius, M. Orendáč, M. Kajčnacová, T. Fennell, S. T. Bramwell, and J. S. Gardner, *J. Phys.: Condens. Mat.* **15**, L9 (2003).
- [70] M. J. Harris, unpublished data.
- [71] K. S. Cole and R. H. Cole, *J. Chem. Phys.* (1941).
- [72] C. J. Gorter and R. de L. Kronig, *Physica* (1936).

- [73] H. B. G. Casimir and F. K. du Pre, *Physica* (1938).
- [74] D. W. Davidson and R. H. Cole, *J. Chem. Phys.* (1950).
- [75] D. W. Davidson and R. H. Cole, *J. Chem. Phys.* (1951).
- [76] A. L. Cornelius and J. S. Gardner, *Phys. Rev. B* **64**, 060406(R) (2001).
- [77] O. A. Petrenko, M. Lees, and G. Balakrishnan, *arXiv:cond-mat/* (2002).
- [78] K. Matsuhira, Z. Hiroi, T. Tayama, S. Takagi, and T. Sakakibara, *J. Phys.: Condens. Mat.* **14**, L559 (2002).
- [79] Z. Hiroi, K. Matsuhira, S. Takagi, T. Tayama, and T. Sakakibara, *J. Phys. Soc. Japan* **72**, 411 (2002).
- [80] R. Siddharthan, B. S. Shastry, and A. P. Ramirez, *Phys. Rev. B* **63**, 184412 (2001).
- [81] A. S. Wills, R. Ballou, and C. Lacroix, *Phys. Rev. B* **66**, 144407 (2002).
- [82] S. T. Bramwell and M. J. Harris, *J. Phys.: Condens. Mat.* **10**, L215 (1998).
- [83] J. S. Gardner, S. Dunsiger, B. D. Gaulin, R. Kiefl, M. D. Lumsden, Z. Tun, N. Raju, I. Swainson, and J. E. Greedan, *Phys. Rev. Lett.* **82**, 1012 (1999).
- [84] J. D. M. Champion, A. S. Wills, T. Fennell, S. T. Bramwell, J. S. Gardner, and M. A. Green, *Phys. Rev. B* (2001).
- [85] G. L. Squires, *Introduction to the Theory of Thermal Neutron Scattering* (Dover Publications, Inc., New York, 1978).
- [86] J. D. Dunitz, *X-Ray Analysis and the Structure of Organic Molecules* (Cornell University Press, Ithaca, 1979).
- [87] L. V. Azároff, *Elements of X-Ray Crystallography* (McGraw-Hill Book Company, London, 1968).
- [88] V. M. Nield and D. A. Keen, *Diffuse Neutron Scattering from Crystalline Materials* (Clarendon Press, Oxford, 2001).

- [89] S. W. Lovesey, *Theory of Neutron Scattering from Condensed Matter: Volume 1, Nuclear Scattering* (Clarendon, Oxford, 1984).
- [90] S. W. Lovesey, *Theory of Neutron Scattering from Condensed Matter: Volume 2, Polarization effects and Magnetic Scattering* (Clarendon, Oxford, 1984).
- [91] C. G. Darwin, *Phil. Mag.* **43**, 800 (1922).
- [92] W. H. Zachariasen, *Acta Cryst.* **23**, 558 (1967).
- [93] P. J. Becker and P. Coppens, *Acta Cryst. A* **30**, 129 (1974).
- [94] P. J. Becker and P. Coppens, *Acta Cryst. A* **30**, 148 (1974).
- [95] V. M. Nield and R. W. Whitworth, *J. Phys.: Condens. Mat.* **7**, 8259 (1995).
- [96] P. J. Brown and J. C. Matthewman, *The Cambridge Crystallography Subroutine Library User's Manual* (Institut Laue Langevin, Grenoble, 2001).
- [97] T. Hahn, *International Tables for Crystallography Volume A: Space Group Symmetry* (D Reidel Publishing Company, Dordrecht, 1983).
- [98] S. Niitaka, K. Yoshimura, K. Kosuge, M. Nishi, and K. Kakurai, *Phys. Rev. Lett.* **87**, 177202 (2001).
- [99] O. Koseki and F. Matusbara, *J. Phys. Soc. Jpn.* **69**, 1202 (2000).
- [100] Our crystals were grown and supplied by the group of B. M. Wanklyn, Oxford.
- [101] J. Rodriguez-Carvajal, *Physica B* **192**, 55 (1993).
- [102] J. C. Matthewman, P. Thompson, and P. J. Brown, *J. Appl. Cryst.* **15**, 167 (1982).
- [103] G. Sheldrick, *Acta Cryst. A* **40**, C440 (1984).
- [104] P. J. Brown, V. Nunez, F. Tasset, and J. B. Forsyth, *Acta Cryst. A* **48**, 236 (1992).

- 
- [105] D. Watkin, *Acta Cryst A* **50**, 411 (1994).
- [106] J. S. Gardner, unpublished hypothesis.
- [107] H. Cole, F. W. Chambers, and H. M. Dunn, *Acta. Cryst* **15**, 138 (1962).
- [108] R. M. Moon and C. G. Schull, *Acta. Cryst* **17**, 805 (1964).
- [109] M. Orendac, communication/unpublished data.
- [110] P. C. W. Holdsworth, communication.
- [111] R. Moessner and S. L. Sondhi, arXiv:cond-mat/ 0303210 (2003).
- [112] T. Sakakibara, T. Tayama, Z. Hiroi, K. Matsuhira, and S. Takagi, *Phys. Rev. Lett.* **90**, 207205 (2003).
- [113] W. C. Hamilton, *Acta Cryst* **18**, 502 (1965).
- [114] G. Balakrishnan, O. A. Petrenko, M. R. Lees, and D. M. Paul, *J. Phys.: Condens. Mat.* **10**, L723 (1998).
- [115] The initial alignment and realignments on PRISMA were carried out by Oleg Petrenko.
- [116] B. Fåk, VCRS data normalisation routines for PRISMA, 2002.
- [117] V. F. Sears, *J. Appl. Cryst.* **17**, 226 (1984).
- [118] B. Fåk, communication.
- [119] T. Fennell, *tslice*: Matlab data manipulation routines for PRISMA, 2001-2.
- [120] M. S. Lehmann and F. K. Larsen, *Acta Cryst A* **30**, 580 (1974).
- [121] G. Shirane, S. M. Shapiro, and J. M. Tranquada, *Neutron Scattering with a Triple Axis Spectrometer* (Cambridge University Press, Cambridge, 2002).
- [122] M. J. Cooper and R. Nathans, *Acta Cryst A* **23**, 357 (1967).
- [123] M. Hagen and U. Steigenberger, *Nucl. Inst. and Methods B* **72**, 239 (1992).

- 
- [124] T. Fennell, Matlab routines for PRISMA resolution convolution in *Mfit*, 2003.
- [125] M. Zinkin, E. Farhi, and D. McMorrow, *Mfit* package for data fitting in Matlab, 1997-9.
- [126] M. Enjalran, communication.
- [127] G. J. McIntyre, communication.
- [128] I thank Simon Banks for production of a Metropolis algorithm at extremely short notice.
- [129] A. P. Ramirez, C. L. Broholm, R. J. Cava, and G. R. Kowach, *Physica B* **280**, 290 (2000).
- [130] S.-H. Lee, C. L. Broholm, W. Ratcliff, G. Gasparovic, Q. Huang, T. H. Kim, and S.-W. Cheong, *Nature* **418**, 856 (2002).
- [131] R. Higashinaka, H. Fukazawa, and Y. Maeno, arXiv:cond-mat/ (2003).
- [132] M. J. P. Gingras, communication.
- [133] W. R. Busing and H. A. Levy, *Acta Cryst. A* **22**, 457 (1967).
- [134] L. V. Azároff, R. Kaplow, N. Kato, R. J. Weiss, A. J. C. Wilson, and R. A. Young, *X-Ray Diffraction* (McGraw-Hill, London, 1974).